Heterogeneously Catalysed Aerobic Oxidation of Alcohols in Microstructured Reactors

Noor Al-Rifai

A thesis submitted for the degree of

Doctor of Philosophy

University College London

April 2016

Department of Chemical Engineering

University College London

I, Noor Al-Rifai, confirm that the work presented in this thesis is my own. Where information has been derived from other sources, I confirm that this has been indicated in the thesis.

Signature: _____

Date: _____

Abstract

The goal of this thesis research was to develop microfluidic platforms for the study of gas-solid and gas-liquid-solid alcohol oxidation reactions. The desired products of these reactions are of great importance industrially due to their value as intermediates in industries such as the fine chemical and pharmaceutical sectors. The application of microreaction technology to these reactions is proving to be beneficial due to their high surface area-to-volume ratio, resulting in fast heat and mass transfer and an ability to circumvent problems such as high exothermicity, mass transfer limitations, and poor control of reaction conditions.

Two types of reaction systems were developed to facilitate this research; a three-phase micro-packed bed reactor for the study of benzyl alcohol oxidation on supported gold-palladium catalyst and a wall-coated microreactor for the study of methanol oxidation to formaldehyde on silver catalyst. Reaction and deactivation flow studies were first conducted in continuous flow microfluidic setups to understand catalyst activation and deactivation behaviour, culminating in the selection of the most stable catalyst formulation. These reaction studies were followed by a series of hydrodynamic and mass transfer investigations, where differences in hydrodynamics to conventional macroscale systems were identified, and a classification of flow regimes applicable to micro-packed bed reactors presented. An understanding of the influence of hydrodynamics on mass transfer, catalyst deactivation and reaction performance has been developed for benzyl alcohol oxidation, resulting in enhancement in flow reactor performance in comparison to batch.

Exploration of different microreactor designs, to cope with challenging process conditions, as well as the application of novel methods for reactor characterization (such as Raman spectroscopy) are also presented.

Acknowledgements

I owe a particular debt of gratitude to my primary supervisor, Professor Asterios Gavriilidis, to whom I am grateful not only for the guidance and mentorship throughout my PhD, but also for enriching my experience with involvement in a variety of projects and collaborations, the results of which have been numerous publications and conference presentations.

I would also like to thank a few other people: Dr Vivek Dua for being my second supervisor, Dr Enhong Cao for taking me on my first steps in microfluidics and for completing experiments on the methanol system; Dr Simon Barrass for the electrical work on the experimental rigs; Dr Steve Firth from the Department of Chemistry for help with the TEM characterisation and the Raman microscope and Steve Etienne from the London Centre of Nanotechnology for training on microfabrication.

Special thanks to members of the Cardiff Catalysis Institute: Dr Sankar Meenakshisundaram and Dr Moataz Morad for the catalyst preparation, Dr Peter Miedziak for TEM characterisation and Professor Graham Hutchings for making this collaboration possible.

I would also like to thank my line manager, Professor Eva Sorensen, for being understanding and supportive during my thesis write-up period.

My family has been a great source of moral and practical support; to my siblings Zeyad, Renda, and Hani: I love you all.

Finally, I would like to dedicate this thesis to my mum and dad, Farah and Hilal. Thank you for the unconditional love and support; all that I am, I owe to you both.

To my parents.

Contents

Appendix C

On-Chip RTD Measurements using Raman Spectroscopy Supplementary Information 306

List of Figures

List of Tables

Nomenclature

A	Reaction component in the gas phase
[A]*	Equilibrium concentration of the gaseous component A in the liquid phase, (mol/cm^3)
a_{GL} or a_L	Gas-liquid interfacial area per unit volume, (m^2/m$_{bed}^3$); for the calculation involving radial dispersion, this is calculated using $a_{GL} = \frac{\varepsilon_b l_{ch}}{\left(\frac{1}{4}\right)\pi {d_t}^2}$
a_P	Particle surface area per unit volume, (m^{-1})
Bo	Bodenstein number: bed Peclet number based on the particle diameter as the characteristic length, $\left[\frac{v d_p}{D}\right]$
[BzOH]	Benzyl alcohol concentration, (mol/kg)
c	Species concentration, (mol/m^3)
Cap_L	Capillary number (liquid phase) $\left[\frac{\mu_L u_{o,L}}{\sigma_L}\right]$
Ca	Capillary number for segmented flow
C_A	Concentration of species A in the liquid phase, mol/m^3
$C_{i,L}$	Liquid concentration of component i, (mol/m^3)
C_{Im}	Conventional impregnation catalyst
C_0	Tracer initial concentration, (mol/cm^3)
$C(t)$	Tracer concentration as a function of time, (mol/cm^3)

C_p	Heat capacity, (J/kgK)
C_{max}	Maximum concentration of tracer, (mol/cm^3)
d_t	Channel hydraulic diameter, (m)
d_p	Particle diameter, (m)
D	Reactor diameter, (m)
D	Axial dispersion coefficient for a flowing fluid (m^2/s)
D	Diffusion coefficient, m^2/s
D_b	Bulk diffusivity, (m^2/s)
D_{eff}	Effective molecular diffusivity, (m^2/s)
$D_{i,L}$	Bulk diffusivity of component i in the liquid phase, $\left[1.1728\times 10^{-16}\frac{T\sqrt{XM_2}}{\eta_2 V^{0.6}}\right]$, (m^2/s)
$D_{rad,i,L}$	Effective radial dispersion component i in the liquid phase, $\left[\varepsilon_b\left(\frac{D_{i,L}}{\tau_b}+0.137 d_p\frac{u_{o,L}}{h_L}\right)\right]$, (m^2/s)
d_p	Particle diameter, (m)
E(t)	Residence time distribution function, (ms^{-1})
E(θ)	Dimensionless output to a step input, the residence time distribution function
F(t)	Dimensionless output to a step input, C/C$_{max}$
F_{PhCHO}	Molar flow rate of benzaldehyde produced, (mol/s)
$F_{PhCH_2OH,0}$	Inlet molar flow rate of benzyl alcohol, (mol/s)
F_{PhCH_3}	Molar flow rate of toluene produced, (mol/s)

g	Gravitational acceleration (m/s^2)
G	Gas flow rate, (NmL/min)
h_L	Liquid holdup, (m^3/m_{void}^3)
k_{1x}	Rate constant for the oxidation reaction pathway (mol/s)
k_{2x}	Rate constant for the disproportionation reaction pathway (mol/s)
k_G, k_L	Mass transfer coefficient at the gas-liquid interface (gas side and liquid side), (m/s)
$k_{GL,A}$	Mass transfer coefficient at the gas-liquid interface, (m/s)
$k_{SL,A}$	Liquid-solid mass transfer coefficient (m/s)
$k_{GL,A}a_L$	Total volumetric mass transfer coefficient of A at the gas-liquid interface (s^{-1})
$k_{SL,A}a_P$	Volume-based solid-liquid mass transfer coefficient of A (s^{-1})
k_t	Thermal conductivity, (W/mK)
k_{w1}	Weight-based reaction rate constant of 1st order ($m^3/kg_{cat}.s$)
K_D^B	Benzyl alcohol dissociation constant (mol/kg)
K_D^O	Oxygen dissociation constant (mol/kg)
l	Characteristic length, (m)
l_{ch}	Length of slab of the G-L interface in the worst case scenario, (m)
L	Liquid flow rate, (µl/min)
L_b	Reactor length, (m)
$M_{Im,\ const}$, $M_{Im,\ vary}$	Modified impregnation catalyst (constant and varying Cl)

mol_{metal}	Moles of metal, (mol)
n	Order of reaction
$N_{W\text{-}P}$	Weisz-Prater number
$[O_2]$	Oxygen concentration, (mol/kg)
$[O_2]^*$	Equilibrium concentration of oxygen in the liquid phase, (mol/m^3)
$P_{b,tot}$	Total power, (W)
Pe	Peclet number
R	Reaction rate, (mol/m^3)
Re_L	Reynolds number (liquid phase) $\left[\frac{\rho_L u_{o,L} d_p}{\mu_L}\right]$
R_O	Weight based oxidation reaction rate, mol/g.s.
R_P	Particle radius, (m)
$R_{v,i}^{obs}$	Observed reaction rate of component i, (mol/m$_{particle}^3$s)
r_o	Oxidation surface reaction rate, (mol/m^{2}s)
r_d	Disproportionation surface reaction rate, (mol/m^{2}s)
S	Selectivity, (%)
S_{PhCHO}	Selectivity to benzaldehyde, (%)
S_{PhCH_3}	Selectivity to toluene, (%)
S_c	Inverse of catalyst specific surface area, (kg/m^2)
t	Time, (ms)
t_1	Time between the tracer injection valve and the microreactor

	entrance, (ms)
t_2	Time between the tracer injection valve and the microreactor exit, (ms)
$\bar{t}$	Mean residence time, (s)
T	Temperature, °C
TOF_D	Disproportionation reaction turnover frequency (s^{-1})
TOF_O	Oxidation reaction turnover frequency (s^{-1})
TOF_T	Total turnover frequency (s^{-1})
$u_{o,L}$	Superficial liquid velocity, (m/s)
$\boldsymbol{u}$	Velocity vector, (m/s)
u_G	Gas superficial velocity, (m/s)
u_L	Liquid superficial velocity, (m/s)
U_b	Bubble velocity, (m/s)
v_{in,O_2}	Oxygen inlet volumetric flowrate (ml/min)
$v_{in,BzOH}$	Benzyl alcohol inlet volumetric flowrate (ml/min)
V_r	Reactor volume, (mm^3)
X	Conversion, %
X_o	Initial conversion, %
X_f	Final conversion, %
w	Weight of catalyst per unit volume of reactor, kg/m^3)

Greek symbols

Λ	Dimensionless flow parameter $\left(\left[\left(\frac{\rho_G}{\rho_A}\right)\left(\frac{\rho_L}{\rho_w}\right)\right]^{0.5}\right)$
Ψ	Dimensionless flow parameter $\frac{\sigma_w}{\sigma}\left[\left(\frac{\mu_L}{\mu_w}\right)\left(\frac{\rho_w}{\rho_L}\right)^2\right]^{1/3}$
ϕ_{rad}	Weisz modulus for radial mass transfer
δ_G	Gas film thickness, (m)
δ_L	Liquid film thickness, (m)
ε_b	Bed voidage, (m^3/m_{bed}^3)
μ_L	Liquid viscosity, (Pa s)
μ_w	Viscosity of water, (Pa s)
ρ_A	Density of air, (kg/m^3)
ρ_c	Catalyst density, kg/m^3
ρ_G	Gas density, (kg/m^3)
ρ_L	Liquid density, (kg/m^3)
ρ_w	Density of water, (kg/m^3)
τ_b	Bed tortuosity, calculated from $\tau_b = \left(\frac{(1-\varepsilon_b)^{\frac{4}{3}}}{\varepsilon_b \phi^2}\right)$ assuming ϕ=0.4
ϕ	Particle sphericity
σ_{st}	Gas-liquid surface tension, (N/m)
σ_w	Water surface tension, (N/m)

η	Effectiveness factor
τ	Residence time, (s)
σ	Standard deviation
σ^2	Variance (s^2)
θ	Dimensionless time $\theta = \frac{t}{\bar{t}}$

I.

Introduction

This chapter presents the background and motivation for the use of microreactors as lab investigation tools in this thesis research. The motivation for the study of the two reaction systems presented in this thesis is explained. Finally, a thesis roadmap is presented at the end of the chapter, outlining the structure of the document.

1.1 Microreactors as Experimental Tools for Research

Microreaction technology is an attractive and rapidly developing interdisciplinary field. It has found applications in many areas such as chemical synthesis [1], portable energy devices [2-5], biological analysis of cells [6;7], reaction kinetics and mechanisms studies [8-13], and more recently in catalyst discovery and reaction optimisation [14-20]. Microreactors are miniaturised reaction systems fabricated by methods of microtechnology and precision engineering, with a characteristic dimension ranging from the submicrometer to the submillimeter scale [1]. They have extremely large surface area to volume ratios, often 100,000 times larger than that of conventional reactors; this means that even the very highly exothermic reactions can be performed isothermally, resulting in higher selectivity, minimal waste and under controlled conditions [21]. The hazard potential of strongly exothermic or explosive reactions can also be drastically reduced: the miniaturisation has an impact on the mechanism of explosion, in that the free radicals responsible for a chain reaction initiating a fire are sufficiently quenched through collisions with the microreactor side walls [22;23].

Microreactors are generally operated in continuous flow mode and there is a growing interest in the use of continuous flow reactors in both laboratory research and in chemical manufacturing. This initiative has stemmed partly from a process intensification perspective – a paradigm shift in process design – leading to size reduction of equipment and plants by 10 to 1000 times. The major advantages of flow chemistry are faster and safer reactions, cleaner products, quick reaction optimisation, easy scale-up, and the integration of typically separate processes. In batch, scaling up synthetic routes to new materials is a laborious task; typically, the best pathway is chosen and reaction conditions are optimised. Once the product moves to the next stage and the demand grows, the whole synthesis process needs to be revised and readjusted for a larger batch size. In contrast, only operation time and flow rate determine the scale of the synthesis in flow chemistry, and the same reactor that was initially used to produce grams of material can be used to produce kilogram quantities. Continuous flow allows integration with in-line analytical tools and seamless automation of reaction analysis in real time. This can be particularly useful when assessing for catalyst deactivation, where the stability of catalysts is typically studied

in batch reactors using a "recover & re-use" strategy, a procedure that is laborious and unrepresentative of typical industrial operation. To this end, continuous micro-fixed bed operation is a good alternative to batch operation, as flow reactors are easily monitored as a function of time on-stream, as well as requiring small inventories of catalyst and reactants.

1.2 Development of Microreaction Systems for Kinetic Studies

Microreaction technology has been used to respond to the demanding challenges posed by highly exothermic processes in which heat and mass transfer issues become significant. Conventionally, heterogeneous catalyst testing is performed in mini tube reactors approximately 5 mm in diameter with catalyst particles packed against a glass frit. Even at this small scale, the reactors are susceptible to thermal and concentration gradients that impact the reliability of the kinetic measurements obtained [24]. At these dimensions, the reactor operates at low Reynolds numbers, and large catalyst diameters often lead to poor heat and mass transfer due to the lack of turbulent mixing and slow diffusion over the larger length scales [25]. In contrast, microreactors have been found to be efficient at obtaining reaction kinetics due to their highly isothermal environment and excellent heat and mass transfer performance. It has been proven that if designed properly, the flow in the channels can be very close to plug flow [26-28] which makes the data analysis and interpretation significantly easier. Further, the increased safety brought about by the small channel dimensions (small scale, no headspace, no accumulation of reactive/toxic intermediates) makes reactions that are normally considered "forbidden", feasible.

1.3 Characterisation of Three-Phase Micro-Packed Bed Reactors

Three-phase microstructured reactors can be based on several different modes of operation [29]:

- Continuous phase contacting, where the fluid phases are separated. Examples include microstructured falling film reactors

- Dispersed phase contacting, where one fluid phase is dispersed in the other phase. Examples include micropacked bed reactors and slurry microreactors.

Micropacked bed reactors operate on similar principles as conventional trickle bed reactors, where gas and liquid phases flow over a solid fixed bed of catalysts. The advantages of using micro-packed bed reactors include the ability to use conventional and commercially available catalysts in pellet form. However, limitations are usually imposed by high pressure drops due to the small channel dimensions [29]. This is where slurry-taylor flow microreactors (catalyst particles are transported as a suspension by means of internal vortices occurring in the liquid slugs of the segmented flow) have been surfacing as an alternative recently [30,31].

Despite their widespread use in catalytic process development and kinetic data acquisition, the phenomena governing operation in three phase micro-packed bed reactors are not yet fully understood [32]. There has been evidence to suggest that the governing phenomena in the microscale are different to those in conventional scale reactors [33]. Therefore, an understanding of the hydrodynamics, mass transfer, and operation characteristics of three-phase micro-packed bed reactors is essential to enable accurate representation of these reactors and their modelling, thus fully exploiting the advantages brought about by the use of microreactors.

1.4 Heterogeneous Catalysis for Alcohol Oxidations

Catalysis has become central to the chemicals, energy and environmental industries as it provides a greener alternative for the production of chemicals and fuels. In particular, the selective oxidation of alcohols to carbonyl compounds is of interest due to the value of the products of these reactions as intermediates in the manufacture of pharmaceuticals, fragrances and fine chemicals. Conventionally, these carbonyl compounds are produced via non-environmentally benign methods, utilising stoichiometric oxidants such as permanganates and chromates, generating copious amounts of wastes that contain heavy metals. Catalytic oxidation using O_2, H_2O_2 and air has received considerable attention as a greener alternative, due to water being the only main by-product in these reactions. Therefore, there is a critical need within the chemical industry to understand and optimise these heterogeneous catalytic processes.

The two alcohol oxidation reaction systems studied in this thesis and the motivation behind their selection will be presented next.

1.4.1 Methanol Oxidation on Silver Catalyst

Formaldehyde is the most important aldehyde produced commercially. About 9 billion pounds per year of the 37-50% aqueous solution, called formalin, are prepared. The global consumption is 26 MT/year making the oxidative dehydrogenation of methanol the largest user of methanol [34]. About half of the formaldehyde produced is used in the preparation of urea-formaldehyde and phenol-formaldehyde resins, which are used in the manufacture of plywood, particleboard, and foam insulation. Two methods are prominent in industrial formaldehyde synthesis: one is performed over an electrolytic silver catalyst under air-lean conditions (Silver catalyst process) and the other is based on a ferric molybdate catalyst by oxidation of methanol at excess air conditions (Formox process). Despite both processes giving similar yields (92%), over 50% of the industrial formaldehyde production capacity in Western Europe is based on the silver catalysed synthesis route. The high temperatures (600-650°C) operated at in this industrial process makes the study of this reaction a challenge. Various authors have attempted to obtain the reaction kinetic models for methanol oxidation through lab studies, but mass transfer limitations, temperature gradients, and high conversions made it difficult to determine the kinetics above 350°C [35;36]. Integral reactor data indicated a transition from the kinetically controlled to the diffusion controlled regime at 350°C. Therefore, the kinetics have only been studied at low temperatures, which are not industrially relevant. This makes the reaction a strong candidate for the application of microreaction technology, where mass transfer limitations can be eliminated.

1.4.2 Benzyl Alcohol Oxidation on Supported Au-Pd Catalyst

Benzyl alcohol oxidation is one of the most studied alcohol oxidation reactions due to the demand for benzaldehyde as an intermediate in the production of fine chemicals, pharmaceuticals, flavourings and fragrances [37]. Benzyl alcohol has commonly been used as a model substrate for selective alcohol oxidations [38-40], particularly in the study of gold catalysts [41;42]. Widely used catalysts for these alcohol oxidation reactions are supported metal nanoparticle based catalysts. Recently, supported

bimetallic Au-Pd nanoalloy catalysts have been reported to be far more superior to their monometallic counterparts [43]. Understanding operation variables such as the effect of hydrodynamics on reaction performance is important to develop these catalytic processes for commercialisation.

1.5 Thesis Objectives & Overview

The motivation for this work combines the need to study catalytic alcohol oxidation reactions, with the advantages brought about by the use of microreactors. In this thesis, two reaction systems are studied:

a. A gas-liquid-solid micro-packed bed reactor system for reaction development of benzyl alcohol oxidation on supported gold-palladium catalyst.
b. A gas phase wall-coated microreactor system for the acquisition of kinetic data for methanol oxidation on silver catalyst, under industrially relevant conditions.

A literature review is first presented in ***Chapter II*** discussing the current status of micro-reaction technology and its applications in the design of catalytic processes. Recent literature in this field is reviewed, including the use of micro-reactors for intrinsic kinetic studies, *in-situ* catalyst characterisation, and as part of automated systems for optimisation of operating conditions and reaction kinetics determination.

In the selection of a suitable catalyst formulation for commercial use, its stability with prolonged time on-stream must be ensured. To this end, continuous flow catalyst deactivation studies on thin film Ag catalyst during methanol oxidation (***Chapter IV***) and supported Au-Pd nanoalloy catalysts during benzyl alcohol oxidation (***Chapter V)*** are presented. Potential catalyst candidates are tested and screened for stability in order to select the most appropriate catalyst formulation for further reaction development studies.

Once a suitable catalyst (that is both active and stable) is identified, it is essential to identify the influence of operating conditions on the overall performance of the process. Three-phase packed bed reactors have unique features and complexities as a result of hydrodynamic and mass transfer effects. In ***Chapter VI***, the hydrodynamics prevalent in a three-phase micro-packed bed reactor are identified, where differences between the

flow regimes observed in the microreactor and what is commonly associated with conventional packed bed reactors are shown.

Flow regimes and other hydrodynamic characteristics of three phase packed bed reactors primarily affect the external mass and heat transfer. In ***Chapters VII*** *and* ***VIII*** hydrodynamic effects on benzyl alcohol oxidation reaction performance are presented, and in ***Chapter IX*** the impact of using ozone (as a substitute for oxygen) on reaction performance is investigated. In ***Chapter X*** a novel on-chip residence time distribution method using Raman Spectroscopy is presented, which was validated using liquid phase flow and tested for gas-liquid segmented flow, with a view of being used as a method of characterising the residence time in three-phase packed bed microreactors.

A variety of microreactors are used in this thesis research, the design and rationale for the changes made are shown in ***Chapter III***. Finally, ***Chapter XI*** presents conclusions and recommendations for future work. An overview of the two reaction systems and the different sections of the thesis are shown in **Figure 1.1.**

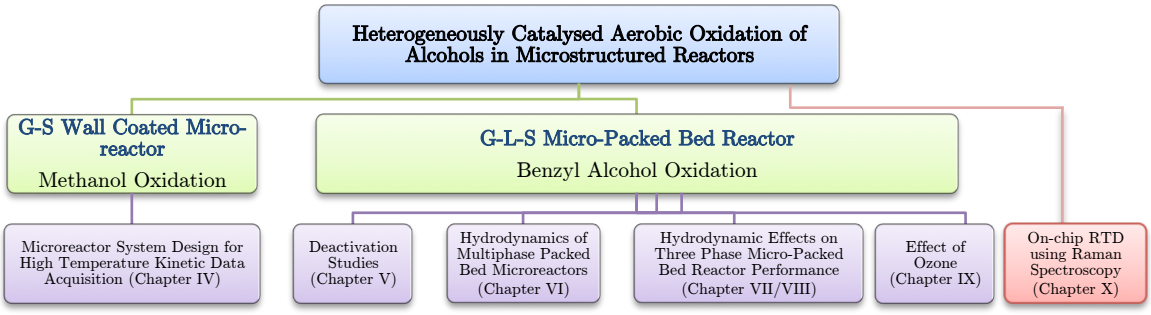

Figure 1.1. *Thesis overview.*

1.6 References

1. Jahnisch, K., Hessel, V., Lowe, H., Baerns, M. **Chemistry in Microstructured Reactors**. *Angewandte Chemie International Edition* 2004, 43:406-446.

2. Holladay, J.D., Wang, Y., Jones, E. **Review of developments in portable hydrogen production using microreactor technology**. *Chemical Reviews* 2004, 104:4767-4789.

3. Zeng, D., Pan, M., Tang, Y. **Qualitative investigation on effects of manifold shape on methanol steam reforming for hydrogen production**. *Renewable Energy* 2012, 39:313-322.

4. Ju, Y., Maruta, K. **Microscale combustion: Technology development and fundamental research**. *Progress in Energy and Combustion Science* 2011, 37:669-715.

5. Tadbir, M.A., Akbari, M.H. **Methanol steam reforming in a planar wash coated microreactor integrated with a micro-combustor**. *International Journal of Hydrogen Energy* 2011, 36:12822-12832.

6. El-Ali, J., Sorger, P.K., Jensen, K.F. **Cells on chips**. *Nature* 2006, 442:403-411.

7. Yin, H., Marshall, D. **Microfluidics for single cell analysis**. *Current Opinion in Biotechnology* 2012, 23:110-119.

8. Santacesaria, E., Di Serio, M., Tesser, R., Turco, R., Tortorelli, M., Russo, V. **Biodiesel process intensification in a very simple microchannel device**. *Chemical Engineering & Processing: Process Intensifcation 2012, 52:47-54.*

9. Kraehnert, R., Baerns, M. **Kinetics of ammonia oxidation over Pt foil studied in a micro-structured quartz-reactor**. *Chemical Engineering Journal* 2008, 137:361-375.

10. Carucci, J.R.H., Kurman, A., Karhu, H., Arve, K., Eranen, K., Warna, J., Salmi, T., Murzin, D.Y. **Kinetics of the biofuels-assisted SCR of NOx over Ag/alumina-coated microchannels**. *Chemical Engineering Journal* 2009, 154:34-44.

11. Arzamendi, G., Uriz, I., Dieguez, P.M., Laguna, O.H., Hernandez, W.Y., Alvarez, A., Centeno, M.A., Odriozola, J.A., Montes, M., Gandia, L.M. **Selective CO removal over Au/CeFe and CeCu catalysts in microreactors studied through kinetic analysis and CFD simulations**. *Chemical Engineering Journal* 2011, 167:588-596.

12. Dubey, V.R., Vaidya, P.D. **Kinetics of steam reforming of acetol over a Pt/C catalyst**. *Chemical Engineering Journal* 2012, 180:263-269.

13. Görke, O., Pfeifer, P., Schubert, K. **Kinetic study of ethanol reforming in a microreactor**. *Applied Catalysis A: General* 2009, 360:232-241.

14. McMullen, J.P., Stone, M.T., Buchwald, S.L., Jensen, K.F. **An Integrated Microreactor System for Self-Optimization of a Heck Reaction: From Micro- to Mesoscale Flow Systems**. *Angewandte Chemie International Edition* 2010, 49:7076-7080.

15. Sugimoto, A., Fukuyama, T., Rahman, M., Ryu, I. **An automated-flow microreactor system for quick optimization and production: application of 10- and 100-gram order productions of a matrix metalloproteinase inhibitor using a Sonogashira coupling reaction**. *Tetrahedron Letters* 2009, 50:6364-6367.

16. Tadbir, M.A., Akbari, M.H. **Integrated methanol reforming and oxidation in wash-coated microreactors: A three-dimensional simulation**. *International Journal of Hydrogen Energy* 2012, 37:2287-2297.

17. Delville, M.M.E., Nieuwland, P.J., Janssen, P., Koch, K., van Hest, J.C.M., Rutjes, F. **Continuous flow azide formation: Optimization and scale-up**. *Chemical Engineering Journal* 2011, 167:556-559.

18. Goodell, J.R., McMullen, J.P., Zaborenko, N., Maloney, J.R., Ho, C.X., Jensen, K.F., Porco, J.A., Beeler, A.B. **Development of an Automated Microfluidic Reaction Platform for Multidimensional Screening: Reaction Discovery**

Employing Bicyclo[3.2.1]octanoid Scaffolds. *Journal of Organic Chemistry.* 2009, 74:6169-6180.

19. Krishnadasan, S., Brown, R.J.C., deMello, A.J., deMello, J.C. **Intelligent routes to the controlled synthesis of nanoparticles**. *Lab Chip* 2007, 7:1434-1441.

20. Kreutz, J.E., Shukhaev, A., Du, W., Druskin, S., Daugulis, O., Ismagilov, R.F. **Evolution of Catalysts Directed by Genetic Algorithms in a Plug-Based Microfluidic Device Tested with Oxidation of Methane by Oxygen**. *Journal of the American Chemical Society* 2010, 132:3128-3132.

21. Worz, O., Jackel, K.P., Richter, T., Wolf, A. **Microreactors, a new efficient tool for optimum reactor design**. *Chemical Engineering Science* 2001, 56:1029-1033.

22. Veser, G. **Experimental and theoretical investigation of H2 oxidation in a high-temperature catalytic microreactor**. *Chemical Engineering Science* 2001, 56:1265-1273.

23. Oyama, S.T., Zhang, X., Lu, J., Gu, Y., Fujitani, T. **Epoxidation of propylene with H2 and O2 in the explosive regime in a packed-bed catalytic membrane reactor**. *Journal of Catalysis* 2008, 257:1-4.

24. Ajmera, S.K., Delattre, C., Schmidt, M.A., Jensen, K.F. **Microfabricated Differential Reactor for Heterogeneous Gas Phase Catalyst Testing**. *Journal of Catalysis* 2002, 209:401-412.

25. Ajmera, S.K., Losey, M.W., Jensen, K.F., Schmidt, M.A. **Microfabricated packed-bed reactor for phosgene synthesis**. *AIChE Journal* 2001, 47:1639-1647.

26. Cao, C., Hu, J., Li, S., Wilcox, W., Wang, Y. **Intensified Fischer-Tropsch synthesis process with microchannel catalytic reactors**. *Catalysis Today* 2009, 140:149-156.

27. Cao, C., Xia, G., Holladay, J., Jones, E., Wang, Y. **Kinetic studies of methanol steam reforming over Pd/ZnO catalyst using a microchannel reactor**. *Applied Catalysis A: General* 2004, 262:19-29.

28. Carucci, J.R.H., Halonen, V., Eranen, K., Warna, J., Ojala, S., Huuhtanen, M., Keiski, R., Salmi, T. **Ethylene Oxide Formation in a Microreactor: From Qualitative Kinetics to Detailed Modeling**. *Industrial & Engineering Chemistry Research* 2010, 49:10897-10907.

29. Hessel, V., Schouten, J.C., Renken, A., Yoshida, J-I. **Heterogeneous Multiphase Reactions**. In *Micro Process Engineering: A comprehensive Handbook, Volume 1.* 2013.

30. Liedtke, A.K., Bornette, F., Philippe, R., De Bellefon C. **Gas-liquid-solid "slurry Taylor" flow: Experimental evaluation through the catalytic hydrogenation of 3-methyl-1-pentyn-3-ol**. 2013, **227:**174-181.

31. Liedtke, A.K., Scheiff, F., Bornette, F., Philippe, R., Agar, D.W., De Bellefon, C. **Liquid-solid mass transfer for microchannel suspension catalysis in gas-liquid and liquid-liquid segmented flow**. 2015, **54:**4699-4708.

32. Faridkhou, A., Hamidipour, M, Larachi, F. **Hydrodynamics of gas-liquid micro-fixed beds - Measurement approaches and technical challenges**. *Chemical Engineering Journal* 2013, 223:425-435.

33. Alsolami, B.H., Berger, R.J., Makkee, M., Moulijn, J.A. **Catalyst Performance Testing in Multiphase Systems: Implications of Using Small Catalyst Particles in Hydrodesulfurization**. *Industrial & Engineering Chemistry Research* 2013, 52:9069-9085.

34. BASF. Formaldehyde. Board on Toxicology and Environmental Health Hazards.Assembly of Life Sciences.National Research Council . 2012.

35. Andreasen, A., Lynggaard, H., Stegelmann, C., Stoltze, P. **A microkinetic model of the methanol oxidation over silver**. *Surface Science* 2003, 544:5-23.

36. Robb, D.A., Harriott, P. **The kinetics of methanol oxidation on a supported silver catalyst**. *Journal of Catalysis* 1974, 35:176-183

37. Hudlicky, M. ***Oxidation in Organic Chemistry***. Washington DC: American Chemical Society; 1990.

38. Ferri, D., Mondelli, C., Krumeich, F., Baiker, A. **Discrimination of active palladium sites in catalytic liquid-phase oxidation of benzyl alcohol**. *Journal of Physical Chemistry* 2006, 110:22982-22986.

39. Choudhary, V.R., Dumbre, D.K. **Solvent-free selective oxidation of benzyl alcohol to benzaldehyde by tert-butyl hydroperoxide over U3O8-supported nano-gold catalysts**. *Applied Catalysis A: General* 2010, 375:252-257.

40. Yamaguchi, K., Mizuno, N. **Supported ruthenium catalyst for the heterogeneous oxidation of alcohols with molecular oxygen**. Angewandte Chemie International Edition 2002, 41:4538-4542.

41. Hou, W.B., Dehm, N.A., Scott, R.W.J. **Alcohol oxidations in aqueous solutions using Au, Pd, and bimetallic AuPd nanoparticle catalysts**. *Journal of Catalysis* 2008, 253:22-27.

42. Meenakshisundaram, S., Nowicka, E., Miedziak, P.J., Brett, G.L., Jenkins, R.L., Dimitratos, N., Taylor, S.H., Knight, D.W., Bethell, D., Hutchings, G.J. **Oxidation of alcohols using supported gold and gold-palladium nanoparticles**. *Faraday Discussions* 2010, 145:341-356.

43. Enache, D.I., Edwards, J.K., Landon, P., Solsona-Espriu, B., Carley, A.F., Herzing, A.A., Watanabe, M., Kiely, C.J., Knight, D.W., Hutchings, G.J. **Solvent-Free Oxidation of Primary Alcohols to Aldehydes Using Au-Pd/ TiO_2 Catalysts**. *Science* 2006, 311:362-365.

II.

Literature Review*

Microreaction technology is an interdisciplinary field that has gained significant momentum in recent years due to the numerous advantages it offers compared to conventional systems, in terms of enhanced heat and mass transfer and safer operation. The experimental efficiency achieved through the well-defined conditions offered by microchannel reactors has been utilised to elucidate intrinsic reaction kinetics, often in reaction spaces that were previously unexplored. In this chapter, the current status of microreaction technology for catalytic processes is reviewed and a perspective is presented on advancing catalytic process development by combined application of microstructured flow reactors with techniques for in-situ catalyst characterisation and mathematical optimisation.

---

* *This chapter is published in the Current Opinion in Chemical Engineering Journal:*
Al-Rifai, N., Cao, E., Dua, V., Gavriilidis, A. ***Microreaction technology aided catalytic process design****. Current Opinion in Chemical Engineering 2013,* ***2:****338-345.*

2.1 Introduction

Catalysis is a key technology in the chemical, energy and environmental sectors. It has helped in protecting the environment, reducing energy consumption and waste products, and it will be crucial for building an emerging, sustainable chemicals sector. The pressure that the chemical industry is facing from new markets and increased environmental restrictions places a demand for innovative and knowledge-based activities to enable more efficient processes and faster development times to plant commissioning [1]. The traditional chemical engineering approach addresses the different design stages starting from the selection of an appropriate catalyst up to transfer into the catalytic manufacturing process in a sequential fashion, and often with a disconnect between the activities carried out at each phase. An integrated design method is more efficient as it focuses on all aspects of the process simultaneously and maintains the link between the catalyst, the reactor, and the final process with a vision of the desired process attributes [2]. However, the rate of its adoption has been relatively low and it has not penetrated the chemical industry to a large extent. Implementing it requires optimisation of the catalyst's nanoscale structure alongside the macroscale catalytic reactor design [3]. This can be facilitated by continuous flow microfluidic technology that can allow rapid manipulation of reaction conditions, fast response times, precise control of the hydrodynamic environment, minimal consumption of reagent and catalyst, and an opportunity to integrate instrumentation, in-line optimisation, and automation methods [4]. The transport intensification inherent to microstructured reactors makes them useful laboratory tools so that even fast, highly exothermic reactions can be performed isothermally and in the absence of mass transfer limitations. This knowledge-rich based approach emanating from efficient acquisition of high quality data can underpin the quest for the catalyst genome [5]. Furthermore, safer operation brought about by the small channel dimensions allows exploration of new reaction pathways, in addition to process intensification through high pressure and temperature chemistries.

Micro process technology is currently burgeoning (for recent reviews see [6-9]) and has the potential to bridge the lab to the plant scale, not only due to the excellent information generation capacity but also due to easier scalability. This chapter

demonstrates the potential of microreaction technology to expedite catalytic process development; this is done by presenting advances in the last four years in the use of microchannel reactors for obtaining reaction kinetics and gaining insight into catalyst operation through spectroscopic characterisation, with a particular focus on heterogeneous catalytic processes. The integration of these aspects with the help of instrumentation and optimisation tools (see **Figure 2.1**) will help increase the quantity, quality, and speed of information generation.

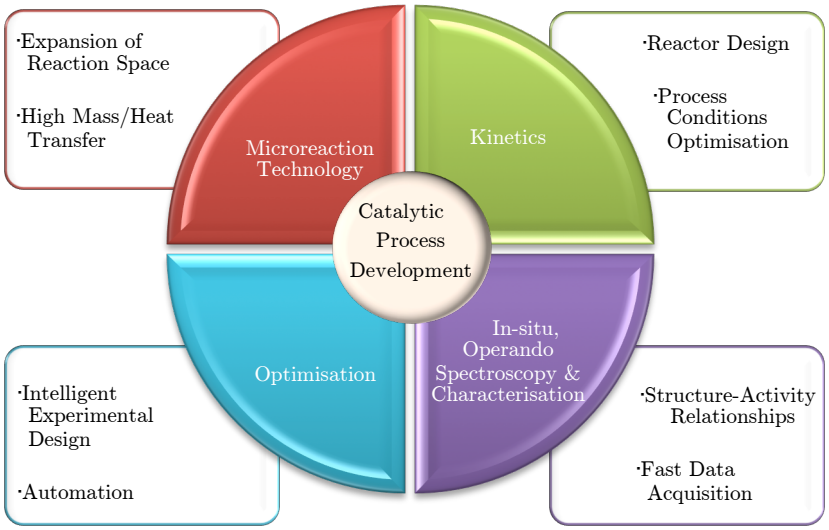

Figure 2.1 *Holistic approach to catalytic process development encompassing the 4 main aspects highlighted in this chapter.*

2.2 Microstructured Devices and Operation Characteristics for Kinetic Studies

In catalytic reaction processes, the quantitative characterisation of reaction kinetics is crucial for reactor design and process conditions optimisation. Microchannel reactors make ideal laboratory experimentation tools due to enhanced mass transfer compared to conventional scale reactors [10]. Heterogeneous catalytic microreactors are based mostly on packed bed and wall-coated catalyst integration principles, although recent work in using catalyst particles in suspension within microchannels is noteworthy [11]. The following present the operation, advantages, and issues for consideration of such reactors and their use for reaction kinetic studies.

2.2.1 Expansion of Reaction Space

The limitations of conventional reactors imposed by limited mass and heat transfer can be circumvented by microstructured reactors. This allows the investigation and exploitation of 'novel process windows' by carrying out reactions under more extreme conditions (e.g. high temperature/pressure, solvent-less and operation in the flammable regime) [12;13]. Microreactors are not inherently safe [14] but have the ability to suppress the propagation of an explosion and to lower the upper detonation limit of reactions, depending on the operating pressures and channel dimensions [15]. It is therefore possible to study reactions under unusual conditions. For example, the strongly exothermic o-xylene oxidation to phthalic anhydride was operated safely in the explosive regime in a steel micro packed bed reactor, even when the adiabatic temperature rise was several 1000 K (**Figure 2.2a**) [16]; CO_2 hydrogenation to methanol using a microcapillary reactor was performed up to a pressure of 950 bar [17]; Pd catalysed cyclohexene hydrogenation was studied in a silicon/glass microreactor at 80–150 bar (**Figure 2.2b**)[18].

When elevated pressure and temperature are required, the connections to the reactor need to be able to withstand the harsh conditions. This is less of a problem for capillary microreactors as conventional fittings can be employed. The use of microfabricated reactors made from glass and silicon offer quite a few additional benefits such as the interfacing of in-situ spectroscopies and this will be discussed further later. However, issues regarding their interconnection to external devices become even more important due to material restrictions. Recently, Marre et al. [19] presented design procedures for microsystems able to withstand temperatures and pressures up to 400°C and 30 MPa. They dealt with the challenges associated with sealing at high temperatures by placing the inlet/outlet connections on a mild temperature area of the chip, away from the reaction zone (**Figure 2.2c**).

2.2.2 Applications of Microreactors for Intrinsic Kinetics Acquisition

The determination of intrinsic reaction kinetics for strongly exothermic, endothermic, and fast reactions can be a challenge due to the difficulty in attaining isothermality

across the catalytic bed. Microreactors have been recently used in the development of kinetic models for various catalytic reactions of this type. To name a few of the most recent studies: Salmi et al. [20] studied the kinetics of ethylene epoxidation, a highly exothermic reaction, in an isothermal stainless steel microchannel reactor on silver catalyst at a temperature of 250°C and total pressure between 1 and 5 bar, while Nijhuis et al. obtained the reaction kinetics and catalyst deactivation for the direct epoxidation of propene at 50–200°C using a 0.9 mm ID stainless steel capillary microreactor packed with Au/TiO2 catalyst [21;22]. A characteristic example of the successful use of a microreactor in improving the efficiency of a process is in the production of SO_3, a chemical which is industrially produced by the strongly exothermal oxidation of a diluted SO_2 feed in a multistage process with interstage cooling, a process complicated by the high adiabatic temperature rise. Benzinger et al. [23] studied the kinetics of a simplified version of the process, where the SO_3 is produced in a single pass using pure oxygen without dilution, made possible due to the high heat transfer rates offered by microchannel reactors. The reaction was studied on Pt catalyst in a microstructured titanium reactor filled with structured foils, each 80 mm long and with 105 microchannels of dimensions 200 mm × 200 mm, at operating temperatures of 400–535°C (**Figure 2.2d**). An isothermal temperature profile was obtained across the catalyst bed, enabling determination of the intrinsic reaction kinetics. Hydrogen peroxide formation is another process that can benefit from the use of a microchannel reactor, as the reduction in scale enables the direct combination of hydrogen and oxygen safely and can potentially provide a simpler production route than the commonly used autoxidation process. On this note, the kinetics of the direct combination of hydrogen and oxygen to produce hydrogen peroxide in the flammable region was investigated using a stainless steel capillary (765 mm ID) packed with Pd/SiO_2 catalyst [24]. The experimental data obtained were fitted reasonably well to the predicted reactor performance from a kinetic model, which can pave the way towards successful reactor design and the determination of optimal reaction conditions. Ethanol reforming to hydrogen is another reaction of high importance, but when studied in a classical laboratory system poses challenges as it often results in the formation of high temperature gradients due to its fast and endothermic nature. In contrast, when carried out in a microchannel reactor even with a low steam to carbon

ratio of 2, it was possible to ensure low methane by-product concentrations by lowering the residence time to 9 ms, something that would be difficult to achieve in a conventional laboratory reactor [25]. The reactor used to carry out this study consisted of a stack of foils with channels of dimensions 200 mm × 200 mm and coated with Rh/CeO_2 (reactor shown in **Figure 2.2e**).

The development of standardised automated systems capable of operating within a wide operational window would speed up the information generation stage of the catalytic design process. This has been demonstrated by Keybl and Jensen [26] who implemented an automated platform capable of conducting kinetic experiments at elevated temperatures and pressures (350°C and 100 bar) and obtained reaction kinetics for the 1-octene hydroformylation with homogeneous Rh catalyst. In addition, Liu et al. developed a silicon microreactor-based platform for heterogeneous catalytic studies of multiphase (gas–liquid–solid) reactions (**Figure 2.2f**) where the optimisation of reaction conditions and screening of catalytic materials was performed for the oxidation of 4-isopropylbenzaldehyde and hydrogenation of 2-methylfuran [27].

2.2.3 The Challenges and the Opportunities

Microreactors are not inherently free from mass/heat transfer limitations and the assumption of ideal conditions must be verified before they can qualify for an intrinsic kinetic study. In many cases one can use the knowledge and approaches from conventional laboratory reactors [28] to verify the absence of transfer limitations. However, due to the low Reynolds numbers, external mass transfer in microreactors is usually dominated by molecular diffusion. Thus, for gas phase catalytic reactions in wall-coated and packed bed microchannel reactors, alternative approaches have been considered to confirm the absence of mass transfer, such as varying the gas phase diffusivity by altering the carrier gas partial pressure or using different carrier gases [29].

With regards to liquid phase systems, there have been efforts to study the liquid-to-particle mass transfer in micro packed beds (80 mm particles) [30] indicating that wall effects are diminished not only for hydraulic to particle diameter ratio >10 as

commonly recommended [31] but also for <4. This is worth contrasting with residence time distribution experiments for larger (2 mm) particles in single pellet string reactors that indicate that such wall effects are still present for liquid flow but diminish for gas–liquid flow [32].

There is increasing evidence that multiphase flow in small channels demonstrates different behaviour than in the macroscale due to the dominance of surface forces. These differences need to be understood for successful microreactor design. In falling film microreactors the liquid film thickness deviates from traditional correlations, in particular for small, deep channels [33;34]. Liquid holdup in micro packed beds (<100μm particles) during gas-liquid flow is much higher compared to larger particles, with a weak dependency on the gas and the liquid superficial velocities [35]. This leads to good wetting characteristics, which are desirable for catalytic gas–liquid–solid reactions. Due to the high liquid holdup, micro-packed bed reactors have more stable hydrodynamic conditions, no matter if the reactor starts up with wet or dry procedures, in comparison to large scale trickle bed reactors where the liquid phase distribution in the bed is affected by the pre-wetting conditions [36].

Visualisation studies of hydrodynamics of gas–liquid flows in micro packed beds showed that flow regime transition from low interaction to high interaction (characterised by rapid displacement of the gas and liquid phases) takes place at much lower liquid-to-gas throughput ratios in micro packed beds than in their macroscale counterparts, indicating vigorous mass transfer even at low gas and liquid Reynolds numbers [36]. Flow pattern maps for gas– liquid flow in closed [38], open [39] or packed microchannels [40;41] differ from their macroscale analogues and in certain cases, new flow patterns have been identified (e.g. ‘liquid-ring’, ‘corner rivulet’ flows). Flow pattern transitions are affected not only by phase superficial velocities and liquid phase surface tension (which are relatively well studied) but also by the inlet region used, as well as the channel wall properties, such as wettability, contamination and roughness.

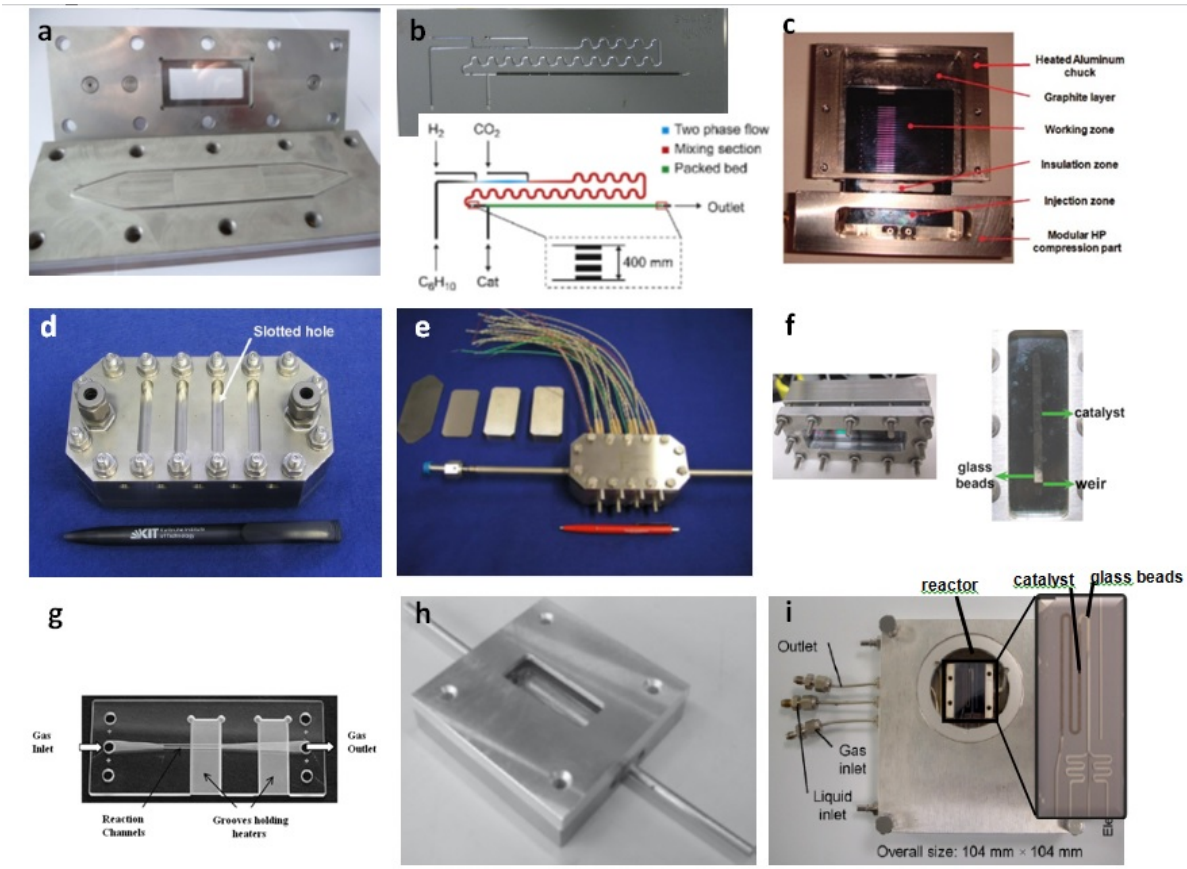

Figure 2.2 *Selected examples of microstructured reactors. (a) Steel microfixed bed reactor for the kinetic study of the oxidation of o-xylene on V_2O_5/TiO_2 catalyst [16]. (b) Silicon/glass microreactor used in the Pd/Al_2O_3 catalysed hydrogenation of cyclohexene [18]. (c) High pressure/high temperature microreactor configuration [19]. (d) Titanium reactor with inner structured foils each with 105 microchannels coated with Pt/TiO_2 used for the kinetic study of SO_2 oxidation [23]. (e) Microreactor used for ethanol reforming kinetic study containing Rh/CeO_2 foils with 200μm x 200μm channels [25]. (f) Packed-bed microreactor for catalytic oxidation of 4- isopropylbenzaldehyde with the front view showing the Pt/Al_2O_3 catalyst [27]. (g) Microstructured quartz reactor used to follow the partial oxidation of propene on a supported molybdenum oxide catalyst by in-situ Raman spectroscopy [48]. (h) Optically accessible DRIFTS microreactor for studying the CO oxidation on a Pt based catalyst [45]. (i) Micropacked bed reactor and stage used in Raman spectroscopy of benzyl alcohol oxidation on Au- Pd/TiO_2 catalyst [52].*

In this section, we have given examples that demonstrate the capability of microreactors to improve the quality of kinetic data, expand the operational space, and allow exploration of demanding reaction conditions to enable acquisition of the true

intrinsic kinetics of reactions. Some of the examples also show that there are other alternative routes that can provide improvements to processes, for example, through the use of undiluted feeds and single pass reactions, without compromising on yields and selectivities. The following sections will illustrate how kinetic data acquisition can be enhanced further via the integration of *in situ* spectroscopy and optimisation/automation tools into these systems.

2.3 *In-situ/operando* Spectroscopies and Catalyst Characterisation

The high impact *in situ* and *operando* spectroscopies have on catalysis lie in their ability to obtain profound understanding of the fundamental relationship between the molecular structure and the observed conversion/selectivity behaviour during a reaction [42]. A hierarchical, multi-technique approach can offer spatial catalyst and reactor characterisation from the nano-scale to the macroscale, providing a more holistic picture, beneficial for the optimisation of catalyst performance [43].

Apart from fast data acquisition, *in situ* spectroscopic analysis has the advantage of revealing the presence of short-lived species that might not be observed with in-line reaction monitoring. Such knowledge is essential in assisting both the verification of mechanistic models and rational catalyst/catalytic process design and goes beyond the catalyst discovery phase with high throughput parallel analysis of catalyst libraries.

2.3.1 How Does a Microreactor Meet the Requirements?

The *in situ* reactor must fulfil many requirements in order to qualify for an *operando* spectroscopic study: it must (i) operate like an ideal plug flow reactor (PFR) or continuous stirred tank reactor (CSTR) for residence time control and to allow straightforward determination of intrinsic reaction rates (ii) have the ability to effectively dissipate any heat generated due to hot spots created by the electromagnetic beam and maintain overall isothermal conditions and (iii) avoid any reaction fluid bypassing the catalyst [44]. These multiple requirements are difficult to attain under working conditions in a conventional reactor, while *in situ* studies are performed in flow cells under non well-defined conditions, often suffering from poor bed hydrodynamics and temperature control. Properly designed microstructured reactors on the other hand

can satisfy the above requirements since they allow better control of heat/mass transfer, hydrodynamics and allow facile access to spectroscopic catalyst characterisation. They have been shown to inhibit light-off and hysteresis effects as compared to lab-scale reactors [45]. Furthermore, microstructured channel reactors (rather than simply a capillary tube) allow easy and modular integration of other functional units (e.g. mixing, separation) and also the incorporation of planar waveguides and optical fibres [46].

2.3.2 *In-situ* Spectroscopy in Catalytic Gas Phase Systems

Many studies have been carried out combining fluorescence, ultraviolet-visible, infrared, Raman and X-ray spectroscopy with microfluidic reactors, but studies relevant to heterogeneous catalysis are rather limited [47]. The impact of altering operating conditions on catalyst morphology and adsorbed species, often with spatial and temporal resolution, has been demonstrated in the gas phase using Raman spectroscopy in the selective oxidation of propene over a molybdenum oxide-based catalyst, revealing information on the structural dynamics of the coated catalyst at different temperatures (reactor shown in ***Figure 2.2g***) [48]. Infrared spectroscopy is another technique that has been used to obtain valuable insights into the reaction mechanism of cyclohexane dehydrogenation in an infrared-enabled Pt/Al_2O_3 catalytic silicon microreactor sealed with KBr for optical access. It was ascertained that the reaction followed a consecutive reaction pathway by tracking the evolution of the reaction species with time on stream [49]. Infrared spectroscopy has also been used to study CO oxidation over a Pt catalyst *in situ,* (reactor shown in ***Figure 2.2h***) a key step in the process of syngas CO cleaning for fuel cell applications. The use of a microreactor demonstrated improved thermal characteristics through a comparison of its thermal runaway behaviour with that of a macroscale fixed bed reactor [45]. Although the amount of information obtainable from X-ray absorption spectroscopy (XAS) is rather limited in comparison to other spectroscopic techniques, it can still be used to probe the catalyst structure. This has been demonstrated for the partial oxidation of methane on Pt– Rh catalysts but in a simple capillary microreactor [50].

2.3.3 *In-situ* Spectroscopy in Catalytic Multiphase Systems

The extension of *in-situ*/*operando* studies to catalytic gas–liquid–solid reaction systems is more demanding and the relevant literature is scarce. The challenge in studying a catalytic multiphase system is that the signals of interest from the catalyst are usually overridden by the signals of the surrounding phase. For Raman spectroscopy, challenges associated with the interference of strong fluorescence can hinder the acquisition of good quality data [51]. Nevertheless, product composition profiles along micro packed beds have been obtained for multiphase benzyl alcohol oxidation on Au/Pd catalysts [52] and cyclohexene supercritical hydrogenation on Pd [53]. In the former [52], laser of different spot sizes had to be focused inside liquid pockets on fully wetted catalyst sections to avoid the strong interfering fluorescence signal (***Figure 2.2i***).

2.4 Optimisation and Automation

Automated continuous flow microfluidic platforms have been successful in enabling design of experiments (DoE) for optimisation of operating conditions (OOC) and reaction kinetics determination (RKD) for homogeneous systems. The use of D-optimal algorithms to identify optimal reaction conditions within a multivariate design space and with off-line analysis has been demonstrated [54;55]. More sophisticated automated microreactor systems with in-line analysis and combined feedback control, utilising various optimisation algorithms (such as Nelder–Mead Simplex, Steepest Descent, SNOBFIT) to select sequential experiments have enabled the determination of operating conditions (OOC) that would maximise a single [56] or a weighted objective function [57] for a reaction. Sugimoto et al. [58] presented a screening method for optimisation and production, but here and in many other cases, reaction optimisation has been carried out primarily in an empirical or semi-empirical manner through a 'black box' type of approach. The implementation of global optimisation techniques can ensure that better operation conditions do not exist and help reduce the number of experiments required.

The rapid determination of reaction kinetics (RKD) has been demonstrated in only 12 experiments and utilising only a few grams of the starting reagents [59]. It consisted of

two main steps, reaction kinetics model discrimination (using information theory and Bayesian statistics) and parameter estimation (using D-optimality). Recently, a knowledge based approach to reduce uncertainty in kinetic parameter estimates in a complex reaction network has been applied [60] The methodology is based upon using maximum likelihood estimation and D-optimal design of experiments. One key challenge for such a complex reaction system is to conduct experiments at conditions of high parameter sensitivity, for which isolating reaction pathways is important. For OOC, Moore and Jensen [61] presented a comparison of three optimisation algorithms (steepest descent, conjugate gradient and Armijo conjugate gradient) for a complex reaction system where the latter located the optimum with fewer experiments.

2.4.1 How Can Microfluidic Flow Systems Assist in Optimisation?

The merit in the use of a continuous flow microsystem for optimisation experiments is the excellent control over reaction conditions so that the experiment has minimal contribution to uncertainties in reaction parameterisation. The majority of the above work used HPLC as the analytical technique and although it can increase the experimental throughput, it is generally not capable of fast generation of experimental data. In the interest of fast optimisation, spectroscopic methods such as IR have been utilised, but predominantly for reaction optimisation studies [61]. All the cases discussed above are for homogeneous systems, which are relatively easier to automate. The application of automation to a gas–liquid or a gas–liquid–solid system is more challenging as it would require additional in-line separation of the gas–liquid mixture and the automated delivery of the gas and/or liquid streams to the analytical instruments. As such, new developments are required for optimisation and automated kinetic studies in multiphase catalytic systems. While some optimisation techniques have made their way to microreaction technology, there are still other optimisation techniques, for example, multi-objective optimal DoE [62] and global optimisation [63] which can further enhance developments in this exciting field. Finally, an area of fruitful future research would be the use of optimisation techniques for integrating optimal DoE and catalyst development for reactor networks that could represent process flow sheets of the scaled-up processes.

2.5 Conclusion

The interconnected nature of catalyst development and reactor design requires the examination of both aspects simultaneously. Paradigm changes in experimentation and analytical integration methods need to take place before this objective can be achieved. We have reviewed successful utilisation of microreactors to study intrinsic kinetics, often in a reaction space that was previously difficult to explore. However, it is important to note that there are differences in behaviour between microscale and macroscale that need to be accounted for. These differences in some cases pose challenges that need alternative approaches to resolve, while in others they offer opportunities to be exploited.

We have shown that the development of a catalytic process can be facilitated by the integration of *in situ* spectroscopy with microsystems and accelerated by experiment optimisation and automation tools. Although there have been efforts to integrate microreactors with spectroscopic characterisation, the technology still remains at its infancy and research will be required for the development of multi technique approaches for operando catalyst characterisation that will facilitate the drive towards faster, information-rich experimentation. Similarly, optimisation techniques integrated with automated reactor systems have not reached their full potential, in particular, in catalytic process development.

2.6 References

1. High Level Group on the Competitiveness of the European Chemicals Industry. Enabler of a Sustainable Future: The European Chemical Industry. 2009.

2. Nehlsen, J., Mukherjee, M., Porcelli, R.V. **Apply an integrated approach to catalytic process design**. *Chemical Engineering Progress* 2007, 103:31-38.

3. Kiwi-Minsker, L., Crespo-Quesada, M. **Integrated approach for the intensification of heterogeneous catalytic processes**. *Chimia* 2011, 65:699-703.

4. McMullen, J.P., Jensen, K.F. **Integrated Microreactors for Reaction Automation: New Approaches to Reaction Development**. *Annual Review of Analytical Chemistry* 2010, 3:19-42.

5. Nørskov, J.K., Bligaard, T. **The Catalyst Genome**. *Angewandte Chemie International Edition.* 2013, 52:776-777.

6. Hessel, V., Vural I., Wang, Q., Noel, T., Lang, J. **Potential Analysis of Smart Flow Processing and Micro Process Technology for Fastening Process Development: Use of Chemistry and Process Design as Intensification Fields**. *Chemical Engingeering Technology.* 2012, 35:1184-1204.

7. Wiles, C., Watts, P. **Continuous flow reactors: a perspective**. *Green Chemistry.* 2012, 14:38-54.

8. Rebrov, E.V. **Use of microtechnologies for intensifying industrial processes**. *Theoretical Foundations of Chemical Engineering.* 2010, 44:791-799.

9. Kashid, M.N., Kiwi-Minsker, L. **Microstructured Reactors for Multiphase Reactions: State of the Art**. *Industrial & Engineering Chemistry Research.* 2009, 48:6465-6485.

10. Kashid, M.N., Renken, A., Kiwi-Minsker, L. **Gas-liquid and liquid-liquid mass transfer in microstructured reactors**. *Chemical Engineering Science* 2011, 66:3876-3897.

11. Ufer, A., Sudhoff, D., Mescher, A., Agar, D.W. **Suspension catalysis in a liquid-liquid capillary microreactor**. *Chemical Engineering Journal* 2011, 167:468-474.

12. Hessel, V. **Novel Process Windows Gate to Maximizing Process Intensification via Flow Chemistry**. *Chemical Engineering & Technology.* 2009, 32:1655-1681.

13. Illg, T., Löb, P., Hessel, V. **Flow chemistry using milli- and microstructured reactors - From conventional to novel process windows**. *Bioorganic & Medicinal Chemistry* 2010, 18:3707-3719.

14. Klais, O., Westphal, F., Benaissa, W., Carson, D. **Guidance on Safety/Health for Process Intensification including MS Design; Part II: Explosion Hazards**. *Chemical Engineering & Technology.* 2009, 32:1966-1973.

15. Liebner, C., Fischer, J., Heinrich, S., Lange, T., Hieronymus, H., Klemm, E. **Are micro reactors inherently safe? An investigation of gas phase explosion propagation limits on ethene mixtures**. *Process Safety and Environmental Protection* 2012, 90:77-82.

16. Lange, T., Heinrich, S., Liebner, C., Hieronymus, H., Klemm, E. **Reaction engineering investigations of the heterogeneously catalyzed partial oxidation of o-xylene in the explosion regime using a microfixed bed reactor**. *Chemical Engineering Science* 2012, 69:440-448.

17. Tidona, B., Urakawa, A., Rudolf von Rohr, P. **High pressure plant for heterogeneous catalytic CO_2 hydrogenation reactions in a continuous flow microreactor**. *Chemical Engineering and Processing: Process Intensification* 2013, 65:53-57.

18. Trachsel, F., Tidona, B., Desportes, S., Rudolf von Rohr, P. **Solid catalyzed hydrogenation in a Si/glass microreactor using supercritical CO_2 as the reaction solvent**. *The Journal of Supercritical Fluids* 2009, 48:146-153.

19. Marre, S., Adamo, A., Basak, S., Aymonier,. C., Jensen, K.F. **Design and packaging of microreactors for high pressure and high temperature applications**. *Industrial & Engineering Chemistry Research.* 2010, 49:11310-11320.

20. Salmi, T., Hernandez Carucci, J., Roche, M., Eranen, K., Warna, J., Murzin, D. **Microreactors as tools in kinetic investigations: Ethylene oxide formation on silver catalyst**. *Chemical Engineering Science* 2013, 87:306-314.

21. Nijhuis, T.A., Chen, J., Kriescher, S.M.A., Schouten, J.C. **The Direct Epoxidation of Propene in the Explosive Regime in a Microreactor - A Study into the Reaction Kinetics**. *Industrial & Engineering Chemistry Research.* 2010, 49:10479-10485.

22. Chen, J., Halin, S.J.A., Schouten, J.C., Nijhuis, T.A. **Kinetic study of propylene epoxidation with H_2 and O_2 over Au/Ti-SiO2 in the explosive regime**. *Faraday Discussions.* 2011, 152:321-336.

23. Benzinger, W., Wenka, A., Dittmeyer, R. **Kinetic modelling of the SO_2-oxidation with Pt in a microstructured reactor**. *Applied Catalysis A: General* 2011, 397:209-217.

24. Voloshin, Y., Lawal, A. **Overall kinetics of hydrogen peroxide formation by direct combination of H_2 and O_2 in a microreactor**. *Chemical Engineering Science.* 2010, 65:1028-1036.

25. Görke, O., Pfeifer, P., Schubert, K. **Kinetic study of ethanol reforming in a microreactor**. *Applied Catalysis A: General* 2009, 360:232-241.

26. Keybl, J., Jensen, K.F. **Microreactor System for High-Pressure Continuous Flow Homogeneous Catalysis Measurements**. *Industrial & Engineering Chemistry Research.* 2011, 50:11013-11022.

27. Liu, X., Ünal, B., Jensen, K.F. **Heterogeneous catalysis with continuous flow microreactors**. *Catalysis Science and Technology* 2012, 2:2134-2138.

28. Kapteijn, F., Moulijn, J.A. **Laboratory Reactors**. In *Handbook of Heterogeneous Catalysis*. Edited by G.Ertl, H.Knozinger, J.Weitkamp. Weinheim: VCH; 1997.

29. Bakhtiary-Davijany, H., Dadgar, F., Hayer, F., Phan, X.K., Myrstad, R., Venvik, H.J., Pfeifer, P., Holmen, A. **Analysis of External and Internal Mass Transfer at Low Reynolds Numbers in a Multiple-Slit Packed Bed Microstructured Reactor for Synthesis of Methanol from Syngas**. *Industrial & Engineering Chemistry Research.* 2012, 51:13574-13579.

30. Tidona, B., Desportes, S., Altheimer, M., Ninck, K., von Rohr, P.R. **Liquid-to-particle mass transfer in a micro packed bed reactor**. *International Journal of Heat and Mass Transfer* 2012, 55:522-530.

31. Hessel, V., Schouten, J.C., Renken, A., Yoshida, J-I. **Heterogeneous Multiphase Reactions**. In *Micro Process Engineering: A comprehensive Handbook, Volume 1.* 2013.

32. Hipolito, A.I., Rolland, M., Boyer, C., de Bellefon, C. **Single Pellet String Reactor for Intensification of Catalyst Testing in Gas/Liquid/Solid Configuration**. *Oil & Gas Science & Technology - Rev. IFP Energies nouvelles.* 2010, 65:689-701.

33. Anastasiou, A.D., Makatsoris, C., Gavriilidis, A., Mouza, A.A. **Application of PIV for investigating liquid film characteristics in an open inclined microchannel**. *Experimental Thermal and Fluid Science* 2013, 44:90-99.

34. Tourvieille, J., Bornette, F., Philippe, R., Vandenberghe, Q., de Bellefon, C. **Mass transfer characterisation of a microstructured falling film at pilot scale**. *Chemical Engineering Journal* 2013;227:182-190

35. Faridkhou, A., Larachi, F. **Two-phase flow hydrodynamic study in micro-packed beds - Effect of bed geometry and particle size**. *Chemical Engineering and Processing: Process Intensification* 2014, 78:27-36.

35. Marquez, N., Castano, P., Moulijn, J.A., Makkee, M., Kreutzer, M.T. **Transient Behavior and Stability in Miniaturized Multiphase Packed Bed Reactors**. *Industrial & Engineering Chemistry Research.* 2010, 49:1033-1040.

37. Faridkhou, A., Larachi, F. **Hydrodynamics of gas-liquid cocurrent flows in micropacked beds-wall visualization study**. *Industrial and Engineering Chemistry Research* 2012, 51:16495-16504.

38. Shao, N., Gavriilidis, A., Angeli, P. **Flow regimes for adiabatic gas-liquid flow in microchannels**. *Chemical Engineering Science* 2009, 64:2749-2761.

39. Zhang, H., Yue, J., Chen, G., Yuan, Q. **Flow pattern and break-up of liquid film in single-channel falling film microreactors**. *Chemical Engineering Journal* 2010, 163:126-132.

40. Faridkhou, A., Larachi, F. **Hydrodynamics of Gas-Liquid Cocurrent Flows in Micropacked Beds - Wall Visualization Study**. *Industrial & Engineering Chemistry Research.* 2012, 51:16495-16504.

41. McGovern, S., Harish, G., Pai, C.S., Mansfield, W., Taylor, J.A., Pau, S., Besser, R.S. **Investigation of multiphase hydrogenation in a catalyst-trap microreactor**. *Journal of Chemical Technology & Biotechnology.* 2009, 84:382-390.

42. Banares, M. **Operando Spectroscopy: the Knowledge Bridge to Assessing Structure-Performance Relationships in Catalyst Nanoparticles**. *Advanced Materials.* 2011, 23:5293-5301.

43. Grunwaldt, J.D., Wagner, J.B., Dunin-Borkowski, R.E. **Imaging Catalysts at Work: A Hierarchical Approach from the Macro- to the Meso- and Nano-scale**. *ChemCatChem* 2013, 5:62-80.

44. Meunier, F.C. **The design and testing of kinetically-appropriate operando spectroscopic cells for investigating heterogeneous catalytic reactions**. *Chemical Society Reviews.* 2010, 39:4602-4614.

45. Daniel, C., Clarté, M-O., Teh, S.P., Thinon, O., Provendier, H., Van Veen, A.C., Beccard, B.J, Schuurman, Y., Mirodatos, C. **Spatially resolved catalysis in microstructured reactors by IR spectroscopy: CO oxidation over mono- and bifunctional Pt catalysts**. *Journal of Catalysis* 2010, 272:55-64.

46. Ashok, P.C., Singh, G.P., Rendall, H.A., Krauss, T.F., Dholakia, K. **Waveguide confined Raman spectroscopy for microfluidic interrogation**. *Lab on a Chip - Miniaturisation for Chemistry and Biology* 2011, 11:1262-1270.

47. Yue, J., Schouten, J.C., Nijhuis, T.A. **Integration of Microreactors with Spectroscopic Detection for Online Reaction Monitoring and Catalyst Characterization**. *Ind.Eng.Chem.Res.* 2012, 51:14583-14609.

48. Beato, P., Kraehnert, R., Engelschalt, S., Frank, T., Schlögl, R. **A micro-structured quartz reactor for kinetic and in situ spectroscopic studies in heterogeneous catalysis**. *Chemical Engineering Journal* 2008, 135, Supplement 1:S247-S253.

49. Tagawa, T., Isobe, M., Tanaka,. M., Yamada, H. **Evaluation of catalyst prepared in microchannel with in situ FT-IR microscopy**. *Chemical Engineering Journal* 2011, 167:427-430.

50. Grunwaldt, J.D., Kimmerle, B., Baiker, A., Boye, P., Schroer, C.G., Glatzel, P., Borca, C.N., Beckmann, F. **Catalysts at work: From integral to spatially resolved X-ray absorption spectroscopy**. *Catalysis Today* 2009, 145:267-278.

51. Stair, P.C. **In Situ Ultraviolet Raman Spectroscopy**. In *In-Situ Spectroscopy in Heterogeneous Catalysis*. Wiley-VCH Verlag GmbH & Co. KGaA; 2002:121-138.

52. Cao, E., Sankar, M., Firth, S., Lam, K.F., Bethell, D., Knight, D.K., Hutchings, G.J., McMillan, P.F., Gavriilidis, A. **Reaction and Raman spectroscopic studies of alcohol oxidation on gold-palladium catalysts in microstructured reactors**. *Chemical Engineering Journal* 2011, 167:734-743.

53. Urakawa, A., Trachsel, F., von Rohr, P.R., Baiker, A. **On-chip Raman analysis of heterogeneous catalytic reaction in supercritical CO_2: phase behaviour monitoring and activity profiling**. *Analyst* 2008, 133:1352-1354.

54. Koch, K., van Weerdenburg, B.J.A., Verkade, J.M.M, Nieuwland, P.J., Rutjes, F., van Hest, J. **Optimizing the Deprotection of the Amine Protecting p-Methoxyphenyl Group in an Automated Microreactor Platform**. *Org.Process Res.Dev.* 2009, 13:1003-1006.

55. Delville, M., Nieuwland, P.J., Janssen, P., Koch, K., van Hest, J., Rutjes, F. **Continuous flow azide formation: Optimization and scale-up**. *Chemical Engineering Journal* 2011, 167:556-559.

56. McMullen, J.P., Stone, M.T., Buchwald, S.L., Jensen, K.F. **An Integrated Microreactor System for Self-Optimization of a Heck Reaction: From Micro- to Mesoscale Flow Systems**. *Angew.Chem.* 2010, 122:7230-7234.

57. McMullen, J.P., Jensen, K.F. **An Automated Microfluidic System for Online Optimization in Chemical Synthesis**. *Org.Process Res.Dev.* 2010, 14:1169-1176.

58. Sugimoto, A., Fukuyama, T., Rahman, M., Ryu, I. **An automated-flow microreactor system for quick optimization and production: application of 10- and 100-gram order productions of a matrix metalloproteinase inhibitor using a Sonogashira coupling reaction**. *Tetrahedron Letters* 2009, 50:6364-6367.

59. McMullen, J.P., Jensen, K.F. **Rapid Determination of Reaction Kinetics with an Automated Microfluidic System**. *Org.Process Res.Dev.* 2011, 15:398-407.

60. Reizman, B.J., Jensen, K.F. **An Automated Continuous-Flow Platform for the Estimation of Multistep Reaction Kinetics**. *Org.Process Res.Dev.* 2012, 16:1770-1782.

61. Moore, J.S., Jensen, K.F. **Automated Multitrajectory Method for Reaction Optimization in a Microfluidic System using Online IR Analysis**. *Org.Process Res.Dev.* 2012, 16:1409-1415.

62. Franceschini, G., Macchietto, S. **Model-based design of experiments for parameter precision: State of the art**. *Chemical Engineering Science* 2008, 63:4846-4872.

63. Baliban, R.C., Elia, J.A., Floudas, C.A. **Biomass to liquid transportation fuels (BTL) systems: process synthesis and global optimization framework**. *Energy Environ.Sci.* 2013, 6:267-287.

III.

Microreactor Designs

The microreactor designs and rationale for the modifications to the designs made in each section of this thesis are outlined in this chapter.

3.1 Microreactor Design Philosophy

A variety of microreactor designs were used in this thesis research. The motivation for the different designs and rationale behind the changes made to the designs are described in this chapter.

3.1.1 Wall-Coated Gas-Solid Reactors: Methanol System (Chapter IV)

In **Chapter IV,** three different reactor prototypes are used: M1, M2 and M3. Each design had limitations, (mainly linked to the maximum operating temperature and its uniformity across the reaction zone) which were addressed with subsequent designs, leading to the optimal design, M3. The designs are presented in **Table 3.1** and will be discussed next.

Reactor Design M1

The initial testing was carried out using the M1 reactor design, heated with a simple stainless steel block powered by four heating cartridges (**Figure 3.1**). To provide the sealing between the microreactor and the inlet/outlet tubing, graphite ferrules were used at the interface between the microreactor top glass surface and the metal tubing used to deliver the reactants to the microreactor and products away from it. This reactor was capable of operating up to temperatures of 550°C, above which the graphite ferrules softened and leaking of gases took place.

A pillar structure was incorporated at the end of the channel, which consisted of microfabricated pillars 60 μm in width with 40 μm spacing – this was designed to enable the reactor to be used as a packed bed (and therefore the pillars would act as a frit to stop the particles from being carried away with the flow).

Reactor Design M2

M2 and M3 reactor designs were implemented for the high temperature operation, required to mimic industrial reactor behaviour. The design overcomes challenges associated with sealing at high temperatures by placing the inlet/outlet connections on a mild temperature area of the chip, away from the reaction zone. M2 reactor had a

similar geometric shape to M1, but with a smaller channel width of 6 mm. M2 was used as a prototype for initial testing of the design concept, which led to the design of the optimised M3 reactor design, discussed later.

To overcome the challenge of sealing at higher temperatures, the high temperature reaction zone was separated from the sealing area by cooling the connectors. This prevented overheating of the O-rings used to provide the sealing. The inlet/outlet connections were cooled through the use of cooling water (**Figure 3.2**).

Reactor Design M3

The M3 reactor was based on a similar operating principle as the M2 design, but was optimised to reduce the temperature variation across the reaction zone (see **Chapter IV**). The microreactor consisted of a serpentine channel with a 1 mm main channel width. The total reactor length was increased to allow maximum separation from the cooled connector end and the heated reaction zone. Variations of the M3 design (the halo-etch and the dumbbell shaped reactors), optimised for high temperature operation (>550°C) are proposed as an outcome of conclusions of a COMSOL heat transfer simulation (see **Chapter IV**).

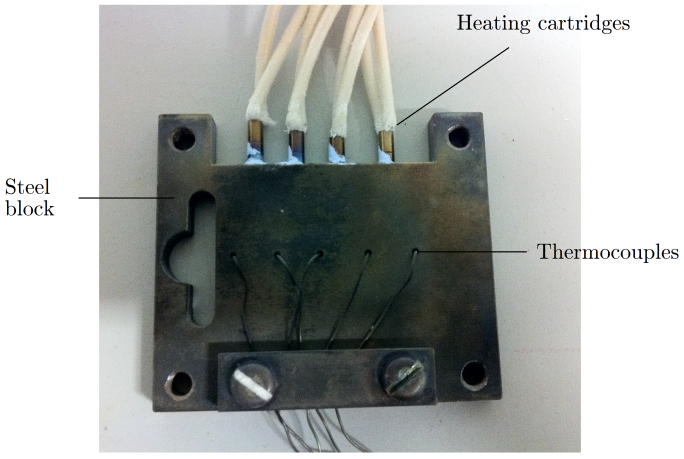

Figure 3.1 *M1 reactor heating plate (viewed from the bottom).*

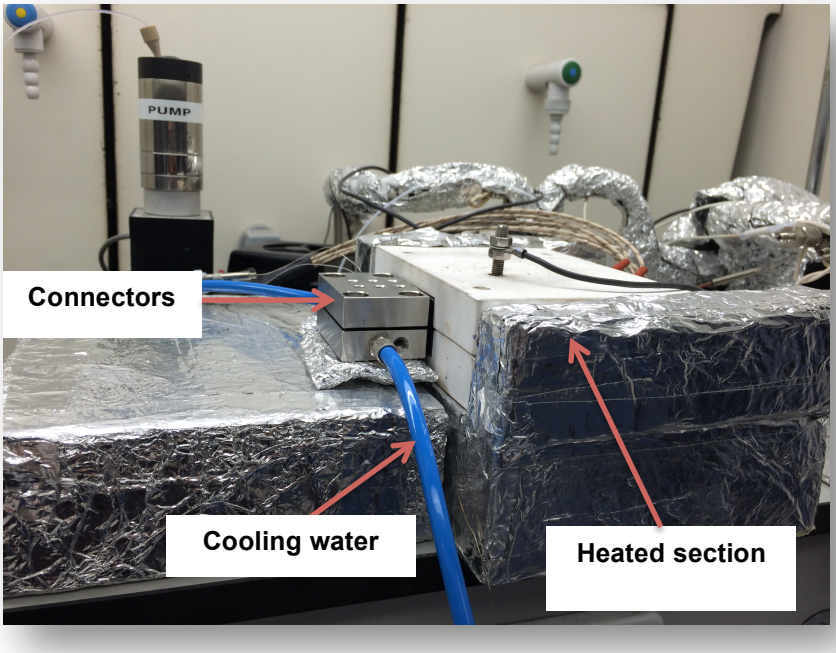

Figure 3.2 *M2/M3 reactor heating assembly.*

3.1.2 Three-Phase Packed Bed Microreactors: Benzyl Alcohol System (Chapters V-IX)

Reactor Design B1 (Chapters V-IX)

The design for the packed bed microreactors was based on a serpentine reactor, with a channel 19 cm in total length. The reaction takes place in the areas packed with solid particles towards the end of the channel and takes up between 2 – 40 mm length. The area preceding the reaction section is designed to allow the reactants to adapt to reaction conditions before reaching the catalytic bed. In addition, glass beads are usually added before the catalyst in order to allow the flow to stabilise over the packing structure before entering the catalyst section. In this reactor, the gas is introduced into a liquid flow path, which – with the presence of a void space upstream the catalytic section – creates gas-liquid slug flow.

Reactor Design B2 (Chapter VIII)

In order to assess the impact of the gas-liquid introduction method into the reactor, the reactor inlet design was altered so that the liquid was introduced directly into the catalytic bed. The main channel dimension was kept the same as the B1 design (1 mm). The thin gas channels were designed to be 15 μm to prevent the liquid from entering the gas lines. The reverse configuration (of having the liquid reactant flow through the two thin outer channels while the gas reactant was flowed through the middle wider channel) was also tested.

3.1.3 Residence Time Distribution (RTD) Reactors (Chapter X)

The RTD reactors were designed to allow signal acquisition with Raman spectroscopy. This imposed constraints such as: (1) availability of an optical window to allow access of the Raman laser (this had implications on the microreactor holder design) and (2) the fabrication of "retention posts" that allow trapping of liquid at the reactor exit, necessary for the acquisition of the Raman signal.

Reactor Design RTD-1 for Liquid Phase RTD Measurements

Initial single phase method validation was carried out using the RTD-1 reactor, which had a simplified design, sufficient for single phase work. Although the RTD-1 reactor was designed to allow flexibility to input both a gas and a liquid reactant, the gas-side (thinner channel) was blocked and only the liquid side was used.

Reactor Design RTD-2 for Gas-Liquid Phase RTD Measurements

The RTD-1 reactor was altered to mimic the B1 reactor gas-liquid introduction method (see T-junction at channel inlet in **Table 3.1**) to yield the RTD-2 reactor, which was used for the gas-liquid RTD studies. This is so that the RTD data acquired can be obtained under conditions as close as possible to those obtained during reaction using the B1 reactor design (the hydrodynamics at the channel inlet has implications on the development of the flow profile, as will be shown in **Chapter VI**).

Table 3.1 List of microreactors used in this thesis with schematics and dimensions.

Microreactor name	Schematic	Channel width (mm)	Channel depth (µm)	Experimental system	Chapter
M1	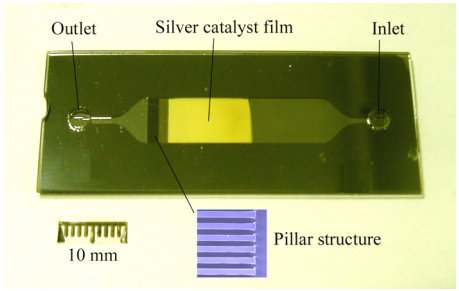	8	120	Methanol oxidation	IV
M2	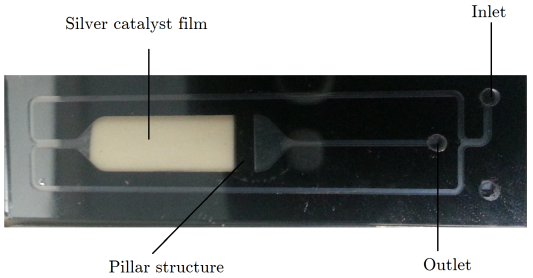	6	120	Methanol oxidation	IV

M3	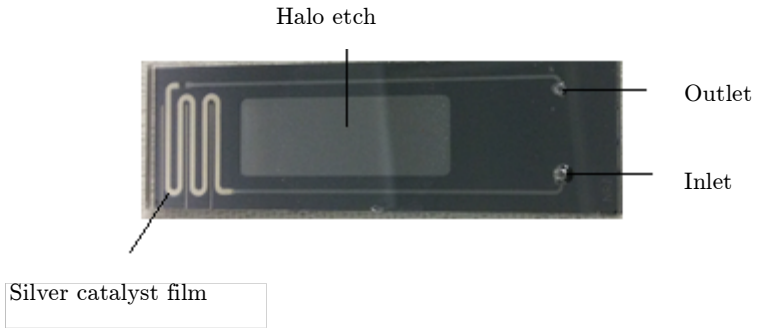	1	120	Methanol oxidation	IV
B1	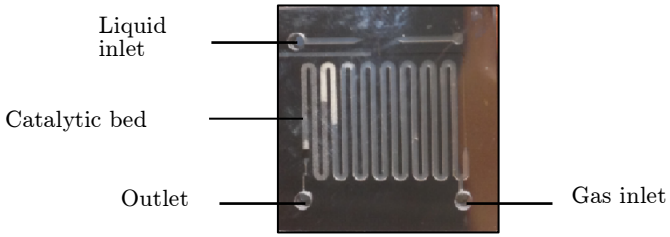	0.6	300	Benzyl alcohol oxidation	V-IX
B2	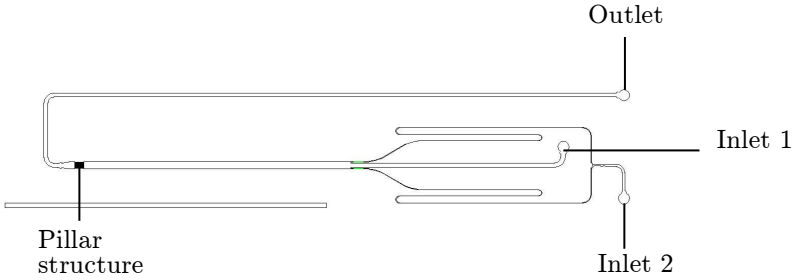	0.6	300	Benzyl alcohol oxidation	VIII

RTD-1	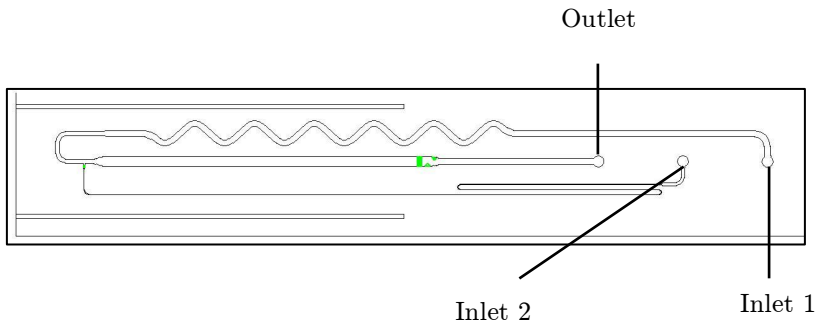	1	320	On-chip residence time distribution measurement (liquid phase)	X
RDT-2	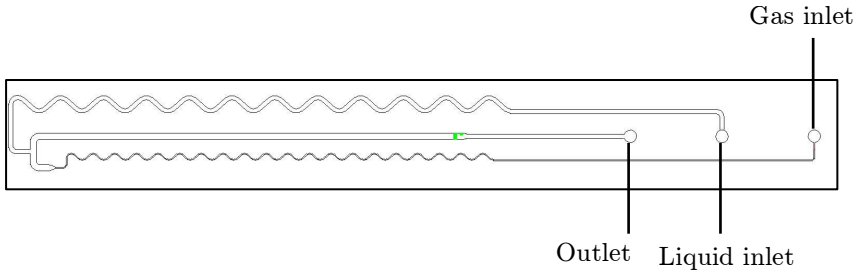	0.6	300	On-chip residence time distribution measurement (gas-liquid phase)	X

IV.

Reaction and Deactivation Studies of Ag Films during Methanol Oxidation to Formaldehyde in a Wall Coated Microreactor

---

In this chapter, an experimental system is developed for the gas phase methanol oxidation in a silver wall-coated microreactor. The challenges overcome were associated with high temperature sealing of a microfluidic silicon-glass device, analysis of a challenging reaction mixture in an automated fashion, and activation of silver catalyst films at high temperatures. The reactor developed is capable of operating up to 800°C and is designed to minimise thermal gradients across the reaction zone to <1°C. The pre-treatment method required to activate the silver film catalyst has been determined and consists of prolonged time on stream until a stable activity is achieved. Initial studies were carried out probing the impact of temperature, reactant concentrations and residence time on reactant conversion and product selectivity. Results demonstrate a dependence of selectivity on residence time, indicating a consecutive reaction pathway to CO_2 formation through the aldehyde. The observed increase in benzaldehyde selectivity and decreasing CO_2 selectivity with temperature is in good agreement with findings in the literature. The system developed can be used to generate experimental data for reaction kinetics determination.

4.1 Introduction

At industrial scale, the oxidative dehydrogenation of methanol on silver catalyst is carried out at 627°C and atmospheric pressure, with a feed consisting of a fuel-rich mixture of methanol and air. Steam is routinely added to increase the selectivity and heat transport as well as prevent carbon deposition. Typically, selectivity to the aldehyde of 90% and an O_2 conversion of 100% are achievable [1].

The oxidative dehydrogenation of methanol takes place in two main parallel reactions:

$$CH_3OH + \frac{1}{2}O_2 \Leftrightarrow H_2CO + H_2O \qquad (4.1)$$

$$CH_3OH \Leftrightarrow H_2CO + H_2 \qquad (4.2)$$

The selectivity to formaldehyde is limited by the following reactions, which produce CO and CO_2:

$$2CH_3OH + 3O_2 \Leftrightarrow 4H_2O + 2CO_2 \qquad (4.3)$$

$$H_2CO + O_2 \Leftrightarrow H_2O + CO_2 \qquad (4.4)$$

$$H_2CO \Leftrightarrow H_2 + CO \qquad (4.5)$$

There is a disagreement in the literature on the mechanism for this reaction; various kinetic models have been proposed (**Table 4.1**). The first kinetic model was proposed by Bhattacharyya [2], which was based on a modified Langmuir Hinshelwood mechanism, while the most recently published model is by Andreasen [1], who formulated a microkinetic model also based on a Langmuir Hinshelwood mechanism using experimental data obtained by Wachs and Madix [3] under ultra-high vacuum (UHV) conditions. They assumed only one type of oxygen species to be active (see **Section 4.2.1**), with a consecutive reaction pathway that produces CO_2 from formaldehyde. The model formulated by Andreasen et al. [1] explained the observed reaction orders, selectivity, and apparent activation enthalpies in the experiments carried out by Wachs and Madix [3] and Robb & Harriott [4]. However, Andreasen

ignored elementary reactions and thus to compensate for this assumption, the inlet oxygen concentration had to be reduced by 20% in the model to explain the experimental observations. Andreasen [5] then simplified the rate expression by using approximations such as the most abundant reaction intermediate (MARI)[†] and the irreversible step[‡] approximations to make the model suitable for practical applications, without losing accuracy.

It is generally assumed that oxygen is strongly adsorbed on silver, while methanol and the products are not significantly adsorbed [7], although they may be adsorbed on top of a layer of adsorbed oxygen. The methanol may therefore react directly from the gas phase with an adsorbed oxygen species or it may adsorb on the oxygen layer and then react [4]. Like oxygen, the intermediate methoxy species is strongly bound to the surface [7].

A particular issue with models presented above is that they are based on experiments carried out at temperatures lower than that industrially relevant and therefore their applicability remains questionable.

[†] *The MARI approximation assesses the reaction scheme for species that adsorb so strongly in comparison to other participants, that they completely dominate the surface. The surface coverage of other intermediates can then be approximated to zero [6]. Andreasen et al. [1] found that O* was the most abundant reaction intermediate at all temperatures in the methanol oxidation to formaldehyde on Ag.*

[‡] *The irreversible step approximation neglects the reverse reactions (of one or several steps) that have very large equilibrium constants. In the methanol oxidation to formaldehyde on Ag catalyst, these two steps relate to the methanol and formaldehyde oxidation reaction steps, (refer to Andreasen's proposed reaction mechanism in* ***Table 4.1****).*

Table 4.1. *Summary of methanol oxidation on Ag reaction mechanisms and their corresponding kinetic expressions.*

Reference	Kinetic model	Reaction mechanism	Kinetic expression	Temperature (K)	Reactor Type
Bhattacharyya (1971) [2]	SSAM "Steady state adsorption model" or Langmuir Hinshelwood	$Reactant + Catalyst_{ox} = Product + Catalyst_{red}$ $Catalyst_{red} + O_2 = Catalyst_{ox}$	$r_m = \left(\frac{2k_o k_m P_{O_2}^{1/2} P_m}{k_m p_m + 2k_O P_O^{1/2}}\right)$	537-563	Differential
Robb & Harriott (1974) [4]	Langmuir Hinshelwood Competitive adsorption of methanol and products	$O_2 + 2S \Leftrightarrow 2(OS)$ $M + (OS) \Leftrightarrow M(OS)$ $M(OS) \Leftrightarrow P + S$ $P + (OS) \Leftrightarrow P(OS)$	$r_m = \left(\frac{kK_m P_m}{1 + K_m P_m + K_p P_p}\right)\left(\frac{k_o P_o^{1/2}}{1 + k_o P_o^{1/2}}\right)$	693	Fixed bed, differential
Andreasen (2003;2005) [1;5]	Langmuir Hinshelwood	$CH_3OH(g) + * \Leftrightarrow CH_3OH*$ (1) $O_2(g) + * \Leftrightarrow O_2*$ (2) $O_2* + * \Leftrightarrow 2O*$ (3) $2CH_3OH* + O* \Leftrightarrow 2CH_3o* + H_2O*$ (4) $CH_3O* + * \Leftrightarrow H_2CO* + H* (slow)$ (5) $H_2CO* \Leftrightarrow H_2CO(g) + *$ (6) $2H* \Leftrightarrow H_2(g) + 2*$ (7) $H_2O* \Leftrightarrow H_2O(g) + *$ (8) $H_2CO* + O* \Leftrightarrow H* + HCOO*$ (9) $HCOO* + * \Leftrightarrow H* + CO_2* (slow)$ (10) $CO_2* \Leftrightarrow CO_2(g) + *$ (11)	$r_m = k_5 K_A \frac{P_m}{P_\vartheta}\left(\frac{P_{O_2}}{P_\vartheta}\right)^{1/4}\left(\frac{P_{H_2O}}{P_\vartheta}\right)^{-1/2}(1-\beta_I)\theta_*^2$ $r_f = k_{10} K_B \frac{P_f}{P_\vartheta}\left(\frac{P_{H_2}}{P_\vartheta}\right)^{-1/2}\left(\frac{P_{O_2}}{P_\vartheta}\right)^{1/2}(1-\beta_{II})\theta_*^2$ $\beta_I = \frac{(P_f/P_\vartheta)(P_{H_2}/P_\vartheta)^{1/2}}{(P_m/P_\vartheta)(P_{O_2}/P_\vartheta)^{1/4} K_{g,I}}$ $\beta_{II} = \frac{(P_C/P_\vartheta)(P_{H_2}/P_\vartheta)}{(P_f/P_\vartheta)(P_{O_2}/P_\vartheta)^{1/2} K_{g,II}}$	200-300	Ultra high vacuum system

k: rate constant; K: equilibrium constant; P: partial pressure; P_ϑ: thermodynamic reference pressure; m: methanol; o: oxygen; p: products; f: formaldehyde; r_m: rate of methanol oxidation; r_f: rate of formaldehyde oxidation; S: active site; OS: oxygen chemisorbed on active site; $catalyst_{ox}$: oxidised catalyst; $catalyst_{red}$: reduced catalyst.

The presence of more than one oxygen species (see **section 4.2.1**) and the possibility of a consecutive reaction scheme, make elucidation of the reaction kinetics a difficult task. In addition, the methanol oxidation to formaldehyde is a high temperature gas phase reaction, hence attaining isothermality within the reaction zone mandates challenging design considerations. Most importantly, there is a need for kinetics at industrial operating temperatures and the use of microreactors will help to eliminate any heat and mass transfer limitations currently observed at the bench scale. Therefore, this chapter will focus on developing a reaction system for the study of methanol oxidation to formaldehyde in a wall-coated microreactor, with the ultimate aim of being used for the acquisition of intrinsic reaction kinetics. An automated analytical sampling method will be presented, capable of analysing for the wide variety of gaseous hydrocarbon and permanent gas products. The behaviour of Ag films while catalysing methanol oxidation is rather complex; these films are known to exhibit a complex behaviour upon heating and reaction with oxygen, resulting in complex activation behaviour and difficulty in stabilising the catalyst. Understanding how this catalyst behaves and the procedure to obtain a stable, active catalyst, necessary for a kinetic study will also be demonstrated in this chapter.

4.2 Background

4.2.1 Reaction Mechanism and the Role of Oxygen

Oxygen species O_α O_β and O_γ

Bao and Schlögl et al. [8] have proposed three different atomic oxygen species that exist on Ag at high temperatures (500-1000K): O_α, O_β and O_γ, desorbing (in UHV) at 600K, 600-850K and 900K respectively (**Table 4.2**). The desorption temperature of O_α is well below the industrial reaction temperature, and therefore it has been suggested that it is not the dominant surface oxygen species involved in the reaction. Andreasen [1] and Ren et al. [9] argued that this conjecture is only valid in UHV conditions, and that O_α could be the active species at industrial conditions. Wachs and Madix [3] studied the reaction by temperature programmed reaction spectroscopy; contrary to Bao [8], they proposed a simple mechanism involving O_α as the only active oxygen species.

Table 4.2 *Different oxygen species (O_α, O_β and O_γ) present during the O_2-Ag interaction and their adsorption/desorption behaviour with temperature.*

Oxygen Species	Method of formation	Location	Desorption Temperature in UHV (K)
O_α	Dissociation of molecular O_2 chemisorbed surface bound oxygen	Silver surface	600
O_β	Dissolution of O_α in the bulk via interstitial diffusion at >450K	Silver lattice	600-850
O_γ	Segregation of O_β from the bulk to the surface via interstitial diffusion at >580K	Embedded in uppermost layer of silver	900

Waterhouse [10] studied the reaction at more realistic temperatures of 923K and formulated a reaction scheme where the oxygen adsorbs dissociatively to form surface atomic oxygen (O_α), or in the vicinity of grain boundaries to form O_γ. Neither of these oxygen species are stable at 923K, so they either desorb as O_2 or diffuse into the catalyst subsurface to form O_β through interstitial and grain boundary diffusion mechanisms. Nagy and Mestl [11] proposed a more detailed mechanism for the oxygen diffusion depending on the temperature. They proposed an "interstitial" bulk diffusion mechanism at temperatures below 973K, where O_β atoms jump from interstitial site to interstitial site between the silver lattice atoms (**Figure 4.1a**). At higher temperatures, an "interstitialcy" bulk oxygen diffusion mechanism (also known as vacancy diffusion or substitutional diffusion) dominates by which O_γ oxygen atoms substitute for silver lattice atoms (**Figure 4.1b**).

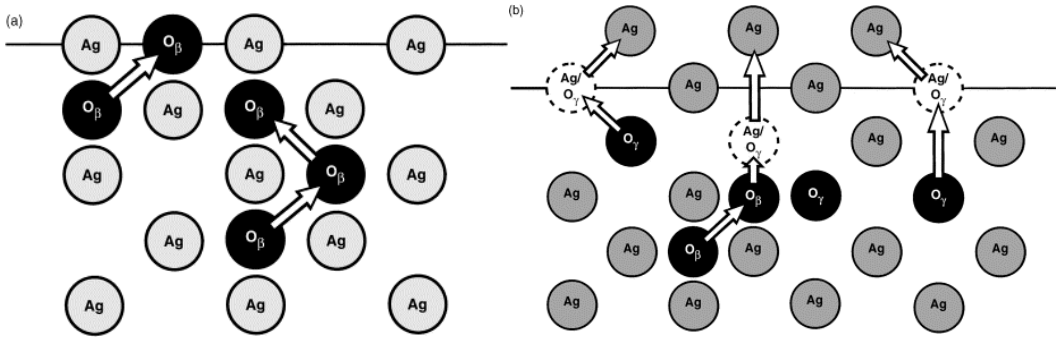

Figure 4.1 *(a) Scheme of the interstitial and (b) interstitialcy bulk oxygen diffusion mechanism in silver [11].*

Duality of reaction mechanism: dependence on temperature

The temperature dependence of the reaction between 500-900K has been studied by Nagy and Mestl [11]. They concluded that it is the different temperature stability of the various oxygen species present during the reaction that explains the temperature dependence of selectivity. They also proposed a model where the O_γ is the active oxygen species required for the direct dehydrogenation of methanol to formaldehyde and hydrogen, whereas the O_α is the species reacting in the oxi-dehydrogenation and total oxidation reaction with methanol to produce formaldehyde and water.

The authors therefore propose a more detailed form of equations 4.1 and 4.2:

$$CH_3OH + O_\alpha \xrightarrow{Ag} H_2CO + H_2O;\ \Delta H = -159\,\frac{kJ}{mol} \qquad (4.6)$$

$$CH_3OH \xrightarrow{AgO_\gamma} H_2CO + H_2;\ \Delta H = +84\,\frac{kJ}{mol} \qquad (4.7)$$

The catalytic nature of O_γ in the dehydrogenation is stressed in equation 4.7. The dehydrogenation reaction is endothermic and therefore thermodynamics dictates that it will dominate at higher temperatures. This combined with the high thermal stability of O_γ results in an optimum reaction condition with high CH_2O selectivities at ~900K (**Figure 4.2**). This hypothesis was also proven by Ren [9], who concluded that the O_γ species on silver represents the active oxygen species that catalyses the direct dehydrogenation of methanol to formaldehyde.

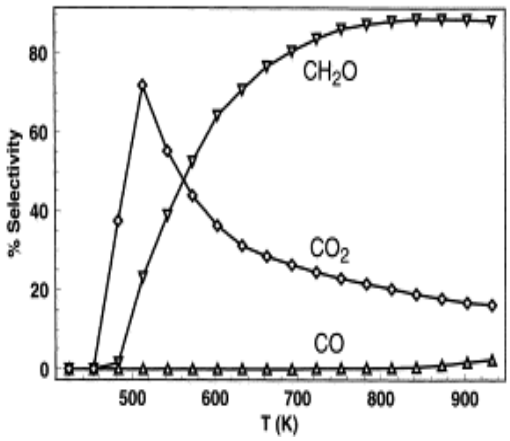

Figure 4.2 *Selectivity to CH_2O (open downward triangles), CO_2 (open diamonds), and CO (open upward triangles) as a function of reaction temperature in the partial oxidation of methanol to formaldehyde [11].*

Formation of CO_2: parallel or consecutive reaction pathway?

Much debate is on-going regarding the route to the formation of CO_2. Methanol can either be converted to formaldehyde and subsequently oxidised to CO_2 and water (consecutive reaction pathway) or directly oxidised to CO_2 (through a parallel reaction pathway). Lefferts [12] studied the reaction near industrial conditions and proposed a scheme where CO_2 is formed via a formaldehyde intermediate. Similar conclusions were drawn by Wachs and Madix [3], who showed that a methoxy intermediate is formed by a reaction between methanol and atomic surface oxygen (O_α), which decomposes to formaldehyde and H_2. The formaldehyde may then be oxidised to CO_2 through the formate intermediate, $HCOO^-$, in a parallel-consecutive reaction pathway. In contrast, other authors such as Robb & Harriott [4] observed constant selectivity to CO_2 and formaldehyde (at low conversions and 420°C) indicating the formation of CO_2 directly from methanol by a reaction parallel to the main reaction. Similarly, Nagy and Mestl [11] monitored conversion of methanol and selectivity to formaldehyde and CO_2 with increasing temperature and proposed that the reaction cannot be of the consecutive type. The observed maxima in CO_2 selectivity at 573 K is attributed to the different thermal stabilities of the O_α (which catalyses the oxi-dehydrogenation and complete oxidation reaction paths, Eq. 4.1, 4.3-4.5) and the O_γ (which catalyses the direct dehydrogenation of methanol to formaldehyde: Eq. 4.2). The different thermal

stabilities of these oxygen species (**Table 4.2**) explains the high selectivity to CO_2 at temperatures of 523-623 K. Improved selectivity to formaldehyde along with an increase in methanol conversion with increasing reaction temperature occurs (shown in **Figure 4.2**). A reaction-in-series model where formaldehyde is the intermediate product and CO_2 the final complete oxidation product would predict the opposite behaviour.

4.2.2 Criteria for Conducting Kinetic Studies

In order to obtain the relevant information with regard to intrinsic catalytic activity, selectivity, and deactivation, the following guidelines have been proposed by Kapteijn [13].

- The reactor must adhere to ideal behaviour: plug flow or CSTR, isothermal bed, absence of mass transfer limitations.
- Data must be compared at low conversions to get an insight into real activity differences.
- Product selectivities must be compared at same conversion levels to avoid interference of conversion differences.

There are different lab catalytic reactor types available for the collection of kinetic data; Carberry [14] classifies these as differential, integral, CSTR, and recycle reactors. A decision is usually made on whether the reactor should be operated in differential or integral mode – a reactor is generally termed differential when the conversion of the reactant through the catalyst bed is less than 5%. Low conversions levels (<60%) are recommended even when operating in integral mode; this is important to ensure that differences observed are not disguised due to the high conversions. As an example, a factor of two increase in activity can yield a pair of conversion levels of 90 and 99%, 30 and 51% or 5% and 9.75%, depending on the used space velocity [13].

There are advantages and disadvantages to both integral and differential reactors in collecting kinetic measurements. The integral reactor is problematic as it exhibits a concentration gradient and the solution of its material balance demands integration. In comparison, the analysis of the kinetic data in the differential reactor is much simpler

as the conversion represents the reaction rate directly and permits the derivation of simple algebraic reactor model equations [15]. However, operating a differential reactor has its own difficulties, as a small incremental conversion is usually difficult to measure experimentally for a complex multicomponent mixture.

4.2.3 Silver Film Catalyst Activation and Deactivation Behaviour

Silver catalyst exhibits a complex behaviour during reaction at high temperatures and this behaviour is greatly impacted by the activation method [16-18]. The start-up and activation behaviour of the catalyst depends largely on the initial surface morphology of the catalyst and the pre-treatment conditions [16;17]. It is therefore important to carry out proper catalyst testing prior to conducting any kinetic studies in order to obtain the relevant information with regard to activation and deactivation behaviour.

Activation by repeated oxidation/reaction cycles

Activation of silver catalyst for the methanol oxidation by repeated oxidation/reaction cycles has previously been demonstrated [16;19;20]. *Operando* Raman studies on the silver catalyst showed that the activity of silver catalyst becomes stable after three oxidation cycles consisting of repeated oxidation in O_2/He (60 min) and reaction in $CH_3OH/O_2/H_2O$/He mixtures (90 min) [19]. The disappearance of what was attributed to an O_γ species upon introduction of the reaction mixture, and the growth of an unidentified Raman band at 610 cm^{-1}, were observed upon repeated oxidation/reaction cycles.

Activation by continuous time-on-stream

Waterhouse et al. followed the changes in morphology, oxygen chemisorption behaviour and performance of the catalysts during the first 96 hours of methanol oxidation operation, under conditions of industrial formaldehyde synthesis (molar feed compositions $CH_3OH/O_2/H_2O$/He = 2.25/1/1.7/20, GHSV = 1.25×10^5 h^{-1}) [16]. The authors found that pre-treatment by continuous time on stream results in a 25-45% increase in methanol conversion for catalysts that possess a grain-like structure, and only a 3-6% increase in the conversion for catalysts with a low degree of surface roughness. This improvement in the activity was attributed to reaction-induced

restructuring of the catalyst surface. “Pinhole defects” were noticeable after 18 hours on stream, which formed at temperatures of 773K. These pinholes and the surface restructuring – occurring as a result of the reaction – are anticipated to have caused the increase in conversion as the reaction was allowed to run for longer. In addition, reaction induced surface restructuring has an impact on the oxygen chemisorption properties of the silver catalyst, enhancing O_γ formation, thus bringing about superior catalytic performance.

4.3 Materials & Methods

4.3.1 Continuous Flow Microfluidic Experimental Setup

General description

A schematic (**Figure 4.3**) and a photograph (**Figure 4.4**) of the experimental setup are shown below. A liquid mixture of methanol (methanol ACS reagent ≥99.8%, Sigma Aldrich) and water was fed into a micro-evaporator/mixer (**Figure 4.5**) using a rotary piston pump (MilliGAT, Presearch). The liquid was mixed with a gas mixture of oxygen and helium, each regulated by a mass flow controller (Brooks 5850TR, Brooks Instrument) and passed through a check valve to prevent backflow of gases. The experimental setup was built with flexibility in mind - it is possible to connect a third mass flow controller if needed (shown by the third gas line in **Figure 4.3**). From the micro-evaporator, the evaporated methanol/water/helium/oxygen mixture passed through a 6-port gas valve, which either directed the flow to the micro-reactor, or through a bypass directly to the gas chromatograph (GC). A gas chromatograph (7890A, Agilent) fitted with a thermal conductivity detector (TCD) was used for the analysis of the reactor feed and effluent streams. Separations were carried out using two columns connected in series: a GS-Carbon PLOT column for the C1 oxygenates (CH_3OH, CH_2O, HCOOH) and a HP-PLOT Molecular Sieve for the permanent gases (O_2, H_2, CO and CO_2). The effluent from the GC was flowed through a separator, where the condensable portion was removed and the non-condensable gases were vented off. The analytical method was developed to allow analysis for all hydrocarbon and permanent gas products within 16.5 minutes. This required careful timing of a sequence of events to prevent the CO_2 from entering and damaging the molecular sieve column.

Detailed information on the analytical method development, GC calibrations and equipment calibrations are presented in **Appendix A**.

Temperature control

All feed and product components were maintained at temperatures higher than their condensation temperatures (~100°C due to the presence of water and formaldehyde in the mixture). This was done by heating all the gas lines from the micro-evaporator/mixer to the reactor and the GC to 105°C by wrapping fibreglass heating coils around the tube lines. The heating coils were initially controlled by power regulators, which were only able to control the temperature to ±20% of the set temperature, resulting in irreproducible results. Consequently, these were replaced with temperature controllers, resulting in a remarkable improvement in the reproducibility of the methanol peaks observed with the GC. The line exiting the GC was bubbled in water in a closed flask to absorb a large proportion of the formaldehyde while the remainder was vented off.

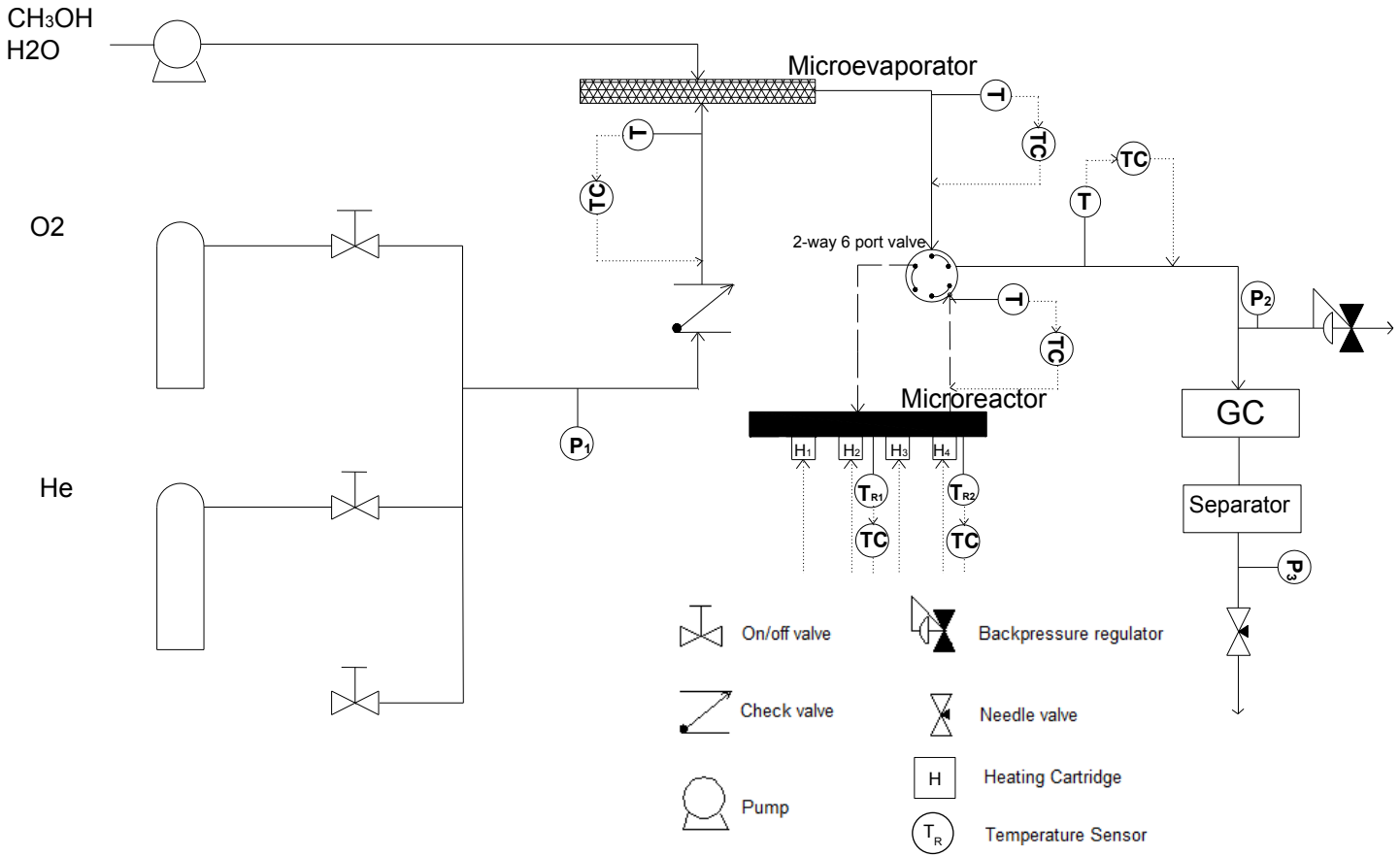

Figure 4.3 *Schematic of gas phase methanol oxidation experimental setup.*

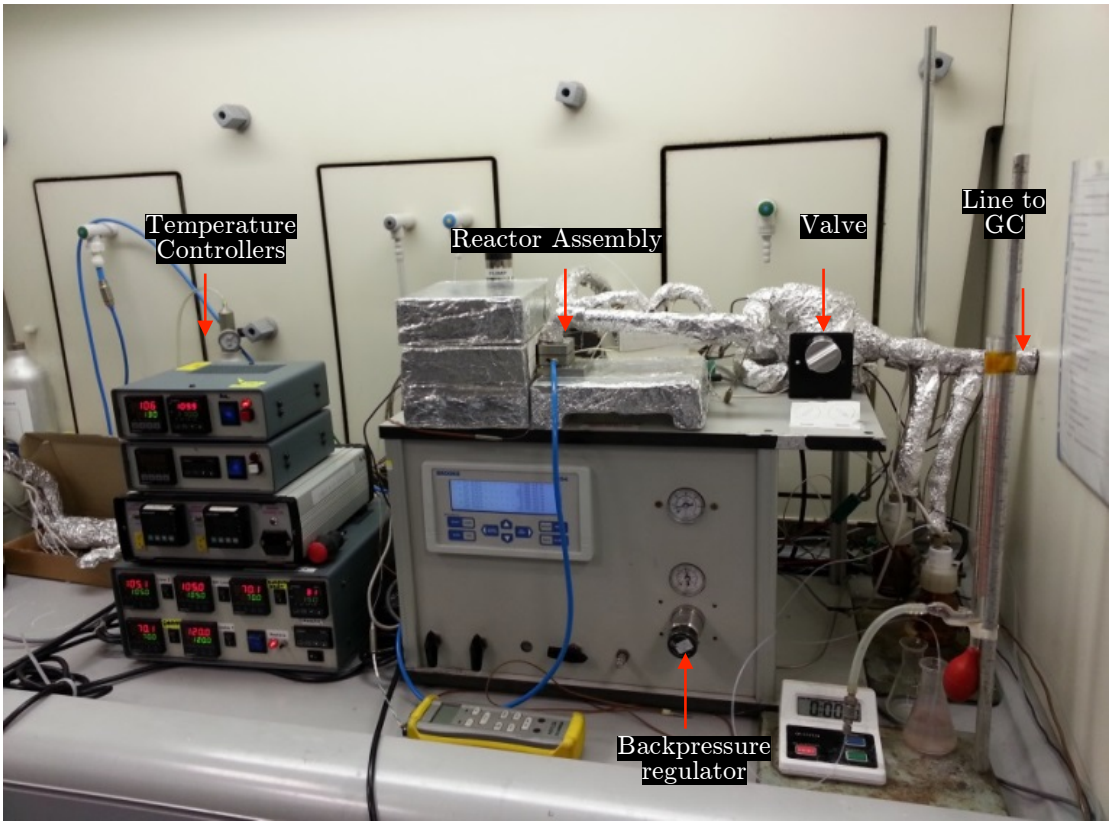

Figure 4.4 *Photograph of gas phase methanol oxidation experimental setup.*

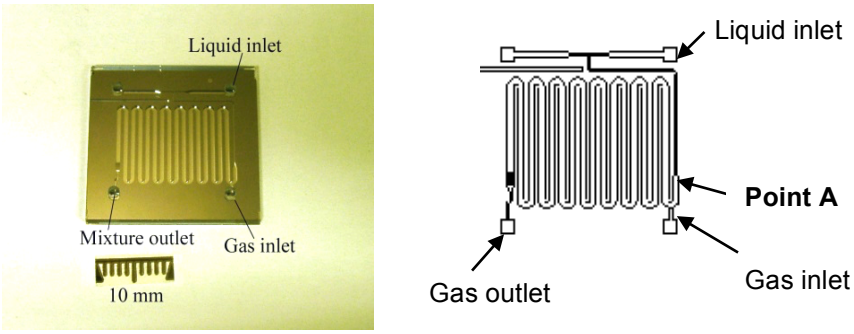

Figure 4.5 *Microevaporator photograph and schematic.*

Pressure control

The pressure was regulated to 1.6 bara using a backpressure regulator fitted between the experimental set-up and the gas chromatograph (at P_2 in **Figure 4.3**). The pressure drop across the gas sampling loop in the gas chromatograph was maintained constant through the use of a pressure control system. This is important as changes in pressure would alter the volume of sample entering the sample loop and thus affect the repeatability of the results. The pressure was therefore monitored at three places: P_1 (before the reactor) P_2 (at the backpressure regulator, before the GC) and P_3 (after the GC). This arrangement allowed for flexibility in terms of changes in flowrate whilst keeping the pressure upstream the GC constant. If there was an increase in flowrate, any extra gas flowed out through the backpressure regulator exit at P_2, and the pressure in the line entering the GC was therefore maintained constant. More information on the effect of pressure on the gas chromatographic results is presented in **Appendix A**.

4.3.2 Microstructured Reactor Designs

Various reactor designs were tested: M1, M2, and M3 – presented earlier in **Table 3.1** and shown in **Figure 4.6**, with dimensions shown in **Table 4.3**. Reactor design M1 consisted of an 8 mm wide channel rectangular reactor heated with a simple stainless steel block powered by four heating cartridges. This reactor was capable of operating up to 550°C. To overcome the challenge of sealing at higher temperatures, M2 and M3 reactor designs were developed, where the high temperature reaction zone was separated from the cooled connection zone, in order to prevent overheating of the O-rings used to provide the sealing. This type of system was demonstrated by Marre et al. [21] who dealt with the challenges associated with sealing at high temperatures by placing the inlet/outlet connections on a mild temperature area of the chip, away from the reaction zone. However, their system was able to withstand temperatures of only 400°C. M2 and M3 designs followed this methodology but are capable of withstanding temperatures of 800°C without compromising on the temperature uniformity within the reaction zone. M2 reactor design had a similar geometric shape to M1, but with a smaller channel width of 6 mm; M3 consisted of a serpentine reactor with a 1 mm main

channel width. Variations of the M3 design (the halo-etch and the dumbbell shaped reactors), optimised for high temperature operation (>550°C) are proposed as an outcome of conclusions of a COMSOL heat transfer simulation. Results will be presented using the initial reactor design M1 at relatively low temperatures (<550°C) and the optimised reactor design M3 for higher temperatures (550°C). M2 was used as a prototype to measure the temperature uniformity and thus no reaction data was obtained using this reactor.

4.3.3 Microreactor Fabrication

The microfabrication was carried out using photolithography and deep reactive ion etching, in accordance with the procedure described in **Appendix A**. Reactor design M3 required various extra steps for the fabrication of the halo feature. Two different methods were investigated to form this halo feature (i) two-step single side photolithography and (ii) two-step double side alignment/photolithography. The latter method was the preferred method for fabricating halo features. These methods are discussed in **Appendix A**.

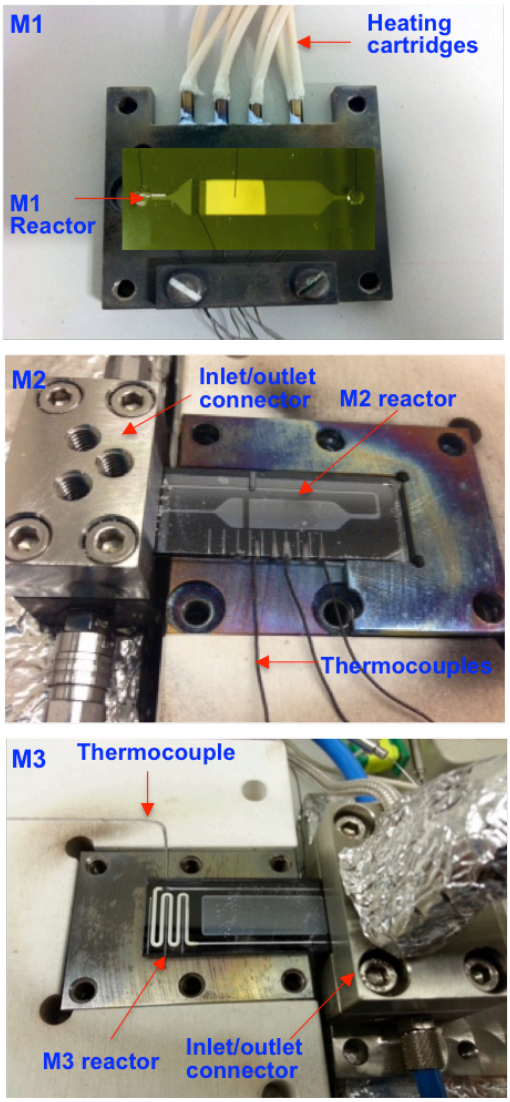

Figure 4.6 *Photographs of the methanol system reactors and heating assemblies.*

Table 4.3 *Main channel dimensions and maximum operating temperatures for all three microreactor designs used in the methanol system: M1, M2, and M3.*

	Width (mm)	Depth (μm)	Maximum Operating Temperature (°C)
M1	8	120	550
M2	6	120	800
M3	1	120	800

Microreactor design for 550°C (M1)[†]

The microstructured reactor designed for the relatively low temperature (up to 550°C) studies contained a single, wide reaction channel, with a main channel width of 8 mm and depth of 120 mm. A pillar structure was incorporated at the end of the reaction channel to enable the use of catalyst in particulate form and consisted of small rectangular posts of 60μm (W) × 2mm (L), arranged in 40μm intervals. The silicon-glass microstructured reactor was heated via a heating block that contained four cartridge heaters (1/8" O.D., Watlow). Five K-type thermocouples (0.5 mm O.D., RS) were located at the back of the block and just 0.5 mm beneath the surface of the block in contact with the microreactor, to measure and control the block temperature. Two pairs of cartridges were controlled separately so that a maximum temperature difference of 5°C was achieved across the reaction zone. Due to the high temperatures used, there were only a few materials that could be used to provide the seal between the reactor and the tubing, such as steel and graphite. Steel was not an option as it would cause the silicon/glass reactor to break with tightening. Therefore, graphite was chosen to provide the sealing between the tubing and the reactor inlet/outlet. A pair of stainless steel clamps with a sealing structure using graphite ferrules was used to provide the interface between the reactor and the inlet/outlet tubing. The whole assembly was encased in ceramic insulation material.

Microreactor design for 800°C (M2 & M3)

Graphite ferrules used in the M1 design began to soften at temperatures of 450°C. Thus, the previous arrangement in design M1 was operated at a maximum temperature of 550°C, above which the graphite ferrules melted. The strain point (the extreme upper limit of serviceability for annealed glass) for the glass (Corning 7740, Newcastle

[†] *The design of reactor M1 was carried out by Dr Enhong Cao, UCL.*

Optical) used is 510°C, and therefore, operation beyond 550°C would pose problems not just for the graphite seals, but also for the glass. SD-2 glass (Hoya Candeo Optronics) has a higher softening temperature than corning 7740 glass and was therefore used in reactor designs M2 and M3. The next section will show the reactor design, heating assembly, and a demonstration of the temperature uniformity achieved using both theoretical and experimental methods, to arrive at the M3 design, capable of reaching temperatures of 800°C. The entire assembly was covered with thermal insulation (WDS Ultra, Morgan Advanced Materials), composed of silicon dioxide and silicon carbide (has a very low thermal conductivity of 0.04 W/mK). Despite the high temperatures used, this reactor is capable of minimising thermal gradients across the reaction zone to <1°C (see **section 4.4.1**). The finalised and optimised heating assembly (M3 design) is shown in **Figure 4.7.**

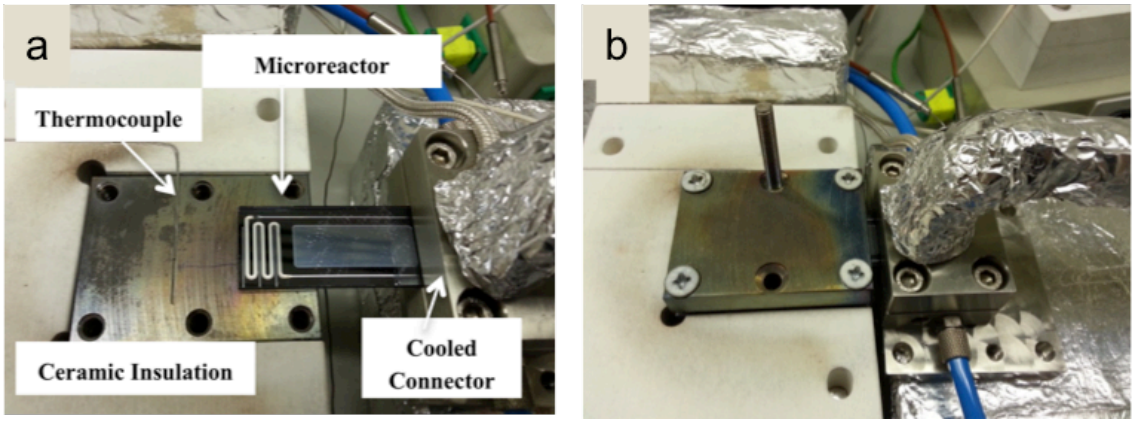

Figure 4.7 *(a) Reactor heating assembly showing the reactor positioned on the heating block for reactor design M3 (b) complete heating assembly.*

4.3.4 Heat Transfer Simulation using COMSOL

Simulations were performed on the methanol heating assembly one-end-cooled connection design, using the Heat Transfer in Solids module provided by COMSOL Multiphysics (version 5.0). The following heat equation is used to solve for the temperature, T:

$$\rho C_p \left(\frac{\partial T}{\partial t}\right) + \nabla \cdot (k \nabla T) = Q \qquad (4.8)$$

where ρ is the density, C_p is the specific heat capacity (which varies depending on the material: silicon/glass/stainless steel holder), T is temperature, Q is the heat flux by conduction, k is the thermal conductivity of the material.

The modelled system consists of a silicon-glass microreactor (resembling the geometry used experimentally in design M2) sandwiched between two stainless steel blocks, each containing four cylindrical heating cartridges (**Figure 4.8**). The boundary conditions were specified as a power input to each of the eight cylindrical heating cartridges and a temperature of the cooling water inlet (**Table 4.4**). The power input was determined by trial and error, to achieve the required temperature in the reactor. The properties used for the different materials are shown in (**Table 4.5**). The COMSOL Laminar Flow interface was coupled with the heat transfer to simulate the flow of water in the cooled-end connector (see **section 8.2.1**. for a description of the laminar flow model).

Table 4.4 *Boundary conditions for COMSOL heat transfer simulation (see Figure 4.8).*

	Boundary 1-8	**Boundary 9**	**Boundary 10**
Type	Total boundary power, $P_{b,tot}$	Temperature, T_o	Temperature, T_o
Location	Cylindrical heating cartridges	Cooling water inlet	Ambient temperature
Value	5.2W	293.15 K	293.15

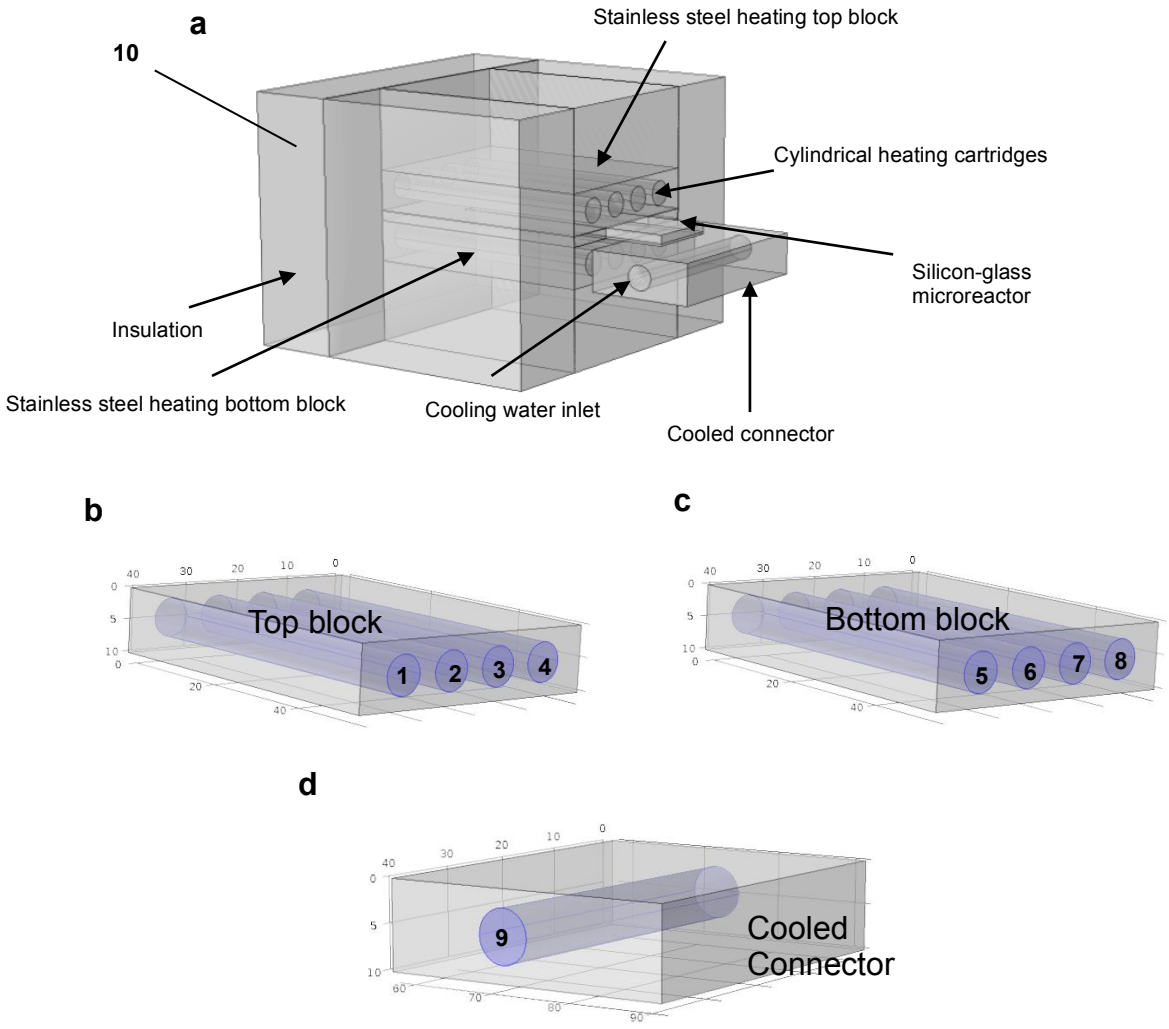

Figure 4.8 *Schematic of geometry used in COMSOL heat transfer simulation.*

Table 4.5 *Parameters used in COMSOL heat transfer simulation.*

	Steel Holder	Insulation	Silicon	Glass
Heat capacity at constant pressure (Cp) [J/(kgK)]	475	0.00105	703	750
Density (ρ) [kg/m^3]	7850	1400	2330	2230
Thermal conductivity (k_t) [W/(mK)]	44.5	0.04	163	1.14

4.3.5 Catalyst Preparation Method

The silver catalyst was deposited on the microreactor by sputter coating pure silver using a sputter coater (K675X Emitech, Quorum Emitech). The sputter coating parameters were selected based on historical data targeting a 250 nm catalyst thickness. The coating parameters are listed in **Table 4.6**.

Table 4.6 *Sputter coating parameters.*

Parameter	Set Value
Current (mA)	150
Number of cycles	3
Sputter time (min:sec)	2:35

4.3.6 Methanol Evaporation

To perform the evaporation, liquid methanol was pumped to the microevaporator where it was mixed with the gas and evaporated. The evaporator was heated via two 50W heating cartridges. The exit stream from the microevaporator was directed to the GC through the 6 port 2-way valve. The set evaporator temperature was varied depending on the total flowrate of the methanol/water mixtures as will be shown in **section 4.4.2**.

4.3.7 Blank Reactions

To confirm the absence of a homogeneous non-catalytic reaction, blank reactions were carried out by flowing liquid methanol through a reactor of the M1 design (with no catalyst) and evaporated in the microevaporator where the temperature was set to 40°C, with the incoming helium heated to 70°C before entering the evaporator. Methanol concentration of 9.8% and oxygen concentration of 9% were used in these tests. The residence time selected was 10 ms for the decomposition (reaction in the absence of oxygen) and 30 ms for the oxidation (reaction in the presence of oxygen) blank experiments. The experiments were carried out at 250°C and 500°C and results will be reported for each.

4.3.8 Silver Film Catalyst Activation Behaviour

Three flow microreactors were used to study the silver catalyst activation behaviour, all of the M1 design. The microreactors had etch depths of 110-130 μm and a 250 nm layer of silver catalyst was deposited at the base of the microchannel. A total gas flow of 55 NmL/min equating to a space time of ~6.7 ms was used for the majority of experiments. The catalyst bed spanned the whole channel width of 8 mm (radially) and extended for 12.5 mm along the channel (axially).

The gas mixture used in the reaction consisted of approximately 9.8% methanol, 4.4% oxygen, 7.6% water, with helium as balance (all gas compositions given in mol%). The concentrations were selected to maintain the CH_3OH/H_2O and CH_3OH/O_2 ratios constant at 1.25 and 2.35 respectively (close to industrial conditions). The liquid CH_3OH/H_2O was made up by mixing 75% v/v methanol with 25% (v/v) water and the methanol/water mixture supplied in one stream through the liquid pump. When oxidation/reaction cycles were used, the oxidation step consisted of flowing 10% oxygen in helium through the reactor for one hour. The pressure in the reaction zone was kept at 1.6 – 1.7 bara. Automated gas sampling was initiated every 16.5 minutes, which was the length of one GC run. The pressure before and after the GC were maintained at 1.6 bara and 1.55 bara respectively in all runs.

4.3.9 Catalyst Characterisation using Scanning Electron Microscopy

Scanning electron microscopy (SEM) micrographs of the catalysts were taken before any treatment (i.e. immediately after sputtering the silver onto the silicon wafer), again following anodic bonding, and finally after reaction, to gain a better understanding of how the catalyst morphology is influenced by heating and reaction. A Jeol JSM-6480LV high-performance, Variable Pressure Analytical Scanning Electron Microscope and a Zeiss EVO SEM were both used for this purpose. Post-mortem characterisation of the catalyst was carried out by retrieving the catalyst from the anodically bonded reactors; this was done by slicing the glass/silicon around the etched microchannel using a dicing saw (DAD3230, Disco) and examining the used catalyst using SEM.

4.3.10 Parametric Studies

Parametric studies probing the impact of temperature, inlet oxygen concentration and residence time were carried out in reactor designs M1 and M3. **Appendix A** shows an example calculation used to calculate the feed flowrates into the microreactor. The component mole fractions used in this work were mainly based on **Table 4.7**.

Table 4.7 *Mole fractions used for parametric studies.*

Component	Mole %
CH_3OH	9.82
O_2	4.36
H_2O	7.44
He	78.38

4.4 Results & Discussion

4.4.1 Heat Transfer Simulation using COMSOL

Figure 4.9 shows the agreement between the actual temperature distribution (measured experimentally with thermocouples) on the silicon surface of the M2 reactor and that simulated by COMSOL. Both experiment and simulation show that there is a uniform hot zone towards the back of the block, furthest away from the cooled end connection; this implies that a longer reactor, positioned towards the end of the block would be ideal.

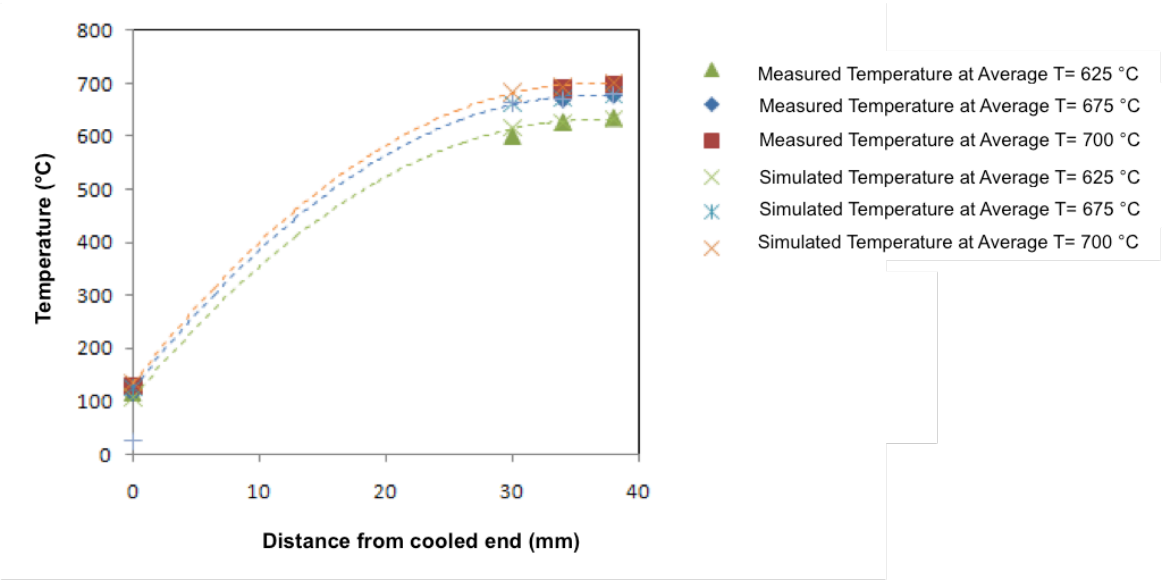

Figure 4.9 *Comparison of experimental temperature distribution and COMSOL simulation in M2 reactor design.*

Figure 4.10a and **Figure 4.10b** show the simulated temperature distribution over the entire reactor silicon wafer, across the axial and radial directions respectively. The rapid decline in temperature in the axial direction is clear, particularly towards the cooled end zone (**Figure 4.10a**). The maxima in temperature in the radial direction is expected – due to heat losses on either side of the block (**Figure 4.10b**). **Figure 4.10c** shows the temperature distribution across the axial direction, focusing on the reaction zone only, where a 7°C temperature difference is observed on both the silicon and glass.

The COMSOL heat transfer model was then used to optimise the temperature distribution, in order to reduce this temperature variance across the reaction zone. Various alternative configurations were tested, this included (**Figure 4.11**):

- Rotation of the heating blocks so that they do not run in parallel with the reactor length
- Movement of the reaction zone backwards towards the uniform hot zone
- Reduced cooling of the connector
- Longer reactor

- Halo etch (creating an air gap) between the heated and cooled zones

Table 4.8 shows results of the listed changes above using the COMSOL model. No significant effect was brought about by rotating the heating cartridges. However, moving the reaction zone backwards, cooling the connector less, increasing the reactor length, and introducing a halo etch – all contributed to a more uniform temperature distribution across the reaction zone, down to an acceptable 1°C. **Appendix A** shows the design mask of the finalised reactors (with three alternate halo etch designs: the halo etch and the dumbbell reactors). The halo etch reactor was used to conduct the reaction experiments, and the experimental temperature measurements for this reactor are shown in **Figure 4.12** where the very small (<1°C) temperature gradient across the reaction zone is shown

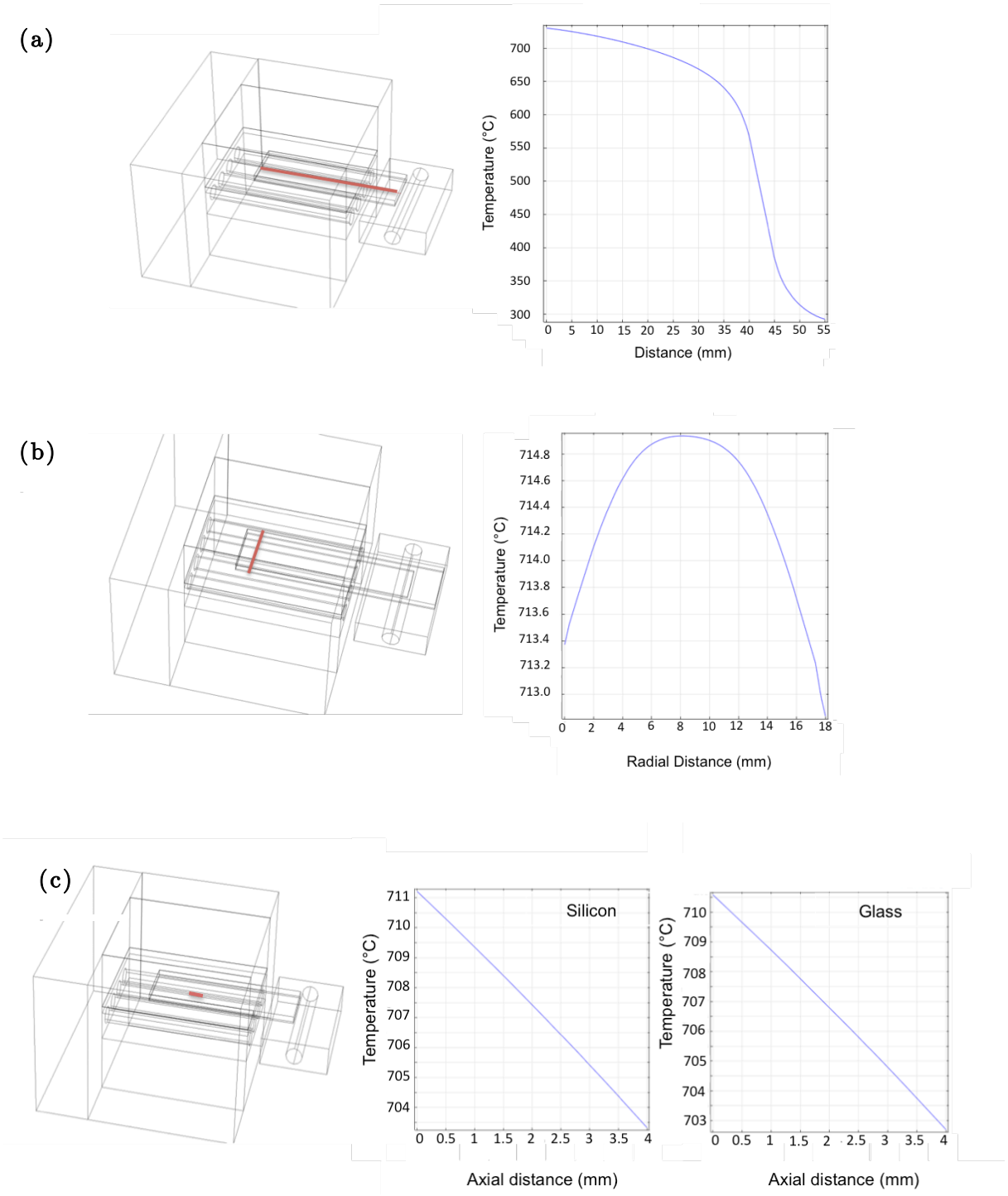

Figure 4.10 *Heat transfer simulation of methanol system reactor M2 (a) whole reactor in the axial direction (b) whole reactor in the radial direction (c) reaction zone in the axial direction.*

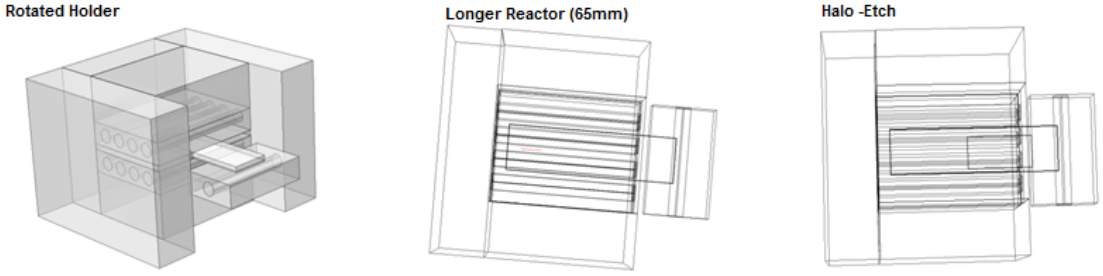

(a) (b (c)

Figure 4.11 *Schematic of reactor modifications to improve temperature uniformity across reaction zone (a) rotated steel holder (b) longer reactor and (c) halo-etch between reaction zone and inlet connection.*

Table 4.8 *COMSOL simulation results of the indicated reactor design changes to optimise the temperature uniformity across the reaction zone. Refer to* ***Table 4.9*** *for a description of each configuration. Temperatures are reported at various axial distances from the cooled end connector, focusing on the reaction zone.*

Distance from cooled connector (mm)	**Temperature (°C)**					
	Initial design	Design A	Design B	Design C	Design D	Design E
0	135.0	135.0	132.5	237.5	227.5	247.0
30	683.5	682.0	-	-	-	-
34	693.0	687.5	684.0	689.0	-	-
38	701.0	696.0	692.5	695.5	-	-
38	-	-	698.5	700.5	-	-
44	-	-	-	-	694.0	695.4
48	-	-	-	-	697.0	696.9
52	-	-	-	-	699.4	698
Temperature difference across reaction zone (°C)	8	8.5	6	5	2.4	1.1

Table 4.9 *Reactor designs studied in COMSOL simulation.*

	Rotated Holder	Reaction Zone Moved Back 4mm	Reduced Connector Cooling	Longer Reactor	Halo Etch
A	✓				
B		✓			
C		✓	✓		
D		✓	✓	✓	
E		✓	✓	✓	✓

Temperature (°C)	
T_1	T_2
526.0	526.7
523.0	523.7
600.0	600.6

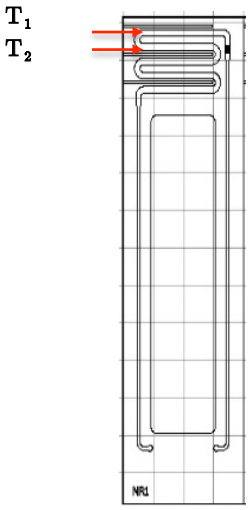

Figure 4.12 *Optimised M3 microreactor design and measured temperature uniformity across reaction zone for three different operating temperatures.*

4.4.2 Evaporation of Liquid Methanol

The flow in microchannels is significantly affected by the surface tension of the liquid, causing the liquid to form small uniformly spaced slugs that fill the channel. Flow boiling in microchannels is often accompanied by flow reversal, caused by expanding bubbles pushing the liquid-vapour interface in both upstream and downstream directions. The inlet temperature of the liquid and the pressure drop upstream have an impact on the evaporation inside the microchannels [22].

The evaporation was carried out between 40-80°C and monitored over time to determine the temperature that would yield the most stable evaporation. **Figure 4.13** shows the impact of evaporator temperature on the reproducibility of the methanol GC peak areas. An increase in the evaporator temperature above 40°C resulted in irregular evaporation. An optical microscope was used to examine the behaviour of the liquid meniscus (at the liquid channel T-junction, point A in **Figure 4.5**) during the evaporation, and it appeared that at temperatures above 40°C, evaporation happened vigorously throughout the channel. This meant that the evaporation was taking place at the liquid inlet port, and if the liquid was not supplied quickly enough by the pump, there would be a disruption to the evaporation. By setting the evaporator to a relatively low temperature (40°C) and allowing the methanol to flow to the gas inlet port (point A in **Figure 4.5**) before turning the gas flow on, a stable liquid front was maintained. The heated gas (temperature set to 70°C in the gas line before entering the evaporator) was then used to evaporate the methanol.

Increasing the methanol concentration (and therefore the amount of liquid requiring evaporation) to values greater than 10 mol% required the manipulation of the evaporator temperature to achieve a stable evaporation. A stable evaporation was assessed by taking multiple samples during the evaporation (a minimum of 4) and if a percentage relative standard deviation (RSD) of less than 5% was obtained, the results were classified as stable. **Table 4.10** shows optimised evaporator temperatures at the different liquid feed flowrates. Changing the gas inlet temperature did not yield any improvements in the evaporation stability.

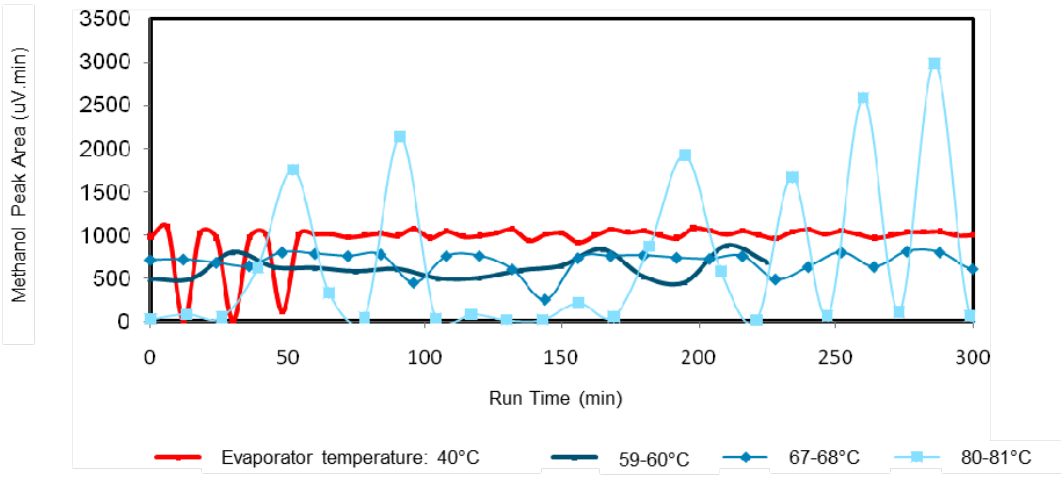

Figure 4.13 *Impact of microevaporator temperature on the gas chromatograph methanol peak areas plotted as a function of time on stream.*

Table 4.10 *Optimised evaporator temperatures for different liquid feed flowrates (75%(v/v) methanol).*

Liquid flowrate (µl/min)	Evaporator temperature (°C)	Evaporator gas inlet temperature (°C)
12.7	40	70
13.7	50	70
16.4	60	70

4.4.3 Blank Reactions

Reactions were carried out without catalyst in order to ensure no homogenous decomposition or oxidation were occurring to a significant degree. **Figure 4.14** shows results of the blank reactions; there does not appear to be a significant decline in the inlet methanol concentration and there is no dependence on the presence of oxygen. Any differences observed are more likely to be due to instability in the evaporation.

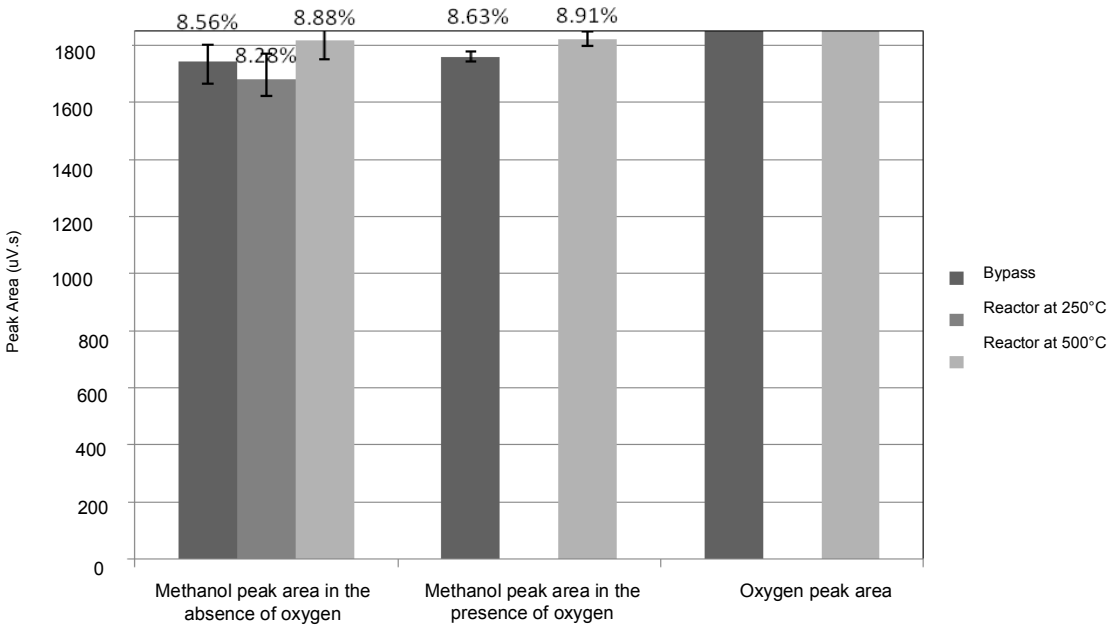

Figure 4.14 *Methanol oxidation blank reaction results conducted in the presence and absence of oxygen. Error bars represent the range in peak areas measured. The values in % at the top of the bars represent the corresponding methanol mole % for that peak area.*

4.4.4 Silver Film Catalyst Activation Behaviour

Scanning Electron Microscopy Characterisation of Silver Catalyst

Figure 4.15 shows SEM images of the silver catalyst that was subjected to varying levels of treatment (heating only, heating with helium flow, and heating with reaction). Comparing the untreated catalyst (**Figure 4.15a**) to a catalyst reacted with oxygen at 500°C (**Figure 4.15 f,g,h**), the agglomeration of the particles from a few hundred nanometers to 1-2μm is clear.

The intermediate images, **Figure 4.15 b,c,d,e** represent the silver film heated to 420°C for 20 minutes, showing the migration of the silver particles into "snow-flake" structures at different magnifications. The size of the particles and the increase in particle size with heating agrees with what has been observed in the literature for a

silver catalyst calcined at ~500°C [19]. The images in **Figure 4.15g,h** also show the wide particle size distribution of the catalyst and the large variation in the morphology of the silver particles after heating and reaction. Pockets on the surface of some of the particles are also visible after reaction (**Figure 4.15h**).

Silver and other metal films have been known to exhibit hillock growth (protrusions on the surface of the film) followed by mass migration and agglomeration [23;24]. Hillock formation is a behaviour shown by thin films but not in bulk solids due to the relatively small dimension of the film measured normal to its plane, as well as the presence of a constraining substrate [25]. When a film is subjected to biaxial stress, local areas relax to different degrees generating a gradient between a relaxed grain and the surrounding film. Consequently, mass flow between the film and the substrate takes place. This results in the relaxed area growing out from the base as a hillock, which is more energetically favourable [25]. As a result of hillock formation, the surface area of the film increases. Ultimately, the neighbouring holes will join causing isolation of regions of the film yielding separate "islands" or large particles, which can be used to explain the underlying cause of the silver particle size enlargement.

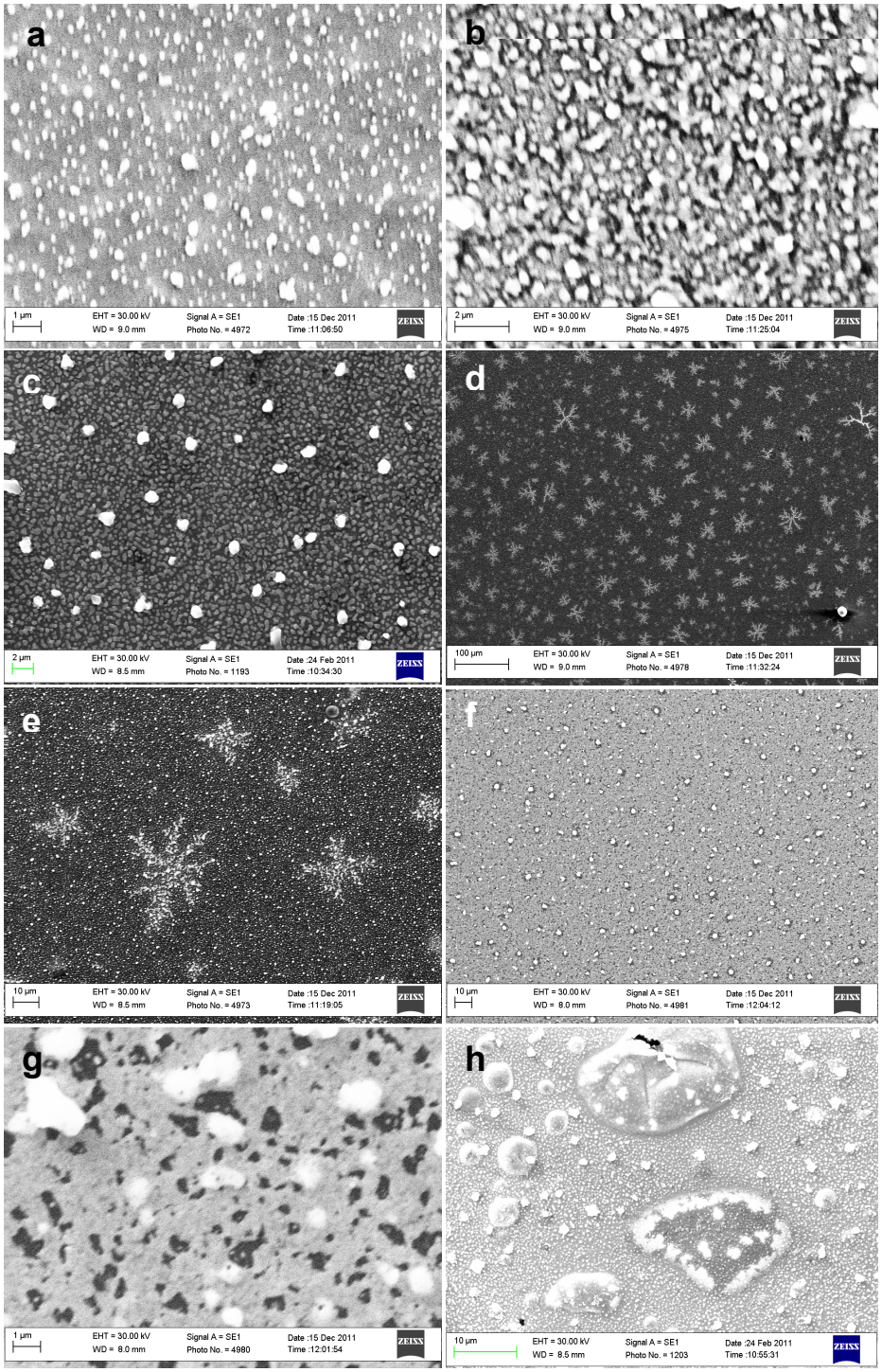

Figure 4.15 *Scanning electron micrographs of silver films at different pre-treatment and reaction steps (a) untreated silver film, (b), (c), (d), (e) silver film heated to 420°C for 20 minutes, (f), (g),(h) silver film that has undergone heating at 500°C and reaction with oxygen.*

Activation by Repeated Oxidation/Reaction Cycles

The pre-treatment steps carried out to activate the catalyst consisted of 8 cycles of oxidation/reaction (1 hour each) whilst monitoring the activity. **Figure 4.16** shows the results of a series of oxidation/reaction runs following this pre-treatment. The results demonstrate that catalyst stability was not achieved, as evidenced by the fluctuating conversion as well as the large variability shown by the error bars.

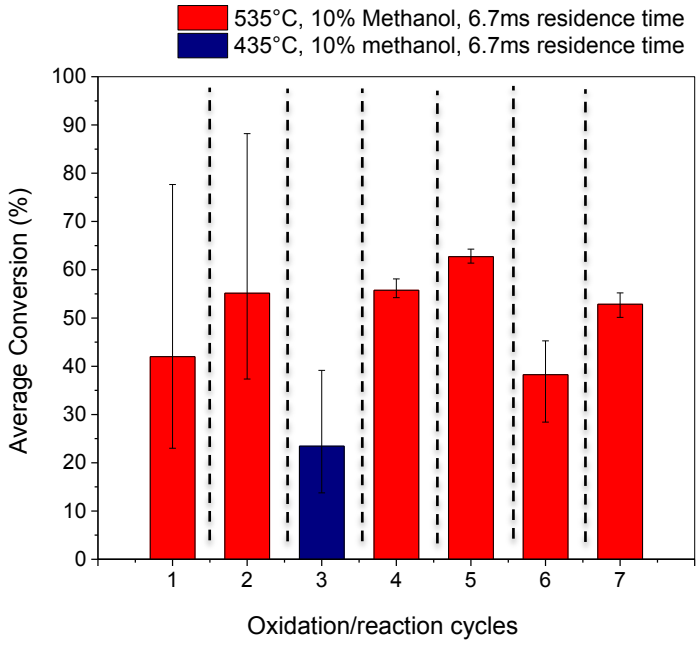

Figure 4.16 *Conversion stability with time on stream following a catalyst activation procedure consisting of repeated oxidation/reaction cycles at 535°C and 435°C. Dashed lines represent treatment with 10% oxygen in helium for 1 hour. Error bars represent the range of three or more samples. The gas mixture consisted of approximately 9.8% methanol, 4.4% oxygen, 7.6% water, with helium as balance.*

Activation by Continuous Time-on-Stream

This method consisted of leaving the reactor on-stream for a prolonged duration. The reactor was monitored upon start-up at 532°C and 452°C (**Figure 4.17**). On day 1, methanol and oxygen conversions of 60% and 75% respectively were obtained (not shown on graph). Following an overnight purge with 10% oxygen at 175°C the conversion reduced to 15% and 24% for methanol and oxygen respectively (time 0 in **Figure 4.17a**). When the reaction was left to run longer, the activity increased gradually at 0.18%/min and 0.33%/min for the methanol and the oxygen respectively (between 0 and 100 min). A process disturbance took place at 100 min, which happened as a result of pressure build-up due to the valve downstream being activated. This disturbance resulted in an unexplainable increase in the conversion. However, the conversion began dropping again on the next sample at 116 min.

Purging the reactor with a 10% oxygen mixture at 200 min resulted in an initial high activity, bringing the methanol conversion to 75%, which decreased and stabilised at 60% conversion with time. The reactor was then left on stream overnight and a gradual decrease in the methanol peak area was observed with time (indicating a continuing increase in methanol conversion) (**Figure 4.17b**). The following day, quantitative analysis was carried out which showed a fairly stable methanol conversion of ~85% (**Figure 4.17c**), with only a few outliers. The outliers could be due to some instability in the methanol evaporation, e.g. in the presence of gas bubbles. The qualitative analysis carried out showed that stability was achieved almost immediately after the change in temperature was investigated (**Figure 4.17d**). The time required to reach stabilisation with an 80°C decrease in the temperature was significantly less than the time required to each stabilisation from start-up to 532°C.

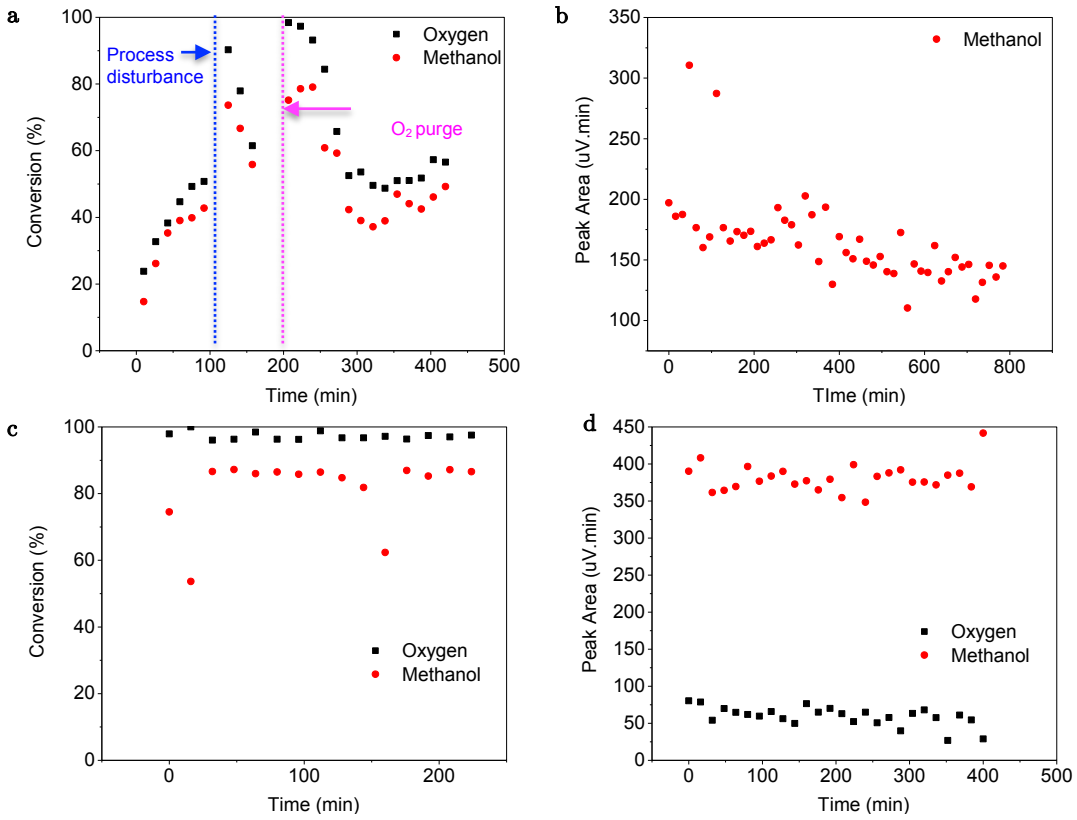

Figure 4.17 *Conversion stability with time on stream using the prolonged time on stream method on day 2 of operation:(a) (b) and day 3 of operation: (c) (d). (a) Methanol and oxygen conversions with time on stream at 532°C; (b) Methanol peak areas with time on stream at 532°C as the reaction is left to run for a further 800 minutes; (c) Methanol and oxygen conversions on day 3 with time on stream at 532°C, following the overnight continuous reaction run shown in b and; (d) Methanol and oxygen peak areas with time on stream for 400 min, after an 80°C change in temperature to 452°C.*

4.4.5 Parametric Studies

Temperature and oxygen-dependence of conversion and selectivity using M1

Experiments probing the impact of oxygen concentration and temperature on conversion will be presented in this section. The continuous time on stream activation method was used to stabilise the catalyst prior to obtaining the data presented here. **Figure 4.18a** shows the impact of oxygen concentration and temperature on methanol conversion levels. There is an optimum oxygen concentration at 6.5 mol% where the methanol conversion is 96%. Although care must be taken as only three data points were used to make this conclusion. The maxima in the methanol conversion with increasing oxygen concentration indicates that oxygen has an inhibiting effect above a certain concentration. The other explanation could be catalytic deactivation at high oxygen concentrations due to the phenomena of "over-oxidation" i.e. competitive adsorption of oxygen with methanol, and when oxygen completely saturates the active sites, inhibits the adsorption of methanol. This result does not agree with the simulations carried out by Andreasen et al. [1], however, Andreasen's results were based on experimental data acquired under UHV conditions that are far from the industrial reaction conditions.

Temperature, on the other hand, has a different impact on the conversion levels, as an 80°C increase in temperature resulted in a 25% increase in the methanol conversion with no optima observed over the temperature range studied (**Figure 4.18b**); this latter trend is an expected dependence of reactant conversion on temperature. The dependence of selectivity to carbon dioxide on oxygen concentration exhibited the same parabolic relationship that was shown between methanol conversion and oxygen concentration (**Figure 4.18c**). Selectivity to CO_2 falls with increasing temperature (**Figure 4.18d)**. The drop in selectivity towards CO_2 with increasing temperature is described by some as a result of the different temperature stability of various oxygen species formed and the influence this has on the dominating reaction pathway. It was shown earlier that O_α is responsible for the oxi-dehydrogenation and complete oxidation products, which dominates at lower temperatures of 250-350°C. Therefore, the drop in selectivity to complete oxidation products (such as carbon dioxide) above the thermal

desorption temperature of O_α, indicates the decreased participation of this species in the reaction [11]. The hydrogen GC signal becomes weak at low hydrogen concentrations and thus the missing data point at 452°C is due to the insensitivity of the GC instrument to hydrogen. Very low CO amounts were detected, a maximum of 0.008%. This is in line with what has been reported in the literature where CO_2 is favoured up to temperatures of 627^0C, above which CO begins to dominate [1].

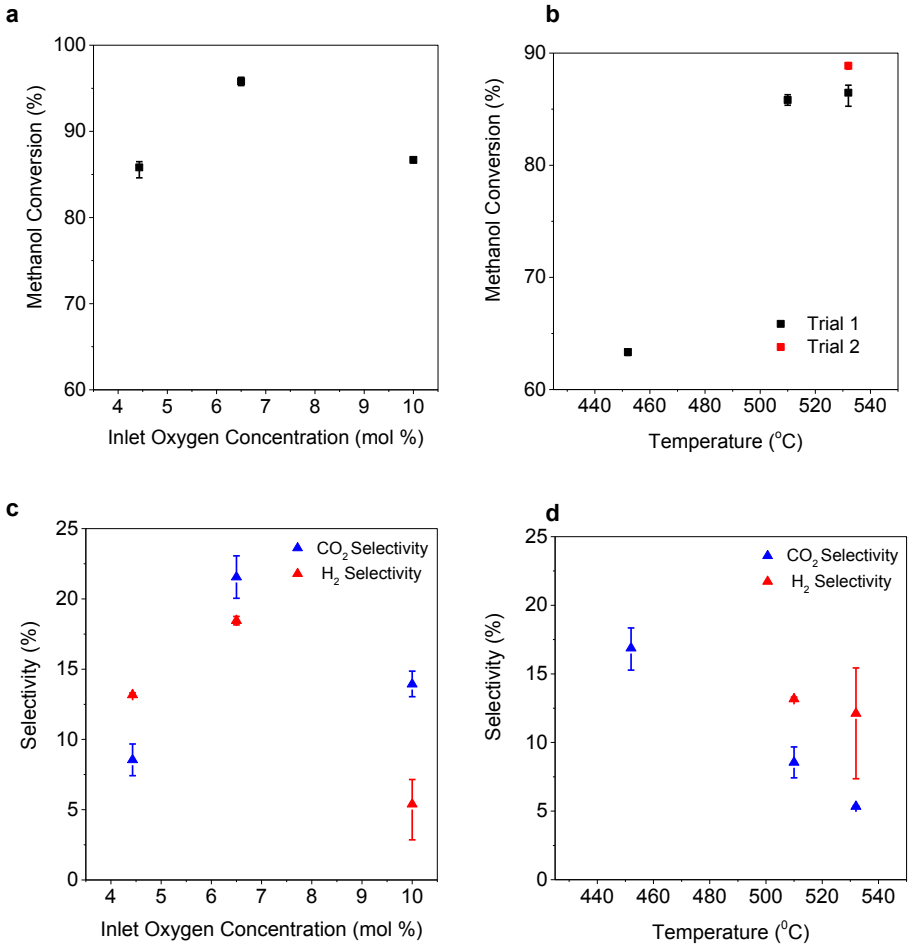

Figure 4.18 *Parametric study results showing methanol conversion and selectivity to CO_2 and H_2 at 532°C, 10 mol% methanol concentration, and using reactor design M1. Impact of oxygen inlet concentration on (a) Methanol conversion and (c) CO_2 and H_2 selectivity. Impact of temperature on (b) Methanol conversion and (d) CO_2 and H_2 selectivity. Repeat of the "standard reaction" shown as "Trial 2" in b was carried out to ensure catalyst stability at the end of the study. Error bars represent the range of 3 or more samples.*

Temperature dependence of conversion and selectivity using M3

The effect of temperature on conversion and selectivity using reactor design M3 is shown in **Figure 4.19**. As expected, and as previously demonstrated for the M1 reactor, methanol conversion increases with temperature. Selectivity to formaldehyde was found to increase with increasing temperature, while the CO_2 selectivity decreased with temperature. This is in agreement with the previous finding with reactor design M1. The selectivity to carbon dioxide in the reactor with the shortest bed length of 1.8 cm (red symbols in **Figure 4.19**) does not decrease with reaction temperature, although the selectivity to the aldehyde does increase. This may be explained by the low carbon balance at the low temperatures (carbon balance of 86%, 91%, 94%, and 95% and 93% at temperatures of 510 °C, 540 °C, 570 °C, 610 °C, and 660 °C respectively), which implies that other byproducts that are unnacounted for are present at low temperatures. The pressure drop in reactor design M3 varied between 0.6 and 1.2 bar depending on the flowrate. This pressure drop was higher than the pressure drop observed with the M1 reactor due to the M3 reactor having a narrower channel.

4.4.6 Dependence of Conversion and Selectivity on Residence Time

Results of the residence time study using reactor design M3 with three reactors (giving three different velocities) are summarised in **Figure 4.20** with more details on the operating conditions given in **Appendix A**. In this M3 reactor, halving the residence time from 14 to 7 ms appears to have no influence on the conversion. It is only until a residence time of 4 ms was used that the conversion began to drop. This indicates that for the M3 reactor, a residence time of <2ms is necessary to achieve integral reactor behaviour for a kinetic study. In addition, the conversion appears to be limited at a residence time above 6 ms. Selectivities to formaldehyde and carbon dioxide show a small decrease and increase with temperature respectively (**Figure 4.20b**), suggesting a consecutive reaction pathway to the carbon dioxide formation.

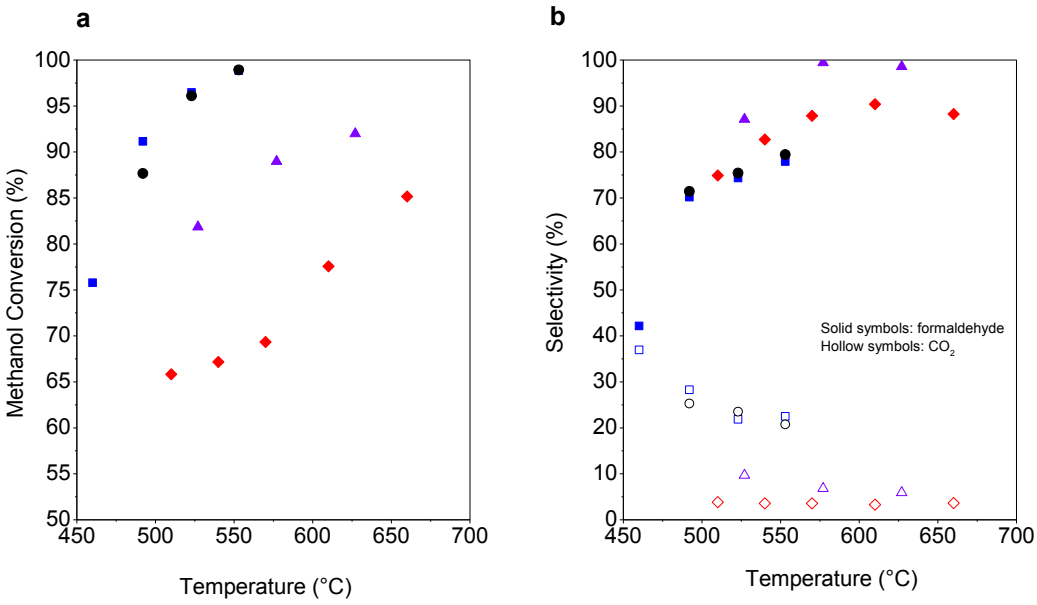

Symbol	Bed length (cm)	Methanol mol%	Oxygen mol%	Methanol: Water ratio	Residence time (ms)
■	8.8	14.7	9.8	0.64	7.42-7.94
●	8.8	14.7	9.8	0.64	4.58-4.78
▲	8.8	25.9	1.6	1.22	6.55-7.15
◆	1.8	10.0	4.1	1.32	7.42-7.94

Figure 4.19 *Effect of temperature on (a) methanol conversion and (b) formaldehyde and CO_2 selectivity using reactor design M3 in two different reactors, one with a bed length of 8.8 cm and a second with a bed length of 1.8 cm.*

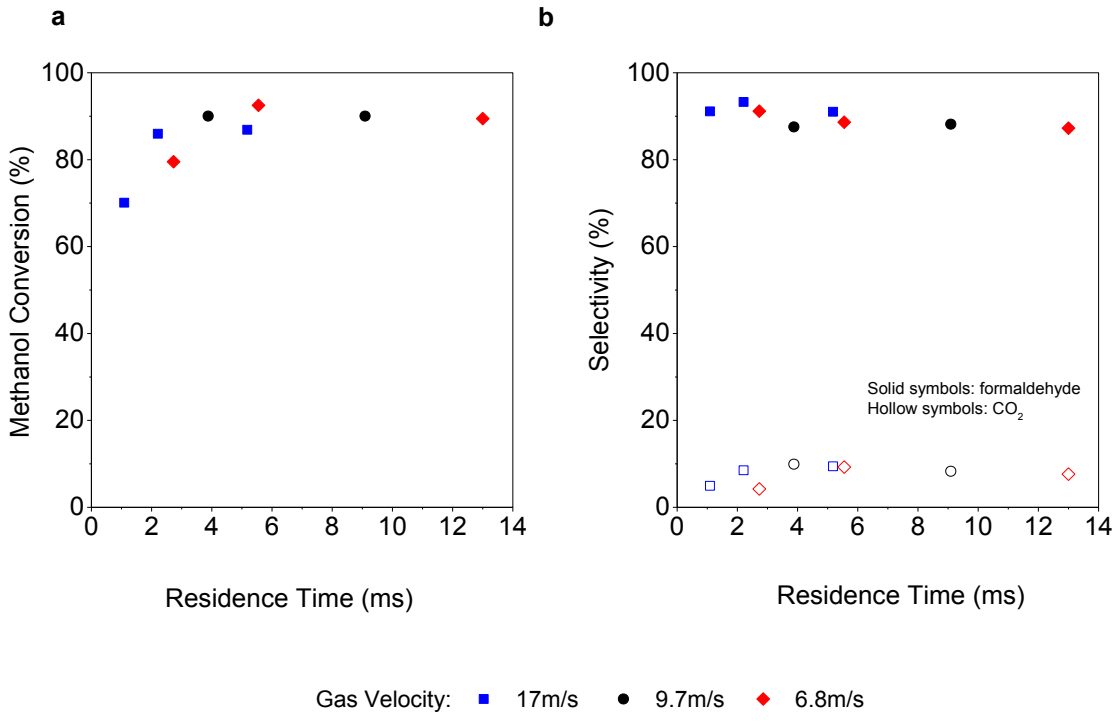

Figure 4.20 *Impact of residence time on methanol conversion using different gas flowrates at 510°C and M3 reactor (each gas flowrate has three data points, conducted in three different reactors with different catalyst lengths). Oxygen concentration: 4.14 mol%; water concentration: 7.54 mol%; methanol concentration: 9.95 mol%.*

4.5 Conclusion

Kinetic expressions for the oxidative dehydrogenation of methanol to formaldehyde over silver catalyst at industrially relevant conditions remain to be found. A continuous flow microfluidic experimental rig with automated in-line gas analysis was developed for this purpose. The analytical method was developed to allow analysis of all hydrocarbon and permanent gas products within 16.5 minutes. Further, the silicon-glass microreactor and its assembly have been designed to withstand temperatures up to 800°C, limited only by the melting temperature of the glass. The microreactor is

especially designed for reaction kinetic studies, with a temperature gradient across the reaction zone of less than 1°C.

The activity was monitored in order to understand the catalytic behaviour of the silver film upon start-up. On examination by scanning electron microscopy, particle size enlargement was detected as the catalyst was heat treated and used to catalyse the reaction. An increase in the silver particle size from a few hundred nanometres to 1-2 μm took place due to heating and reaction. This rapid restructuring of the silver film manifested in a complex activation behaviour. The silver catalyst showed an initial high activity, which declined quickly. The activity can be regained and stabilised by a prolonged reaction time on stream.

Parametric studies were performed probing the impact of temperature, oxygen and methanol concentration on methanol conversion. An oxygen concentration of 6.5% resulted in a maximum methanol conversion, which declined at either lower or higher oxygen concentrations. The effect of reaction temperature was investigated at 452°C, 510°C and 532°C. Increasing the reaction temperature resulted in an increase in methanol conversion, which is an expected result that is line with previous work.

Studies varying the residence time showed that selectivity to carbon dioxide increased with residence time, while the formaldehyde selectivity decreased, therefore indicating that the formation of carbon dioxide is through a consecutive and not parallel pathway.

4.6 References

1. Andreasen, A., Lynggaard, H., Stegelmann, C., Stoltze, P. **A microkinetic model of the methanol oxidation over silver**. *Surface Science* 2003, 544:5-23.

2. Bhattacharyya, S.K., Nag, N.K., Ganguly, N.D. **Kinetics of vapor-phase oxidation of methanol on reduced silver catalyst**. *Journal of Catalysis* 1971, 23:158-167.

3. Wachs, I.E., Madix, R.J. **The oxidation of methanol on a silver (110) catalyst**. *Surface Science* 1978, 76:531-558.

4. Robb, D.A., Harriott, P. **The kinetics of methanol oxidation on a supported silver catalyst**. *Journal of Catalysis* 1974, 35:176-183.

5. Andreasen, A., Lynggaard, H., Stegelmann, C., Stoltze, P. **Simplified kinetic models of methanol oxidation on silver**. *Applied Catalysis A: General* 2005, 289:267-273.

6. Chorkendorff, I, Niemantsverdriet, J.W. ***Concepts of modern catalysis and kinetics***. Weinheim: VCH; 2003.

7. Montoya, A., Haynes, B.S. **Methanol and methoxide decomposition on silver**. *Journal of Physical Chemistry C* 2007, 111:9867-9876.

8. Bao, X., Muhler, M., Pettinger, B., Schlögl, R., Ertl, G. **On the nature of the active state of silver during catalytic oxidation of methanol**. *Catalysis Letters* 1993, 22:215-225.

9. Ren, L.P., Dai, W.L., Yang, X.L., Xu, J.H., Cao, Y., Li, H., Fan, K. **Direct dehydrogenation of methanol to formaldehyde over pre-treated polycrystalline silver catalyst**. *Catalysis Letteres* 2005, 99:83-87.

10. Waterhouse, G.I.N., Bowmaker, G.A., Metson, J.B. **Oxygen chemisorption on an electrolytic silver catalyst: a combined TPD and Raman spectroscopic study**. *Applied Surface Science* 2003, 214:36-51.

11 Nagy, A., Mestl, G. **High temperature partial oxidation reactions over silver catalysts**. *Applied Catalysis A: General* 1999, 188:337-353.

12. Lefferts, L., van Ommen, J.G., Ross, J.R.H. **The oxidative dehydrogenation of methanol to formaldehyde over silver catalysts in relation to the oxygen-silver interaction**. *Applied Catalysis* 1986, 23:385-402.

13. Kapteijn, F., Moulijn, J.A. **Laboratory Reactors**. In *Handbook of Heterogeneous Catalysis*. Edited by G.Ertl, H.Knozinger, J.Weitkamp. Weinheim: VCH; 1997.

14. Carberry, J. ***Chemical and Catalytic Reaction Engineering***. New York: McGraw Hill; 2001.

15. Balasubramanian, S., Viswanath, D.S. **A Model for Catalytic Oxidation of Hydrocarbons in the Vapor Phase**. *Industrial & Engineering Chemistry Fundamentals* 1975, 14:158-165.

16. Waterhouse, G.I.N., Bowmaker, G.A., Metson, J.B. **Influence of catalyst morphology on the performance of electrolytic silver catalysts for the partial oxidation of methanol to formaldehyde**. *Applied Catalysis A: General* 2004, 266:257-273.

17. Qu, Z., Cheng, M., Huang, W., Bao, X. **Formation of subsurface oxygen species and its high activity toward CO oxidation over silver catalysts**. *Journal of Catalysis* 2005, 229:446-458.

18. Qu, Z., Cheng, M., Dong, X., Bao, X. **CO selective oxidation in H2-rich gas over Ag nanoparticles - effect of oxygen treatment temperature on the activity of silver particles mechanically mixed with SiO_2**. *Catalysis Today* 2004, 93-95:247-255.

19. Cao, E., Firth, S., McMillan, P.F,, Gavriilidis, A. **Application of microfabricated reactors for operando Raman studies of catalytic oxidation of methanol to formaldehyde on silver**. *Catalysis Today* 2007, 126:119-126.

20. Cao, E., Gavriilidis, A. **Oxidative dehydrogenation of methanol in a microstructured reactor**. *Catalysis Today* 2005, 110:154-163.

21. Marre, S., Adamo, A., Basak, S., Aymonier, C., Jensen, K.F. **Design and packaging of microreactors for high pressure and high temperature applications**. *Industrial & Engineering Chemistry Research* 2010, 49:11310-11320.

22. Kandlikar, S.G. **Fundamental issues related to flow boiling in minichannels and microchannels**. *Experimental Thermal and Fluid Science* 2002, 26:389-407.

23. Sharma, S.K., Spitz, J. **Hillock formation, hole growth and agglomeration in thin silver films**. *Thin Solid Films* 1980, 65:339-350.

24. Sharma, S.K., Spitz, J. **Hillock growth and agglomeration in thin silver films**. *Thin Solid Films* 1979, 61:L13-L15.

25. Chaudhari, P. **Hillock growth in thin films**. *Journal of Applied Physics* 1974, 45:4339-4346.

V.

Reaction and Deactivation Studies of Au-Pd Catalysts during Benzyl Alcohol Oxidation in a Micro-Packed Bed Reactor

---

Supported Au-Pd catalysts have been tested for catalysing benzyl alcohol oxidation in a silicon-glass micro-packed bed reactor. In particular, the effect of Au/Pd composition and anion content on the catalyst deactivation behaviour was studied. A relationship between the deactivation rate and the amount of Cl^- and Au used in the catalyst formulation has been observed: whilst Au aids in enhancing the selectivity to the desired product and the Cl^- ions help the formation of uniform 1-2 nm nanoparticles, above a certain amount, both Au and Cl^- become detrimental to the catalyst stability. The formation of an amorphous surface film was observed via TEM in catalysts with high Cl^- and Au; this was confirmed by the detection of carbon species on the catalyst surface using Raman Spectroscopy. Catalyst regeneration was possible by oxidising with oxygen at reaction conditions. The most stable catalyst formulation (without compromising on activity) was the MI_m 0.05wt% Au – 0.95wt% Pd/TiO_2, which was chosen as the catalyst for further reaction development studies.

5.1 Introduction

Gold-palladium nanoalloy catalysts have been demonstrated to be highly active, particularly for aerobic oxidation reactions [1]. The catalyst preparation method plays a central role in determining the size of these nanoparticles, with smaller particles being the most catalytically active [2]. Trade-offs exist between complexity of preparation method and the catalytic activity of the resulting catalyst. The simplest method of preparing Au-Pd nanoalloy catalysts is conventional impregnation. However, this method produces nanoparticles with a wide particle size distribution ranging from 1 to 10 nm, together with occasional large >10 nm particles. Catalysts prepared by sol-immobilisation, a method that uses stabiliser ligands to control the particle size and avoid the formation of catalytically inactive larger particles, were found to have a high catalytic activity but have the disadvantage of being unstable [3]. Recent studies on the use of an excess anion modified impregnation (M_{Im}) method in the preparation of supported gold-palladium catalysts have been reported [4;5]. It has been shown that through the addition of excess chloride ions to the metal precursors during the impregnation stage, a catalyst that possesses a very tight particle size distribution can be produced. The improvement in activity is postulated to be due to the interaction of chloride anions with Au in the aqueous medium, which facilitates the formation of a more uniform metal dispersion [4].

One of the major challenges in commercialising promising catalyst candidates is their deactivation under industrially relevant conditions [6]. Determining the catalytic behaviour of promising catalyst candidates under continuous flow is therefore necessary to assess their industrial viability. Initial stability studies have shown that a particular formulation – M_{Im} 0.5 mol% Au-0.5 mol% Pd/TiO_2 – is stable with time on stream for several days without deactivation, outperforming the stability of catalysts prepared via sol-immobilisation [5]. However, the effects of the Au:Pd ratio and chloride anion content on the M_{Im} catalyst stability are yet to be determined.

The objective of this chapter is to investigate the stability of supported Au-Pd catalyst formulations when catalysing the benzyl alcohol oxidation. Three catalyst preparation methods will be investigated: conventional impregnation and two types of modified

impregnation methods, where an excess of anion during the wet impregnation stage is used. The influence of Au and Cl^- ion contents on catalyst stability will be determined, and a possible deactivation mechanism will be presented aided by the following characterisation techniques: scanning electron microscopy (SEM), transmission electron microscopy (TEM), x-ray photoelectron spectroscopy (XPS), atomic emission spectroscopy (AES), and Raman Spectroscopy. This work will aid in the identification of the most appropriate synthesis methodology for industrial applications and shed light on possible reactivation methods.

5.2 Background

5.2.1 Benzyl Alcohol Oxidation on Supported Au-Pd Catalysts

A generalised reaction scheme for the oxidation of benzyl alcohol on Au-Pd catalysts is presented in **Figure 5.1**. In the presence of oxygen, the oxidation of benzyl alcohol leads in the first instance to the formation of benzaldehyde. With further oxidation of the benzaldehyde molecule, benzoic acid is produced [7]. The formation of benzyl benzoate is through an esterification reaction between the initial alcohol and the (i) generated aldehyde (in the presence of oxygen) or (ii) the generated benzoic acid [8]. Benzoic acid, benzyl benzoate, and dibenzyl ether are classified as side products as they are produced in much smaller quantities relative to benzaldehyde and toluene (<2%) [9]. The use of Au-Pd catalyst similar to the one used in this chapter for catalysing benzyl alcohol oxidation amongst other alcohol oxidations has been demonstrated in previous studies [10-13].

5.2.2 Modes of Deactivation in Pt-group Metal Catalysts

The deactivation of solid catalysts in liquid phase reactions is usually caused by physical, thermal, or chemical changes of the catalyst [14]. Four main modes of deactivation have been identified in Pt-group metal catalysed reactions: (1) change of oxidation state of the active metal site ("over-oxidation"), (2) irreversible adsorption of products or polymeric species, and loss of metal surface area either by (3) leaching or by (4) sintering [15;16].

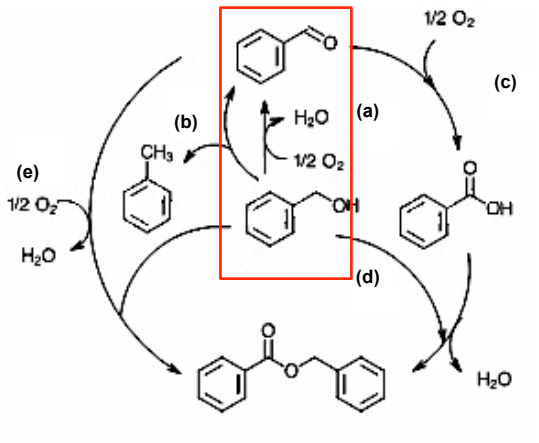

Figure 5.1 *Benzyl alcohol oxidation reaction network: (a) oxidation of benzyl alcohol to benzaldehyde; (b) disproportionation of benzyl alcohol to benzaldehyde and toluene; (c) oxidation of benzaldehyde to benzoic acid; (d) esterification of benzyl alcohol and benzoic acid, (e) esterification of benzyl alcohol and benzaldehyde under oxidative conditions to benzyl benzoate. Main reaction highlighted in red box. Adapted from [8].*

In the oxidation of alcohols, the reaction mechanism involves dehydrogenation of the alcohol on the metal surface, followed by elimination of hydrogen by reaction with adsorbed oxygen. If the oxygen coverage on the metal surface increases, alcohol adsorption is progressively suppressed and the conversion reaches a plateau. This mode of deactivation is termed "over-oxidation", which is caused by the formation of a surface metal oxide covering the metal particles. The extent of deactivation due to over-oxidation is thus dependent on the affinity of the metal nanoparticles for oxygen, as well as the relative rates of the dehydrogenation of alcohol and the removal of the adsorbed hydrogen from the metal site by the oxidant (to form H_2O) for the next turnover [17].

The adsorption of products and other species is another common mode of deactivation; several studies for various types of metal catalysts have reported strongly adsorbed species such as CO [6;19-21], carbonaceous species [22;23], acid [19], self-poisoning caused by destructive adsorption of reactant [24] and poisons present in the feedstocks [15]. Various methods can be employed to reverse deactivation by adsorption of unwanted species on the catalyst surface, and this includes treatment with a gas such as oxygen [24].

Leaching is usually the main cause of deactivation in liquid phase reactions [15]. This form of deactivation is promoted by acidic pH, where the presence of carboxylic acids in solution has been associated with the promotion of metal leaching from catalytic surfaces [6]. The simultaneous presence of oxygen and acid may result in loss of noble metal by ionisation and dissolution [17]. For Au/TiO_2 in liquid phase oxidation, leaching of the Au has been demonstrated and was resolved by adding 5wt.% Fe_2O_3 to the catalyst formulation, which increased the binding strength of the Au by creating a protecting Fe_2O_3 surface film [18].

Sintering of metal particles and metal dissolution are forms of deactivation that can happen as a result of metal atom migration across the support, or by metal dissolution followed by redeposition onto other metal nanoparticles [15] resulting in particle size enlargement and loss of active surface area [22]. Metal dissolution is generally found to be facilitated by acidic or strongly alkaline pH [22].

5.2.3 Effect of Cl on Catalyst Stability

The inhibitory effect of chlorine when used in the metal precursor has been investigated, but primarily for gas phase reactions [25;26]. Peri et al. raised the possibility that the activation phenomenon (the increase in catalytic activity with time on stream on start-up) in catalysts prepared from chlorinated precursors, could be due to the slow removal of chlorine with time [25]. The negative effect of residual chlorine on the catalyst has been attributed to several causes, including partial blockage of metal particles by chlorine [27] and the generation of metal oxychloride species that have higher reduction temperatures and lead to a less active oxidation site [28]. A mechanism for the mobility of chloride ions during reduction and reaction has been presented [27]. The reduction of the catalyst has been postulated to cause mobility of the chloride ions from the surface of the metal particles to the interior of the particles and on the support. The introduction of the oxidant is then hypothesised to cause movement of the chlorine to the metal particle surface again. The use of $H_2 + H_2O$ treatment has been shown to favour the definitive chlorine elimination from the catalyst (i.e. H_2O reacts with the Cl to produce HCl).

5.3 Materials & Methods

5.3.1 Catalyst Preparation Methods*

Two main catalyst preparation methods were used in this study: Conventional Impregnation (C_{Im}) and Modified Impregnation (M_{Im}). Within the modified impregnation category, there exists two types: Modified Impregnation Constant Cl ($M_{Im,const}$) and Modified Impregnation Varying Cl ($M_{Im,vary}$). The catalyst preparation methods for each of these catalysts will be presented next.

Conventional Impregnation, C_{Im}

The Conventional Impregnation (C_{Im}) preparation procedure for supported Au-Pd catalysts relies on a wet-impregnation method, which has been reported in previous articles [4]. In a typical synthesis, the metal precursors $PdCl_2$ and $HAuCl_4.3H_2O$ (Sigma Aldrich) were wet impregnated on to the solid support TiO_2 (Evonik P25). This was done by adding the requisite amount of solid $PdCl_2$ to a predetermined volume of an aqueous solution of $HAuCl_4.3H_2O$ and stirring vigorously at 80°C for a few minutes until the palladium salt had apparently dissolved. The requisite amount of the support was then added to this solution under vigorous stirring conditions until it formed a paste, which was then dried at 120°C for 16 h and then reduced in a stream of 5% H_2 in Ar at 400°C for 4 h.

Modified Impregnation, M_{Im}

In the Modified Impregnation M_{Im} procedure, an excess of Cl was added to the formulation; this was done in one of two ways (**Figure 5.2**):

(1) Mixing of HCl and the $PdCl_2$ palladium precursor first, followed by addition of the $HAuCl_4.3H_2O$ gold precursor (**$M_{Im,vary}$**: the amount of Cl *varies* with Pd loading);

---

* *All catalysts featured in this thesis were prepared by the Cardiff Catalysis Institute. Full details of catalyst preparation can be found in [29].*

(2) Mixing of the $HAuCl_4.3H_2O$ aqueous gold precursor, $PdCl_2$ palladium salt, and a fixed amount of HCl (9.7×10^{-4} mol) ($\mathbf{M_{Im,const}}$: the amount of Cl is *constant* with Pd loading).

The solution was then immersed in an oil bath sitting on a magnetic stirrer hot plate and stirred vigorously at 1000 rpm, while raising the temperature from 27 to 60°C. The metal oxide support material TiO_2 (Degussa P25) was then added over a period of 8 to 10 min with constant stirring. The formed slurry was stirred at 60°C for 15 min and the temperature of the oil bath was raised to 95°C. The slurry was stirred at that temperature for a further 16 h until all the water evaporated, leaving a dry solid. This powder was transferred into a mortar and pestle and ground thoroughly to form a uniform mixture. The resulting powder was reduced by raising the temperature from 30 to 400°C (at a heating rate of 10 K/min) under a steady flow of 5%H_2 in Ar for 4 h.

A summary of the catalysts used in the study are shown in ***Table 5.1*** and a schematic of the preparation steps is shown in **Figure 5.2**. A comparison of the amount of Cl used in the catalyst preparation and how that varies with the amount of palladium in the formulation is presented in **Figure 5.3**. **Appendix B** shows detailed procedures and tables showing final moles of Cl for any possible catalyst combination.

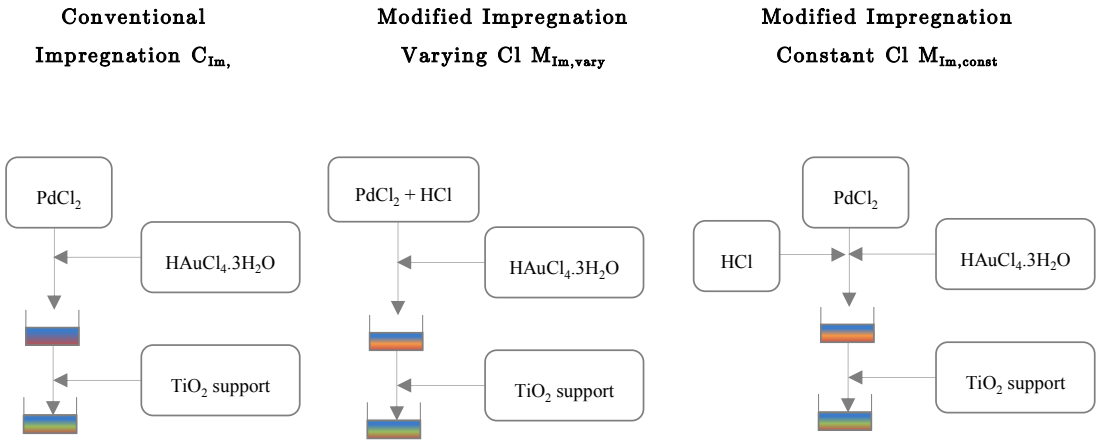

Figure 5.2 *Steps performed in the preparation of catalysts via three methods: Conventional Impregnation, Modified Impregnation Changing Cl, and Modified Impregnation Constant Cl.*

Table 5.1 *Summary of Au-Pd/TiO_2 catalysts (loading and preparation methods).*

Abbreviation	Catalyst Name	Preparation Method	Au wt%	Pd wt%	Mol Cl*	Cl:Pd Mol ratio†
CIm	**C**onventional **Im**pregnation	Conventional Impregnation	0.8	0.2	4×10^{-4}	10.6
MIm	**M**odified **I**mpregnation	Modified Impregnation Varying Cl	0.65	0.35	1.07×10^{-3}	20.6
MIm HEC	**M**odified **Im**pregnation with **H**igh **E**xcess **C**hloride	Modified Impregnation Constant Cl	0.8	0.2	1.37×10^{-3}	36.1
MIm LEC	**M**odified **I**mpregnation with **L**ow **E**xcess **C**hloride	Modified Impregnation Varying Cl	0.8	0.2	7.87×10^{-4}	20.9
MIm LAu	**M**odified **Im**pregnation with **L**ow **Au**	Modified Impregnation Varying Cl	0.05	0.95	2.22×10^{-3}	12.4

**This includes the Cl from the metal precursors (4×10^{-4} moles for 2g of catalyst) and any excess Cl. C_{Im} will contain Cl only from the precursors. † Cl based on calculated amount added during preparation.*

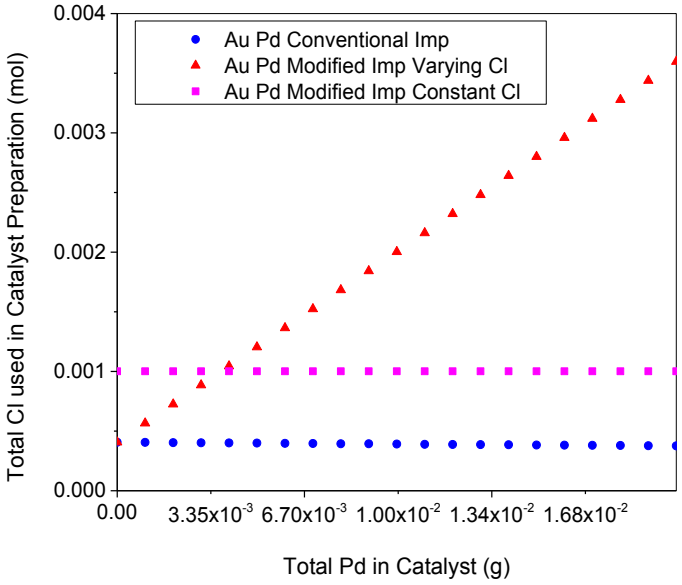

Figure 5.3 *Variation in chloride amount (as a function of amount of palladium in the catalyst formulation) for the different catalyst preparation methods.*

5.3.2 Catalyst Analysis

Scanning Electron Microscopy (SEM)

A JEOL 7401 high resolution field emission scanning electron microscope was used to image the catalysts before use. The backscattered electrons (BSE) were analysed to illustrate contrast in composition between the TiO_2 and the Au-Pd to get an initial estimation of particle size and location of metal particles within the support.

TEM Imaging†

TEM was carried out using a JEOL 2100 with a LaB_6 filament operating at 200 kV. Samples were prepared by dispersing the powder catalyst in ethanol and dropping the suspension onto a lacey carbon film over a 300 mesh copper grid.

High Resolution-Scanning Transmission Electron Microscopy (HR-STEM) & Energy Dispersive X-ray Spectroscopy (EDS)

A JEOL 1010 Transmission Electron microscope was used to carry out HR-STEM with EDS to identify the Au and Pd metal on the support. The samples were prepared for TEM by placing a droplet of the powder material dispersed in ethanol (sonicated for 5 minutes in an ultrasonic bath) on a carbon-coated-mesh grid.

X-ray Photoelectron Spectroscopy (XPS)‡

Samples were characterized using a Kratos Axis Ultra-DLD photoelectron spectrometer, using monochromatic Al Kα radiation, at 144 W (12 mA × 12 kV) power. High resolution and survey scans were performed at pass energies of 40 and 160 eV respectively. Spectra were calibrated to the C (1s) signal for adventitious carbon at 284.78 eV and quantified using CasaXPS v2.3.1517, utilizing sensitivity factors supplied by the manufacturer.

---

† *TEM imaging carried out by the Cardiff Catalysis Institute.*
‡ *XPS carried out by the Cardiff Catalysis Institute.*

Atomic Emission Spectroscopy (AES)[§]

An Agilent MP-AES 4100 was used to detect metal leaching into the reaction solution. Samples were tested for gold and palladium using a gold wavelength of 242.795 nm and palladium wavelength of 363.470 nm. The samples were diluted in 2:1 propanol to benzyl alcohol. Three repeats of each sample were conducted. Standards (1,5 and 10 ppm for Au and Pd) and blanks were made in 2:1 propanol to benzyl alcohol for matrix mapping of solutions.

Raman Spectroscopy

Raman measurements were carried out using a Renishaw inVia Raman spectrometer coupled to a Leica microscope. Spectra were excited using the 514.5 nm line from a LaserPhysics argon ion laser. Raman scattered light was detected using a CCD detector. Spectra were recorded with an integration time of 10s and averaged once. The microreactor was positioned beneath the microscope as shown in **Figure 5.4a** and the catalyst surface was located by using the light microscope mode and observing the texture of the catalyst surface, which is shown in **Figure 5.4b**. Once the catalyst surface was located, the Raman laser was used to scan its surface at different positions along the microreactor.

5.3.3 Continuous Flow Microfluidic Experimental System

Microstructured Reactor Design

The microreactors were fabricated by photolithography and deep reactive ion etching as described in **Appendix A**. The serpentine microchannel reactor B1 (**Table 3.1**) was used with dimensions of 600 μm (W) × 300 μm (H) × 190 mm (L). The gas was introduced into the liquid flow path via a T-junction, and the gas-liquid mixture travelled down the serpentine channel in slug flow before reaching the catalytic bed. At the end of the microchannel, 60 μm width retention posts with 40 μm gaps were used to

[§] *AES carried out by the Cardiff Catalysis Institute.*

retain the catalyst. A schematic of the microreactor and a magnified image of the catalytic bed is shown in **Figure 5.5**.

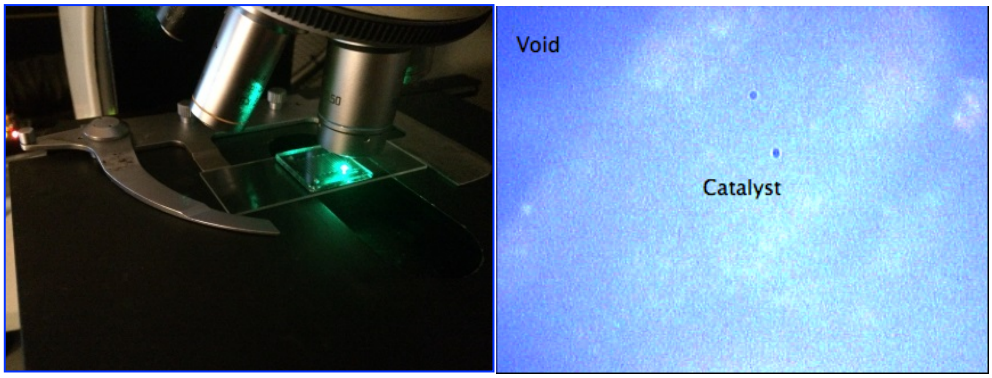

(a) (b)

Figure 5.4 *(a) Photograph of Raman microscope being used for the detection of surface species on the catalyst surface and (b) light microscope image of catalyst surface during Raman spectroscopic analysis.*

Catalyst Pelletisation and Loading

The powder catalyst prepared in **section 5.3.1** was first pelletised using a pellet press. The powder was compressed to 40 kN in a die with a diameter of 10 mm. The pellet was then crushed using a mortar and pestle and sieved. 4 mg of the sieved catalyst granules (50-60 μm) were loaded into the microreactor by applying a vacuum to the outlet port. Glass beads 60-70 μm in particle size were placed before the catalytic bed (to stabilise the flow before entering the bed) and after the catalytic bed (as a secondary precaution to prevent catalyst leaving the reactor). The length of glass beads was 3 mm preceding and 1 mm succeeding the catalytic bed.

Flow Setup

Continuous flow experiments were performed at 120°C and pressures ranging between 0-1 barg using a dual microreactor experimental set up (**Figure 5.6**). A Harvard syringe pump (PhD Ultra, Harvard Apparatus) equipped with 2 x 2.5 ml syringes was used to deliver liquid alcohol (benzyl alcohol 99.98%, Sigma–Aldrich) to the reactors in a semi-continuous mode, (due to the limitation of the syringe volumes which required

refilling every ~13 h). Two mass flow controllers (Brooks 5850TR, Brooks Instruments) were used to deliver oxygen gas (N5.5 grade, BOC) to each reactor, and a pressure gauge (SS BP Regulator, Swagelok) upstream of each reactor was used to monitor the pressure. Instrument calibrations can be found in **Appendix B**.

The effluent from the reactor flowed into a 2 ml glass vial located in a cold trap (iced beaker), where gas and liquid were separated by and the liquid product collected for analysis. The temperature was controlled to 120°C using a hotplate regulated by a temperature controller (Watlow CAL 9900, Watlow Ltd). Thermocouples (Omega) 0.2 mm in diameter were inserted on-chip to regulate the temperature at the microreactor surface. The pressure in the microreactor was near atmospheric, and was dictated by the pressure drop across the bed. The pressure drop ranged between 0.2 – 0.6 bar. Deactivation and catalyst regeneration studies were carried out, the operating parameters for each set of experiments can be found in **Table 5.2**.

Quantitative analysis was carried out on the liquid samples using a gas chromatograph (Agilent 6890) with an FID detector, a HP-INNOWax (19091- 133) capillary column and an auto-liquid-sampler. For GC analysis, 10μL of the collected sample was diluted with 0.5 ml of 3% (v/v) butanol in o-xylene as an external standard (full procedure in **Appendix B**).

Table 5.2 *Operating parameters for deactivation and regeneration studies.*

	Gas Flowrate (Nml/min)	Liquid Flowrate (μl/min)	Catalyst Amount (mg)
Deactivation	0.6	3	4
Regeneration	0.8	7.5	10

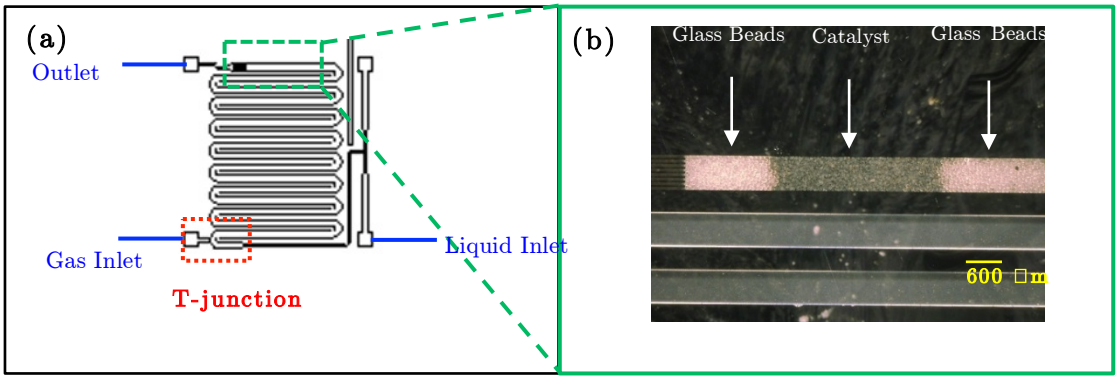

Figure 5.5 Schematic of the microchannel reactor showing 50-60 μm catalyst and 60-70 μm glass beads.

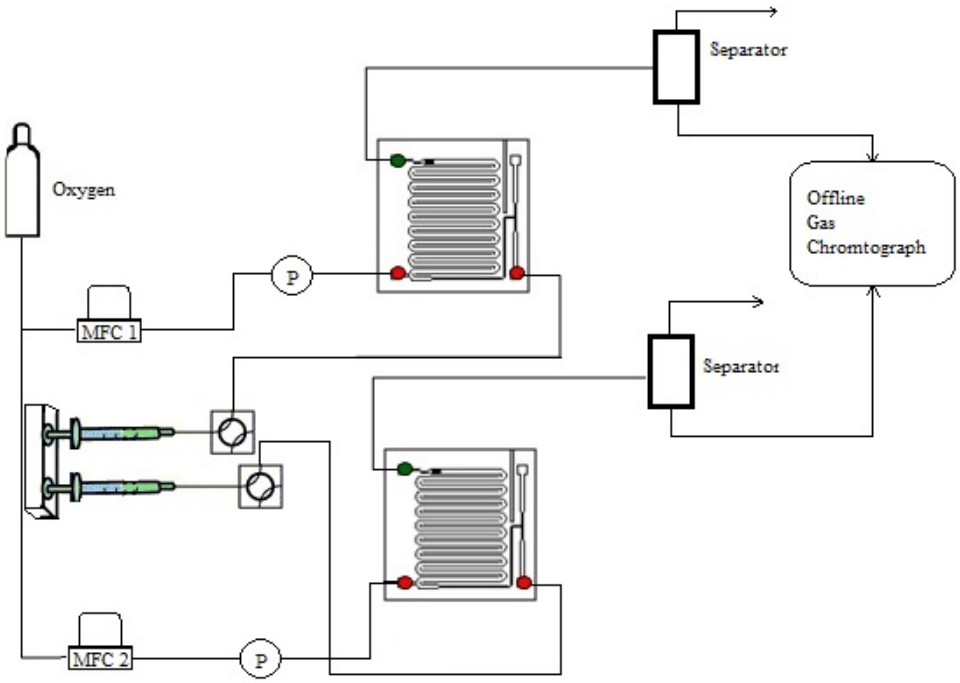

Figure 5.6 *Microfluidic experimental setup used for Au-Pd deactivation studies.*

5.4 Results & Discussion

Catalysts will be referred to in terms of their Au-Pd ratios as a percentage of the total 1 wt% metal (i.e. 80-20 Au-Pd is 0.8wt% Au – 0.2wt% Pd/TiO_2).

5.4.1 Effect of Preparation Method on Catalytic Activity

All M_{Im} catalysts had similar initial activities, with initial conversions of ~80% (**Figure 5.7**). The activities of M_{Im} catalysts were considerably higher than the C_{Im} catalyst possessing the same formulation. The superior performance of M_{Im} catalysts is due to the improved control over particle size and composition as discussed in **section 5.1**.

5.4.2 Effect of Au and Cl on Catalyst Stability

The stability of M_{Im} catalysts varied depending on the Au and Cl used in the catalyst preparation. **Figure 5.8** displays a comparison of the extent of deactivation as a function of mole of chloride, grouping together catalysts with the same Au-Pd ratio. Within the same catalyst formulation – 80-20 Au-Pd – there is an exponential relationship between the Cl amount and the deactivation rate. The M_{Im} HEC 80-20 Au-Pd catalyst with 1.37×10^{-3} moles of Cl deactivated by 75% over 50 h. In contrast, 13% deactivation is observed with the M_{Im} LEC 80-20 Au-Pd catalyst, which had lower moles of Cl used in its preparation (7.87×10^{-4} mol). Little deactivation was observed with the C_{Im} 80-20 Au-Pd catalyst, which had 4.00x10-4 moles of Cl, used in its preparation. In contrast, low Au formulations showed good stability, despite the high Cl used in its preparation; the 5-95 Au-Pd with a higher Cl content than the 80-20 HEC ($2.22\text{x}10^{-3}$ compared to $1.37\text{x}10^{-3}$ mol Cl) was the most stable. M_{Im} 65-35, the catalyst with relatively low gold and moderate Cl ($1.07\text{x}10^{-3}$ moles of Cl) was also resistant to deactivation. This indicates that amount of Au has an equally prominent effect on stability as amount of Cl, and a high chloride content has a detrimental effect only on the catalysts with a substantial Au amount (>65% Au of total metal). The presence of a high amount of Cl during the catalyst preparation method may be exposing more of the Au catalyst to the nanoparticle surface, which affects the deactivation. This will be discussed further in subsequent sections in this chapter.

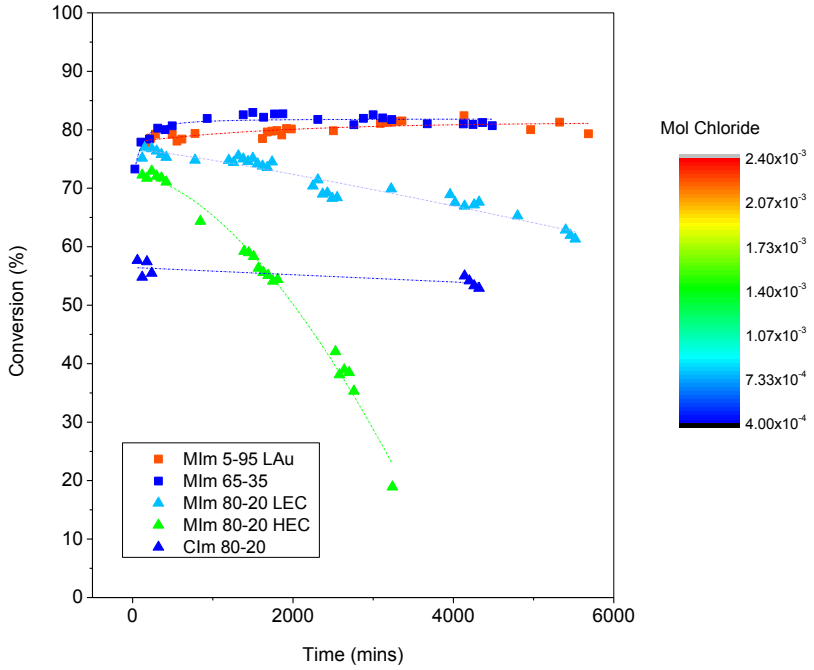

Catalyst	Au (wt%)	Pd (wt%)	Mol Cl
5-95 MIm LAu	0.05	0.95	2.24E-03
65-35 MIm	0.65	0.35	1.08E-03
80-20 MIm LEC	0.8	0.2	7.90E-04
80-20 MIm HEC	0.8	0.2	1.40E-03
80-20 CIm	0.8	0.2	4.00E-04

Figure 5.7 *Deactivation profiles of MI_m and CI_m catalysts of differing chloride ion and Au:Pd ratios. Mol Cl reported is the amount used in the catalyst preparation.*

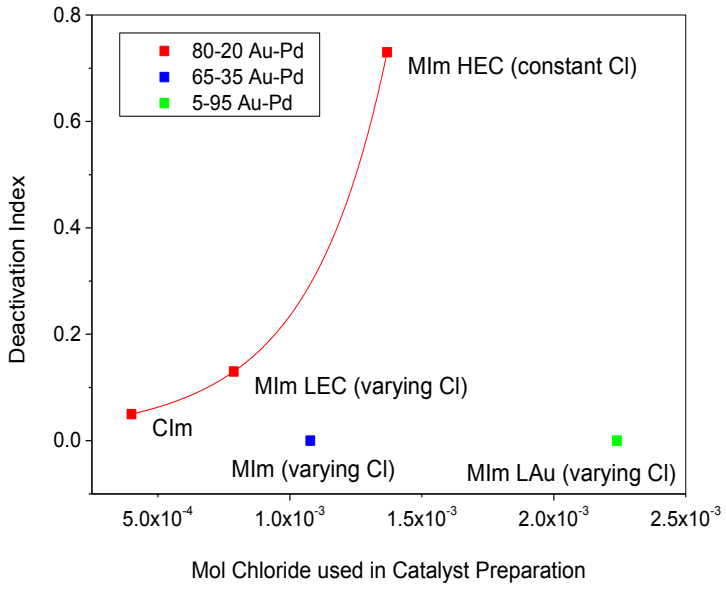

Figure 5.8 *Deactivation index* $\left[\frac{X_o - X_f}{X_o}\right]$ *(extent of deactivation) as a function of amount of chloride in the formulation, where* X_o *is initial conversion and* X_f *is conversion after 3000 min.*

5.4.3 Catalyst Characterisation

The fresh and used catalyst samples were characterised using HR-STEM coupled with energy EDS mapping. The three main modes of catalyst deactivation are investigated next: (1) adsorption of species (investigated indirectly via TEM of the catalyst morphology and Raman Spectroscopy) (2) sintering (via TEM and SEM of the particle size) and (3) metal dissolution (via AES of the liquid product mixture). XPS was carried out on the fresh and used catalyst to determine the presence or absence of residual Cl.

Catalyst Composition

XPS carried out on the M_{Im} HEC 80-20 Au-Pd catalyst showed no significant difference in composition between the fresh and used catalyst (**Table 5.3** and **Figure 5.9**). XPS also revealed that Au and Pd metals were in their metallic states before and after reaction. The XPS analysis was particularly important to confirm the absence of Cl in the fresh catalyst. The analysis showed no residual Cl in the fresh or used catalyst.

This result cannot be taken as confirmation of the absence of Cl, as quantification of Cl at such low metal loadings is anticipated to be difficult (XPS is ~8 times more sensitive to Pd and Au than it is for Cl). Thus it can be concluded that the Cl (if present) is below the XPS detection limits, which is around 0.1at% for Cl. Further characterisation using SEM-EDS or TEM-EDS would be more appropriate to confirm the amount of Cl on the catalyst.

Table 5.3 *XPS of fresh and used MI_m HEC 80-20 Au-Pd.*

	XPS Derived Molar Concentration (at%)					Metal Binding Energy (eV)	
	Pd	*Au*	*O*	*Ti*	*C*	*$Pd(3d_{5/2})$*	*$Au(4f_{7/2})$*
Fresh	0.07	0.03	35.32	14.73	49.84	334.8	83.3
Used	0.08	0.03	36.46	13.53	49.90	334.8	83.3

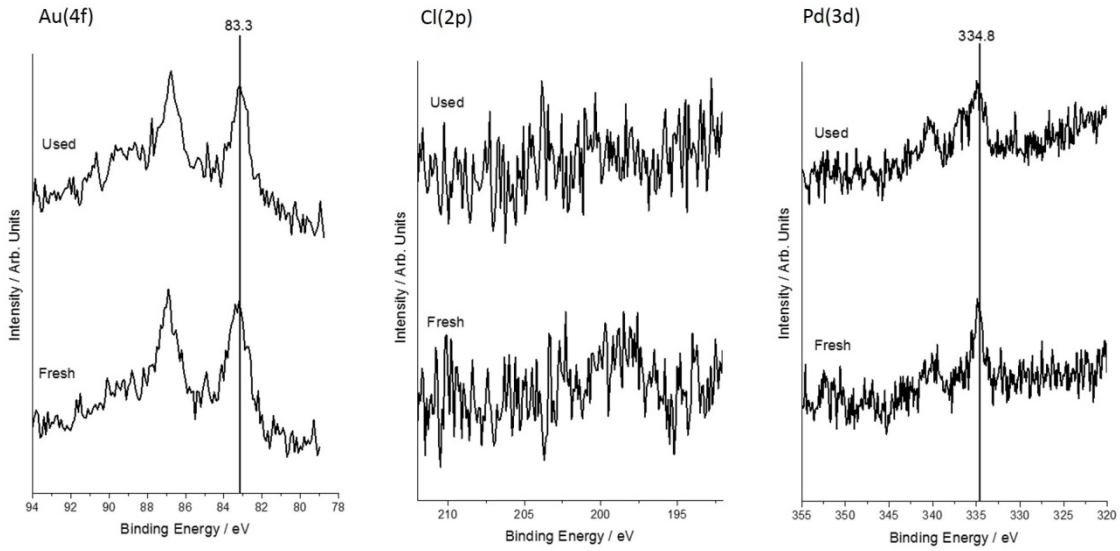

Figure 5.9 *XPS graphical results of fresh and used MI_m HEC 80-20 Au-Pd.*

Metal Leaching into Solution

All solutions obtained after 2000 min of reaction analysed using AES had no gold or palladium above the levels that can be detected with AES (for gold and palladium, intensities become differentiated to the background noise at 0.1 ppm).

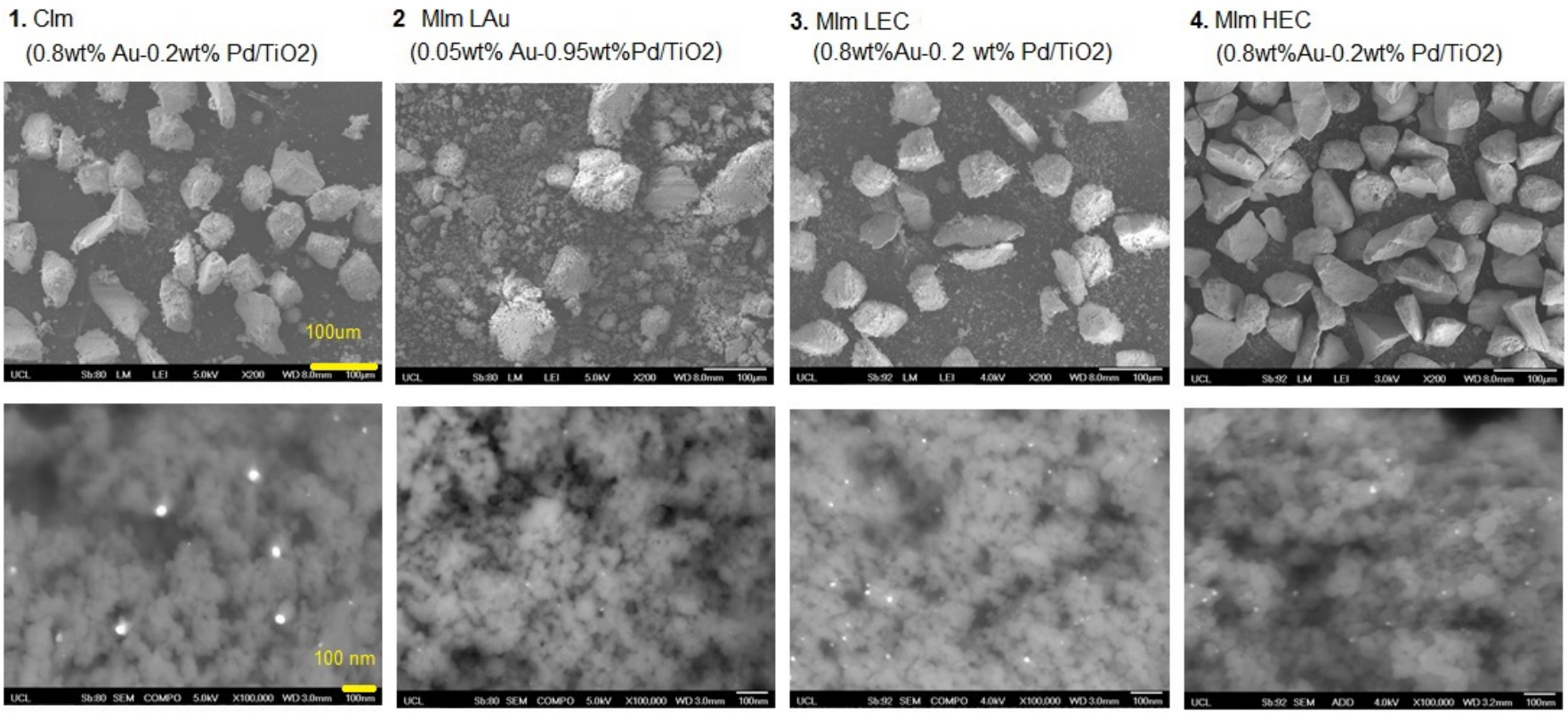

Figure 5.10 *SEM and BSE-SEM images of fresh CI_m and MI_m catalysts.*

Elemental Analysis

Figure 5.10 shows SEM and BSE images of the M_{Im} catalysts. Metal particles in the specimen backscatter the high-energy electrons more strongly and therefore appear brighter than the TiO_2 support. These metal particles (or clusters of particles, due to their large size) were visible in all three M_{Im} catalysts. Nanoparticles that are 1-2nm would not be visible at these scales and will therefore be examined with TEM later in this section. The large clusters observed in the SEM images represent a small percentage of the overall number of particles, however, are observable in larger numbers in the catalysts which had a higher rate of deactivation - M_{Im} HEC and LEC – and not observable in the stable M_{Im} catalyst: M_{Im} LAu. However, this is unlikely to have an effect on the catalyst stability as initial particle size is not expected to affect the stability of the catalyst.

To investigate the bright particles observed with BSE imaging, the catalysts were analysed with HR-STEM coupled with EDS to identify the elements constituting these clusters. Electron images were first obtained to locate the clusters within the specimen and an elemental analysis was then carried out on these clusters. The results shown in **Figure 5.11** and **Figure 5.12** confirm that the clusters observed are metal clusters, which are gold rich when the catalyst is mainly Au (i.e. in the HEC/LEC 80-20 Au-Pd) and palladium rich when the catalyst formulation is mainly Pd (i.e. in the LAu 5-95 Au-Pd). Atomically dispersed gold and palladium species were also observed in the area surrounding the metal clusters, in line with previous observations of this catalyst in the literature [4]. The images shown are representative of the entire catalyst sample (multiple areas were imaged and the results are shown for one sample area).

Morphological Changes

Used catalysts were retrieved from the micro-packed bed reactor and examined for morphological changes and deposition of species on the catalyst surface. To retrieve the catalyst, acetone was used to flush the reactor and deliver the catalyst into a vial, where it was collected. The catalyst dispersed in reaction mixture/acetone solution was flushed repeatedly with acetone to dissolve reactant/products and left to dry in air. The C_{Im} catalyst support morphology was unchanged after reaction (**Figure 5.13**).

However, the M_{Im} support morphology did undergo a change, the degree of which depended on the excess chloride amount (**Figure 5.13**). The M_{Im} HEC had the most noticeable morphological change showing an amorphous carbon coating (**Figure 5.14**).

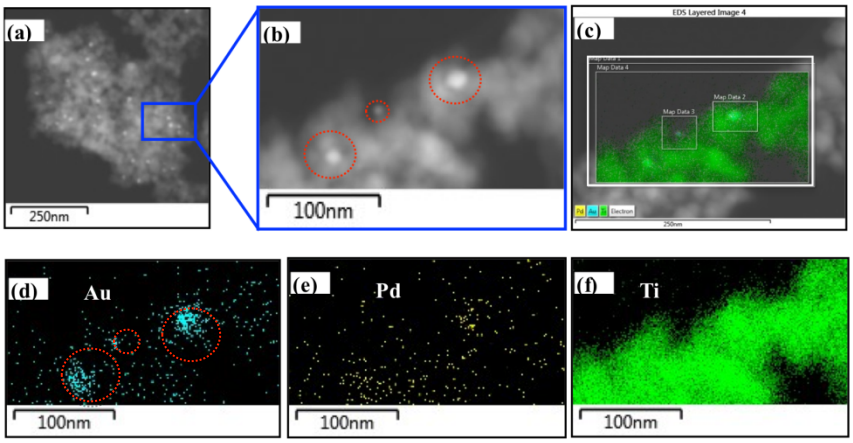

Figure 5.11 *HR-STEM EDS of MI_m HEC 80-20 Au-Pd (a), (b) electron image showing metal clusters highlighted with red circles (c) the entire mapped area (d) mapped Au signal (e) mapped Pd signal and (f) mapped titanium signal.*

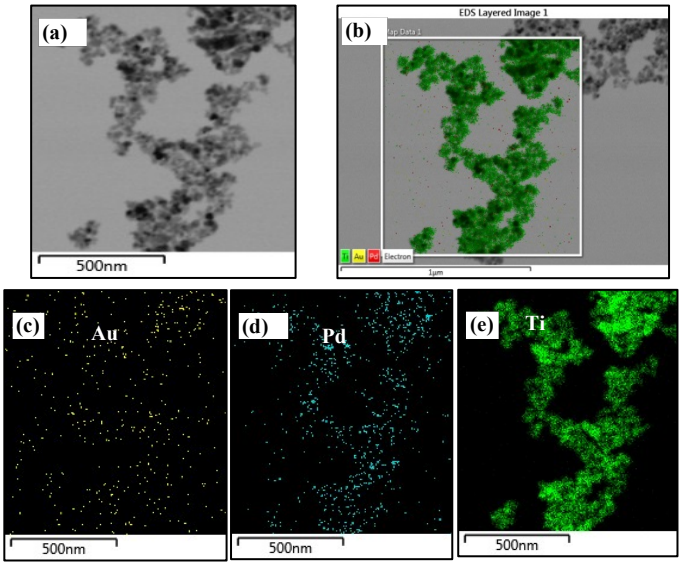

Figure 5.12 *HR-STEM EDS MI_m LAu 5-95 Au-Pd (a) electron image (b) the mapped area (c) the entire mapped area (d) mapped Au signal (e) mapped Pd signal and (f) mapped titanium signal.*

In the fresh catalyst, particles found were in the 1-2 nm range, with very few 10-20 nm nanoparticles also visible. The average metal particle size was 3.3 nm, 0.81 nm, 1.25 nm for M_{Im} HEC, M_{Im} LEC, and M_{Im} LAu, respectively obtained by averaging 150 particles via TEM (**Figure 5.15**). Despite the M_{Im} catalysts having a stability in the order M_{Im} LAu > M_{Im} LEC > M_{Im} HEC, no similar correlation is observed with particle size. The poor reaction stability of the M_{Im} HEC catalyst may therefore be attributed to the observed morphological changes via TEM. To investigate the nature of this surface film, Raman spectroscopy was carried out post-reaction, the results of which are presented in the next section.

An interesting observation is that 1-2 nm metal particles could not be observed post-reaction in any of the M_{Im} catalysts, despite the AES analysis showing no metal leaching into solution. Further investigation of this is necessary as another form of deactivation (that involves metal leaching or dissolution and redeposition onto larger particles) is possible in all catalysts, but happening at a much slower rate.

In comparison with work in the literature, carbon species covering the catalyst after reaction have been observed with methane dry reforming reactions that involve CH_4 cracking and CO disproportionation, where carbon deposition over the catalyst surface is inevitable [30;31].

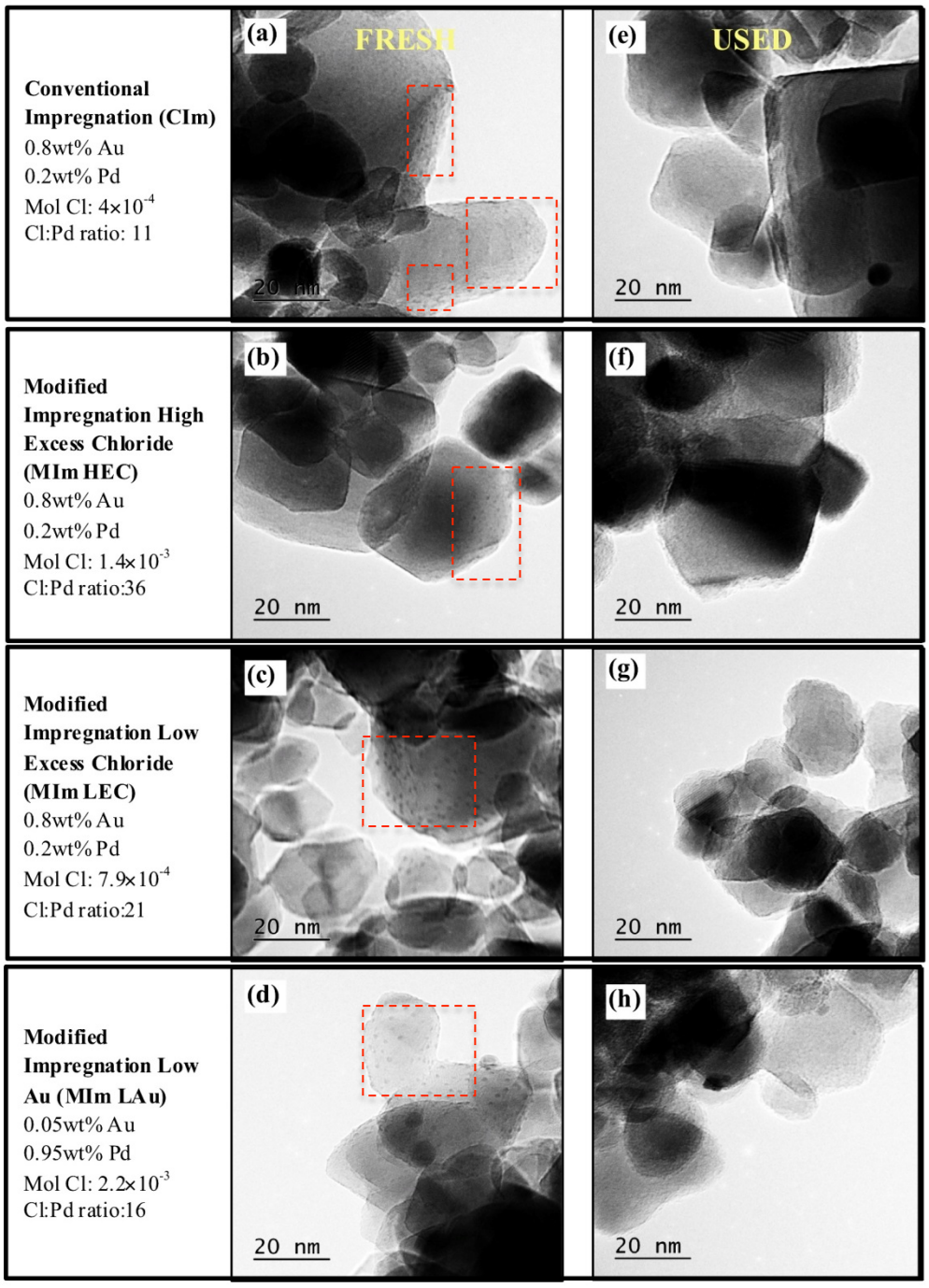

Figure 5.13 *TEM images of MI_m HEC/LEC/LAu, CI_m (a-d) fresh catalyst and (e-h) used catalyst. Dashed boxes highlight the areas with nanoparticles.*

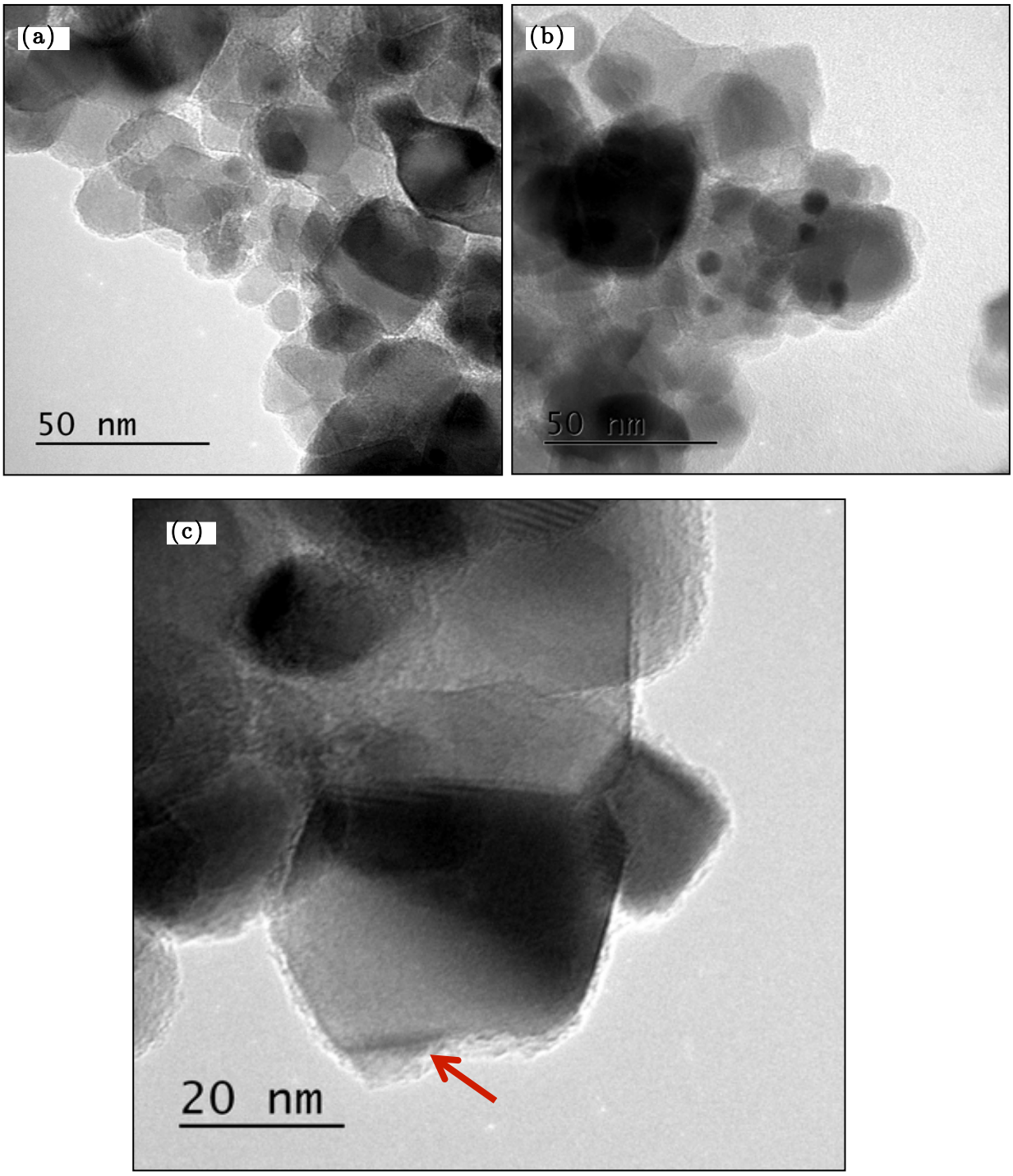

Figure 5.14 *(a), (b), (c) TEM images of used MI_m HEC 80-20 Au-Pd catalyst showing surface film.*

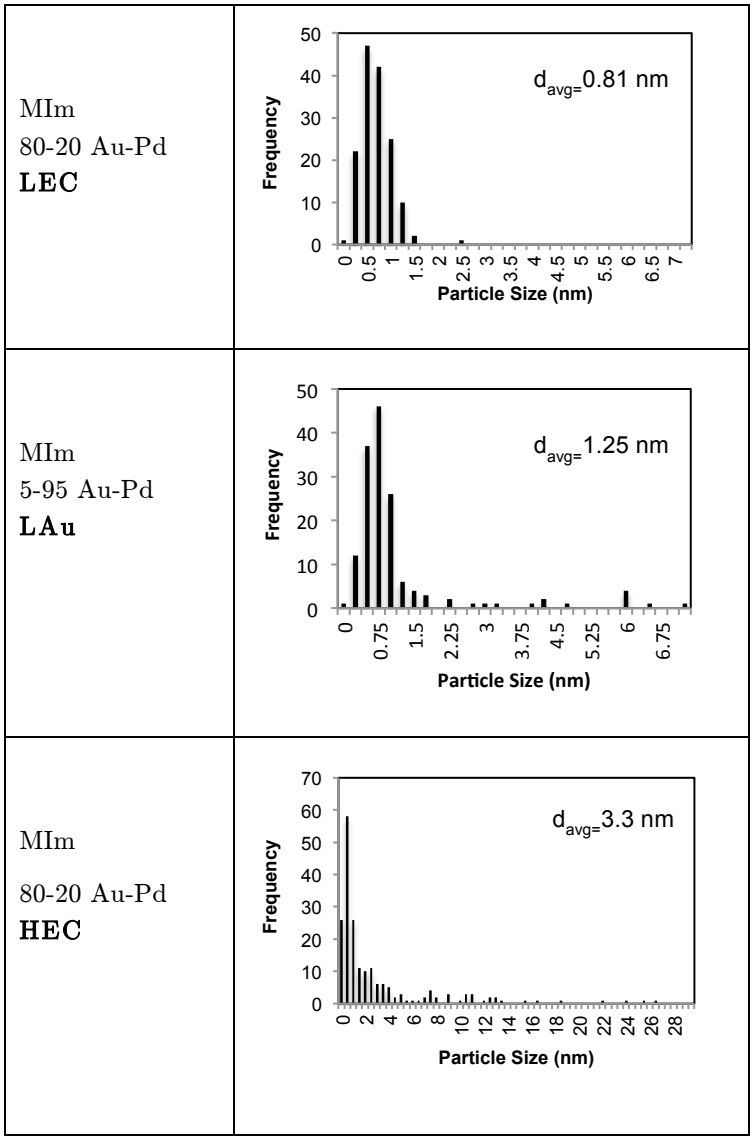

Figure 5.15 *Particle size distributions for the fresh MI_m catalysts.*

Raman Spectroscopy

Raman spectra for the catalyst at different locations within the microreactor are shown in **Figure 5.16**. The peaks at Raman Shifts of 143, 395, 517 and 634 cm^{-1} are typical peaks of the catalyst support TiO_2 (anatase). The metallic Au-Pd particles have no intrinsic Raman spectrum. Broad features were observed at 1350 cm^{-1} (D band) and 1585 cm^{-1} (G band), which are indicative of the presence of carbon species [32] – these could be deposits of reaction products. The D band, also known as the disorder-induced band, is mainly due to structural imperfections, which exist in defective, polycrystalline

graphite and other carbonaceous materials; the G band is attributed to graphitic carbon which arises from the in-plane carbon-carbon stretching vibrations of pairs of sp^2 carbons. The presence of Cl during the catalyst preparation may be affecting the structure of Au-Pd particles (i.e. alloy or a core-shell structure) and thus their reactivity and susceptibility for carbon adsorption. These results are in agreement with the surface film morphology observed with the TEM imaging. A different degree of carbon deposition is found on catalyst particles sampled at different reactor positions, with a higher amount of carbon found towards the end of the reactor. This indicates that the deactivation mechanism is one of a series nature – i.e. the carbon deposits are formed from the products (or by-products), and if these are absent in the feed, none can be formed at the entrance of the bed [33]. Hence development of carbon profiles that increase with bed length is obtained.

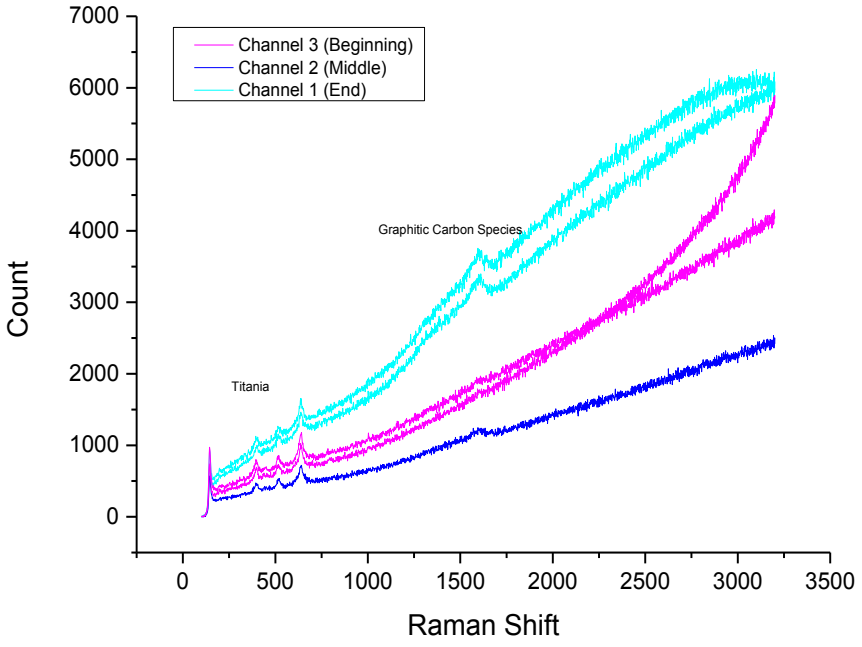

Figure 5.16 *Raman spectra of M_{Im} HEC 80-20 Au-Pd catalyst post-reaction at different locations in the microreactor.*

Catalyst Regeneration

The regeneration of coked catalyst can usually be achieved by gasification of the coke deposits with oxygen, carbon dioxide, hydrogen, or steam [34]. An experiment was conducted on the M_{Im} HEC 80-20 Au-Pd catalyst, whereby the reaction was carried out until the activity dropped from an initial ~60% to 10-20% (**Figure 5.17**) (note that the gas and liquid flowrate is different in this experiment to the deactivation experiments presented in previous sections, and therefore, the rate of deactivation is different to what was previously seen – see **section 5.3.3** for details of the operating parameters used in each of the experiments). After a total period of 120 hr, the liquid flow was stopped, leaving only oxygen flow through the reactor. The liquid flow was then reintroduced into the reactor and the activity of the catalyst was monitored. The catalyst was regenerated by O_2 flow, and a benzyl alcohol conversion of around 60% was restored. Therefore, the oxygen must be removing the carbon deposits from the catalyst surface by their oxidation.

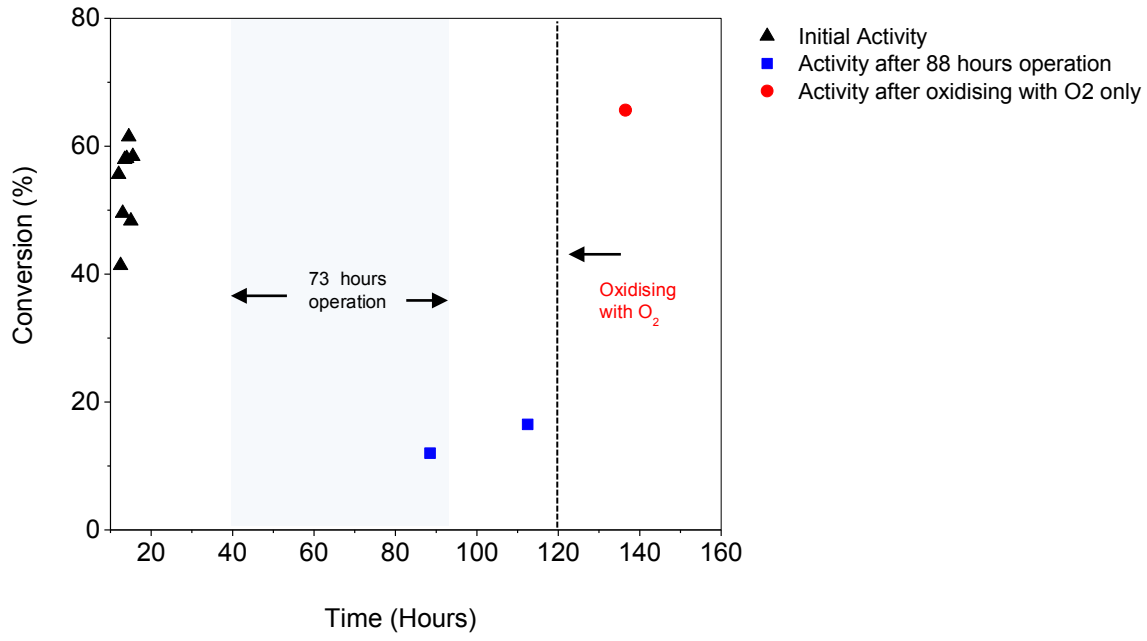

Figure 5.17 *Regeneration of the MI_m HEC 80-20 Au-Pd catalyst by flowing 0.8 Nml/min O_2 at 120°C.*

5.5 Conclusion

The deactivation behaviour of Au-Pd catalysts supported on TiO_2 was studied in a microfluidic experimental setup. Analysis of the stability with time on stream revealed a catalyst deactivation rate that is dependent on the amount of chloride used in its preparation. This dependence is prominent in catalysts containing Au amounts in excess of 65% of the total metal content. The most stable M_{Im} catalysts were the 5-95 Au-Pd M_{Im} LAu (due to its low gold content) and 65-35 Au-Pd M_{Im} (due to its low Cl in conjunction with moderate Au).

TEM examination of catalysts post-reaction showed an amorphous surface film covering the catalyst surface. This surface film could be poisoning the catalyst surface and blocking access to the active sites-containing metal. This hypothesis is supported by Raman spectroscopy, which revealed the presence of carbon species on the catalyst surface that was dependent on the axial position in the reactor, suggesting that the carbon deposits are formed from reaction products. This deactivation mechanism could be facilitated by the presence of Cl in the catalyst preparation, through its influence on the morphology of the Au-Pd alloy (core shell or alloy structure). Different alloy morphologies mean that different metals could be exposed on the catalyst surface, which may be more susceptible to deactivation.

Oxidative regeneration of the catalyst was possible by flowing oxygen through the reactor. Further catalyst characterisation using methods such as temperature programmed oxidation (TPO) and thermogravimetric (TG) analysis would be useful to determine the nature of the observed carbon deposits. More importantly, it would be important to characterise the structure of the metal nanoparticles (i.e. alloy, core-shell, distinct Au, distinct Pd) prepared via the different methods.

The most stable catalyst formulation due to its low Au content – M_{Im} 5-95 Au-Pd/TiO_2 – was chosen to conduct further hydrodynamic and reaction studies in chapters VI-VIII.

5.6 References

1. Hou, W.B., Dehm, N.A., Scott, R.W.J. **Alcohol oxidations in aqueous solutions using Au, Pd, and bimetallic AuPd nanoparticle catalysts**. *Journal of Catalysis* 2008, 253:22-27.

2. Daniel, M.C., Astruc, D. **Gold Nanoparticles: Assembly, Supramolecular Chemistry, Quantum-Size-Related Properties, and Applications toward Biology, Catalysis, and Nanotechnology**. *Chemical Reviews* 2004, 104:293-346.

3. Villa, A., Wang, D., Su, D.S., Prati, L. **Gold Sols as Catalysts for Glycerol Oxidation: The Role of Stabilizer**. *ChemCatChem* 2009, 1:510-514.

4. Sankar, M., He, Q., Morad, M., Pritchard, J., Freakley, S.J., Edwards, J.K., Taylor, S.H., Morgan, D.J., Carley, A.F., Knight, D.W., Kiely, C.J., Hutchings, G.J. **Synthesis of Stable Ligand-free Gold-Palladium Nanoparticles Using a Simple Excess Anion Method**. *ACS Nano* 2012, 6:6600-6613.

5. Morad, M., Sankar, M., Cao, E., Nowicka, E., Davies, T.E., Miedziak, P.J., Morgan, D.J., Knight, D.W., Bethell, D., Gavriilidis, A., Hutchings, G.J. **Solvent-free aerobic oxidation of alcohols using supported gold palladium nanoalloys prepared by a modified impregnation method**. *Catalysis Science & Technology* 2014, 4:3120-3128.

6. Ide, M.S., Falcone, D.D., Davis, R.J. **On the deactivation of supported platinum catalysts for selective oxidation of alcohols**. *Journal of Catalysis* 2014, 311:295-305.

7. Albonetti, S., Mazzoni, R., Cavani, F. **Chapter 1: Homogeneous, Heterogeneous and Nanocatalysis**. In *Transition Metal Catalysis in Aerobic Alcohol Oxidation*. The Royal Society of Chemistry; 2015:1-39.

8. Skupien, E., Berger, R., Santos, V., Gascon, J., Makkee, M., Kreutzer, M., Kooyman, P., Moulijn, J.A., Kapteijn, F. **Inhibition of a Gold-Based Catalyst in**

Benzyl Alcohol Oxidation: Understanding and Remediation. *Catalysts* 2014, 4:85-115.

9. Cao, E., Sankar, M., Firth, S., Lam, K.F., Bethell, D., Knight, D.K., Hutchings, G.J., McMillan, P.F., Gavriilidis, A. **Reaction and Raman spectroscopic studies of alcohol oxidation on gold-palladium catalysts in microstructured reactors**. *Chemical Engineering Journal* 2011, 167:734-743.

10. Meenakshisundaram, S., Nowicka, E., Miedziak, P.J., Brett, G.L., Jenkins, R.L., Dimitratos, N., Taylor, S.H., Knight, D.W., Bethell, D., Hutchings, G.J. **Oxidation of alcohols using supported gold and gold-palladium nanoparticles**. *Faraday Discussions* 2010, 145:341-356.

11. Enache, D.I., Edwards, J.K., Landon, P., Solsona-Espriu, B., Carley, A.F., Herzing, A.A., Watanabe, M., Kiely, C.J., Knight, D.W., Hutchings, G.J. **Solvent-free oxidation of primary alcohols to aldehydes using Au-Pd/TiO_2 catalyst**. *Science* 2006, 311:362-365.

12. Cao, E., Sankar, M., Nowicka, E., He, Q., Morad, M., Miedziak, P.J., Taylor, S.H., Knight, D.W., Bethell, D., Kiely, C.J., Gavriilidis, A., Hutchings, G.J. **Selective suppression of disproportionation reaction in solvent-less benzyl alcohol oxidation catalysed by supported Au-Pd nanoparticles**. *Catalysis Today* 2013, 203:146-152.

13. Sankar, M., Nowicka, E., Tiruvalam, R., He, Q., Taylor, S.H., Kiely, C.J., Bethell, D., Knight, D.W., Hutchings, G.J. **Controlling the Duality of the Mechanism in Liquid-Phase Oxidation of Benzyl Alcohol Catalysed by Supported Au-Pd Nanoparticles**. *Chemistry – A European Journal* 2011, 17:6524-6532.

14. Sadaba, I., Lopez Granados, M., Riisager, A., Taarning, E. **Deactivation of solid catalysts in liquid media: the case of leaching of active sites in biomass conversion reactions**. *Green Chemistry* 2015, 17:4133-4145.

15. Besson, M.l., Gallezot, P. **Deactivation of metal catalysts in liquid phase organic reactions**. *Catalysis Today* 2003, 81:547-559.

16. Besson, M., Gallezot, P. **Selective oxidation of alcohols and aldehydes on metal catalysts**. *Catalysis Today* 2000, 57:127-141.

17. Mallat, T., Baiker, A. **Liquid-phase oxidation of 1-methoxy-2-propanol with air: I. Lead and bismuth promotion and deactivation of palladium catalysts**. *Applied Catalysis A: General* 1991, 79:41-58.

18. Liu, Y., Wei, Z., Xing, T., Lu, M., Li, X. **Performance of Au/FeOx-TiO2 catalyst for liquid phase selective hydrogenation of phthalic anhydride to phthalide**. *Journal of Industrial and Engineering Chemistry* 2015, 23:321-327.

19. Keresszegi, C., Ferri, D., Mallat, T., Baiker, A. **Unraveling the Surface Reactions during Liquid-Phase Oxidation of Benzyl Alcohol on Pd/Al_2O_3: an in Situ ATR-IR Study**. *Journal of Physical Chemistry B* 2005, 109:958-967.

20. Mondelli, C., Grunwaldt, J.D., Ferri, D., Baiker, A. **Role of Bi promotion and solvent in platinum-catalyzed alcohol oxidation probed by in situ X-ray absorption and ATR-IR spectroscopy**. *Physical Chemistry Chemical Physics* 2010, 12:5307-5316.

21. Ferri, D., Baiker, A. **Advances in infrared spectroscopy of catalytic solid-liquid interfaces: The case of selective alcohol oxidation**. *Topics in Catalysis.* 2009, 52:1323-1333.

22. Mallat, T., Baiker, A. **Oxidation of Alcohols with Molecular Oxygen on Solid Catalysts**. *Chemical Reviews* 2004, 104:3037-3058.

23. Zou, X., Qi, S., Xu, J., Suo, Z., An, L., Li, F. **Study on Au/Al2O3 catalysts for low-temperature CO oxidation in situ FTIR**. *Journal of Natural Gas Chemistry* 2010, 19:307-312.

24. Mallat, T., Bodnar, Z., Hug, P., Baiker, A. **Selective Oxidation of Cinnamyl Alcohol to Cinnamaldehyde with Air over Bi-Pt/Alumina Catalysts**. *Journal of Catalysis* 1995, 153:131-143.

25. Peri, S.S., Lund, C.R.F. **The Role of Chlorine in Induction Periods During the Oxidation of Methane over Pd/SiO_2**. *Journal of Catalysis* 1995, 152:410-414.

26. Marécot, P., Fakche, A., Kellali, B., Mabilon, G., Prigent, P., Barbier, J. **Propane and propene oxidation over platinum and palladium on alumina: Effects of chloride and water**. *Applied Catalysis B: Environmental* 1994, 3:283-294.

27. Marceau, E., Che, M., Saint-Just, J., Tatibouët, J.M. **Influence of chlorine ions in Pt/A12O3 catalysts for methane total oxidation**. *Catalysis Today* 1996, 29:415-419.

28. Fuentes, G.A., Gamas, E.D. **Towards A Better Understanding of Sintering Phenomena in Catalysis**. In *Studies in Surface Science and Catalysis - Catalyst Deactivation 1991*. Volume 68. Edited by Bartholomew CH & Butt JB. New York: Elsevier; 1991:637-644.

29. Moataz, M. **Development of new highly active nano gold catalysts for selective oxidation reactions**. 2014. University of Cardiff. Thesis/Dissertation.

30. Wang, N., Yu, X., Shen, K., Chu, W., Qian, W. **Synthesis, characterization and catalytic performance of MgO-coated Ni/SBA-15 catalysts for methane dry reforming to syngas and hydrogen**. *International Journal of Hydrogen Energy* 2013, 38:9718-9731.

31. Dudder, H., Kahler, K., Krause, B., Mette, K., Kuhl, S., Behrens, M., Scherer, V., Muhler, M. **The role of carbonaceous deposits in the activity and stability of Ni-based catalysts applied in the dry reforming of methane**. *Catalysis Science & Technology* 2014, 4:3317-3328.

32. Liu, D., Quek, X.Y., Cheo, W.N.E., Lau, R., Borgna, A., Yang, Y. **MCM-41 supported nickel-based bimetallic catalysts with superior stability during carbon dioxide reforming of methane: Effect of strong metal-support interaction**. *Journal of Catalysis* 2009, 266:380-390.

33. Anderson, J.R., Boudart, M. ***Catalysis: Science and Technology***. Tokyo: Springer-Verlag; 1984.

34. Balsco, V., Royo, C., Menendez, M., Santamaria, J., Fierro, J. **Non-uniform sintering in oxyregeneration of fixed bed catalytic reactors**. In *Catalyst Deactivation 1991 Vol 68*. Edited by C.H.Bartholomew, J.B.Butt. Amsterdam: Elsevier Science Publishers; 1991:629.

VI.

Hydrodynamics of Multiphase Packed Bed Microreactors

The hydrodynamics of a silicon-glass micro-packed bed reactor was studied at benzyl alcohol oxidation reaction conditions. The following topics were considered: flow regime transitions, particle size effect on flow regimes, and comparisons with macro-scale reactors. Results show flow regime transitions that are different to what is commonly known in conventional reactors; namely a classification of flow regimes applicable only to micro-packed bed reactors is presented here.

6.1 Introduction

The chemicals industry relies heavily on multiphase catalytic reactions in which gas and liquid phases flow concurrently through a fixed bed of solids. This flow pattern provides efficient contact between the phases and is therefore preferable in multiphase reactions [1]. A reduction in the scale at which this is carried out has several advantages from both a productivity and lab investigation tool standpoint [2;3]. A good understanding of the flow regimes within a packed bed reactor is necessary to fully understand their implications on reactor performance. Although recent studies on characterising micro-packed bed reactor hydrodynamics are noteworthy [4-10], the current literature does not address flow regime transitions on the micro-scale adequately. Most of those efforts have been dedicated to the identification of differences to the macro-scale in relation to various parameters: liquid hold-up, pressure drop, porosity and flow regime transition. The results of those studies have shown that the influence of gas and liquid flow rate on liquid holdup in micro-packed beds is similar to conventional reactors [5], but the absolute value of the liquid holdup in micro-packed beds is under-predicted by conventional hydrodynamic models [11], attributed to the stronger capillary forces; values of 0.65 - 0.85 are found for liquid-holdup in micro-packed beds [12] compared to the 0.28 - 0.37 found in conventional trickle bed reactors [13].

Figure 6.1 shows Bond* numbers for micro-packed bed reactor studies (Inoue et al [14], Losey et al. [9], Larachi and Faridkhou et al. [5], and the current study) in comparison to a conventional scale reactor (Charpentier et al. [15]). As shown in the figure, the Bo number in micro-packed bed reactors is three orders of magnitude smaller than conventional scale systems. This can be correlated with the lower characteristic length in the microreactor studies. This in turn has an effect on the flow distributions within the micro-packed bed, meaning that established TBR correlations

---

** The dimensionless Bond number* $\frac{[(\rho_L-\rho_G)gl^2]}{\sigma}$ *can be used to quantitatively assess for the relative importance of the gravitational and capillary forces.*

cannot be extrapolated. The high capillary pressure has adverse effects on the two-phase pressure drop and influences liquid spreading across the porous medium, resulting in the liquid phase displacement from the high porosity zone near the wall to the low porosity region near the centre [11]. Further discussion of the differences in behaviour between conventional and micro-scale reactors can be found elsewhere [7].

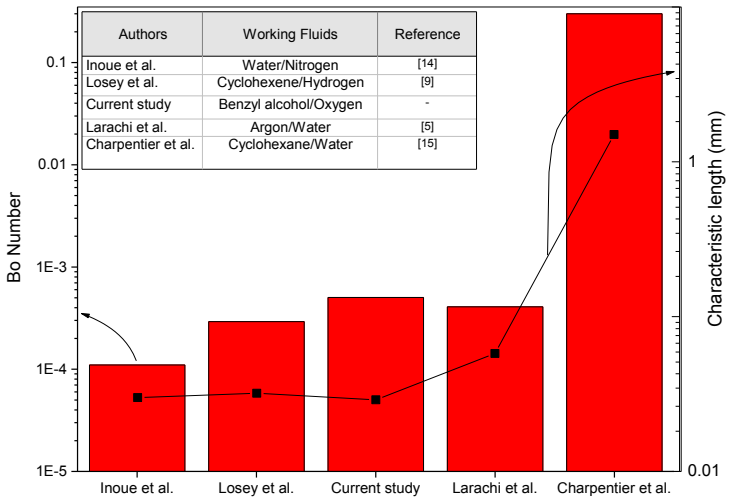

Figure 6.1 *Bond numbers for micro-packed bed reactor studies in comparison to a conventional scale reactor. Characteristic length used is the particle diameter.*

Microscale reactors do not necessarily possess ideal behaviour, as the small particle diameter commonly used in these reactors leads to high capillary forces. As a result, they have been found to cause liquid maldistribution and channelling in some instances [6]. There have been various studies on gas–liquid flows in micro-packed bed reactors that focused on evaluation of reaction performance and highlighting the advantages of micro-reaction technology for such applications [9;16]. Less attention has been paid to the fundamental transport phenomena occurring and their interplay with chemical kinetics, which will be investigated over the course of the next two chapters. The focus of this chapter is the identification of flow types present in a micro-packed bed reactor and mapping of those flow regimes based on their dependence on gas/liquid flowrates as well as particle size.

6.2 Background

6.2.1 Flow Patterns in Conventional Trickle Bed Reactors

The flow regime in a conventional trickle bed reactor is dependent on the flowrates of the gas and liquid phases, the properties of the flowing fluids, and the size and shape of the stationary packing. The flow regimes are broadly classified in terms of high-interaction and low-interaction. At low gas and liquid flow rates, the liquid trickles over the packing while the gas forms the continuous phase, fully occupying the void space [1]. This regime is termed the trickle flow regime, and can feature partially or fully wetted catalyst particles, depending on how high/low the gas/liquid flowrates are. At the particle level, the liquid flow can take several forms (such as liquid film flow and rivulets). Trickle flow operation is essentially a steady-state condition, whereby factors such as the liquid hold-up, pressure drop, etc are independent of time.

As the gas and/or the liquid flowrate is increased, a transition from the steady trickling flow to a time-dependent flow behaviour, known as pulse flow, is obtained. The pulse flow regime results from an increase in either gas or liquid flowrates, provided the flowrate of the other phase is sufficient. This flow regime is usually dynamic and characterised by alternating gas-rich and liquid-rich slugs. Various authors have attempted to physically interpret the onset of pulsing; Sicardi and Hofmann [17] have attributed pulsing due to the formation of waves with large amplitudes that block the packing channel. The Froude number $\left(\frac{u_o}{\sqrt{g_o l_o}}\right)$, which is essentially a speed-length ratio, is often used, whereby a certain threshold needs to be exceeded for the transition to pulsing flow to occur [18].

With sufficiently high gas flowrates and low liquid flowrates, the spray regime prevails, where the gas forms the continuous phase and the liquid is sheared to small droplets by the high velocity gas phase. On the opposite end of the hydrodynamic spectrum, at low gas flowrates and high liquid flowrates, the liquid becomes the continuous phase and the gas becomes dispersed in the form of small bubbles, known as the bubbly flow [1].

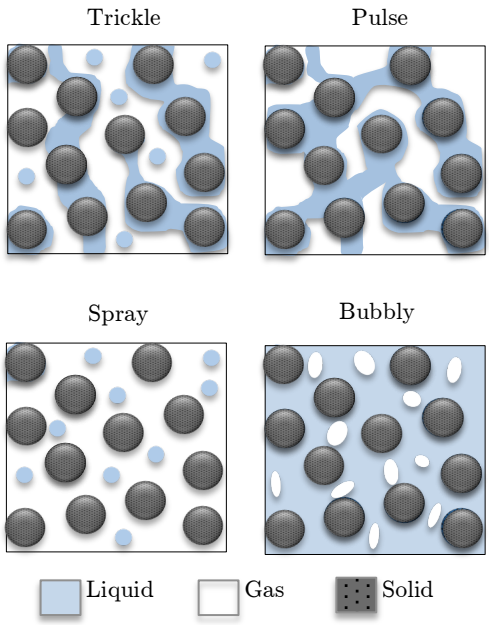

Figure 6.2 *Schematic representation of flow regimes in a conventional three-phase packed bed reactor.*

A multitude of hydrodynamic states can exist on the particle level and a number of factors determine which of the states are encountered within the reactor. These factors include (1) bulk conditions (2) reaction characteristics (3) component properties (4) catalyst properties and (5) reactor features. The catalytic pellets can be completely wetted and completely liquid-filled. This pellet state can occur when under the trickle, pulse, or bubbly flow regimes. Reactants are supplied from the bulk and diffuse through the catalyst pores to the active sites, where they react. The particle will remain liquid filled unless the reaction is very exothermic or the reactants are volatile. Catalyst pellets can also be completely dry externally and internally and are encountered under a multitude of scenarios: (1) operation under the spray flow regime (2) liquid channelling and poorly designed liquid distributors (3) the reaction is sufficiently exothermic and the liquid reactant has finite volatility. Generally, the rates and temperatures are higher in gas-filled catalysts, this is because (1) mass transfer is higher in gas-filled pores than in liquid filled pores and (2) exothermic reaction heat is removed much less effectively by a flowing gas than by a flowing liquid external to the catalyst (book). However, this may lead to hot spot formation, which is unfavourable because of the possible initiation of side reactions, catalyst deactivation and reaction

runaway. Catalysts that are partially wetted externally (by a single or a multiple of rivulets) can be fully wetted internally (due to capillary force). This particle state typically occurs when the liquid flow rate is sufficiently low (under trickle flow operation), or if severe liquid maldistribution occurs. The major source of intrapellet liquid irrigation is liquid that flows over the catalyst and penetrates into the pores by capillarity. A secondary source of liquid can be supplied when a porous catalytic pellet is exposed to a gas containing a condensable component, because of a reduced vapour pressure. The conditions that favour capillary condensation are sufficiently low temperature, small pores, and a gas phase that is saturated with a condensable component. Therefore, this can lead to situations where the catalyst is externally dry, but wetted internally. This pellet state can occur under the spray and trickle flow regimes [1;19].

6.2.2 Analysis of Forces Across the Length Scales

The underlying phenomena dictating the dominating hydrodynamics in a three-phase packed bed reactor is dependent on the governing forces such as the interfacial, gravitational, inertial, and viscous forces. The equations below refer to the relevant dimensionless numbers governing the hydrodynamics in a trickle bed reactor.

$$Re_L = \frac{\rho_L u_{o,L} d_p}{\mu_L} \qquad \frac{inertial\ force}{viscous\ force}$$

$$Ca_L = \frac{\mu_L u_{o,L}}{\sigma_L} \qquad \frac{viscous\ force}{capillary\ force}$$

$$\mathbf{Bo} = \frac{(\rho_L - \rho_G) g {d_p}^2}{\sigma_L} \qquad \frac{gravitational\ force}{capillary\ force}$$

In **Table 6.1**, a comparison of these dimensionless numbers is made between reactors of different scales. The values in **Table 6.1** demonstrate the dominance of the viscous and capillary forces in relation to inertial and gravitational forces in the MPBR; the very low Reynolds (0.01-0.03) number in the MPBR indicates a liquid flow that is laminar in nature and the low Bond (2.12×10^{-3}) and Capillary (1.8×10^{-6}-7.4×10^{-6}) numbers indicate the relative strength of the capillary forces in comparison to conventional laboratory and industrial trickle bed reactors.

Table 6.1 *Values of key dimensionless parameters in various reactor scales.*

	Micro-Packed Bed Reactor	**Typical Lab Scale Reactor***	**Industrial Trickle Bed****
Reactor Diameter, (m)	0.0004	0.1	1
Particle Diameter, (m)	6.50E-05	3.00E-03	3.00E-03
Re_L	0.01-0.03	1.5-40	31.2
Ca_L	1.8×10^{-6}-7.4×10^{-6}	7.3×10^{-6}-2.2×10^{-4}	1.86E-04
Bond	2.12×10^{-3}	1.16	4.66

**Dimensionless numbers calculated from Charpentier & Favier study for air/water [15].*

*** Industrial trickle bed reactor data obtained from Alsolami et al [20].*

6.2.3 Dispersion Criteria and Applicability to Micro-Packed Bed Reactors

Axial Dispersion

Operation under plug flow in fixed bed catalytic reactors is usually preferred in most situations, especially for kinetic studies. Axial dispersion results in adverse mass velocity effects and can be minimised by selecting an appropriate ratio of bed length to particle diameter (L_B/d_p). Criteria have been developed for the ratio of the bed length to particle size for the assumption of plug flow to be valid. This was based on the work of Mears [21] who used a one-dimensional plug-flow model with longitudinal dispersion superimposed, yielding a differential equation describing the steady-state concentration profile in an isothermal reactor.

$$D_a^L \frac{d^2 c_i^L}{dz^2} - u_L \frac{dc_i^L}{dz} - r_j = 0 \qquad (6.1)$$

Perturbation solutions of this equation were obtained by Burghardt and Zaleski [22] for appropriate boundary conditions, considering small deviations from plug flow (large peclet number) and a first-order reaction. A criterion was presented for small values of reaction rates (less than 90% conversion):

$$\frac{L_b}{d_p} > \frac{8n}{Bo} \times ln\left(\frac{1}{1-X}\right) \qquad (6.2)$$

Using this criterion, the maximum allowable particle diameter d_p can be calculated for a given reactor length. **Table 6.2** shows the calculation of this criterion (using typical micro-packed bed reactor conditions used in this chapter). The criterion in **equation 6.2** is not fulfilled for the 65μm particles used, however, it is not far from it; for the criterion to be fulfilled, a smaller particle size of 43μm should be used.

Table 6.2 *Calculation for the criterion assessing for axial dispersion for the micro-packed bed reactor used in this work (equation 6.2).*

$Pe_{p,ax}$	0.1‡
n	1
X	0.8
L_b (m)	0.0055
d_p (m)	6.5E-05
$\frac{L_b}{d_p}$	84.62
$\frac{8n}{Pe_p} \times ln\left(\frac{1}{1-X}\right)$	128.76

‡ Value obtained from van Herk et al. for a 2 mm diameter packed bed with particles of 100μm diameter obtained from 'cold-flow' experiments [10].

Radial Dispersion

Radial dispersion is usually neglected for a small ratio of reactor diameter to length (D/L_b) and large fluid velocity [13]. However, recent studies have shown that the high capillary forces found in micro-packed beds differ significantly from that of larger scale reactors and result in higher values for the liquid hold-up [6;11] and poorer radial dispersion characteristics [20], thus rendering this criterion inapplicable at such reduced scales. For the assessment of radial dispersion within the micro-packed bed, a criterion was developed by Alsolami et al. [20] for micro-packed beds, termed the Wesiz Modulus:

$$\phi_{rad} = \left(\frac{h_L}{a_{GL}}\right)^2 \left(\frac{n+1}{2}\right) \left(\frac{(1-\varepsilon_b)(1-b)R_{v,i}^{obs}}{D_{rad,i,L}C_{i,L}}\right) < 0.15 \qquad (6.3)$$

Two cases will be considered next, a best and worst case scenario that rely on extreme assumptions made on the distribution of gas and liquid within the packed bed. The component analysed for here is the oxygen.

Case 1: G-L interface is assumed to be a single slab across the longitudinal cross section

It is assumed here that all liquid flows through one side of the bed and there is only gas flowing through the other side of the bed. Assuming a first order reaction, ε_b (bed voidage) of 0.35, h_L (liquid hold-up) of 0.75 (both are recent values typical for micro-packed bed reactors) [12], the calculated value for the Weisz modulus is $\phi_{rad} = 278.7$, which indicates poor radial mass transfer.

Case 2: G-L interfacial area per unit volume is assumed to be equal to the particle surface area per unit volume

Under this assumption, the liquid forms a film covering the particle surface and $a_{GL} = a_p$, where a_{GL} is the gas-liquid interfacial area per unit volume and a_p is the particle surface area per unit volume. This assumption gives $\phi_{rad} = 0.034$ indicating good radial mass transfer. Therefore, significant improvements in the radial mass transport results from the increase in G-L interfacial area, moving between these two extreme case scenarios.

Impact of Gas Flowrate on Dispersion

The introduction of gas into a liquid phase impacts the dispersion in the packed bed by perturbing the flow of liquid through the network of particles. Van Herk et al. [10] found that the mean liquid residence time was lower in the presence of the gas phase (as compared to single phase flow), but further increase in gas flowrate had minimal effect on the liquid phase residence time. However, the gas flowrate range studied by van Herk was very narrow (up to 85 mm/s) and differences in behaviour between such small gas flowrates may be difficult to detect. A slightly conflicting study showed that the dispersion characteristics are very similar in the gas-liquid case as to the single phase case [12] suggesting that the fluid mechanical interaction between the gas and

the liquid is very limited (within the gas and liquid ranges studied) and the dispersion Peclet number Pe_p is a weak function of the gas flowrate. Their argument is that for small hydrodynamic diameters, the interstitial voids are almost saturated with liquid and as a result, the dispersion for a gas-liquid flow will closely resemble the liquid only situation. Only a moderate amount of additional dispersion was found to exist due to gas-liquid interaction. Consequently, the authors advocate that single phase models for dispersion can be used for gas-liquid micro-packed bed reactors. This conjecture is yet to be confirmed by other similar studies in micro-packed bed reactors.

6.3 Materials & Methods

Flow mapping experiments were performed with benzyl alcohol as the liquid feed, oxygen as the gas feed and typical reaction temperature (120°C) and pressure (1 barg). Superficial velocities were calculated based on the reaction conditions (flow setup shown in **Figure 6.3**). The flow maps were generated using 0.05% Au – 0.95% Pd/TiO_2 catalyst particles of 65µm ± 14µm particle size (preparation procedure specified in **Chapter V**). The typical catalyst bed length was 3.2 mm. The microreactor used was the B1 reactor (**Table 3.1**) identical to the serpentine reactor described in **Chapter V**. A microscope image of the microreactor with a magnified image of the catalyst packing are shown in **Figure 6.4**.

Flow observation was carried out via visualisation of the contacting patterns using a microscope (VHX-600 Digital Microscope, Keyence). To aid visualisation of the liquid, benzyl alcohol soluble red dye (Sepisol Fast Red, Bima 83) was dissolved in the flow medium. The dye tends to colour pink-yellow when the thickness of the liquid layer is large and red when the liquid layer is thin. The pressure drop during flow mapping was <0.35 bar. Flow mapping experiments were conducted by altering the gas or liquid flow rate until a transition was observed. Subsequently, it was probed further by smaller modifications to the gas and liquid flow until the exact transition point was determined. Spot-checks were carried out where the same point was repeated (once the bed was subjected to a different flow history) to ensure no significant hysteresis effects.

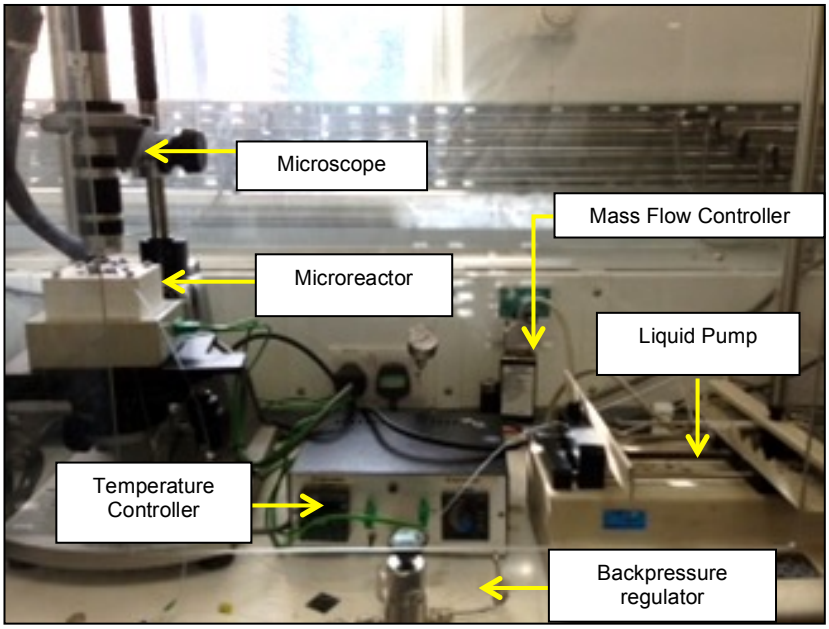

Figure 6.3 *Experimental setup used for flow observation.*

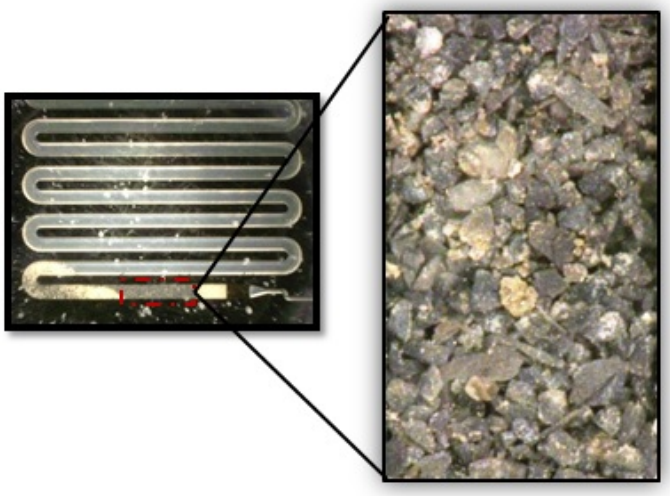

Figure 6.4 *Microchannel with packed particles and a high magnification image of the catalytic bed.*

6.4 Results & Discussion

6.4.1 Flow Pattern Dependence on Gas/Liquid Flowrates

Five main types of flow regimes were identified in the micro-packed reactor (**Figure 6.6** and **Figure 6.5**): Liquid-dominated slug, segregated, gas-continuous (fully wetted), gas-continuous (partially wetted), and a gas phase regime. The flow regime transitions occurred as a result of changes in the gas (G) and liquid (L) flow rates. High gas in conjunction with low liquid flow rates favoured gas-continuous flow, while low gas and high liquid flow rates favoured liquid-dominated slug flow. Liquid-dominated slug flow exhibited regions of gas and liquid, where liquid occupied the majority of the bed and covered the particle interstitial voids, while the gas formed large elongated slugs, leaving the gas-liquid surface to reside at the interface of a few gas voids (**Figure 6.6a**). Under this flow regime, slug flow was observed upstream the packed bed, causing liquid rich waves or "pulses" to traverse the bed length at regular time intervals. The term slug also identifies the behaviour inside the packed bed, as at some points in time, the fluid extends throughout the channel cross-sectional area. This is a form of induced pulsing, usually achieved in conventional reactors by on-off liquid or gas flow modulation. Natural pulse flow (which forms as a result of global convective instability in the packed bed region) is usually associated with better mass transfer than trickle flow. Similar to natural pulsing, the motivation for induced pulsing (via on-off flow modulation) is to reduce the resistance to the gas transfer caused by the presence of the liquid film.

With an increase in gas and decrease in liquid flow rate, a transitional flow regime existed – segregated flow – where the gas and liquid had a similar and constant share of the bed without significantly perturbing each other (**Figure 6.6b**). Wavy-annular flow in the empty channel upstream of the packed bed was usually observed with this type of flow and the resulting segregated flow pattern in the packed bed was often dynamic in nature – caused by liquid waves propagating from the empty channel upstream. The transition to gas-continuous flow took place with a further increase in gas/decrease in liquid flow rate. This flow regime consisted of a continuous gas phase whilst the liquid formed a more uniformly distributed thin film surrounding the catalyst particles (**Figure 6.6c**) – a flow pattern which has been associated with trickle flow in

conventional trickle bed reactors. The term “trickle” is not used in this work due to the dominance of capillary forces. At elevated gas-to-liquid ratios, partial drying of the catalyst particles took place, where the liquid traveled along the packed bed in the form of “rivulets” rather than in the form of a film, leaving some parts of the particles exposed to the gas (**Figure 6.6d**). Finally, with a further increase in gas velocity the flow transitioned into a gas phase regime (**Figure 6.6e**). In order to capture the onset of this transition accurately, this transition line was calculated based on vapour-liquid equilibria, using the vapor pressure of benzyl alcohol and the ideal gas law to determine the gas flow rate at which all benzyl alcohol would be in the gas phase for each liquid flow rate. It is important to note that this transition relates to the inlet conditions prior to the packed bed. The situation is more complex inside the packed bed where capillary condensation and evaporation would be taking place. This may result in pellets that are non-wetted on the external surface but that are partially filled with liquid due to capillary condensation.

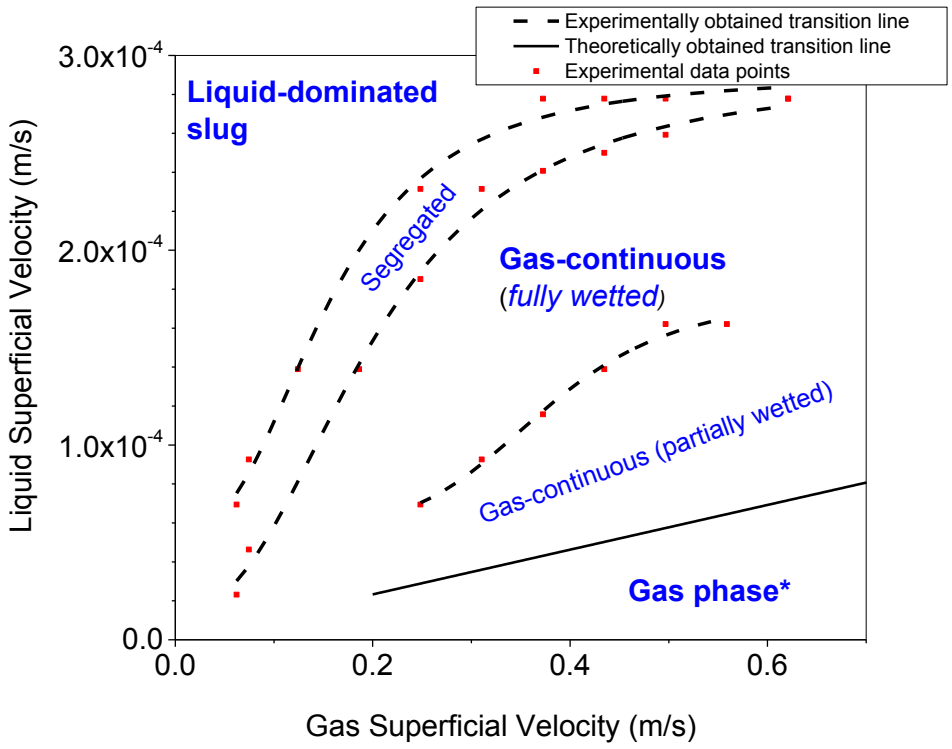

*Gas phase at inlet conditions

Figure 6.5 *Flow regimes observed in the micro-packed bed reactor for benzyl alcohol/oxygen flow system under representative reaction conditions (120°C, 1 barg). Experimental data points utilised to obtain the curves are marked with red symbols.*

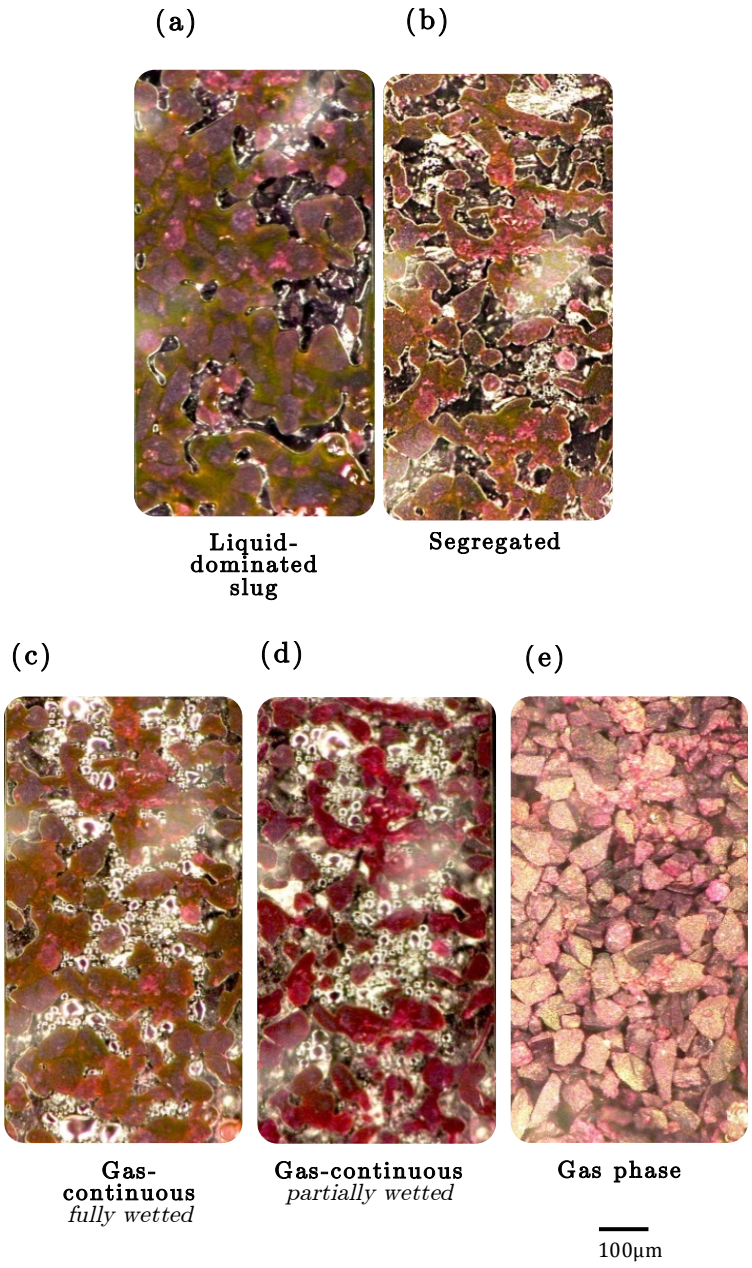

Figure 6.6 *Microscope images of the micro-packed bed reactor showing the flow regimes corresponding to* ***Figure 6.5****. (a) Liquid-dominated slug (b) Segregated (c) Gas-continuous (fully wetted) (d) Gas-continuous (partially wetted) (e) Gas phase.*

6.4.2 Flow Pattern & Dynamics: Dependence on Upstream Flow Conditions

The dynamic state inside the catalytic bed was highly dependent on the flow pattern establishment upstream, which in itself was dependent on the gas-liquid introduction method. The microreactor used in this work introduces gas into a liquid flow path via a T-junction, producing either slug or annular flow, depending on the gas-to-liquid (G:L) flow rate ratio. At low G:L, the flow pattern preceding the bed is slug flow, which manifested in dynamic behaviour in the catalytic bed, consisting of periodic wetting and drying of the particles (high interaction). The liquid-dominated slug flow regime is analogous to induced pulsing in conventional reactors, where the liquid is modulated on/off to promote the gas-solid mass transfer in between liquid bursts. Intermediate G:L resulted in wavy-annular flow upstream, causing slight movement of the gas-liquid boundary layer as the wave propagated through the packed bed. High G:L resulted in annular flow upstream and consequently stable flow conditions in the packed bed, with the gas and liquid not significantly engaging with each other (low interaction).

The segregated and gas continuous flow regimes are analogous to trickle flow in conventional trickle bed reactors. The segregated flow regime is characterised by a thick liquid film segregating the gas domains, while the gas-continuous has a thin film covering the catalyst particles, which changes to thin rivulets at very high (low) gas (liquid) flow rates, leading to partial wetting. Using the classification in **Table 6.3** it is possible to predict the flow regime in the catalytic bed by observing the flow pattern in the empty channel preceding it.

Table 6.3 *Characterisation of the flow regimes observed in the micro-packed bed reactor and their relationship with the flow pattern upstream the packed bed section.*

G:L Ratio	Flow Regime Upstream of packed bed	Flow Regime in Packed Bed	Dynamic /Steady-State	High/Low Interaction	Analogous to – in the Macroscale
High	Annular	Gas-continuous & gas phase	Steady-state	Low	Trickle (thin film and rivulet flow)
Intermediate	Wavy-annular	Segregated	Dynamic	Low	Trickle (thick liquid film)
Low	Slug	Liquid-dominated slug	Dynamic	High	Induced pulsing

6.4.3 Comparison with Macro-scale Flow Maps

Figure 6.7 shows the flow regime transitions observed in the current work (transition from liquid-dominated slug to segregated) compared to that of the Charpentier & Favier flow map (transition from pulse to trickle) for a conventional trickle bed plotted on the Baker coordinates [15]. The transition from high interaction to low interaction regimes appears to take place at L:G ratios one order of magnitude smaller in the micro-packed bed reactor (in the current work), a difference that is not surprising given the previous analysis of forces.

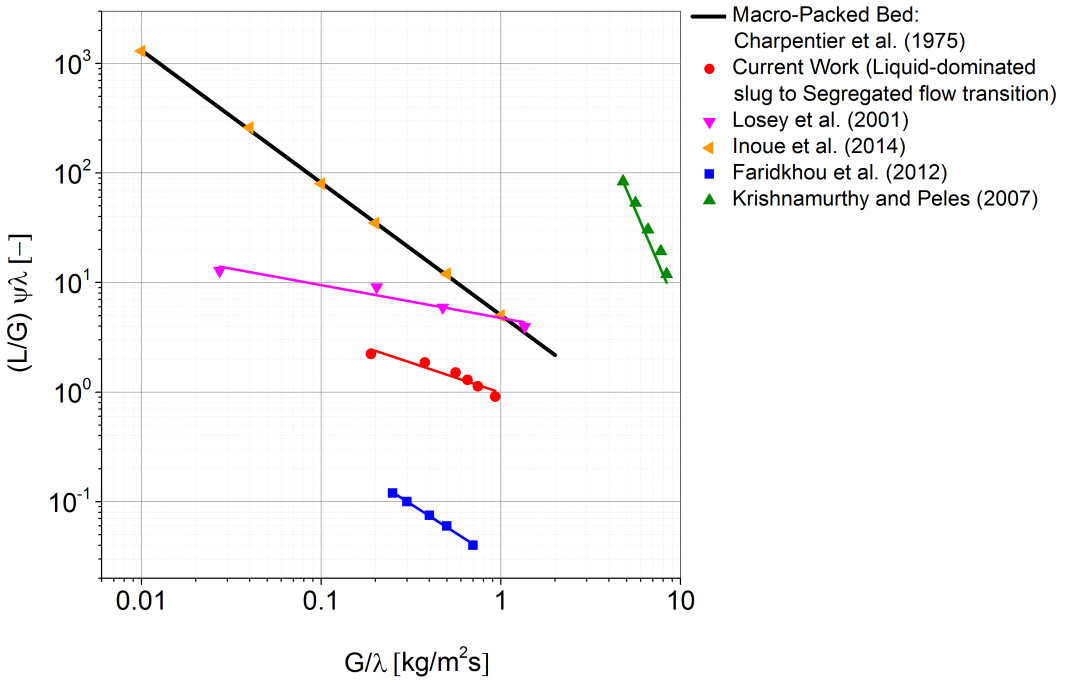

Figure 6.7 *Flow map comparison of a conventional trickle bed reactor Charpentier and Favier (1975) [15] and micro-packed reactors: Faridkhou and Larachi (2012) [5], Losey et al. (2001) [9], Krishnamurthy and Peles [8] and Inoue et al. (2014) [14] using the Baker Chart Parameters* $\lambda = \left[\left(\frac{\rho_G}{\rho_A}\right)\left(\frac{\rho_L}{\rho_w}\right)\right]^{0.5}$ *and* $\psi = \frac{\sigma_w}{\sigma}\left[\left(\frac{\mu_L}{\mu_w}\right)\left(\frac{\rho_w}{\rho_L}\right)^2\right]^{1/3}$.

Studies existing in the literature on flow regimes identified in micro-packed bed reactors differs in the reactor design, the flow regime classification, and their agreement with the conventional Charpentier & Favier flow map. Whilst some authors reverted to the conventional terminology of "trickle" and "pulse" commonly used in conventional reactors [9;14], others have designated new classifications for the observed flow regimes [5]. It is important to note the differences between the designs of microchannel reactors and that of conventional packed bed reactors, which has direct implications on the flow pattern development. In a microchannel reactor, the gas and liquid are commonly introduced upstream of the packed bed via a T-junction configuration. The presence of a void space between the inlet and the packed bed region gives rise to the formation of a Taylor flow pattern, with alternating gas and liquid slugs traversing the packed bed. Faridkhou and Larachi [5] have identified this as an instability and therefore introduced the liquid directly into the packed bed section, to preclude the formation of liquid slugs and to imitate typical operation in conventional reactors. The transition from high interaction to low interaction was found to take place at L:G ratios three orders of magnitude smaller than Charpentier's, indicating that the differences in the flow regime transition are due to differences in the dominant forces within the packed bed, in addition to the gas-liquid introduction method. Conversely, Losey et al – who had a similar type of inlet design to the current study [9] – found a transition line between pulse and trickle which was 1-2 orders of magnitude lower than the Charpentier flow map. The similarity in microreactor designs between this study and that of Losey et al. (in terms of gas-liquid introduction method that results in a void upstream the packed bed) may have led to the similarity in the flow regime transition. Contrary to all other microreactor studies, Inoue et al [14] had flow maps which agreed very well with Charpentier's and attributed this to the gas flow stabilisation by a pressure drop mechanism (applying a high pressure drop on the gas side upstream the microreactor). The difference of the flow transition (between bubbly slug and annular flow regimes) obtained by Krishnamurthy and Peles [8] may be related to the nature of the bed which was a forest of isolated microfabricated posts. In addition, glass beads were used by Faridkhou et al. [5] whereas porous catalyst particles were used in the remaining studies, which may have contributed to the observed differences. Therefore, comparisons between hydrodynamic studies in micro-packed beds are difficult to make

given the differences in geometries of the gas/liquid inlet, as well as the type of packing used, which all play a role in the type of flow pattern that forms. Furthermore, at these reduced dimensions, effects of wall roughness, wettability and flow confinement become important [23].

In contrast to macro-scale reactors, natural pulsing was not observed. The origin of pulsing detected at low G:L ratios was induced by the slug flow upstream of the packed bed section. This lack of natural pulsing behaviour has been reported in previous hydrodynamic studies in micro-packed bed reactors [10] and is not surprising for a Reynolds number of the order of 1, where inertia-induced pulsing is unlikely. The usual mode of entry for gas and liquid phases in a conventional packed bed reactor is at the top of the column, where a liquid distributor is used to irrigate the bed evenly with the liquid phase. The forced pulsation is therefore usually achieved in conventional reactors by forced time varying liquid [24] or gas flow rates [25]. The spray regime commonly observed in conventional packed bed reactors was not observed in the micro-packed bed, and this is attributed to the dense packing and small interstitial voids, precluding the existence of liquid droplets between the catalyst particles. Instead, a predominantly gas phase regime exists in the micro-packed bed reactor.

6.4.4 Flow Pattern Dependence on Particle Size

Smaller particles have been found to initiate the high interaction regime at lower gas flowrates when studied in a micro-packed bed reactor [4]. Aside from flow regime transition, particle size has also been shown to affect hysteresis in micro-capillary reactors, where wetting pattern hysteresis was found to decrease with decreasing particle size. This is due to the bed texture being more prone to staying constantly wet rather than constantly dry for smaller particles, which stems from the stronger capillary forces in smaller particles [4]. In this study, no particular trend was observed between the different particle sizes in terms of initiating the onset of flow regime transition (**Figure 6.8**).

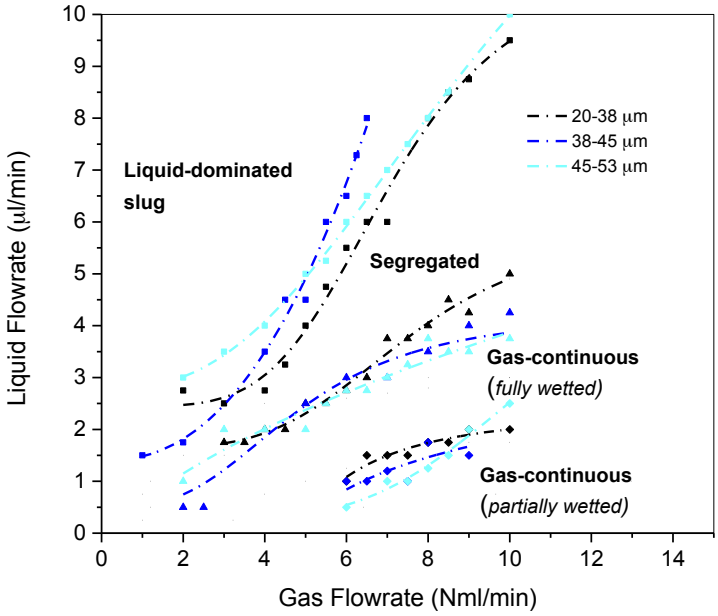

Figure 6.8 *Dependence of flow regime transition on particle size. Particles used are* MI_m *0.05wt% Au-0.95wt% Pd/*TiO_2*. Operating conditions: Temperature: 120°C, Pressure: 1 barg.*

6.5 Conclusion

In this chapter, the gas-liquid hydrodynamics in a packed bed microreactor have been investigated. Results show hydrodynamics that are different from what is commonly observed in conventional multiphase packed bed reactors. Five flow regimes were identified and termed liquid-dominated slug, segregated, gas-continuous (fully wetted), gas-continuous (partially wetted) and gas phase flow. There are similarities to the hydrodynamics in conventional packed bed reactors; for instance, the gas continuous flow regime observed in the microreactor is common among trickle bed reactors. However, there are also differences, such as the absence of natural pulsing (due to the lack of inertial forces) and spray (due to smaller size voids) flow regimes.

Thick liquid layers were observed at low gas and high liquid flowrates, which are anticipated to result in low gas-liquid interfacial areas and consequently poor gas-liquid mass transfer. The transition from liquid-dominated slug to gas-continuous flow deviates from the conventional Charpentier & Favier pulse to trickle transition by liquid-to-gas ratios one order of magnitude smaller. However, one has to be careful with

this comparison as the flow pattern establishment upstream the packed bed in the microreactor plays a significant role in the dynamics and flow regime in the packed bed section.

Particle size was found to have no significant effect on flow regime transition within the particle size range studied (20-53μm).

6.6 References

1. Ranade, V., Chaudhari, R., Gunjal, P. ***Trickle Bed Reactors: Reactor Engineering & Applications***. Oxford: Elsevier; 2011.

2. Kockmann, N. ***Transport Phenomena in Micro Process Engineering***. Berlin: Springer-Verlag; 2008.

3. Al-Rifai, N., Cao, E., Dua, V., Gavriilidis, A. **Microreaction technology aided catalytic process design**. *Current Opinion in Chemical Engineering* 2013, 2:338-345.

4. Faridkhou, A., Larachi, F. **Two-phase flow hydrodynamic study in micro-packed beds - Effect of bed geometry and particle size**. *Chemical Engineering and Processing: Process Intensification* 2014, 78:27-36.

5. Faridkhou, A., Larachi, F. **Hydrodynamics of Gas-Liquid Cocurrent Flows in Micropacked Beds - Wall Visualization Study**. *Industrial & Engineering Chemistry Research* 2012, 51:16495-16504.

6. Moulijn, J.A., Makkee, M., Berger, R.J. **Catalyst testing in multiphase micro-packed-bed reactors; criterion for radial mass transport**. *Catalysis Today* 2016, 259:354-359.

7. Faridkhou, A., Hamidipour, M., Larachi, F. **Hydrodynamics of gas-liquid micro-fixed beds - Measurement approaches and technical challenges**. *Chemical Engineering Journal* 2013, 223:425-435.

8. Krishnamurthy, S., Peles, Y. **Gas-liquid two-phase flow across a bank of micropillars**. *Physics of Fluids* 2007, 19:043302.

9. Losey, M.W., Schmidt, M.A., Jensen, K.F. **Microfabricated Multiphase Packed-Bed Reactors: Characterization of Mass Transfer and Reactions**. *Industrial & Engineering Chemistry Research* 2001, 40:2555-2562.

10. van Herk, D., Kreutzer, M.T., Makkee, M., Moulijn, J.A. **Scaling down trickle bed reactors**. *Catalysis Today* 2005, 106:227-232.

11. Iliuta, I., Hamidipour, M., Schweich, D., Larachi, F. **Two-phase flow in packed-bed microreactors: Experiments, model and simulations**. *Chemical Engineering Science* 2012, 73:299-313.

12. Marquez, M. **Hydrodynamics of multi-phase packed bed micro-reactors**. 2010. Thesis/Dissertation.

13. Delgado, J.M.P.Q. **A critical review of dispersion in packed beds**. *Heat and Mass Transfer* 2005, 42:279-310.

14. Inoue, T., Adachi, J., Ohtaki, K., Lu, M., Murakami, S., Sun, X., Wang, D.F. **Direct hydrogen peroxide synthesis using glass microfabricated reactor - Paralleled packed bed operation**. *Chemical Engineering Journal* 2014, In Press.

15. Charpentier, J.C., Favier, M. **Some liquid holdup experimental data in trickle-bed reactors for foaming and nonfoaming hydrocarbons**. *AIChE Journal* 1975, 21:1213-1218.

16. Kiwi-Minsker, L., Renken, A. **Microstructured reactors for catalytic reactions**. *Catalysis Today* 2005, 110:2-14.

17. Sicardi, S., Gerhard, M., Hoffman, M. **Influence of gas velocity and packing geometry on pulsing inception in trickle bed reactors.** *Chemical Engineering Journal* 1980, 20:251.

18. Blok, J.R., Varkevisser, J., Drinkenburg, A.M. **Transition to pulsing flow, holdup and pressure drop in packed columns with cocurrent gas-liquid downflow**. *Chemical Engineering Science* 1983, 38:687.

19. Becker, E.R., Pereira, C.J. ***Computer-Aided Design of Catalysts.*** New York: Marcel Dekker; 1993.

20. Alsolami, B.H., Berger, R.J., Makkee, M., Moulijn, J.A. **Catalyst Performance Testing in Multiphase Systems: Implications of Using Small Catalyst Particles in Hydrodesulfurization**. *Industrial & Engineering Chemistry Research* 2013, 52:9069-9085.

21. Mears, D.E. **The role of axial dispersion in trickle-flow laboratory reactors**. *Chemical Engineering Science* 1971, 26:1361-1366.

22. Burghardt, A., Zaleski, T. **Longitudinal dispersion at small and large Peclet numbers in chemical flow reactors**. *Chemical Engineering Science* 1968, 23:575-591.

23. Shao, N., Gavriilidis, A., Angeli, P. **Flow regimes for adiabatic gas-liquid flow in microchannels**. *Chemical Engineering Science* 2009, 64:2749-2761.

24. Boelhouwer, J.G., Piepers, H.W., Drinkenburg, A. **Liquid-induced pulsing flow in trickle-bed reactors**. *Chemical Engineering Science* 2002, 57:3387-3399.

25. Xiao, Q., Cheng, Z.M., Jiang, Z.X., Anter, A.M,, Yuan, W.K. **Hydrodynamic behavior of a trickle bed reactor under forced pulsing flow**. *Chemical Engineering Science* 2001, 56:1189-1195.

VII.

Hydrodynamic Effects on Three Phase Micro-Packed Bed Reactors

Part I: Effect of Flow Regime on Au-Pd Catalysed Benzyl Alcohol Oxidation Reaction Performance*

The hydrodynamic effects on gold-palladium catalysed benzyl alcohol oxidation were studied in a silicon-glass microstructured reactor. The catalyst used for this study was highly active Au-Pd supported on TiO_2 with an average particle size of 65 μm. Significant improvements in the conversion of benzyl alcohol and selectivity to benzaldehyde were observed with increasing gas-to-liquid ratios, coinciding with a change in the flow pattern from liquid-dominated slug to the gas-continuous flow regime. The observed enhancement is attributed to improved external mass transfer, associated with an increase in the gas-liquid interfacial area and reduction in the liquid film thickness.

*This chapter, in combination with Chapter VI, is in press in the Chemical Engineering Science Journal with the title: ***Hydrodynamic effects on three-phase micro-packed bed reactor performance – gold-palladium catalysed benzyl alcohol oxidation. doi:*** *doi:10.1016/j.ces.2016.03.018*

7.1 Introduction

Alcohol oxidation to aldehydes is an important process in organic chemistry due to the significance of the products as high value building block molecules for further manufacture into every-day consumer products. Developing clean and selective reactions is the latest paradigm in organic synthesis, underpinned by an effort to reduce the economic and environmental costs of chemical production. Catalytic methodologies are greener, low cost processes, replacing traditional metal oxides that are responsible for environmentally damaging wastes and poor atom efficiencies. However, the presence of both gaseous and liquid reactants results in added complexity to the transport of reactants from their respective phases to the catalytic active sites. The characteristic times for transport processes can range between 10 to 10^{-3}s [1] hence interference of these physical processes with reaction kinetics can limit the reaction performance significantly, affecting the observed activity and product selectivity.

Typically, reactants in the gaseous and liquid phases diffuse through the boundary layer and into the catalyst pores before reacting. Fast reactions in particular are often limited by mass transfer steps, and for partial oxidation reactions, the characteristic reaction time can be only a few milliseconds (the same order of magnitude as the physical processes), thus the reaction becomes highly dependent on parameters involving the diffusion behaviour between the gas and liquid phases, the size of the catalyst particle, the pore size diameter, physical properties of the fluids and flow conditions of the gas and liquid reactants [1].

Complex interactions between the flowing fluid phases and the stationary solid particles lead to differing flow patterns that depend on a number of factors: packing density, gas and liquid velocities, particle size, and physical properties of the fluid phases [2]. Identification of the flow characteristics is central to understanding reactor behaviour due to their direct impact on other transport processes, such as heat and mass transfer around the catalyst. The influence of flow regime on reaction performance has been the subject of various trickle bed reactor studies. It has been demonstrated that an enhancement in reactor performance is possible while operating under pulsing flow [3] as well as externally forced cyclic operation [4-7]. The enhancement in mass transfer under pulsing flow was attributed to the strong interaction between the phases within

the pulses as well as the periodic nature of the flow environment around the stationary catalyst. Most of these studies featured reactions where the gas-side mass transfer was not significantly influenced by the flow regime, owing to the assumption that the liquid phase is always saturated with gas (i.e. high gas solubility in the liquid phase). The influence of hydrodynamics on reaction performance therefore depends on which of the mass transfer steps governs the reaction rate.

In the solvent-free oxidation of benzyl alcohol on gold-palladium catalysts, the two main reaction pathways are (1) direct catalytic oxidation, yielding benzaldehyde exclusively and taking place in the presence of gaseous oxygen, and (2) disproportionation of two molecules of benzyl alcohol to give equal amounts of benzaldehyde and toluene [8;9] (**Figure 7.1**).

The parallel reaction scheme presents both conversion and selectivity issues; there is strong evidence to suggest that catalyst design (support and metal type) as well as reactor operating conditions (temperature and pressure) are crucial in determining the dominating reaction pathway [8;10]. The active site for the disproportionation is the Pd catalyst, thus using a monometallic Au catalyst has the ability to suppress the disproportionation reaction. However, pure Au catalysts do not have turnover rates as high as the bimetallic Au-Pd catalysts. The acidity/basicity of the support can also influence the dominating reaction pathway, with supports such as MgO and ZnO being the most effective at promoting the oxidation reaction path, giving a selectivity to benzaldehyde as high as 99% [11].

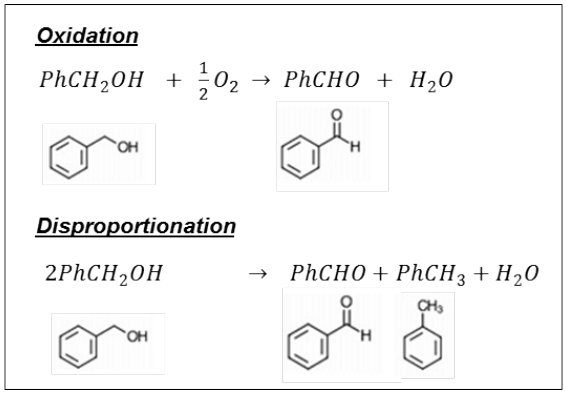

Figure 7.1 *Simplified benzyl alcohol oxidation reaction scheme.*

From a reaction engineering perspective, the global transformation rate can also be limited by transport phenomena, and the relative importance of these transport phenomena is dictated by the chemical reaction kinetics. As a result, it is possible that the reaction performance is diminished compared to the maximum performance attainable in the kinetic regime.

The turnover frequencies for the individual reactions: oxidation (TOF_O), disproportionation (TOF_D) and the overall reaction (TOF_T) can be quantified as was previously demonstrated by Sankar et al. [11]. Toluene is formed exclusively from disproportionation, and therefore, the amount of toluene formed can be used as a measure of the extent of the disproportionation reaction. According to the stoichiometry of the reaction, the number of moles of benzyl alcohol consumed in disproportionation is twice the number of moles of toluene formed,

$$2PhCH_2OH \rightarrow PhCHO + PhCH_3 + H_2O \qquad (7.1)$$

therefore, a disproportionation turnover frequency (TOF_D) can be quantified:

$$TOF_D = \frac{2 \cdot F_{PhCH_3}}{mol_{metal}} = \frac{2 \cdot F_{PhCH_2OH,0} \cdot X \cdot S_{PhCH_3}}{mol_{metal}} \qquad (7.2)$$

where F_{PhCH_3} is the molar flowrate of toluene produced (mol/s), $F_{PhCH_2OH,0}$ is the benzyl alcohol inlet molar flowrate (mol/s), X is the benzyl alcohol conversion, S_{PhCH_3} is the selectivity to toluene and mol_{metal} is the total metal moles used in the reaction. Since benzalehyde is formed from both reactions, the moles of benzaldehyde formed by disproportionation is equal to the number of moles of toluene formed. By subtraction, the moles of benzaldehyde formed by the oxidation reaction can then be calculated and converted to a turnover frequency using the following equation:

$$TOF_O = \frac{F_{PhCHO} - F_{PhCH_3}}{mol_{metal}} = \frac{F_{PhCH_2OH,0} \cdot X \cdot (S_{PhCHO} - S_{PhCH_3})}{mol_{metal}} \qquad (7.3)$$

where F_{PhCHO} represents the molar flowrate of benzaldehyde produced (mol/s) and S_{PhCHO} is the selectivity to benzaldehyde. The total turnover frequency represents the overall reaction and is calculated from the moles of benzyl alcohol consumed:

$$TOF_T = \frac{F_{PhCH_2OH,0} \cdot X}{mol_{metal}} \quad (7.4)$$

The purpose of this study is to assess the practical implications of the hydrodynamic changes (discussed in the previous chapter) on alcohol oxidations, by studying the hydrodynamic impact on the performance of Au-Pd/TiO_2 catalysed benzyl alcohol oxidation. We are interested in a higher benzaldehyde yield and will therefore be looking at the conversion and selectivity as performance indicators.

7.2 Materials & Methods

The $M_{Im,vary}$ 0.05 wt% Au - 0.95 wt% Pd/TiO_2 catalyst powder (see **section 5.3.1** for preparation procedure) was pelletised, crushed, and sieved to obtain the required sieve fraction (63-75 μm). Catalyst granules were loaded into the microreactor by applying a vacuum to the outlet port, with 1 mm and 3 mm length of glass beads 60-70 μm in particle size preceding and succeeding the catalytic bed respectively. The catalyst amount ranged between 1-4 mg (depending on the liquid flow rate) to keep the contact time constant in all experiments. Liquid alcohol (benzyl alcohol 99.98%, Sigma–Aldrich) was delivered into the reactor by a syringe pump (PhD Ultra, Harvard Apparatus) and oxygen (N5.5 grade, BOC) delivered and regulated by a mass flow controller (Brooks 5850TR, Brooks Instrument). The effluent from the reactor flowed into a 2 ml glass vial located in a cold trap (iced beaker), where gas and liquid were separated and the liquid product was collected for analysis. The reactor temperature was controlled at 120°C using a heating and temperature control unit (Watlow CAL 9900, Watlow Ltd) consisting of a ceramic packing containing thermocouples and heating cartridges. The pressure was regulated to 1 barg in all experiments using a backpressure regulator (SS BP Regulator, Swagelok).

Start-up procedures consisted of oxygen flow at reaction temperature for one hour, followed by introduction of the gas and liquid. Sampling was carried out every 30 minutes until stable operation was reached. Two to three samples were taken once steady state was reached and an average was taken of the duplicate or triplicate samples. When studying the effect of flow regimes, the gas flow rate was increased sequentially from low-to-high to avoid the interference of any hysteresis effects. Standard reaction runs (L=3 µl/min; G=0.6 Nml/min; 4 mg catalyst; 120°C; 1 barg) were carried out every 5-6 data points to ensure that the catalyst activity and selectivity did not change with time on stream.

Blank experiments were carried out where a typical reaction mixture (containing benzyl alcohol, benzaldehyde and toluene at a composition representative of 70% conversion) was fed into a microreactor filled with glass beads at reaction conditions (120°C and 1 barg) and the sample analysed at the exit. The condition chosen was a high G:L ratio at the low liquid flowrate (G:L=2000, L=0.75 µl/min) to ensure the absence of homogeneous reactions and that no loss of components into the gas phase was taking place at high G:L.

Operating conditions were selected such that variables other than the gas and liquid flowrates (such as the contact time) were controlled and kept constant, yielding an experiment that probes solely the effect of hydrodynamics on reaction performance. The contact time, defined as the mass of catalyst over the mass flowrate of alcohol, was kept constant at 76 $g_{cat} \cdot g_{alc}^{-1} \cdot s$ in the micro-packed bed reactor (MPBR). This was achieved by altering the mass of catalyst as the liquid flowrate was changed (i.e. the bed was re-packed for different liquid flow rates). The bed density was ~0.75 g/cm^3 and did not vary significantly with re-packing, as the channel depth was maintained at ~300µm (± 10µm) and the particles were from the same batch of sieved catalyst particles (~65µm ± 14µm). Standard reaction runs were performed once the reactor was re-packed to ensure repeatability.

7.2.1 Microreactor Designs

All silicon-glass microreactors used in this work were fabricated by photolithography and deep reactive ion etching and sealed via anodic bonding to glass, as described in **Appendix A**. Two reactor designs were investigated as discussed below.

Microreactor used to study effect of hydrodynamics on reaction performance, B1

The microreactor used for the bulk of this work is the serpentine microreactor presented in **section 5.3.3** (**Figure 5.5**) with a microchannel depth of 300 μm and a width of 600 μm. The catalyst particle size used was 65 μm on average, unless otherwise indicated.

Microreactor used to study effect of gas-liquid introduction method, B2

A microreactor with a different gas-liquid introduction structure was designed and required a different experimental setup (**Table 3.1** and **Figure 7.2**). A hotplate connected to a temperature controller (Watlow CAL 9900, Watlow Ltd) was used for this reactor to provide the temperature control to 120°C.

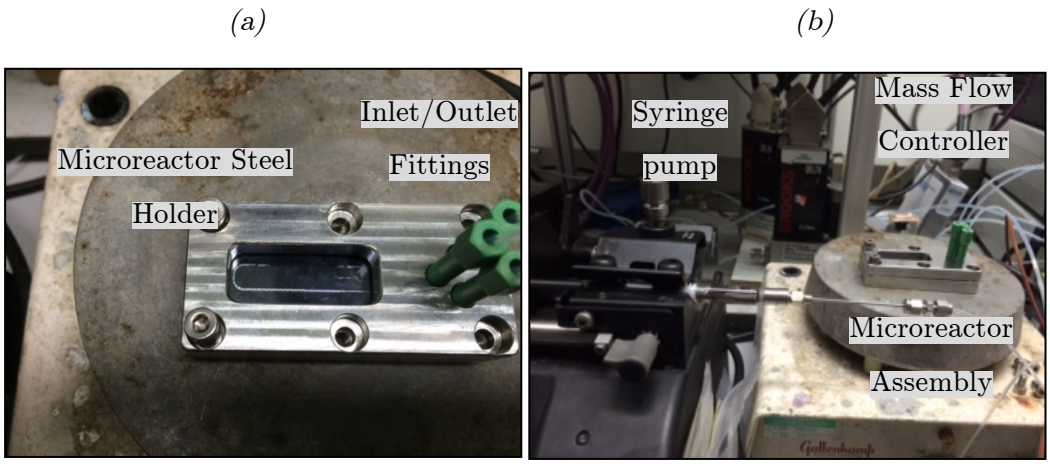

Figure 7.2 *(a) Microreactor assembly and (b) whole experimental setup for reactor design B2.*

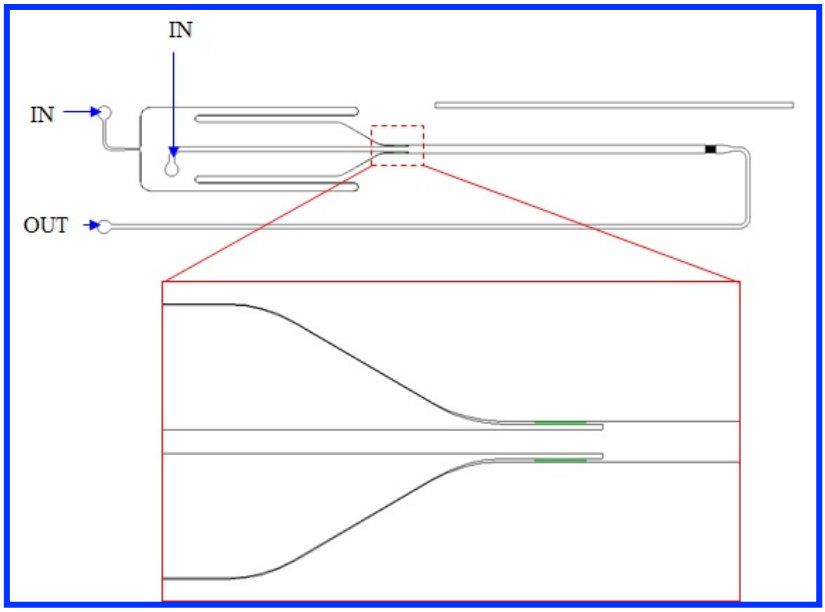

Figure 7.3 *Microchannel design B2 with a different gas-liquid inlet design to B1 serpentine channel reactor. The microreactor consists of two inlets and one outlet. The two inlets can be used for gas or liquid interchangeably.*

The microreactor B2 consists of a straight channel (where the reaction takes place), one inlet port that feeds directly into the main channel, and a second inlet port that branches out into two channels feeding into both sides of the main reaction channel (**Figure 7.3**). The microreactor assembly consisted of a steel holder with inlet/outlet ports positioned to one side of the reactor and a window to aid visualisation on the other side of the reactor (**Figure 7.2a**).

7.2.2 Reaction Analysis

Gas Chromatography

Quantitative analysis of the liquid phase reaction products was carried out on the liquid samples using a gas chromatograph (Agilent 6890) with an FID detector, a HP-INNOWax (19091- 133) capillary column and an auto-liquid-sampler. For GC analysis, 10 µL of the collected sample was diluted using 0.5 mL of 3% (v/v) butanol in o-xylene as an external standard (analytical details can be found in **Appendix B**).

Raman Spectroscopy

Raman measurements were carried out on the used catalyst following deactivation. This was done using a Renishaw inVia Raman spectrometer coupled to a Leica microscope as outlined in **Chapter V, section 5.3.2**.

7.2.3 Batch Glass Stirred Reactor§

Batch experiments were carried out in a Radleys carousel reactor using a 50 mL glass stirred reactor (GSR) agitated using a magnetic bar. In a typical reaction, the requisite amounts of catalyst (20 mg) and substrate (2 g) were charged into the reactor at room temperature. The reactor was then purged with the required gas (O_2) three times before the reactor was sealed using a Teflon screw threaded cap. The reactor was always connected to the gas-line to ensure the consumed gas was replenished. The pressure was monitored using the pressure gauge fitted in the inlet line.

The reaction started by commencing stirring inside the reactor at 1000 rpm. After 1 hr reaction time, the stirring was stopped and the reactor was immediately cooled in an ice bath. The reactor with the reaction mixture was loaded into a preheated heating block, which was maintained at the reaction temperature of 120°C and pressure of 1 barg. After cooling for 10 min, the reactor was opened slowly and the contents were centrifuged. An aliquot of the clear supernatant reaction mixture (0.5 ml) was then diluted with mesitylene (external standard, 0.5 ml) for GC analysis. It was also verified that no reaction occurred in the absence of the catalyst or in the presence of the catalyst support alone. This experimental method is identical to the standard reaction protocols for solvent-free benzyl alcohol oxidation reported elsewhere [25].

---

§ *Batch reactor experiments conducted by the Cardiff Catalysis Institute.*

Comparisons are made throughout the chapter to batch reactor experiments conducted at a contact time of 38 $g_{cat} \cdot g_{alc}^{-1} \cdot s$, where contact time in the glass stirred reactor is defined as the mass of catalyst multiplied by the reaction time over the initial mass of alcohol. Preliminary studies with the micropacked bed reactor showed that selectivity was not affected for contact time >5 $g_{cat} \cdot g_{alc}^{-1} \cdot s$ (**Figure 7.4**) and therefore the differences in the contact times between the two reactors can be ignored when making comparisons on selectivity.

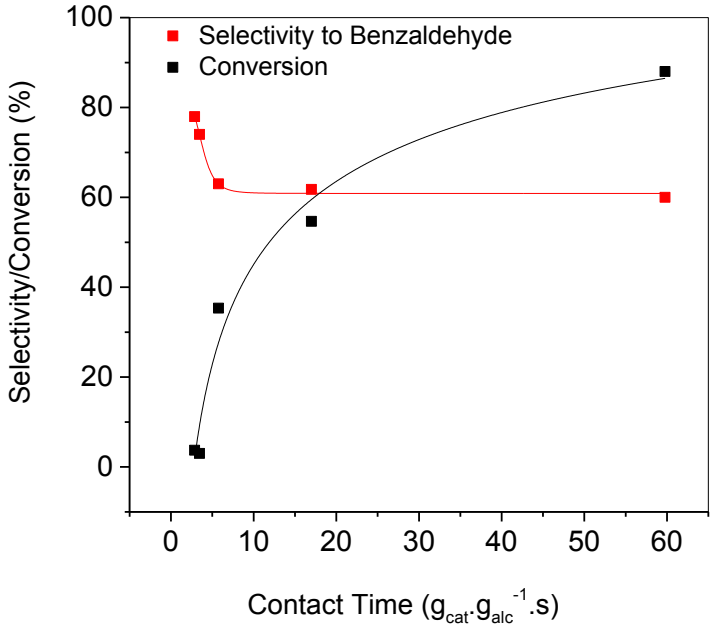

Figure 7.4 *Effect of contact time on benzyl alcohol conversion and selectivity to benzaldehyde. Liquid flow rate: 5 µl/min; G:L Ratio: 200; Temperature: 120°C; Pressure: 1 barg.*

7.3 Results & Discussion

7.3.1 Batch Reactor Performance

Reaction performance was first determined using a glass stirred reactor. The reaction products were predominantly benzaldehyde and toluene, with traces of benzoic acid and benzyl benzoate. Conversion in the glass stirred batch reactor at 1 hr reaction time was 75.6%, and selectivity to benzaldehyde and toluene were 73.9% and 23.6% respectively.

7.3.2 Micro-Packed Bed Reactor Performance

Blank Experiments

Results showed the mixture composition was unchanged during the blank experiment, indicating the absence of a homogeneous reaction and confirming no loss of components into the gas phase (**Table 7.1**).

Table 7.1 *Benzyl alcohol oxidation blank reaction experimental results.*

	Feed	**Exit**
Benzyl Alcohol Conversion (%)	88	86
Benzaldehyde Selectivity (%)	69	68
Toluene Selectivity (%)	20	21

Liquid-dominated slug and segregated flow

Figure 7.5a shows the change in reaction performance as the hydrodynamics change from liquid-dominated slug flow to segregated flow with increase of gas flowrate. The increase in conversion and selectivity with increasing gas flowrate is attributed to an enhancement in the external mass transfer, which comes as a result of the increase in the gas-liquid interfacial area and decrease in liquid film thickness. A high availability of oxygen at the active sites favours the oxidation reaction pathway (**Figure 7.1**), producing more benzaldehyde.

Figure 7.6 shows the dependence of TOF_O, TOF_D and TOF_T on gas superficial under the liquid-dominated slug/segregated flow regimes. The TOF_D decreases and the TOF_O increases as the gas superficial velocity is increased, indicating the enhancement of the desired oxidation reaction pathway, leading to an increase in the benzaldehyde selectivity. The overall turnover frequency, TOF_T, increases with gas superficial velocity, which conforms to the increase in conversion observed in **Figure 7.5**.

A high dependence of mass transfer on gas flowrate under pulse flow in a conventional trickle bed reactor (analogous to the liquid-dominated slug) has been demonstrated in

the past. The influence that gas flow rate has on the gas-liquid mass transfer rate has been attributed to an increase in the interaction between the gas and liquid phases as well as the spreading of liquid [2;12]. The underlying phenomena governing this relationship between gas flowrate and increase in the gas transfer to the solid, is a decrease in the characteristic length (film thickness) across which the gas has to travel – this results in a higher gas-liquid mass transfer coefficient, k_{GL}, according to the film theory of diffusion (k_{GL} is the mass transfer coefficient corresponding to the liquid side of the gas-liquid interface. As the gas phase is pure oxygen, it is plausible to assume no mass transfer resistances exist at the gas side of the gas-liquid interface). The observed increase in gas-liquid interfacial area, a_{GL}, also has an effect on the overall rate of mass transfer across the gas-liquid interface [13].

Evidence of increase in mass transfer with gas flow rate due to an enhancement in the liquid-solid mass transfer, k_{LS}, is not widespread [2] although an improvement in the liquid-solid mass transfer is possible with higher gas flow rate due to the larger linear velocities, as well as improvements in wetting and contacting between the packing and the flowing liquid [14;15]. For smaller packing (<0.5mm), liquid-solid mass transfer rates were found to be slightly higher in liquid beds without gas flow, and this was attributed to the fact that in a packed bed with smaller particles, the entire external area is not effective for mass transfer and this effect predominates over the effect of an increase in velocity [15].

Gas-continuous (fully wetted and partially wetted) flow

Figure 7.5b shows the reaction performance in the gas-continuous (fully wetted) and gas-continuous (partially wetted) flow regimes. Initially, no significant change in selectivity occurs and conversion plateaus with increasing gas flow rate. This indicates that the increase in gas flow rate – whilst operating in the gas-continuous flow regime – does not affect mass transfer significantly, as the liquid film is sufficiently sheared and any further increase in gas flow has only a small additional benefit.

Under partial wetting, the selectivity to benzaldehyde continues to increase and reaches values >90%, however, a dramatic decline in the conversion is observed (**Figure 7.5b**).

The packed bed reactor begins to outperform the batch reactor (in terms of selectivity) under this partially wetted state, where there is the added benefit of gas-solid mass transfer at exceptionally high gas-to-liquid ratios. Selectivity to benzaldehyde reaches 93%, but this comes at the cost of approx. 80% reduction in conversion.

At a gas-to-liquid flow rate ratio of 8000 (0.55 m/s gas superficial velocity, $u_{G,}$ in **Figure 7.5b**) approximately 90% of the benzyl alcohol at the reactor inlet evaporates to the gas phase. At this point, there is direct contact between the catalyst surface and the oxygen on the dry surface of the catalyst particle, already wetted internally due to capillary forces, resulting in the aforementioned increase in benzaldehyde selectivity to 93%. The drop in conversion is postulated to be due to poor utilisation of the catalyst particles caused by incomplete wetting (despite some liquid remaining due to capillary forces, maintaining some reactant conversion).

In the liquid-dominated slug flow regime, the combination of a liquid film that is incompletely saturated with oxygen and a rapid reaction, leads to a rate that is limited by the external supply rate of the gaseous reactant. In such a situation, the more effective supply route for the gaseous reactant is through the non-wetted surface, where there is no resistance to its mass transfer. However, at sufficiently high gas and low liquid flow rates (partially wetted state), the fraction of the surface wetted by the liquid is sufficiently low that the mass transfer of the liquid reactant becomes limiting. **Figure 7.5a** and **Figure 7.5b**, indicate that a maximum in the conversion exists at an intermediate level of wetting (the gas-continuous fully wetted flow regime). This maximum results from a competition between two different limiting regimes: at sufficiently low liquid coverage, the reaction is limited by the supply of the liquid reactant, whereas at higher liquid coverage it is gas-reactant-limited. Such behaviour has been observed previously by Funk et al. [16] in the hydrogenation of α-methylstyrene, as well as Hodoshima et al. [17] in the dehydrogenation of decalin.

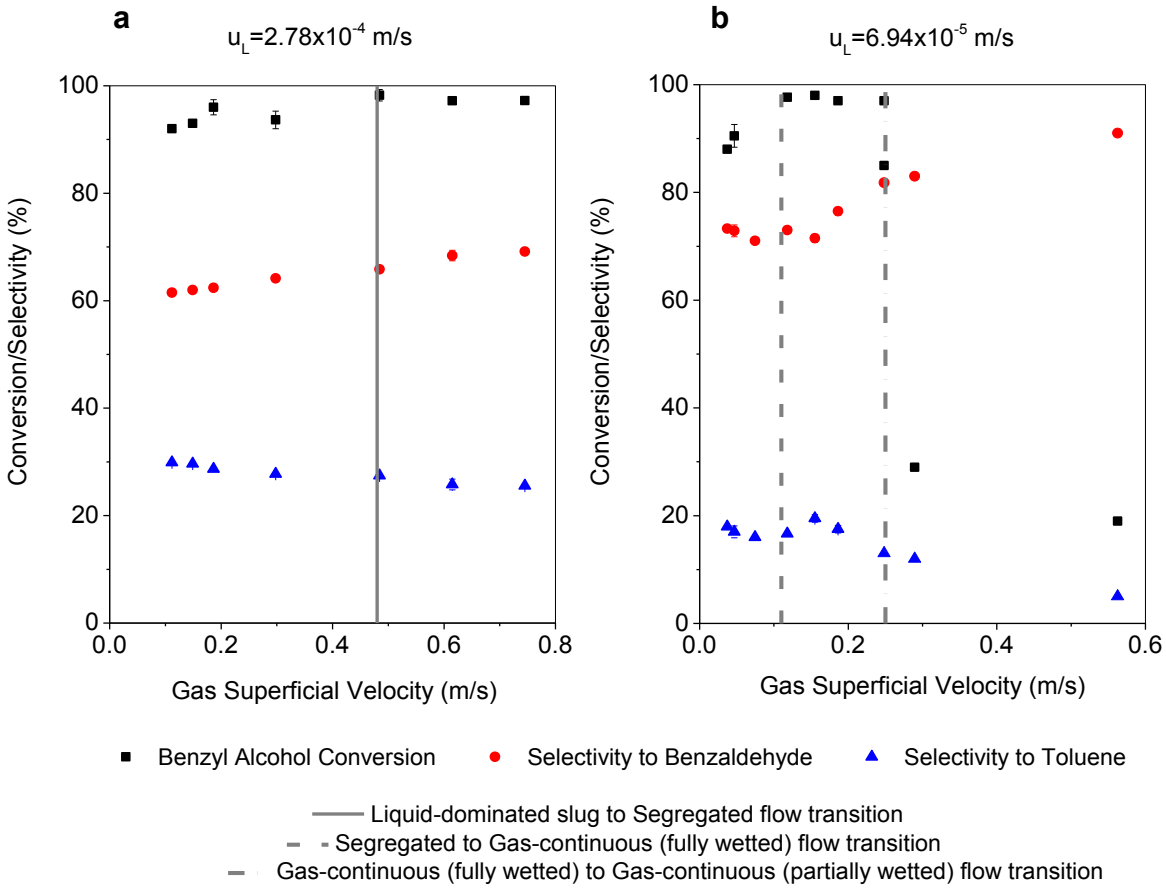

Figure 7.5 *Conversion of benzyl alcohol and selectivity to benzaldehyde and toluene at various flow regimes obtained by increasing gas flow rate: (a) Liquid-dominated slug transitioning into segregated flow regime at liquid flow rate 3 µl/min (b) Segregated transitioning into gas-continuous (fully wetted) and subsequently to gas-continuous (partially wetted) flow regime at liquid flow rate 0.75 µl/min.*

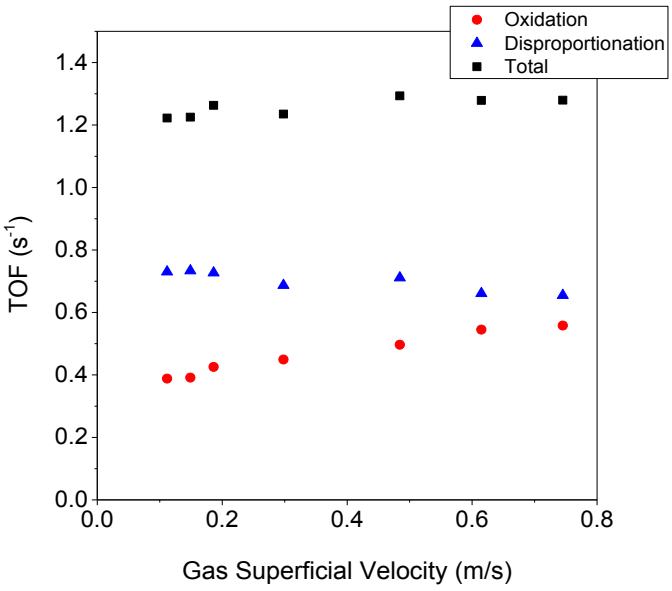

Figure 7.6 *Dependence of TOF_O, TOF_D and TOF_T on gas superficial velocity, corresponding to the data points in* ***Figure 7.5a****.*

The abruptness of the drop may be due to a critical phenomenon where a percolation threshold has been reached, and the links between the rivulets flowing along the packed bed are disconnected due to the increase in gas flow rate. This drop in conversion was difficult to reproduce quantitatively in repeated experiments (***Figure 7.7***). This was possibly because the liquid may be distributed differently within the packed bed each time a new reactor was loaded. Some evidence of deactivation was also observed in this partially wetted state, the degree of which was dependent on the gas flow rate and duration of operation, and was (in some cases) irreversible upon re-wetting of the catalytic bed. It is possible to increase the conversion by packing the microreactor with more catalyst and effectively increasing the contact time. Experiments were carried out with seven times more catalyst (7 mg), which resulted in an increase in conversion from 20% to 81%, while the selectivity was maintained at 92%. Such performance is superior to the batch glass stirred reactor in terms of both conversion and selectivity.

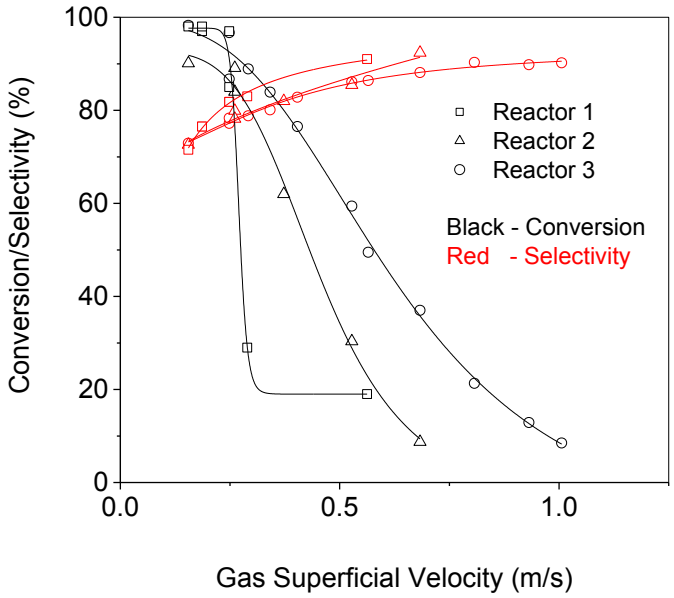

Figure 7.7 *Repeatability in the gas-continuous (partially wetted) flow regime using three different reactors, each re-packed with a new bed of catalyst. Liquid superficial velocity: 6.94E ×10^{-5} m/s, Catalyst mass: 1mg.*

With regards to existing studies in the literature investigating hydrodynamic effects on reaction, studies on periodic flow operation have shown that this type of operation is beneficial in gas-limiting reactions, where the direct access of the gaseous reactant to the solid surface improves the gas-to-catalyst mass transfer [2]. The reactor type can also influence the mass transfer, where structured packings (in the form of catalytically active membranes) have also been used as a solution to reactions with liquid phase transport resistance, by acting as a means of segregating the gas and liquid, thus providing direct access of the gas to the catalyst surface [18].

Studies comparing mass transfer coefficients in gas-liquid reactions between trickle bed reactors (TBR), hollow fibre membrane reactors (HFR) and stirred tank reactors (STR) have shown that the ranking of reactors, in terms of mass transfer, was HFR>TBR>STR. While the enhancement in the TBR is attributed to minimisation of the liquid resistance to mass transfer due to the thinner liquid film, the HFR outperformed both other reactors due to a large surface area-to-volume ratio and the absence of a liquid film (barrier to gas transfer) [19]. Operating a micro-packed bed

reactor (which has a large surface-area-to-volume ratio) in the gas-continuous flow regime (where there is minimal liquid phase resistance) therefore brings together the advantages of both the TBR and the HFR.

7.3.3 Relating Reaction Performance to the Flow Map

Further experiments were conducted to validate the proposed association between flow regime and reaction performance, as well as extend the operating window into the gas phase regime. A total of 42 experiments were used to generate a colour mapped dot plot of selectivity to benzaldehyde and benzyl alcohol conversion, superimposed on the flow regime map, shown in **Figure 7.8** and **Figure 7.9**. There is a clear relationship between selectivity and flow pattern shown in **Figure 7.8**. Improved distribution of liquid, a thinner liquid film and a larger gas-liquid interfacial area are obtained with increasing gas velocity, enhancing mass transfer and therefore the transfer of oxygen to the catalyst active sites, promoting the oxidation reaction that produces benzaldehyde exclusively. With partial drying of the catalyst particles, direct gas-solid mass transfer is promoted, which further enhances the overall oxidation reaction rate, increasing benzaldehyde selectivity.

The colour mapped dot plot for conversion (**Figure 7.9**) shows a slightly different pattern to that of the selectivity graph, where the aforementioned drop in conversion in the partially wetted flow and gas phase regimes is clear. It is worth noting that the observed variability in conversion at high gas flow rate (***Figure 7.7***) has an impact only for $u_G = 3420\ u_L$, where partial wetting begins to severely affect the conversion, however, it does not have an effect on the overall trends observed.

Figure 7.8 and **Figure 7.9** were plotted using results from all three reactors in ***Figure 7.7*** in addition to extra experiments.

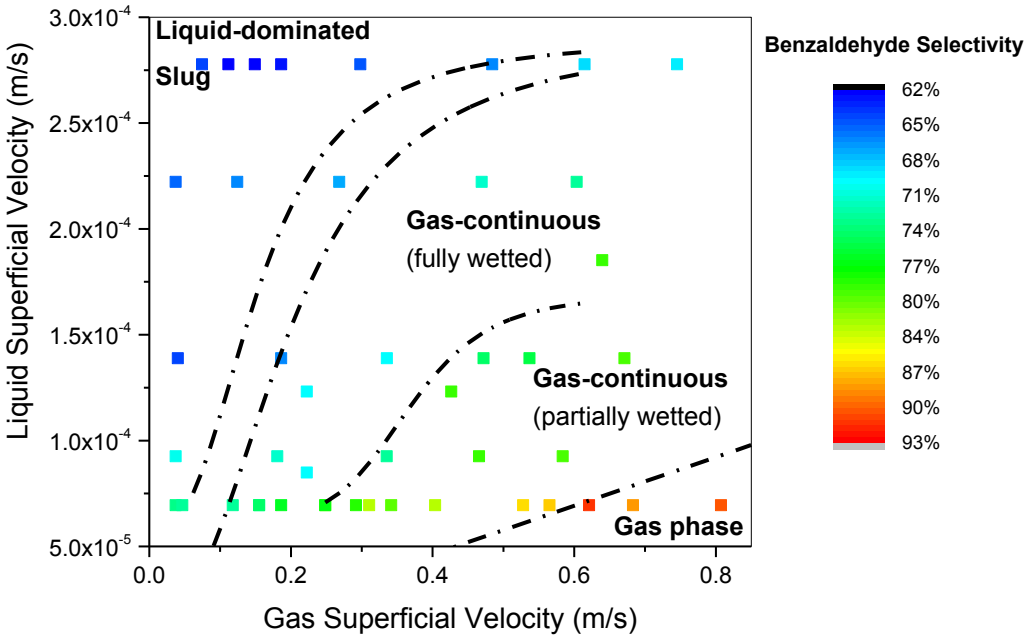

Figure 7.8 *Benzaldehyde selectivity colour-mapped dot plot superimposed on the flow regime map.*

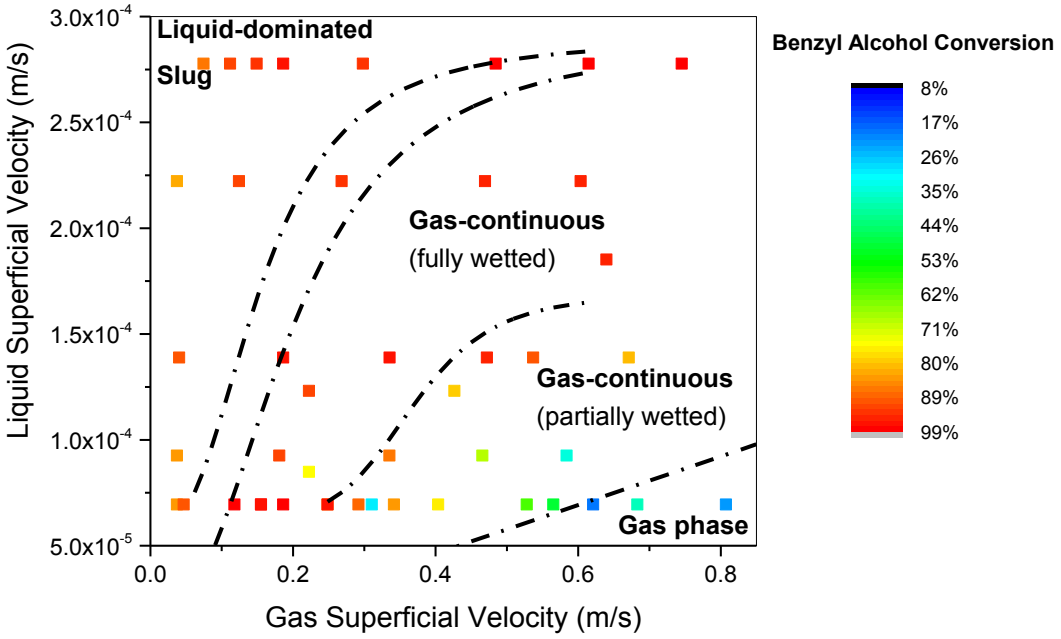

Figure 7.9 *Benzyl alcohol conversion colour-mapped dot plot superimposed on the flow regime map.*

7.3.4 Effect of Reactor Inlet Design on Reaction Performance

So far, the effect of hydrodynamics has been demonstrated using one single reactor design. The effect of microchannel reactor design on reaction performance remains to be explored. A newly fabricated reactor that introduces the liquid directly into the packed bed (precluding the formation of liquid slugs) was used (**Figure 7.3** - reactor B2). Results were compared to the original serpentine reactor design with a T-junction (**Figure 4.5** - reactor B1). The hydrodynamic impacts of the gas/liquid introduction method as well as the results of the reaction under the different configurations are presented. Two different configurations of operating reactor B2 were investigated:

1. liquid is introduced into the middle channel while the gas is introduced into the two outer channels;
2. liquid is introduced into the two outer channels, while the gas is introduced into the middle channel.

Microscopic visualisation of the hydrodynamics at the gas-liquid inlet with the two different configurations described above are shown in **Figure 7.10**. It is clear from the images that annular flow is generated in the immediate vicinity of the gas-liquid mixing area, regardless of the gas-liquid introduction configuration. **Table 6.2** shows results of the new reactor design with the two different configurations. A 17.5% increase in the conversion is noticeable with the B2 reactor in comparison with the B1 reactor. This result indicates that preventing pulsation in the gas-liquid zone prior to the catalytic bed (by introducing the liquid directly into the bed) is beneficial for the conversion of the benzyl alcohol and could be linked to the absence of liquid-rich slugs as a result of the different gas-liquid introduction method. The selectivity appears to be unaffected by the change in reactor design, suggesting that the performance enhancement mechanism is different to that brought about by changes in hydrodynamics shown in **section 7.3.2**.

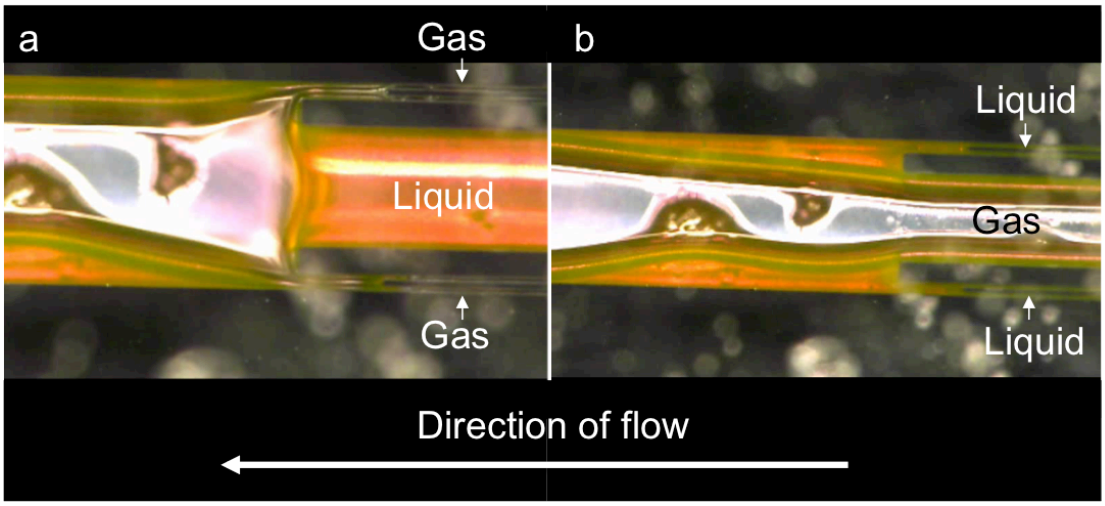

Figure 7.10 *Microscope image of B2 microreactor design showing the gas-liquid introduction section with (a) liquid in middle channel (b) liquid in thin outer channels. Gas flowrate: 0.6 Nml/min; Liquid flowrate: 3 µl/min; NTP (20° C, 1 bara).*

Table 7.2 *Reaction performance comparison between B1 and B2 reactor designs and two gas-liquid introduction configurations within the B2 reactor design. Gas flowrate: 0.8 Nml/min; Liquid flowrate: 3 µl/min; Pressure: 1 barg; Catalyst amount: 4 mg; Contact time: 76* $g_{cat}g_{alc}^{-1}s$.

Reactor Design	Inner Channel	Outer Channel	Conversion (%)	Selectivity (%)
B1	n/a	n/a	80	62
B2	Liquid	Gas	94	62
B2	Gas	Liquid	94	61

7.4 Conclusion

Hydrodynamic effects on benzyl alcohol oxidation in a packed bed microreactor have been investigated. Operating the micro-packed reactor in the gas-continuous flow regime benefits from a sufficiently wetted catalyst with a gas continuous flow path, maximising the gas-liquid interfacial area and minimising the liquid film thickness, thus enhancing the external mass transfer. In the benzyl alcohol oxidation, this enhanced mass transfer promotes the oxidation reaction pathway, improving benzaldehyde

selectivity and reactant conversion. Selectivity higher than a conventional batch reactor was observed when operating in the gas-continuous partially wetted flow regime, where it reached a maximum of 93%. The conversion dropped significantly under this partially wetted state, possibly due to inefficient catalyst utilisation. The conversion can be increased to 81% maintaining the 93% selectivity by operating at a higher contact time of 530 $g_{cat}.g_{alc}^{-1}.s$.

The hydrodynamic region leading to the best reaction performance (i.e. high conversion and selectivity) is located in the gas-continuous flow regime, where relatively high gas flow rates are used in conjunction with moderate liquid flow rates ensuring high gas-liquid mass transfer with a sufficiently wetted catalyst.

The effect of microreactor design on reaction performance was studied by changing the gas-liquid introduction method in a manner that does not generate liquid slugs upstream the packed bed. The results of this change in reactor design were higher benzyl alcohol conversion, possibly linked to the annular flow regime generated by the specially designed gas-liquid introduction method.

7.5 References

1. Hessel, V., Renken, A., Schouten, J., Yoshida, J. ***Micro Process Engineering: A comprehensive handbook***. Weinheim: Wiley-VCH; 2009.

2. Ranade, V., Chaudhari, R., Gunjal, P. ***Trickle Bed Reactors: Reactor Engineering & Applications***. Oxford: Elsevier; 2011.

3. Wilhite, B.A., Wu, R., Huang, X., McCready, M.J., Varma, A. **Enhancing performance of three-phase catalytic packed-bed reactors**. *AIChE Journal* 2001, 47:2548-2556.

4. Khadilkar, M.R., Al-Dahhan, M.H., Dudukovic, M.P. **Parametric study of unsteady-state flow modulation in trickle-bed reactors**. *Chemical Engineering Science* 1999, 54:2585-2595.

5. Lange, R., Gutsche, R., Hanika, J. **Forced periodic operation of a trickle-bed reactor**. *Chemical Engineering Science* 1999, 54:2569-2573.

6. Atta, A., Roy, S., Larachi, F., Nigam, K. **Cyclic operation of trickle bed reactors: A review**. *Chemical Engineering Science* 2014, 115:205-214.

7. Wilhite, B.A., Huang, X., McCready, M.J., Varma, A. **Effects of Induced Pulsing Flow on Trickle-Bed Reactor Performance**. *Industrial & Engineering Chemistry Research* 2003, 42:2139-2145.

8. Meenakshisundaram, S., Nowicka, E., Miedziak, P.J., Brett, G.L., Jenkins, R.L., Dimitratos, N., Taylor, S.H., Knight, D.W., Bethell, D., Hutchings, G.J. **Oxidation of alcohols using supported gold and gold-palladium nanoparticles**. *Faraday Discussions* 2010, 145:341-356.

9. Enache, D.I., Edwards, J.K., Landon, P., Solsona-Espriu, B., Carley, A.F., Herzing, A.A., Watanabe, M., Kiely, C.J., Knight, D.W., Hutchings, G.J. **Solvent-free oxidation of primary alcohols to aldehydes using Au-Pd/TiO_2 catalyst**. *Science* 2006, 311:362-365.

10. Cao, E., Sankar, M., Nowicka, E., He, Q., Morad, M., Miedziak, P.J., Taylor, S.H., Knight, D.W., Bethell, D., Kiely, C.J., Gavriilidis, A., Hutchings, G.J. **Selective suppression of disproportionation reaction in solvent-less benzyl alcohol oxidation catalysed by supported Au-Pd nanoparticles**. *Catalysis Today* 2013, 203:146-152.

11. Sankar, M., Nowicka, E., Tiruvalam, R., He, Q., Taylor, S.H., Kiely, C.J., Bethell, D., Knight, D.W., Hutchings, G.J. **Controlling the Duality of the Mechanism in Liquid-Phase Oxidation of Benzyl Alcohol Catalysed by Supported Au-Pd Nanoparticles**. *Chemistry - A European Journal* 2011, 17:6524-6532.

12. Hirose, T., Toda, M., Sato, Y. **Liquid phase mass transfer in packed bed reactor with cocurrent gas-liquid downflow**. *Journal of Chemical Engineering of Japan* 1974, 7:187-192.

13. Doraiswamy, L.K. ***Organic Synthesis Engineering***. New York: Oxford University Press; 2001.

14. Hirose, T., Mori, Y., Sato, Y. **Liquid-to-particle mass transfer in fixed bed reactor with cocurrent gas-liquid downflow**. *Journal of Chemical Engineering of Japan* 1976, 9:220-225.

15. Goto, S., Smith, J.M. **Trickle-bed reactor performance. Part I. Holdup and mass transfer effects**. *AIChE Journal* 1975, 21:706-713.

16. Funk, G.A., Harold, M.P., Ng, K.M. **Experimental study of reaction in a partially wetted catalytic pellet**. *AIChE Journal* 1991, 37:202-214.

17. Hodoshima, S., Arai, H., Takaiwa, S., Saito, Y. **Catalytic decalin dehydrogenation/naphthalene hydrogenation pair as a hydrogen source for fuel-cell vehicle**. *International Journal of Hydrogen Energy* 2003, 28:1255-1262.

18. Yang, M-C., Cussler, E.L. **A hollow-fiber trickle bed reactor**. *AIChE Journal* 1987, 33:1754.

19. Orgill, J.J., Atiyeh, H.K., Devarapalli, M., Phillips, J.R., Lewis, R.S,, Huhnke, R.L. **A comparison of mass transfer coefficients between trickle-bed, hollow fiber membrane and stirred tank reactors**. *Bioresource Technology* 2013, 133:340-346.

VIII.

Hydrodynamic Effects on Three Phase Micro-Packed Bed Reactors

Part II: Effect of Flow Regime on Mass Transfer and Catalyst Deactivation

---

In this chapter, the mass transfer characteristics of the three-phase micro-packed bed reactor used in the Au-Pd catalysed benzyl alcohol oxidation presented in **Chapter VII** are studied. Differential reactor mass transfer experiments are used to obtain information on the rate-limiting mass transfer step and to qualitatively elucidate the gas-liquid mass transfer coefficient in the liquid-dominated flow regime. COMSOL mass transfer simulations confirmed that liquid film thickness has an impact on the oxygen concentration at the catalyst surface, which in turn influences the oxidation reaction rate and product distribution. Au-Pd catalyst stability was significantly affected by the hydrodynamics, with evidence of deposition of by-products at high G:L ratios.

8.1 Introduction

Gas-liquid multiphase reactions require the reacting gas to be efficiently transferred to the liquid phase, followed by its diffusion to the catalyst (**Figure 8.1**). These mass transfer processes depend on many factors including the hydrodynamics, temperature, catalyst activity, physical properties of the gas and liquid and solubility of the gas in the liquid phase. Two types of mass transfer need to be considered in fluid-solid reactions, external and internal mass transfer. Both types of mass transfer have the potential to limit the performance of the reactor and influence the product selectivity.

In order to characterise mass transfer characteristics of three-phase reactors, mass transfer coefficients are commonly investigated in non-reactive systems [1]. However, concentration profiles in the liquid film are strongly influenced by the presence of a fast chemical reaction and therefore, the results from these analyses can be misleading. Experimental methods for delineating mass transfer coefficients during reaction have also been demonstrated [2-4]. The experiments aim to obtain information on the behaviour of the reaction system in response to changes in process conditions, such as catalyst weight and particle size.

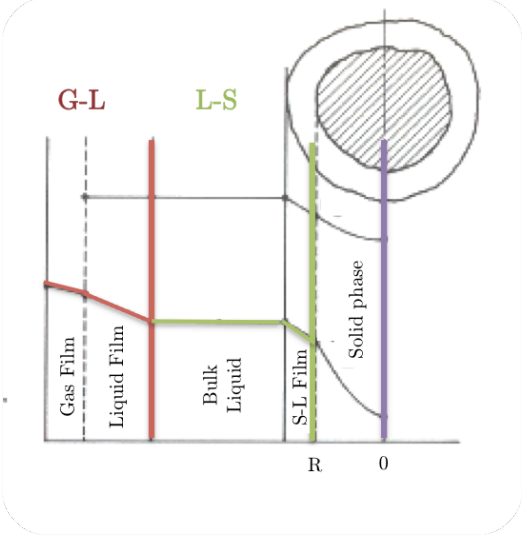

Figure 8.1 *Mass transfer steps in a three-phase reaction catalysed by a solid. Adapted from [3].*

The results of a study in which external diffusion effects are important were presented in **Chapter VII**. It has been shown that hydrodynamics affects the conversion and selectivity for the Au-Pd catalysed benzyl alcohol oxidation reaction, with significant enhancements at higher G:L ratios. In this chapter, the external and internal mass transfer for this reaction system will be characterised using experimental and theoretical methods. Modelling and experimental approaches will be used in an attempt to delineate the mechanism of mass transfer enhancement and qualitatively determine the magnitude of mass transfer coefficients, where possible.

8.2 Materials & Methods

8.2.1 External Mass Transfer Analysis

COMSOL Modelling of External Mass Transfer – Model Description

The COMSOL Multiphysics (version 5.0) Chemical Reaction Engineering module was used to model the evolution of the chemical reaction along the catalytic bed. For simplification purposes, the reaction was modelled in 2D on a flat catalyst surface. The geometry modelled is shown in **Figure 8.2** and is a simplified representation of the real system, consisting of a flat catalyst surface, a liquid film, and a gas film. The dimensions of the domain modelled are chosen to relate to the real system as much as possible (i.e. in terms of the liquid film thickness).

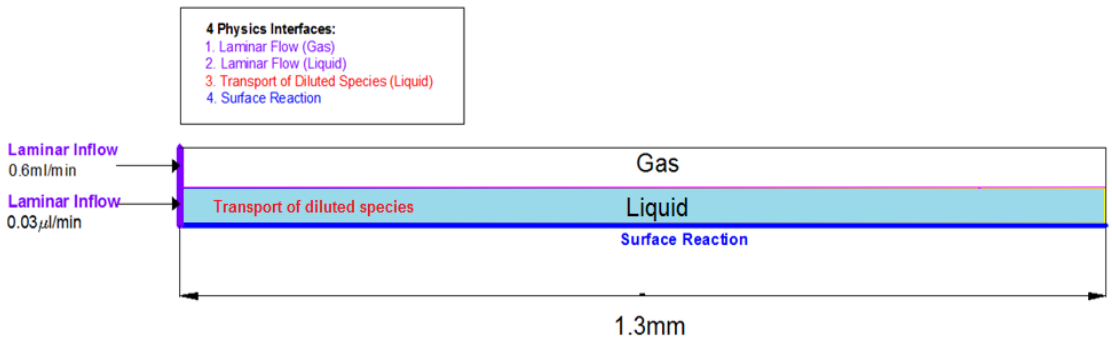

Figure 8.2 *Schematic of geometry used in COMSOL simulation of mass transfer.*

The kinetic rate expressions used are based on a previous study [5] where the heterogeneous reaction rates as a function of the species concentrations are shown in **Table 8.1.** These chemical source terms were coupled with a laminar fluid flow

COMSOL module to compute the velocity and pressure fields for the flow of each phase. The equations solved by the laminar flow module are the Navier-Stokes equations for conservation of momentum and the continuity equation for conservation of mass. A transport of diluted species interface within COMSOL was used to compute the concentration fields, assuming chemical species transport through diffusion and convection by implementing the mass balance equation:

$$\frac{\partial c}{\partial t} + \boldsymbol{u}\,\nabla \cdot c = \nabla \cdot (D\nabla c) + R \qquad (8.1)$$

Where c is the concentration of the species (mol/m^3), D denotes the diffusion coefficient (m^2/s), R is a reaction rate expression for the species (mol/(m^{3}s)) and $\boldsymbol{u}$ is the velocity vector (m/s). The first term on the left hand side of the mass balance, $\frac{\partial c}{\partial t}$, corresponds to the change in concentration of the species with time. At steady-state, this value is zero and the mass balance becomes:

$$0 = -\boldsymbol{u}\,\nabla \cdot c + \nabla \cdot (D\nabla c) + R \qquad (8.2)$$

Table 8.1 *Benzyl alcohol oxidation on Au-Pd reaction rate expressions [5].*

Reaction	Rate Expression
$PhCH_2OH + \frac{1}{2}O_2 \rightarrow PhCHO + H_2O$	$r_o = \frac{[PhCH_2OH]}{K_D^B + [PhCH_2OH]} \times \frac{k_{1x}\,.\,[O_2]}{K_D^O + [O_2]}$
$2PhCH_2OH \rightarrow PhCHO + PhCH_3 + H_2O$	$r_d = k_{2x} \times \frac{[PhCH_2OH]}{K_D^B + [PhCH_2OH]}$

The $\boldsymbol{u}\,\nabla \cdot c$ term accounts for the convective transport due to a velocity field $\boldsymbol{u}$; this field was coupled with a laminar fluid flow COMSOL physics interface. The term $\nabla \cdot (D\nabla c)$ describes the diffusion transport, accounting for interaction between the dilute species (oxygen) and the solvent (benzyl alcohol). R represents the chemical reaction. In order for the chemical reaction to be specified, a COMSOL reaction node was used where the reaction rate expressions from **Table 8.1** were specified. At the

gas-liquid interface, a concentration boundary condition for the oxygen concentration was used (7.91 mol/m^3) which is the equilibrium concentration of dissolved oxygen at the gas-liquid interface*. **Table 8.2** summarises the parameters inputted into the COMSOL simulation. The kinetic rate constants were estimated from [5] and the procedure for their derivation is shown in **Appendix B**.

Table 8.2 *Summary of input data to COMSOL simulation of mass transfer.*

PARAMETER	VALUE	DESCRIPTION
k_{1x}	6.05×10^{-6} [mol/s]	Oxidation reaction rate constant
k_{2x}	5.82×10^{-5} [mol/s]	Disproportionation reaction rate constant
K_D^B	3.8 [mol/kg]	Benzyl alcohol dissociation constant
K_D^O	0.01031 [mol/kg]	Oxygen dissociation constant
S_c	0.48 [kg/m^2]	Inverse of catalyst specific surface area
v_{in,O_2}	0.6[ml/min]	Oxygen inlet volumetric flow rate
$v_{in,BzOH}$	3×10^{-8} [ml/min]	Benzyl alcohol inlet volumetric flow rate
$[O_2]$*	7.91 [mol/m^3]	Equilibrium concentration of oxygen in liquid phase

Table 8.3 *Reaction rate expressions used in COMSOL simulation of mass transfer.*

VARIABLE	VALUE	DESCRIPTION
r_o	$S_c \frac{[PhCH_2OH]}{K_D^B+[PhCH_2OH]} \frac{k_{1x}.[O_2]}{K_D^O+[O_2]}$ $[mol/m^2s]$ †	Rate of oxidation reaction
r_d	$S_c\, k_{2x} \frac{[PhCH_2OH]}{K_D^B+[PhCH_2OH]}$ $[mol/m^2s]$ †	Rate of disproportionation reaction

† *To express the reaction rates r_o and r_d in terms of mol/m^{2}s (required by COMSOL to simulate the surface reaction) an inverse catalyst specific surface area, S, of 0.48kg/m^2 was assumed.*

* *The equilibrium concentration of oxygen in benzyl alcohol was calculated using a Henry's constant of 2240 bar (unpublished work).*

Table 8.4 *Boundary conditions used in COMSOL simulation of mass transfer.*

BOUNDARY	BOUNDARY CONDITION	VALUE/EQUATION
1	Inflow	v_{in,O_2}
2	Inflow	$v_{in,BzOH}$
3	Pressure	0 Pa (gauge)
4	Pressure	0 Pa (gauge)
5	Wall (no-slip)	u=0
6	Concentration, slip	$[O_2]^*$
7	Wall (no slip)	u=0

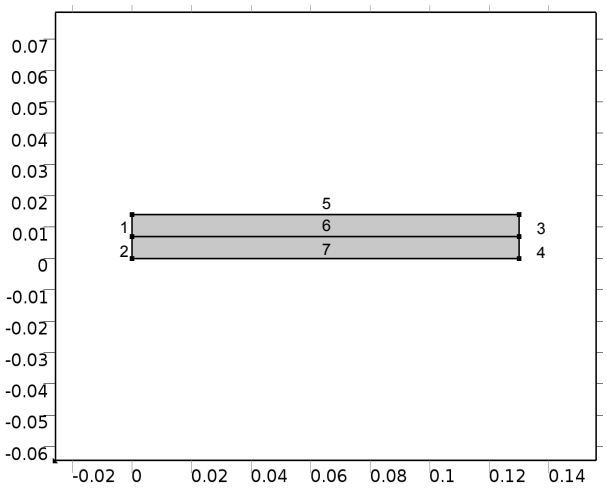

Figure 8.3 *Schematic of geometry used in COMSOL with numbered boundaries*

Experimental Mass Transfer Analysis

The system under study involves mass transfer across the gas and liquid films, followed by a catalytic reaction on the surface of the catalyst. For the gaseous reactant, three external mass transfer steps can be identified; across the gas and liquid films at the gas-liquid interface, followed by transfer across the liquid-solid film (**Figure 8.1**). Mass transfer across the gaseous film δ_G can be neglected, as pure oxygen is used. As none of the experiments presented in the following section were conducted in the partially wetted flow regime, direct-gas solid mass transfer can also be neglected.

Considering a first order reaction, the total resistance to reaction can be expressed as the sum of the gas-liquid and liquid-solid mass transfer resistances to give [3]:

$$\frac{[O_2]^*}{R_O} = \frac{1}{k_{GL,A}a_{GL}} + \frac{1}{k_{SL,A}a_p} + \frac{1}{k_{w1}\eta w} \tag{8.3}$$

where $[O_2]^*$ is the equilibrium concentration of the gas in the liquid, R_O is the weight-based oxidation reaction rate, $k_{GL,A}$ is the gas-liquid mass transfer coefficient, a_{GL} is the gas-liquid interfacial area, $k_{SL,A}$ is the liquid-solid mass transfer coefficient, a_p is the particle specific surface area, k_{w1} is the kinetic rate constant, η is the catalyst effectiveness factor and w is the catalyst weight per unit volume. Assuming spherical catalyst particles, the interfacial area a_p can be expressed as:

$$a_p = \frac{6w}{\rho_c d_p} \tag{8.4}$$

where ρ_c is the catalyst bulk density and d_p is the catalyst particle diameter. Substituting this in equation 8.3 gives:

$$\frac{[O_2]^*}{R_O} = \frac{1}{k_{GL,A}a_{GL}} + \frac{\rho_c d_p}{6w}\left(\frac{1}{k_{SL,A}} + \frac{6}{\eta\rho_c d_p k_{w1}}\right) \tag{8.5}$$

Conventionally in a slurry reactor, the experiment is carried out by increasing the catalyst weight per unit volume, w, while the volume is fixed by the amount of liquid in the reactor. Thus, a plot of $\frac{[O_2]^*}{R_O}$ versus $\frac{1}{w}$ gives a straight line with a slope proportional to $k_{SL,A}$ and k_{w1} and an intercept equal to the reciprocal of $k_{GL,A}a_{GL}$. Herein, we introduce a method enabling the use of this analysis in a packed bed flow reactor. Accordingly, a diluted bed is employed, where the total volume of the packed bed is kept constant using inert support particles while the catalyst mass is increased

between 0.45 mg and 1.4 mg in order to achieve different catalyst weight per unit volume w in the reactor (**Figure 8.4**). The catalyst used in this study is a 5% Pd/TiO_2, a catalyst with high activity.

Experiments were conducted in the B1 reactor, varying the catalyst mass, while keeping all other parameters constant (gas flowrate: 0.8 Nml/min liquid flowrate: 20 µl/min; catalyst: 5%Pd/TiO_2, 0.45 mg – 1.4 mg, 53-63 µm; diluent: TiO_2 support 53-63 µm; total reactor volume: 1.62 mm^3). This resulted in operation under the liquid-dominated flow regime. The study was undertaken in a differential reactor mode, keeping the conversion of benzyl alcohol less than 25% to be able to use the reaction rates observed experimentally without integration.

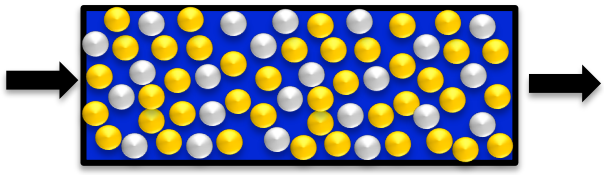

Figure 8.4 *Schematic of diluted micro-packed bed reactor used in benzyl alcohol oxidation external mass transfer studies.*

8.2.2 Internal Mass Transfer Analysis

In this section, the Weisz-Prater criterion for internal mass transfer is first assessed, followed by an experimental investigation under different hydrodynamic flow regimes with varying particle size.

Theoretical Assessment of Particle Size on Reaction Performance using the Weisz-Prater Criterion

Compared with dimensions of a typical laboratory trickle bed reactor, the catalyst particles used here represent a 100-fold increase in the surface-to-volume ratio, which is anticipated to result in higher interfacial areas and enhanced internal mass transfer.

The intent of this exercise is to assess the effect of internal pore resistance to oxygen on the reaction performance, by examination of the Weisz-Prater criterion:

$$N_{W-P} = \frac{R_{v,i}^{obs} R_P^2}{C_A D_{eff}} \qquad (8.6)$$

The most important factors affecting the outcome of this evaluation are the effective diffusivity of the solute in the catalyst pores, D_{eff}; the rate of reaction, $R_{v,i}^{obs}$; the catalyst particle size, R_P , and the concentration of the solute at the catalyst surface, C_A. The Weisz-Prater (N_{W-P}) criterion for negligible pore resistance, for a first order reaction is $N_{W-P} \leq 0.3$. When the centre of the particle is starved of reactant, $N_{W-P} > 4$ [3].

Experimental Assessment of Particle Size on Reaction Performance

An experiment was conducted where particles of different diameters were tested for performance. The particle size was varied between 15-65 μm under both the liquid-dominated slug flow and the gas-continuous (fully wetted) flow regime. The temperature and pressure were maintained at 120°C and 1 barg in all experiments.

Experiments with either 1 mg or 4 mg amount of catalyst were used, keeping the contact time constant at 76 $g_{cat}g_{alc}^{-1}s$ by altering the liquid flow rate (0.75 μl/min and 3 μl/min for 1 mg and 4 mg respectively). The gas flowrate was selected such that the flow regime was liquid-dominated slug flow (0.6 Nml/min G at 3 μl/min L and 4 mg catalyst) and gas-continuous fully wetted flow (2 Nml/min G at 0.75 μl/min L and 1 mg catalyst). The catalyst used was the M_{Im} 0.05 wt% Au – 0.95 wt% Pd/TiO_2 (catalyst preparation procedure detailed in **section 5.3.1** and **Appendix B**).

8.3 Results & Discussion

8.3.1 External Mass Transfer Analysis using COMSOL Simulation

Effect of Liquid Film Thickness on Oxygen Concentration Profile

The effect of liquid film thickness on the oxygen concentration profile was assessed by varying the depth of the liquid film between 0.1-10μm while keeping the gaseous domain unchanged. The velocity profiles for the gas and liquid domains are shown in **Figure 8.5**.

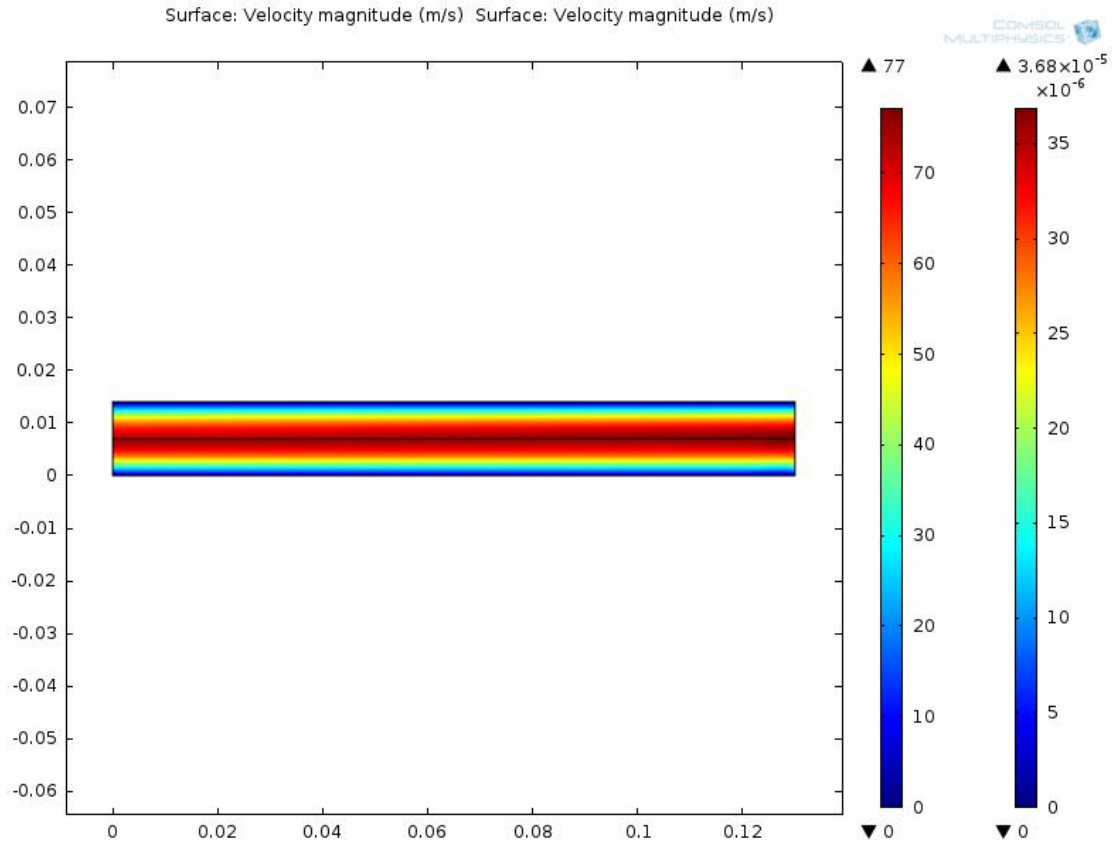

Figure 8.5 *Velocity profiles for the gas and liquid domains simulated using COMSOL.*

Figure 8.6 shows the variation in the oxygen concentration across the liquid film for two film thicknesses. This was implemented in COMSOL by manually adjusting the liquid domain thickness and re-running the simulation. An oxygen concentration gradient across the liquid film is observed due to the low solubility of oxygen in the

benzyl alcohol and the high reaction rate. The resulting concentration of oxygen near the catalyst surface is very low in the 7 μm film (~1.5 mol/m^3) in comparison to the thinner film of 2.5 μm where the oxygen concentration is almost double (~3 mol/m^3). This effect has implications on the conversion and selectivity as will be demonstrated next.

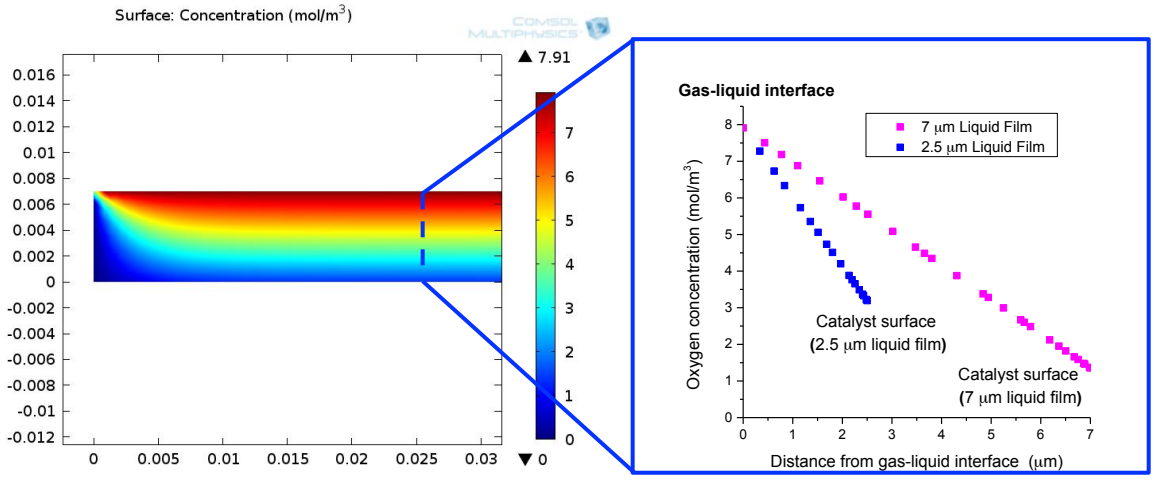

Figure 8.6 *COMSOL simulation results of external mass transfer (a) 2D surface map of oxygen concentration gradient across the liquid film (b) oxygen concentration gradient with radial distance from the catalyst at an axial location of 0.025 mm from the entrance, for two liquid film thicknesses: 2.5 μm and 7 μm.*

Effect of Liquid Film Thickness on Conversion & Selectivity

Figure 8.7 shows the simulated conversion and selectivity with decreasing film thickness. To account for the velocity profile across the channel, the concentrations at the outlet were calculated based on the "cup mixed" concentration. According to the two-film theory of diffusion, two resistances to gas transport in a three-phase reactor exist: diffusion of the gas from the bulk gas to the interface and diffusion of gas from the interface to the bulk liquid. The gas (k_G) and liquid (k_L) side mass transfer coefficients depend inversely on the gas and liquid film thickness, where $k_G = \frac{D}{\delta_G}$ and

$k_L = \frac{D}{\delta_L}$ [6]. Since pure oxygen is used, then no concentration gradients will be present in the gas phase, and thus δ_G will not be limiting. On the other hand δ_L is expected to have a significant impact on the overall gas-liquid mass transfer rate, due to the low solubility of oxygen in benzyl alcohol. As shown in **Figure 8.7**, reduction in the liquid film thickness resulted in higher conversion and selectivity to benzaldehyde. This is in qualitative agreement with the experimental data and implies that the improvement in the interphase mass transfer is due to a reduction in the liquid film thickness.

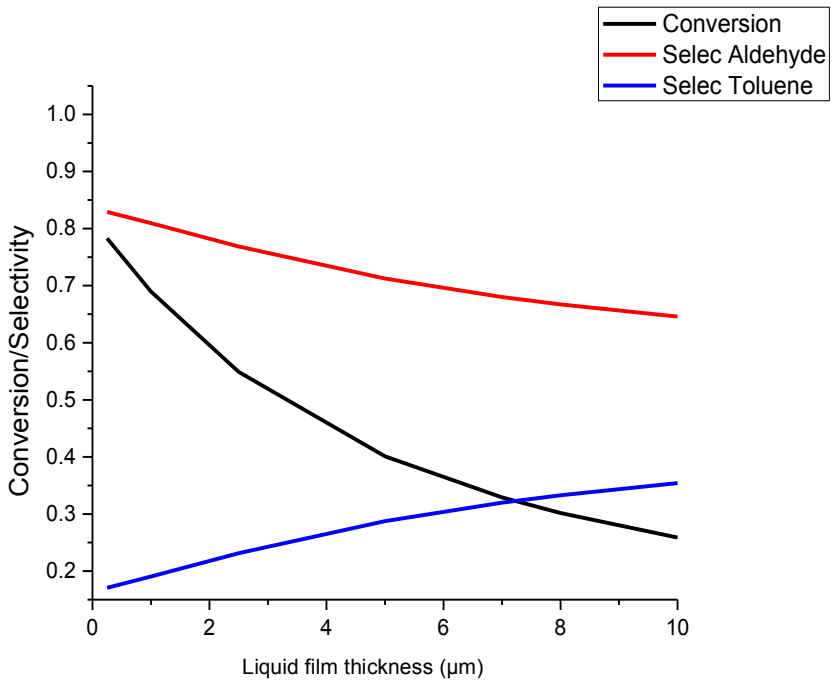

Figure 8.7 *Benzyl alcohol fractional conversion and selectivity (for the reaction system in* ***Figure 8.2****) as a function of liquid film thickness obtained by COMSOL simulation.*

8.3.2 External Mass Transfer Analysis using Experiments

Results of the experimental external mass transfer analysis are reported in ***Figure 8.8*** which shows the variation in inverse catalyst weight per unit volume with inverse oxidation reaction rate. The experiment resulted in a graph with a finite slope, indicating the presence of some gas-liquid resistance. From the intercept of the graph, it is possible to obtain the gas-liquid mass transfer coefficient, $k_{GL,A}a_{GL} = 23.6\ s^{-1}$. Due

to the spread in the experimental data points, the error of the intercept is quite large (intercept = 0.04244; standard error = 0.03995 shown in **Table 8.5** and confidence bands shown in **Figure 8.9**). Disregarding the experimental data point at $\frac{1}{w} = 3.24$ which appears to be an outlier, gives an intercept of ~0.01 s, giving a $k_{GL,A}a_{GL}$ value of 100 s^{-1}.

The mass transfer coefficient was obtained assuming first order reaction kinetics with respect to the oxygen, and this may further affect its accuracy if the assumed order is not correct. This $k_{GL,A}a_{GL}$ value is in agreement with the values obtained in microreactors from the literature, where figures between 3-8 s^{-1} [7] and 5-15s^{-1} [4] have been reported. These values are two orders of magnitude larger than the values found in conventional trickle bed reactors, which range between 0.01 – 0.05s^{-1}. As the mass transfer performance in a microstructured reactor is up to two orders of magnitude higher than in conventional tubular reactors, the reactor performance can be sufficiently increased, leading to the desired intensification of the process. In addition, as the experiment was conducted under the liquid-dominated flow regime, it is anticipated that the value for the mass transfer coefficient would be higher under the gas-continuous (fully wetted) flow regime.

The significance of this calculated mass transfer coefficient depends on the characteristic reaction time. To eliminate mass transfer resistances in practice, the mass transfer time should be one order of magnitude smaller than the characteristic reaction time [8].

Table 8.5 *Standard error in estimation of mass transfer parameters.*

	Value	*Standard Error*
Intercept $\left[1/k_{GL}a_{GL}\right]$	0.04244	0.03995
Slope $\left[1\Big/\frac{\rho_c d_p}{6}\left(\frac{1}{k_{SL,A}}+\frac{6}{\eta\rho_c d_p k_{w1}}\right)\right]$	0.09351	0.01639

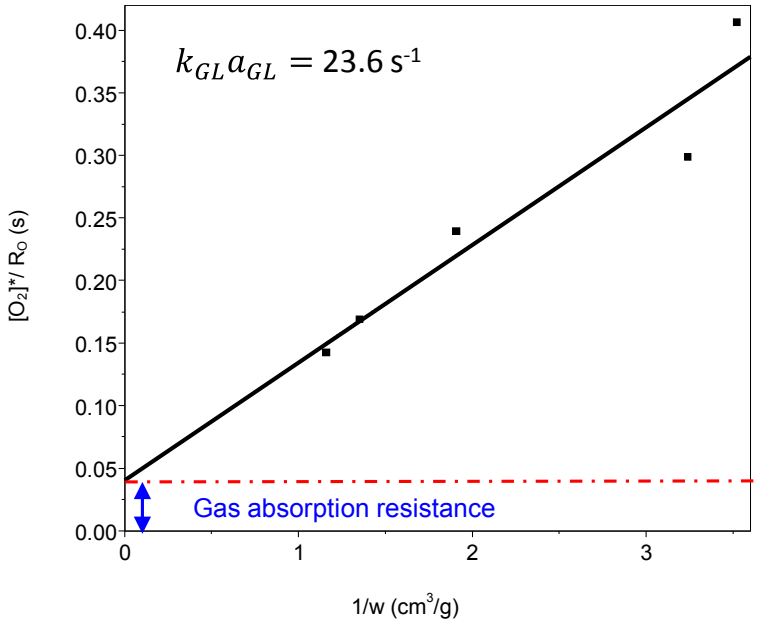

Figure 8.8 *Plot of $[O_2]^*/(R_O)$ versus 1/w under the liquid-dominated flow regime where R_O refers to the oxidation reaction rate. G: 0.8 Nml/min; L: 20 µl/min; Catalyst: 5%Pd/TiO_2, 0.45 mg – 1.4 mg, 53-63 µm; Diluent: TiO_2 support 53-63 µm; total reactor volume: 1.62 mm^3.*

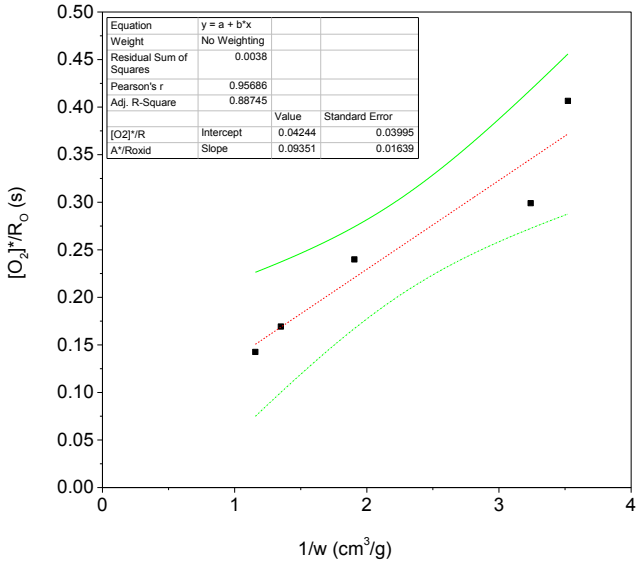

Figure 8.9 *Data presented in* ***Figure*** **8.8** *showing confidence bands for 95% confidence.*

8.3.3 Internal Mass Transfer Analysis using Experiments and Theory

Weisz-Prater Criterion

Details of the calculation carried out to obtain the Weisz-Prater (W-P) number are shown in **Appendix B**. The analysis was carried out on results obtained from the gas-continuous flow regime, as (according to the results in **Chapter VII**) external mass transfer can be assumed to be non-limiting under this flow regime. The calculation results in a W-P number of 1.55, indicating an effectiveness factor that is <80%. This means that with this highly active catalyst, operating under non-limiting external mass transfer – which adds to the high reaction rate – results in significant pore diffusional limitations. To complement this result with experiment, the effect of particle size on reaction performance was assessed experimentally in the next section.

Effect of Particle Size on Conversion and Selectivity

Figure *8.10* shows the change in conversion and selectivity with particle size. Particle size has a clear influence on conversion, which could be due to one of two reasons (1) the mass transfer resistance overcome by the reduction in particle size is internal (2) the reduction in particle size increases the L-S mass transfer area and therefore enhances the external mass transfer rate. To elucidate the route cause of this enhancement and to determine which of these two factors is responsible, the same experiment was conducted under two different flow regimes: one with external mass transfer resistance (liquid-dominated slug flow) and one without external mass transfer resistance (gas-continuous flow). The enhancement with reduction in particle size (in terms of both conversion and selectivity to the aldehyde) is clear even when operating in the gas-continuous flow regime. This indicates that the enhancement is due to improvement in the internal mass transfer, supported by the Weisz-Prater calculations presented in the previous section, which showed that at 65 μm particle size there are significant internal mass transfer limitations.

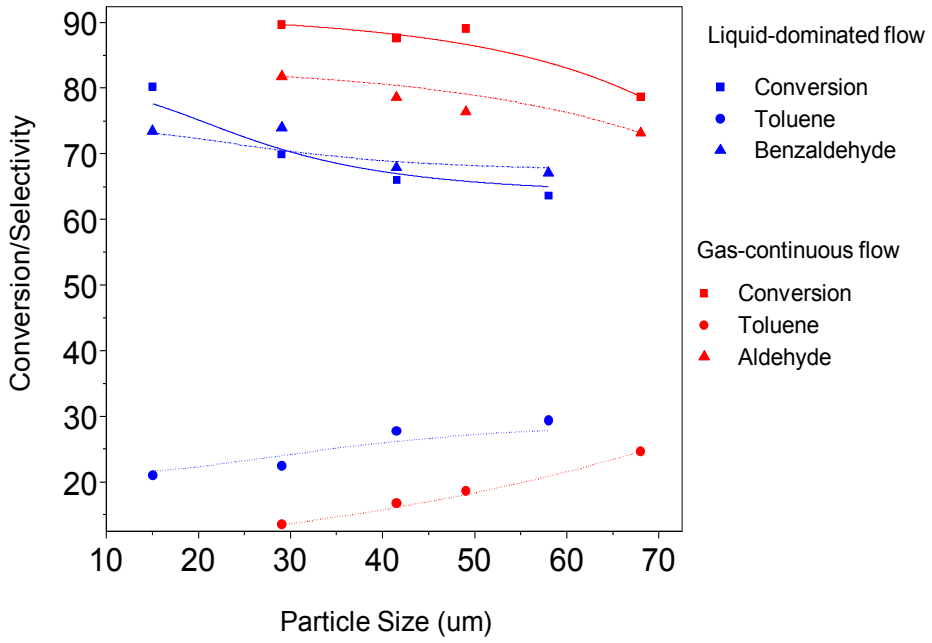

Figure 8.10 *Dependence of conversion and selectivity on Au-Pd catalyst particle size at different flow regimes. Temperature: 120*°C; Pressure: 1 barg.

8.4 Hydrodynamic Effects on Catalyst Deactivation Behaviour

The impact of catalyst preparation method on the deactivation behaviour of Au-Pd/TiO_2 catalyst was covered extensively in **Chapter V** under the liquid-dominated flow regime. Determining the stability of the catalyst at different hydrodynamic conditions is equally important. A series of experiments were carried out where the gas flow rate was increased until operation was close to the gas phase regime, while monitoring the conversion. The flow rate was then decreased to assess for hysteresis and deactivation effects. The catalyst used in these studies was the MI_m 0.05 wt% Au - 0.95 wt% Pd/TiO_2, which was shown to be stable at low G:L (liquid-dominated slug flow regime) in **Chapter V**.

Figure 8.11 shows the effect of an increase in gas flowrate on conversion while transitioning from the gas-continuous (fully wetted) to the partially wetted state (where the previously observed drop in conversion takes place due to poor catalyst

wetting). With decrease in gas flowrate back to the initial fully wetted conditions, a 5% drop in the initial activity at G=2.5 Nml/min is observed, indicating the presence of deactivation as a result of the catalyst having operated in the partially wetted state. It is difficult to determine whether there are added hysteresis effects (due to the existence of multiple hydrodynamic states depending on the flow history of the catalytic bed – as demonstrated in **Figure 8.12**) or if the change in behaviour with decrease in gas flow rate is purely due to catalyst deactivation. The exit mixture product composition is presented in **Figure 8.13**. There is a decline in the observed selectivity of the dibenzyl ether (DBE), benzyl benzoate, and benzoic acid with increasing and subsequent decreasing of gas flowrate. The drop in the observed selectivity of these components while increasing the gas flowrate implies their adsorption on the catalyst surface (and thus less of the component exits the reactor in the liquid mixture). As the gas flowrate is decreased, the selectivity to DBE and benzyl benzoate remains low, implying a change to the catalytic active sites that alters the product distribution. The high boiling point of these components could also mean that they would stay in the liquid inside the pores if not washed away, and this effect could be compounded in the gas phase flow regime where there are no liquid slugs to effectively refresh the stagnant liquid pockets. The hypothesis of the adsorption of by-products implies that there is unsteady state behaviour at each gas flowrate, and therefore subsequent samples with time-on-stream should show differing amounts of benzoate and ether. Although this date is not available to be discussed here, it presents an area of future work.

Another experiment was conducted reaching higher gas flowrates of 16 Nml/min (**Figure 8.14**). The conversion dropped from around 95% to 15%, and the activity was irrecoverable with decrease in gas flowrate. The deactivation was irreversible upon stopping the gas and rewetting the catalytic bed with liquid flow only (shown by the star symbol in **Figure 8.14**). The selectivity to benzaldehyde was also affected by the hysteresis; there was a small increase in the selectivity to benzaldehyde when decreasing the gas flowrate. This could be due to a higher gas to solid mass transfer rate when the catalyst is in a drier state as a result of the previous flow history (hysteresis effect shown in **Figure 8.12**). Raman spectra of the used catalyst at three different locations in the microreactor showed some signs of carbon deposits, as evidenced by the bands at around 1500 cm^{-1} (**Figure 8.15**), although the signals

observed are very weak. No clear trend between position in the reactor and size of the observed signal was observed.

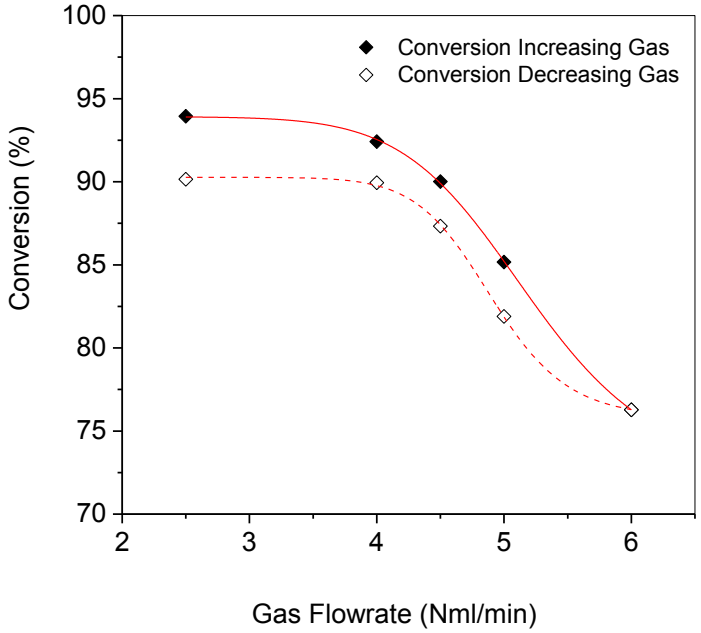

Figure 8.11 *Hysteresis in conversion with increasing/decreasing gas flow rate. Liquid flow rate: 0.75 µl/min; Temperature: 120°C; Pressure: 1 barg; Catalyst mass: 1 mg.*

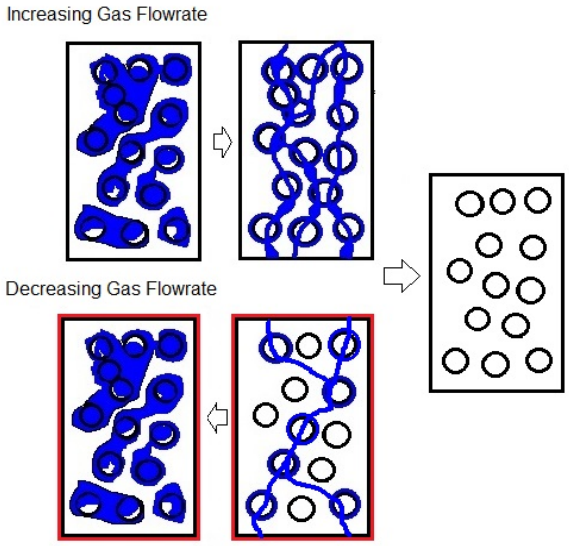

Figure 8.12 *An illustration of hysteresis in a packed bed reactor as a result of the flow history of the catalytic bed, demonstrating the difficulty in restoring the liquid supply network with decreasing gas flowrate and therefore resulting in poor catalyst wetting.*

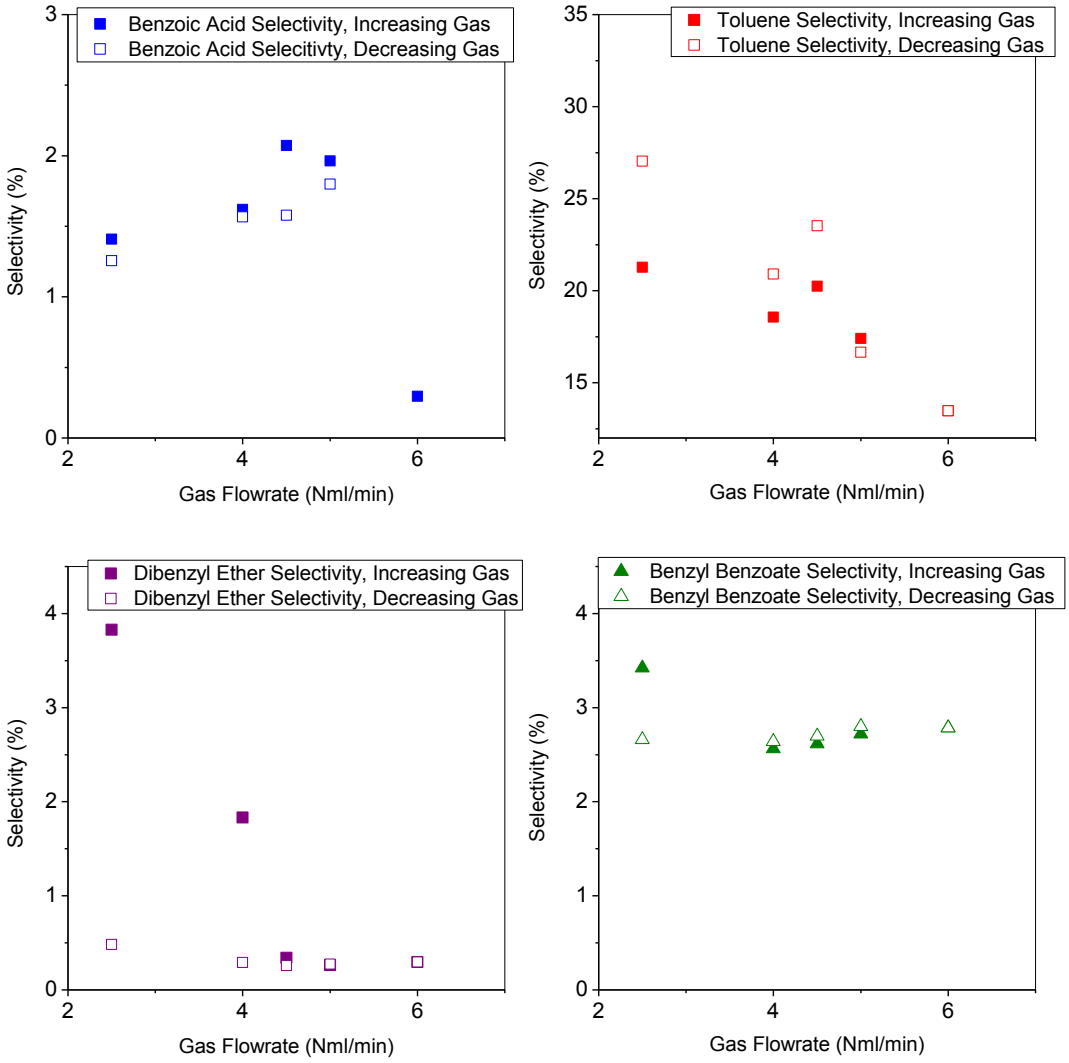

Figure 8.13 *Hysteresis in selectivity to by-products with increasing/decreasing gas flowrate. Liquid flow rate: 0.75 µl/min; temperature: 120°C; pressure: 1 barg.*

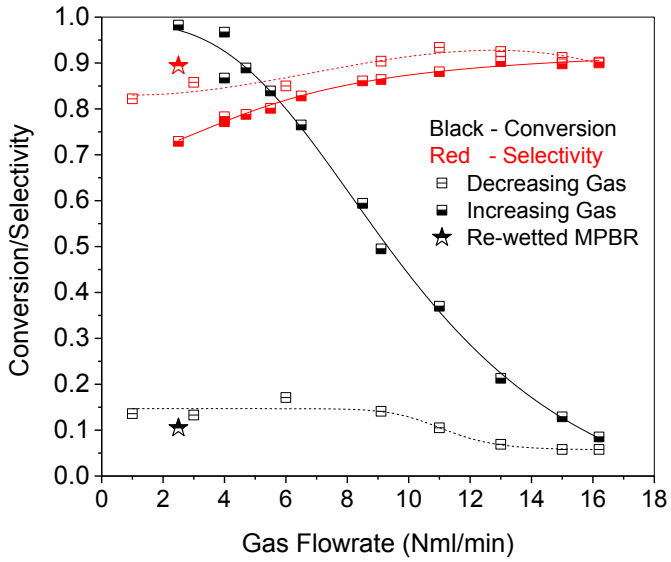

Figure 8.14 *Effect of gas flowrate on fractional conversion and selectivity spanning the gas continuous (fully wetted), gas continuous (partially wetted) and gas phase regimes. Liquid flowrate: 0.75 µl/min. Catalyst mass: 1 mg. Temperature: 120°C. Pressure: 1 barg.*

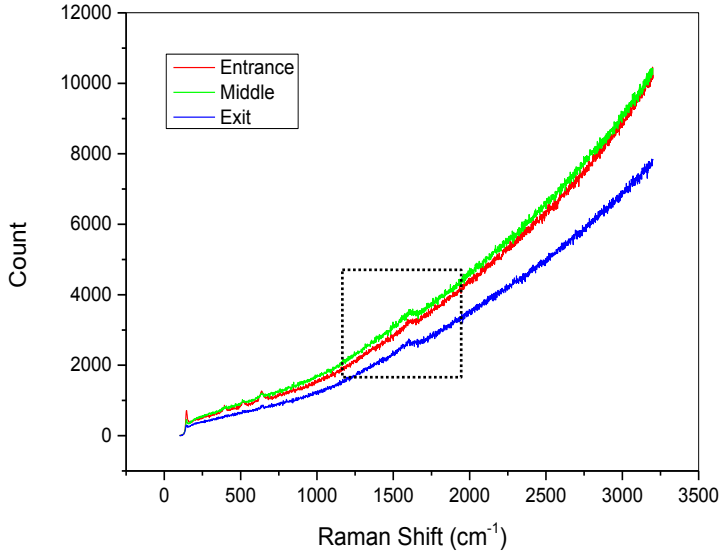

Figure 8.15 *Raman spectra at different positions in the reactor after being subjected to the experiments shown in* ***Figure 8.14****.*

8.5 Conclusion

Three-phase packed bed microreactors have enhanced mass transfer due to the small characteristic dimensions. However, it has been shown here that for highly active catalysts, internal and external mass transfer resistances can exist. The former can be reduced by reducing particle size, while the latter can be minimised by operating at high G:L flow ratios. Operating at elevated G:L ratios results in high benzaldehyde selectivity, however, beyond a certain point hydrodynamics change significantly and deactivation is observed, possibly due to deposition of heavy molecular weight by-products.

COMSOL simulations confirmed the positive influence of a reduction in liquid film thickness on the oxygen concentration in the liquid phase, which in turn affects the oxidation reaction rate and the product distribution positively. The G-L mass transfer coefficient obtained was $k_{GL,A}a_{GL} = 23.6$ s^{-1}, which suggests that G-L mass transfer may not be the only limiting mass transfer step while operating in the liquid-dominated slug flow regime.

While operating in the gas-continuous (partially wetted) flow regime was found to be superior in terms of selectivity to the aldehyde, considerable deactivation was observed, which has been linked to the drop in selectivity of heavy molecular weight by-products, suggesting their deposition on the catalyst surface.

8.6 References

1. Nauman, E.B. **Multiphase Reactors**. In *Chemical Reactor Design, Optimization, and Scaleup*. John Wiley & Sons, Inc.; 2008:385-431.

2. Ramachandran, P.A., Chaudhair, R.V. ***Three-phase catalytic reactors***. New York: Gordon and Breach Science; 1983.

3. Doraiswamy, L.K. ***Organic Synthesis Engineering***. New York: Oxford University Press; 2001.

4. Losey, M.W., Schmidt, M.A., Jensen, K.F. **Microfabricated Multiphase Packed-Bed Reactors: Characterization of Mass Transfer and Reactions**. *Industrial & Engineering Chemistry Reseach* 2001, 40:2555-2562.

5. Meenakshisundaram, S., Nowicka, E., Miedziak, P.J., Brett, G.L., Jenkins, R.L., Dimitratos, N., Taylor, S.H., Knight, D.W., Bethell, D., Hutchings, G.J. **Oxidation of alcohols using supported gold and gold-palladium nanoparticles**. *Faraday Discussions* 2010, 145:341-356.

6. Cussler, E.L. ***Diffusion***, 3rd Edition. Cambridge: Cambridge University Press; 2009.

7. Hessel, V., Lob, P., Lowe, H. **Development of microstructured reactors to enable organic synthesis rather than subduing chemistry**. *Current Organic Chemistry* 2005, 9:765.

8. Hessel, V., Renken, A., Schouten, J., Yoshida, J. ***Micro Process Engineering: A comprehensive handbook***. Weinheim: Wiley-VCH; 2009.

IX.

Ozonation of Benzyl Alcohol Catalysed by Au-Pd in a Three Phase Micro-Packed Bed Reactor

---

The use of ozone as a replacement for oxygen was found to have a profound impact on the overall reaction rates and product distribution. Ozonation of benzyl alcohol in the presence of supported Au-Pd catalyst resulted in conversions of up to 37% at temperatures as low as 60°C, while oxygen was only able to convert 1% of the benzyl alcohol under these conditions. Ozone, being a stronger oxidising agent, altered the dominating reaction pathway – promoting the oxidation reaction path even further – to the extent that 30% benzoic acid is produced, and virtually no toluene was produced, indicating the complete suppression of the disproportionation reaction path in the presence of ozone. It was found that the majority of the reaction in the presence of ozone was non-catalytic.

9.1 Introduction

Ozone is widely used in environmental processes such as water treatment, purification of indoor air and gaseous industrial streams. It falls under the class of environmentally acceptable oxidants due to water and dioxygen being the two products as a result of the decomposition of these compounds. In comparison to molecular oxygen, ozone is a stronger oxidising agent; this is reflected by the (factor of two) lower temperatures required for complete catalytic oxidation (e.g. of VOCs) using ozone, leading to considerable energy savings [1].

Ozone reacts with most substances at room temperature. This includes organic and organometallic functional groups, C-H, C-O, C-N and C-S bonds, where it reacts as an electrophile at points of high electron density. The non-catalytic chemistry of ozone is very rich and its reaction with aromatics leads to a variety of compounds. However, the diversity of possible reactions also means that controlling the selectivity of products is a problem. In many cases where catalysts are not used, partial oxidation products are formed, including oxalic, glyoxalic and acetic acids. Therefore, using catalysts in conjunction with ozone offers the ability to control reaction pathways for precise chemical synthesis.

Catalytic oxidation of hydrocarbons using ozone has been demonstrated for substrates such as gaseous benzene over SiO_2 supported metal oxides (Mn, Fe, Co, Ni, Cu) at 70°C [2], cyclohexane at room temperature [3] and toluene (between 22°C – 100°C) on alumina-supported manganese oxide [1]. Interestingly, lower Mn loadings were found to have higher activities for the oxidation of toluene but deactivation is usually found due to the build-up of by-products (such as formate) when ozone is used.

The liquid phase oxidation of benzyl alcohol with ozone without a catalyst has been demonstrated producing 84% benzoic acid yields as a result of preferential oxidation of the oxy-methyl group [4]; with the introduction of cobalt (II) acetate, it was possible to raise the benzoic acid yield to 95% [4]. It was suggested that benzoic acid was produced from benzaldehyde through a consecutive reaction scheme.

While the ozonation of benzyl alcohol in the absence of catalyst has been demonstrated in the past, the catalytic ozonation of benzyl alcohol has not been conducted yet, and it is the purpose of this study to determine the benefits of carrying out the ozonation of benzyl alcohol in the presence of a catalyst that was previously demonstrated to be effective in the presence of oxygen.

9.2 Materials & Methods

9.2.1 Experimental setup

Oxygen (N5.5 grade, BOC) was delivered to a mass flow controller (Brooks 5850TR, Brooks Instrument) set to a flowrate of 1 Nml/min. To produce the ozone, 1 Nml/min of oxygen gas was flowed through an ozone generator (BMT 803N, BMT Messtechnik GMBH) and an ozone analyser (BMT 964, BMT Messtechnik GMBH) was used to measure the concentration of ozone produced in the oxygen stream. The ozone generator works by ionisation. This involves generating a high voltage electrical discharge and passing oxygen past it; the corona ionises the oxygen molecules into individual oxygen atoms, which then recombine into oxygen (O_2) and ozone (O_3). The generated ozone/oxygen mixture was passed to the microreactor where it reacted with the incoming benzyl alcohol (benzyl alcohol 99.98%, Sigma Aldrich) feed, delivered via a syringe pump (PHD Ultra, Harvard). Only a fraction of the oxygen was converted to ozone (approximately 7 %v/v) and the concentration of ozone produced was dependent on the flowrate and pressure at the ozone generator (**Table 9.1**).

The microreactor used was the serpentine B1 reactor design (**Table 3.1**). The temperature was controlled using a heating and temperature control unit (Watlow CAL 9900, Watlow Ltd) consisting of a ceramic packing containing thermocouples and heating cartridges, using the same reactor holder used in **Chapter V**. The pressure was regulated to 1 barg in all experiments using a backpressure regulator (SS BP Regulator, Swagelok) and the temperature at 60°C. The catalyst used for the experiment was the 0.05 wt%Au - 0.95 wt% Pd/TiO_2 presented in **Chapter V**. A catalyst mass of 4 mg was used with an average particle size of 65 μm. A liquid flowrate of 3 μl/min and a gas flowrate of 1 Nml/min was used. The serpentine reactor shown in **Figure 5.5** was used for this work. The product mixture was flowed through

a gas-liquid separator, chilled with ice to condense all the hydrocarbons. The liquid product was collected for GC analysis (as described in **section 5.3.3** and **Appendix B)** while the gas was passed through a catalytic ozone destructor (Carulite catalyst, Carus) consisting of manganese dioxide/copper oxide catalyst, before being released into the fume hood. A flow diagram of the setup is shown in **Figure 9.1**

Table 9.1 *Ozone concentration generated by ozone generator and its dependence on the gas flowrate.*

Flowrate (Nml/min)	Ozone Concentration (g/Nm^3)
5	113
10	116
15	123
35.5	132

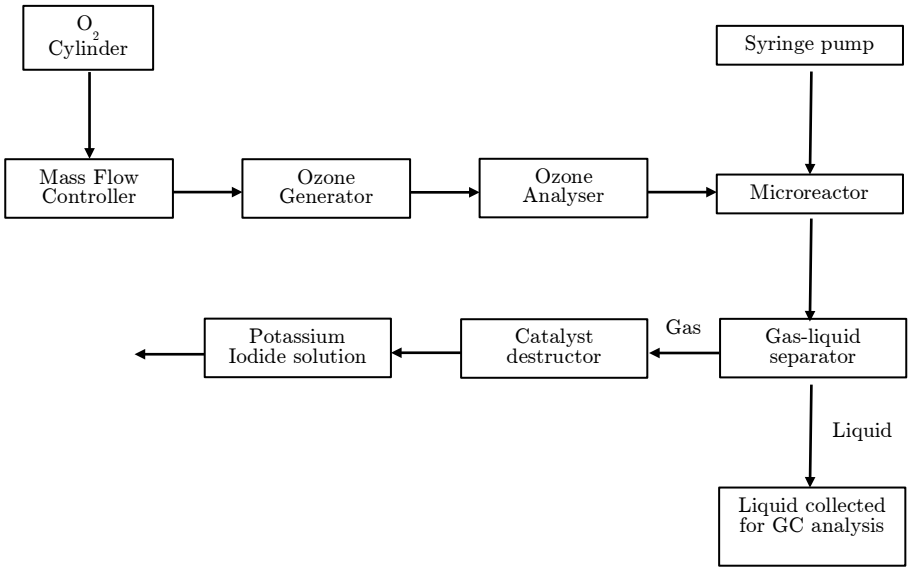

Figure 9.1 *Flow diagram of the benzyl alcohol ozonation experimental setup.*

9.2.2 Ozone generation

The ozone generator was greatly impacted by the oxygen flowrate as shown in **Table 9.1**. Ozone is thermodynamically unstable, and its decomposition is exothermic. Therefore, once generated, ozone has a half-life, which depends on the medium that the

ozone is kept in. The ozone concentration was measured at the exit of an empty reactor and the results in **Table 9.2** show that the ozone did not decompose in the microreactor, even at temperatures as high as 120°C.

Table 9.2 *Measured ozone concentration at the reactor exit at different operating temperatures.*

Temperature (°C)	Measured ozone concentration at reactor exit (g/Nm^3)
80	157
120	146

9.3 Results & Discussion

9.3.1 Effect of Ozone on Conversion

Table 9.3 shows results of the experiments conducted with

1. **Catalytic (ozone):** catalyst is present with ozone as the oxidant
2. **Catalytic (oxygen):** catalyst is present with oxygen as the oxidant
3. **Non-catalytic (ozone):** ozone only with no catalyst

In comparison to oxygen, the reaction rate with ozone is considerably higher. Only 1.12% of benzyl alcohol was converted when oxygen was used in the presence of a catalyst, while 35.54% was converted when ozone was used as the oxidant under the same conditions. A substantial amount of benzyl alcohol was converted without the catalyst, indicating the presence of direct oxidation of benzyl alcohol with ozone in the liquid phase. The enhancement brought about by using a catalyst along with ozone could be due to a higher ozone concentration of 200 g/Nm^3 in the catalytic experiment compared to 125 g/Nm^3 in the non-catalytic experiment.

9.3.2 Effect of Ozone on Product Distribution

There is a marked difference in the product distribution with the introduction of ozone into the gaseous mixture (**Table 9.3**). Approximately 50% of benzaldehyde and 30% of benzoic acid are produced in the presence of ozone. In comparison to the pure oxygen

reaction results (65% benzaldehyde, 35% toluene product distribution (**Chapter VII**), there is a significant shift in the products from toluene to benzoic acid. The high benzoic acid selectivity in the non-catalytic reaction (27.1%) could be explained by further oxidation of benzaldehyde to the acid (as shown in **Figure 9.2**). As almost no toluene was produced, this suggests that either the disproportionation reaction does not take place in the presence of ozone, or the produced toluene via disproportionation is further converted to the acid.

Table 9.3 *Performance comparison between catalytic and non-catalytic oxidation of benzyl alcohol using ozone and oxygen at a reaction temperature of 60°C.*

	[O_3] g/Nm³	X	P* (psi)	BAld	Benzoic Acid	Benzyl Benzoate	Tol	DBE
Catalytic (Ozone)	200	35.54%	9	53.64%	27.12%	9.34%	0.28%	0.14%
Catalytic (Oxygen)	0	1.12%	7.8			§		
Non-catalytic (Ozone)	125	29.63%	1.54	53%	22.60%		†	

*§ Conversion was too low to obtain an accurate estimate of the product distribution in the catalytic (oxygen) experiment. Typical selectivity to benzaldehyde with oxygen is around 65% under this flow regime. *Pressure upstream of microreactor. † Rough analysis of products was carried out; therefore selectivity to by-products was not obtained.*

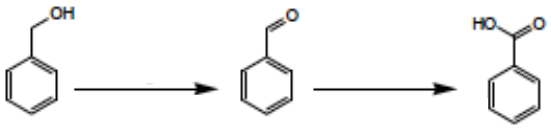

Figure 9.2 *Reaction scheme showing dehydrogenation of benzyl alcohol to benzaldehyde and further oxidation to benzoic acid.*

9.4 Conclusion

A preliminary investigation of the catalytic ozonation of benzyl alcohol at 60°C was performed in a micro-packed bed reactor with Au-Pd/TiO_2 catalyst. Using ozone as a substitute for oxygen resulted in significant enhancement in the conversion of benzyl alcohol, as well as a shift in the product distribution, favouring the production of benzoic acid (27%) as a substitute for toluene. This is due to the stronger oxidation potential of ozone in comparison to oxygen, resulting in either the inhibition of the disproportionation reaction path that produces toluene, or further oxidation of toluene

and benzaldehyde to benzoic acid. However, the majority of the conversion was found to take place without a catalyst.

9.5 References

1. Rezaei, E., Soltan, J., Chen, N. **Catalytic oxidation of toluene by ozone over alumina supported manganese oxides: Effect of catalyst loading**. *Applied Catalysis B: Environmental* 2013, 136-137:239-247.

2. Einaga, H., Maeda, N., Nagai, Y. **Comparison of catalytic properties of supported metal oxides for benzene oxidation using ozone**. *Catalysis Science & Technology* 2015, 5:3147-3158.

3. Einaga, H., Futamura, S. **Oxidation behavior of cyclohexane on alumina-supported manganese oxides with ozone**. *Applied Catalysis B: Environmental* 2005, 60:49-55.

4. Potapenko, E.V., Andreev, P.Y. **Oxidation of benzyl alcohol and benzaldehyde with ozone in acetic acid**. *Russian Journal Applied Chemistry* 2010, 83:1243-1247.

5. Einaga, H., Futamura, S. **Oxidation behavior of cyclohexane on alumina-supported manganese oxides with ozone**. *Applied Catalysis B: Environmental* 2005, 60:49-55.

X.

On-chip Residence Time Distribution Measurement using Raman Spectroscopy

A novel method for the on-chip characterisation of residence time distributions using Raman spectroscopy is presented in this chapter. A microreactor was designed specifically for integration with Raman spectroscopic analysis. The method was validated using single-phase liquid measurements and tested for gas-liquid flow in an empty channel. Challenges associated with measurement of Raman signals with gas-liquid flow are overcome by exploiting different microstructured reactor designs.

10.1 Introduction

The residence time distribution (RTD) is a probability distribution function used to characterise the time of contact and contacting pattern within reactors. Obtaining the liquid phase RTD enables determination of the liquid holdup, a relevant hydrodynamic parameter in design equations and correlations for heat and mass transfer coefficients in three-phase reactors. The RTD experiment can also help in diagnosing deviations from ideal fluid flow patterns and contacting schemes (e.g. extensive retention of some elements and bypassing) which may lead to offsets from what is ideally expected in terms of conversion and mass transfer. Results of such RTD analyses would help to make modifications to existing reactor designs/operating conditions to improve performance and efficiency. Similarly, it is important to characterise reactors used for the study of reaction kinetics; these reactors are usually designed to have plug flow (PF) – leading to uniform temperature and concentration gradients – and dispersion can invalidate this PF assumption. To confirm plug flow behaviour and guarantee the measurement of true kinetics, hydrodynamics and residence time distributions are therefore paramount prior to a kinetic study.

Developing microreactors either as production units or as laboratory investigation tools for reaction and kinetic studies relies strongly on their capability to perform real-time analyses. A detailed review of the integration of microreactors with spectroscopic detection for online reaction monitoring and catalyst characterisation is presented in [1] where the use of spectroscopic analyses such as fluorescence, ultraviolet-visible, infrared, Raman, X-ray, and nuclear magnetic resonance spectroscopy has been shown. With regards to on-chip RTD characterisation, a variety of methods have been presented in the literature, this includes: microscopy imaging, spectroscopy, and fibre optics. These techniques have been utilised primarily for liquid phase or gas-liquid flow in empty channels/capillaries. Their use in three phase gas-liquid-solid reactors has not been applied as of yet [2]. The injection of tracer is usually carried out using a valve located upstream the reactor. However, there are great advantages associated with on-chip injection and detection as it eliminates dispersion upstream/downstream of the reactor. Whilst on-chip *detection* has been made possible via microscopy and spectroscopy, very few have carried out on-chip *injection* of tracer due to the

microfabrication challenges associated with it. Traschel et al. used on-chip piezoelectrically actuated sample injection, releasing 100 nl of tracer liquid into a microchannel, and then monitored the tracer with fluorescence microscopy to obtain RTDs for gas-liquid Taylor flow [3] (**Figure 10.1b**). A similar type of injection system was used in conjunction with optical fibres introduced into the liquid channels for the detection [4] (**Figure 10.1c**). Optical activation of a caged fluorescent dye, where UV light was used to activate the injection of a dye to generate an ideal pulse or a continuous step input signal has also been demonstrated (**Figure 10.1a**) [5].

No work has been conducted using Raman Spectroscopy for RTD measurements to date. Further, no work has been carried out to obtain RTDs on-chip for microstructured reactors packed with catalyst particles (although work by the Larachi group [6] is note-worthy, micro-capillaries do not constitute on-chip microstructured devices). This is partly due to the difficulty in using spectroscopy in conjunction with packed solid particles in micro-structured devices. The purpose of this study is to bridge this gap and to develop a novel on-chip spectroscopic technique for characterising RTD characteristics in silicon-glass microstructured reactors, which will build the foundations for the measurement of RTDs in three phase micro-packed bed reactors.

10.2 Materials & Methods

10.2.1 Residence Time Distribution Measurements for Single Phase Flow

Experimental setup

The experimental setup for single phase RTD measurements consisted of (1) a syringe pump (PhD Ultra, Harvard Apparatus) (2) an automated 6-port 2-way valve (Valvemate) (3) microreactor assembly and (4) Raman probe 532 nm wavelength (Ventana-32, Ocean Optics). The sampling valve was connected to a sampling loop (0.15 ml) filled with cyclohexane to introduce a step tracer input. A normal experimental run began with introducing benzyl alcohol through the sampling valve (bypassing the sample loop) and to the microreactor. At the switch of the valve, the flow was directed through the sampling loop (containing the tracer) and into the

reactor. The Raman probe was positioned on-chip at the microreactor main channel entrance in order to obtain the input signal. At the same time as the valve switch, the Raman data acquisition was initiated. This gave t_1. The procedure was repeated with the Raman probe positioned at the reactor exit to obtain the output signal t_2.

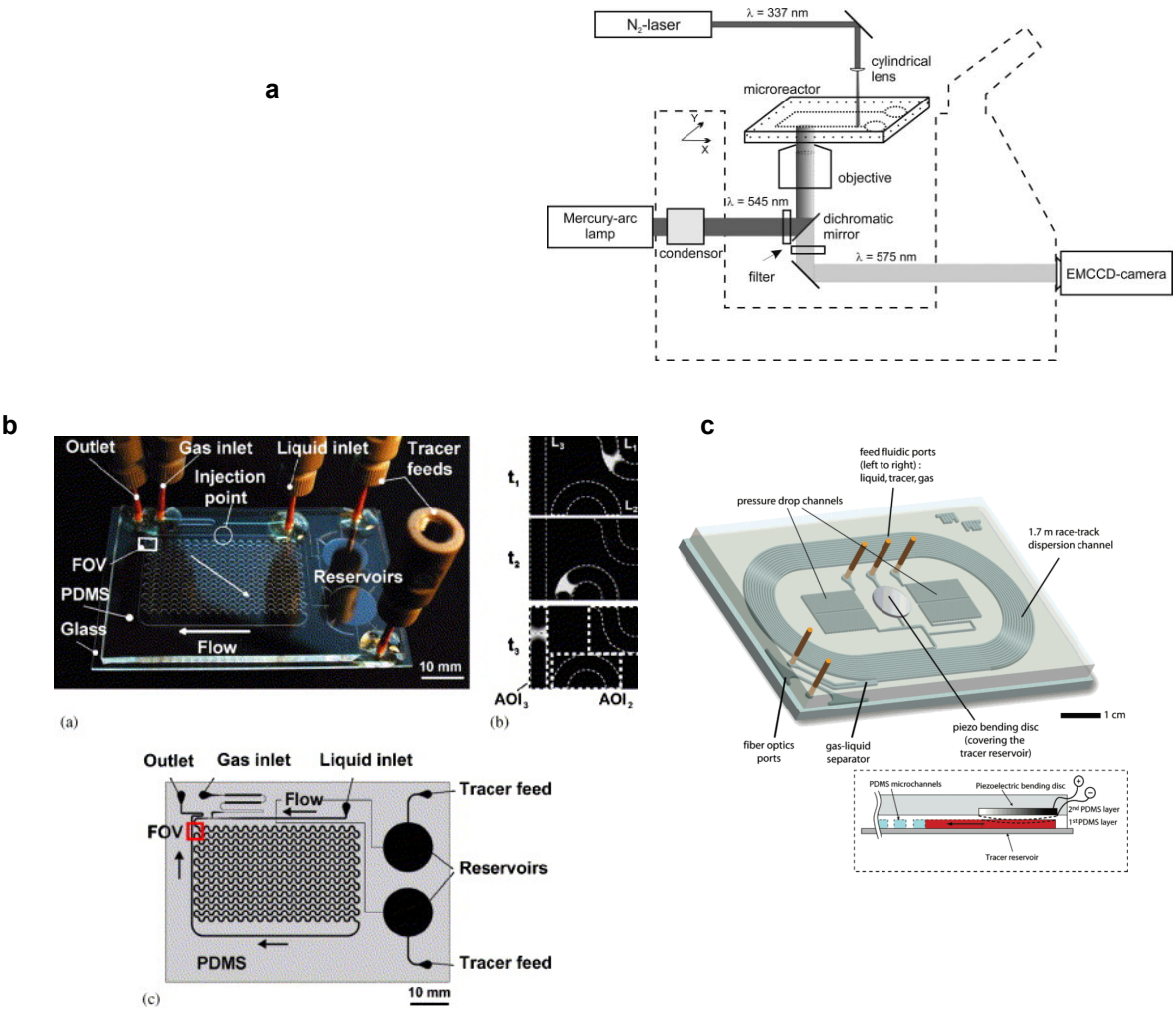

Figure 10.1 *Examples of on-chip RTD techniques for liquid and gas-liquid phase flow monitoring: (a) Optical activation of fluorescent dye using UV [5];(b)&(c) Piezoelectrically activated sample injection [3;4].*

Tracer selection

Initial tests using benzaldehyde as a tracer resulted in a significant shift in the baseline with the introduction of the tracer. This made the data analysis difficult, as baseline subtraction had to be carried out before peak integration. Alternative chemicals were tested and cyclohexane was selected as a tracer due to its ability to maintain a stable baseline when mixed with benzyl alcohol. With the introduction of cyclohexane, the Raman band at 2900 cm^{-1} (corresponding to the CH_2 out of phase stretch) increased in height (**Figure 10.2**). The band at 2850 cm^{-1} also increased in height with the introduction of cyclohexane, however, the signal at 2900 cm^{-1} was stronger and was therefore used as the tracer signal.

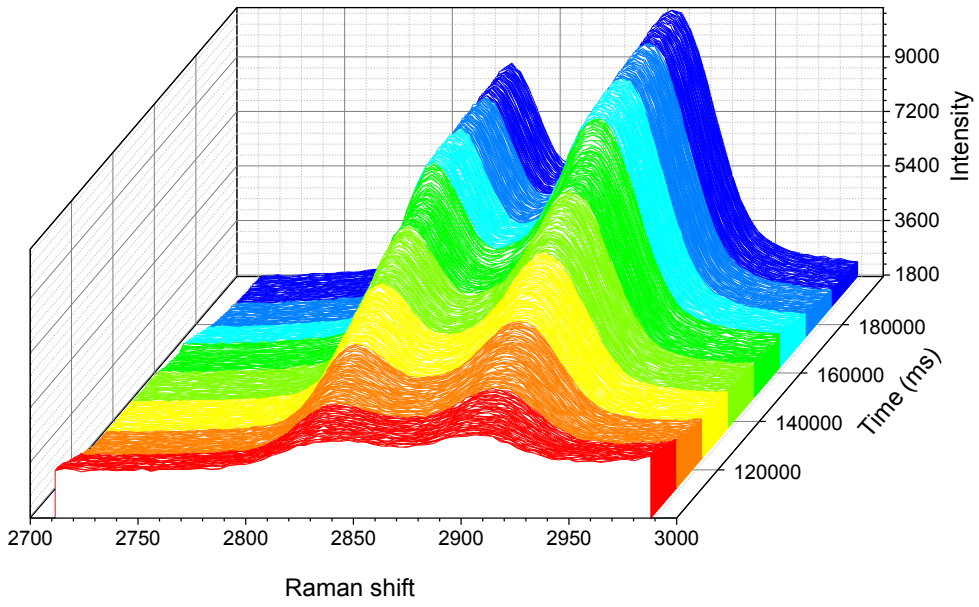

Figure 10.2 *Spectra of cyclohexane input signal with time. Peaks at 2850 cm^{-1} and 2900 cm^{-1} increase in height with time.*

Microdevice Design for Liquid Phase RTD Measurement

The microreactor used to measure the liquid phase residence time is shown in **Figure 10.3** (RTD-1 reactor in **Table 3.1**). The liquid was introduced into the wider serpentine channel, while the thin channel (usually used for the gas) was intentionally closed off for this liquid phase work. The output signal was obtained just before the retention posts.

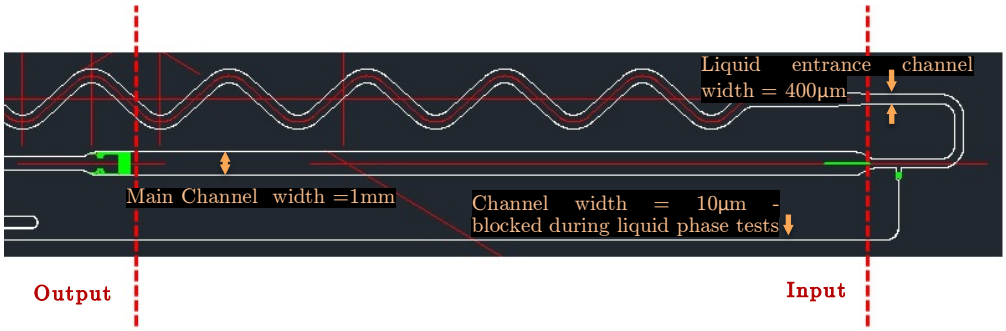

Figure 10.3 *Schematic of RTD-1 microreactor used for liquid phase residence time distribution studies. Dotted red lines indicate the input and output step locations.*

10.2.2 Residence Time Distribution Measurements for Gas-Liquid Flow

In order to study the effect of gas-to-liquid ratio on the RTD and the dispersion of the liquid, RTD experiments for the oxygen/benzyl alcohol system were performed at different gas flowrates, keeping the liquid flowrate constant.

Experimental Setup

For the gas-liquid work, an experimental setup equipped with a (1) syringe pump (Nemesys, Cetoni GmBH) for the liquid delivery (2) mass flow controller (Brooks 5850TR, Brooks Instrument) for the gas delivery (3) an automated 6-port 2-way valve (Valvemate) for tracer injection (4) a microreactor assembly (5) an automated stage to manoeuvre the microreactor and position accurately beneath the Raman probe and (6) a Raman probe (Ventana-32, Ocean Optics) were used (**Figure 10.4**).

The microreactor used in this experiment had a cross sectional area of 600 µm (channel width) x 180 µm (channel depth) (**Figure 10.5**). The sampling valve was connected to a sampling loop (0.15 ml) filled with cyclohexane. An experimental run began with the introduction of benzyl alcohol through the sampling valve (bypassing the sample loop) and to the microreactor. "Cold-flow" conditions were used (i.e. no heating). However, the system was pressurised to 2.6 barg, which helped stabilise the Taylor/slug flow generation in the channel.

At the switch of the valve, the flow was directed through the sampling loop (containing cyclohexane) introducing the tracer into the reactor, where the Raman probe was positioned at the entrance, in order to obtain the input signal. At the same time as the valve switch, the Raman data acquisition was initiated. This gave t_1. The procedure was repeated with the Raman probe positioned at the reactor exit to obtain the output step at t_2. The RTD test was stopped when the Raman peak at 2900 cm^{-1} was at its maximum, indicating the complete exit of the tracer from the reactor. Raman spectra were obtained every 100 ms.

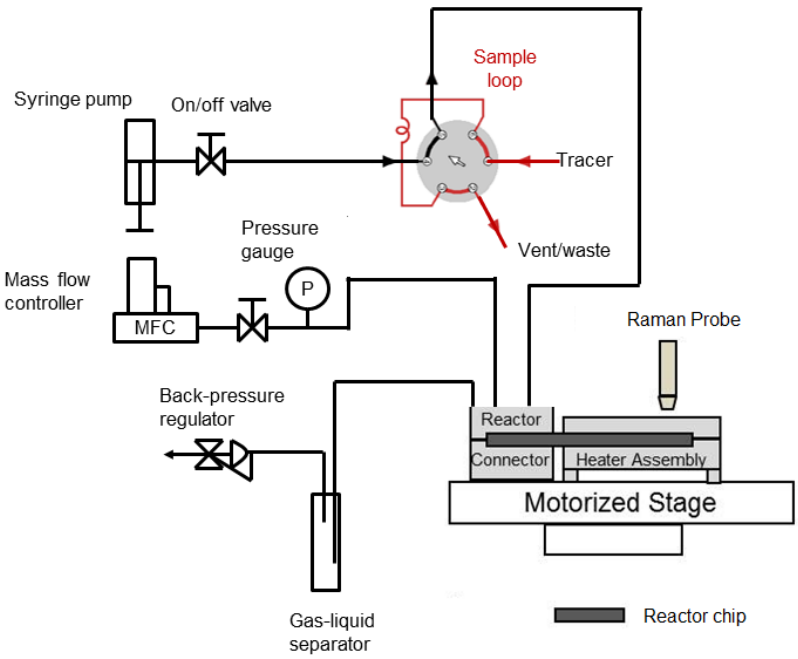

Figure 10.4 *Schematic of microfluidic setup used for gas-liquid flow residence time distribution studies.*

Microreactor Design for Gas-Liquid Flow RTD Measurement

The microreactor used for the gas-liquid RTD experiments is shown in **Figure 10.5** (RTD-2 in **Table 3.1**). The challenges are greater when using Raman to analyse gas-liquid segmented flow in comparison to liquid only, as Raman spectroscopy is insensitive to the gas phase and therefore no signal is acquired when a gas bubble passes through the microchannel. This results in very noisy spectra with fluctuating signals that make data interpretation very difficult. A microfabricated "liquid trap" which was created using diversion posts (consisting of a series of silicon posts) in order to trap a pocket of liquid for tracer detection as it passed through the reactor (see **Figure 10.5** magnified image). This was only necessary for the output signal, as the input signal was taken in the liquid channel, just before the gas and liquid had merged. Tests were carried out using red dye to investigate the renewal of liquid in and around the liquid traps (**Figure 10.6**). The results showed complete renewal of the colourless liquid with the red dye, indicating the absence of dead-zones in that area.

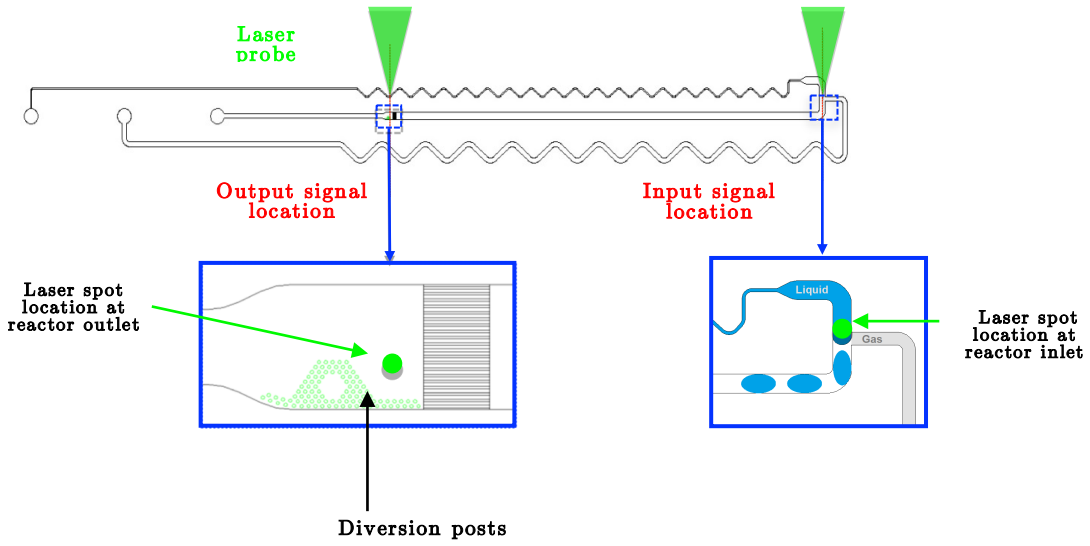

Figure 10.5 *Schematic of RTD-2 microreactor used for gas-liquid flow residence time distribution studies. Drawing is not to scale.*

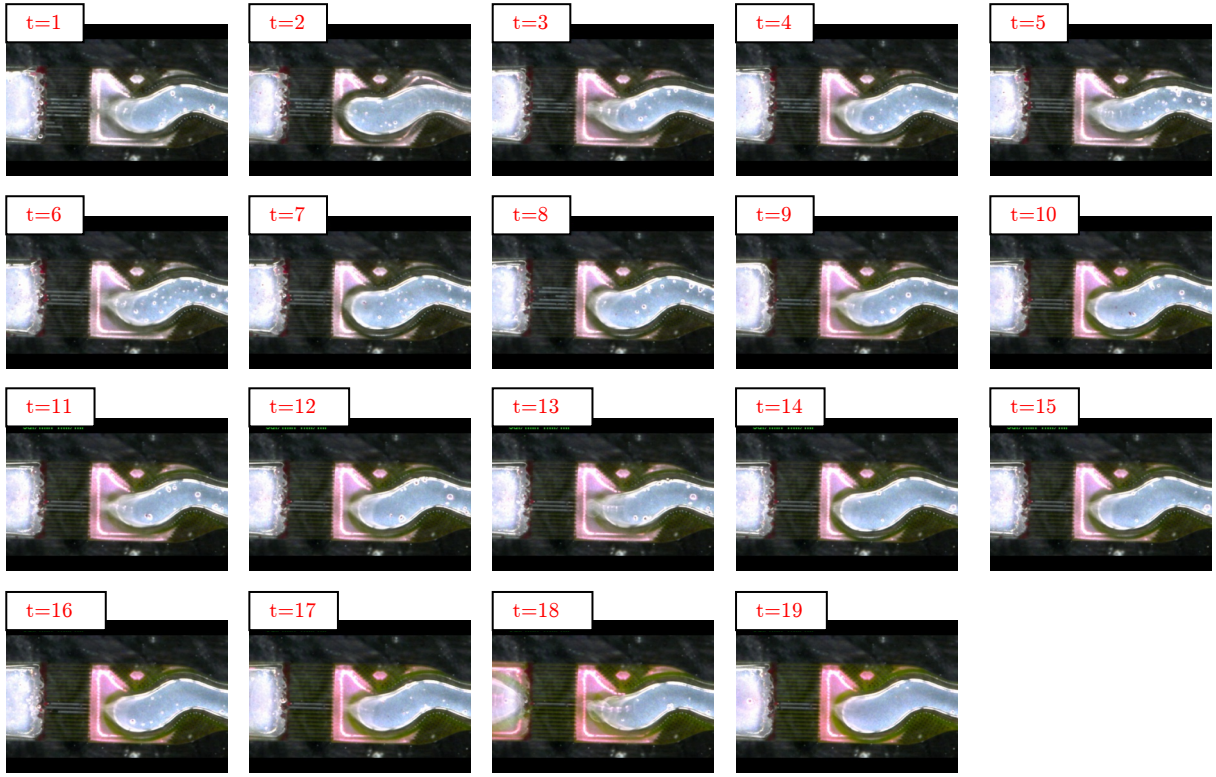

Figure 10.6 *Flow visualisation of the liquid trap microstructured reactor design used in RTD measurements. At t (time)=0 s, the clear liquid shown is benzyl alcohol being delivered at 3 µl/min with 1 Nml/min of oxygen. At t=1 s the liquid feed was switched to (coloured) benzaldehyde delivered at 3 µl/min along with 1 Nml/min of oxygen gas.*

Data Processing

Figure 10.7 shows a graph that can be used to determine the type of flow for a given system, using information on the fluid being used (Schmidt number), the flow conditions (Reynolds number), and vessel geometry (L/d_t, where d_t is the characteristic length, which is the channel hydraulic diameter in this case; L is the channel length). This chart is only applicable for laminar flow, and applies in this system as Re=0.06 for the liquid phase experiments, where d_t=0.417mm, L=32.3mm, u=1.40mm/s, and **D**=5.1x10^{-4}mm^2/s (value for **D** obtained from [7]). The operating point is shown in **Figure 10.7** indicating that the axial dispersion model can be used, although it is worth to note that the operating conditions are close to the "intermediate regime" that separates the axial dispersion model and the convection model.

The spectra acquired with Raman were analysed using OriginPro 9.0 where the area of the peak at 2900 cm^{-1} was obtained by baseline subtraction and integration. Following the acquisition of the E-curve, (see *Mean Residence Time Calculations* below) a calculation was made to determine whether the measured RTDs did indeed conform to the Gaussian distribution function (that is, that the curves are symmetric around their mean). This test is important as for curves symmetric around their mean, the mean residence time can be determined directly from the E curve, as the time for which E is a maximum. The dimensionless parameter that is commonly used to measure the extent of axial dispersion is $\frac{\boldsymbol{D}}{uL}$ where **D** is the dispersion coefficient (m^2/s), u is the fluid velocity (m/s), and L is the reactor length (m). The parameter **D** determines the level of dispersion in the system.

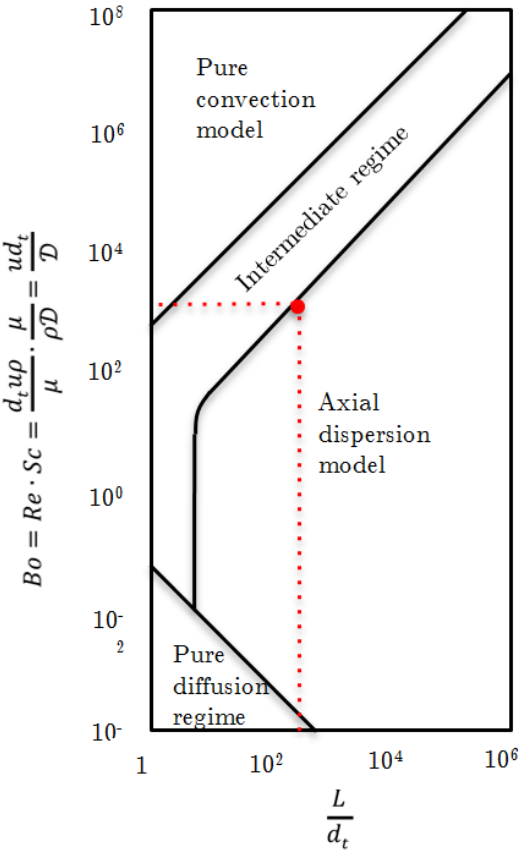

Figure 10.7 *Map showing criteria based on the type of fluid (Schmidt number), the flow conditions (Reynolds number), and vessel geometry (L/d_t), which aids in determining which flow model should be used in any situation [8]. The operating point for the liquid phase RTD studies investigated in this chapter is located on the map.*

The dimensionless parameter $\frac{D}{uL}$ can be used to determine the extent of axial dispersion by using the assumptions below:

$$\frac{D}{uL} \to 0 \text{ negligible dispersion, hence plug flow}$$

$$\frac{D}{uL} \to \infty \text{ large dispersion, hence mixed flow}$$

For small extents of dispersion (i.e. $\frac{D}{uL} < 0.01$) the tracer curve does not significantly change in shape as it passes the measurement point. This is termed the "small deviation" assumption. Under these conditions, the solution to the differential equation

representing the dispersion model gives a symmetrical curve; the width of the peak at 61% of the maximum ($E_{\theta max}$) is a value that is known, and occurs at $\theta = 1 + \sigma_\theta$. The standard deviation σ_θ can therefore be calculated and the Dispersion number, $\frac{\boldsymbol{D}}{uL}$, can be found through the following relationship [8]:

$$\sigma_\theta^2 = 2\frac{\boldsymbol{D}}{uL} \qquad (10.1)$$

The dispersion number $\frac{\boldsymbol{D}}{uL}$ was calculated to be 0.004 for the liquid phase only experiment and up to 0.013 in the gas-liquid phase experiments (see Results section). This is in agreement with the previous analysis carried out using **Figure 10.7** where it was found that the conditions for this experiment lied in the axial dispersion model regime, bordering the intermediate regime. The assumption that the inlet tracer signal was a very sharp step with minimal dispersion was made, and hence no convolution of the inlet data was required. This assumption was made to enable simpler data analysis, however, it should be noted that the dispersion factors reported here represent the worse case scenario, as they include dispersion associated with the upstream section prior to the reactor inlet.

Mean Residence Time Calculations

Each curve of Raman signal peak area versus time, corresponding to the concentration of tracer, was normalised to obtain the dimensionless curve $F(t)$.

$$F(t) = \frac{C(t)}{C_{max}} \qquad (10.2)$$

The $F(t)$ curve was then differentiated to obtain the RTD function $E(t)$.

$$E(t) = \frac{dF(t)}{dt} \tag{10.3}$$

The mean residence time, $\bar{t}$, is:

$$\bar{t} = \frac{\int_0^\infty t \cdot E(t)dt}{\int_0^\infty E(t)dt} \tag{10.4}$$

where $E(t)dt$ is the fraction of fluid exiting the reactor that has spent between t and $t + dt$ inside the reactor. It is useful to use the dimensionless or normalised RTD function E_θ when dealing with flow models. If the parameter θ is defined as:

$$\theta = \frac{t}{\bar{t}} \tag{10.5}$$

and the dimensionless function E_θ is defined as:

$$E_\theta = \bar{t} \cdot E(t) \tag{10.6}$$

E_θ can then be plotted as a function of θ. The purpose of creating this normalised distribution function is that the flow performance inside reactors of different sizes can be compared directly.

The measured residence time distribution is a cumulative signal consisting of the distribution of the reactor itself and that of the upstream segment between the valve injection and the microreactor. Usually, this overall signal is deconvoluted mathematically in order to describe the performance of the reactor solely. However, as the purpose of this study is to demonstrate the use of Raman spectroscopy for on-chip RTD measurements and develop the system with a view to be used for gas-liquid-solid RTD measurements, the deconvolution was not carried out. Provided the RTD signals are symmetrical, then the difference in time at maximum heights of the input and

output signals represents the mean residence time. In addition, the dispersion numbers reported are worst-case scenarios, as they include dispersion from the upstream tubing section.

10.3 Results & Discussion

The residence time method was first validated with liquid only flow, and then used for the gas-liquid flow to determine mean residence time and trends with changing G:L flowrate ratio.

10.3.1 Liquid Phase Residence Time Distribution Method Validation

The procedure outlined in the experimental section was used to obtain the liquid phase residence time at a liquid flowrate of 16.2 µl/min. The reactor used had an etch depth of 320 µm on average, a width of 1 mm and a length of 32.3 mm which gave a reactor volume of 10.34 mm^3. At a liquid flowrate of 16.2 µl/min, this should give a residence time of 38.28 s (calculated based on $\tau = {}^{V_r}/_{v_o}$, where V_r is the reactor volume and v_o is the volumetric flowrate). The input signal was repeated in order to test the reproducibility of the method. Input and output tracer signals are shown in **Appendix C.**

The dimensionless E-curves are shown in **Figure 9.8** and a comparison between the actual and measured residence time is made in **Table 9.1.** The measured residence time was 35.25 s on average, which is 7.9% different to the calculated value for this channel geometry and liquid flowrate. Possible sources of error may not be wholly associated with the RTD measurement method itself, but other factors such as: delay between data start and valve switching (due to manual operation), variation in channel etch depth eg. 20 µm difference in etch depth can change the residence time by 3 s and therefore give rise to the observed % deviation from the actual residence time.

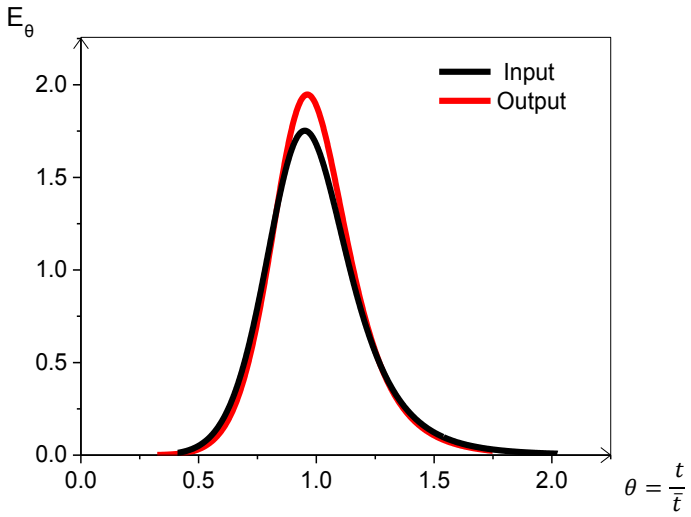

Figure 10.8 *Dimensionless E-curves for liquid phase RTD studies.*

Table 10.1 *Numerical comparison between the actual and measured liquid phase residence time using on-chip Raman Spectroscopy.*

Actual Residence Time† (s)	38.00
Average Measured Residence Time (s)	35.25
Difference between Actual and Measured Residence Time (%)	7.9

† *Residence time calculated based on a reactor volume of 10.34 mm³ and a liquid flowrate of 16.2μl/min.*

10.3.2 Residence Time Distribution Measurements for Gas-Liquid Flow

Results in the following section are for gas-liquid flow in an empty channel utilising the reactor in **Figure 10.5**.

Effect of Gas Flowrate on Liquid Phase Residence Time and Dispersion

The gas-to-liquid ratio was adjusted by increasing the gas flowrate while keeping the liquid flowrate constant at 20 µl/min. **Figure 10.9** shows E(t) curves for the input and output signals at the various gas flowrates while **Figure 10.10** shows a plot of the average residence time with increasing gas flowrate. **Appendix C** contains the F(t) and dimensionless E curves corresponding to the data presented in **Figure 9.9**.

Figure 10.10 reveals an increase in the average residence time with G:L ratio that plateaus at around 4 Nml/min gas flowrate. This coincides with a transition in the flow pattern from Taylor (slug flow) to churn/annular (very fast moving disturbed slugs, bordering on wavy annular). The dependency of residence time on gas flowrate at $G < 4$ Nml/min is an unexpected result as the gas is expected to propel the liquid and decrease its residence time. The plateau at around 4 Nml/min can be explained by flow regime transition. Residence time and liquid holdup are coupled to the gas flowrate for segmented flow – as the gas and liquid slugs remain discrete and influence each other along the capillary. As the flow transitions to annular, the gas and liquid flows become decoupled, each occupying their own specific space, and the flowrate of the gas begins to have less of an influence on the liquid phase residence time. Therefore, no change in average residence time is observed under the annular flow regime [10;11].

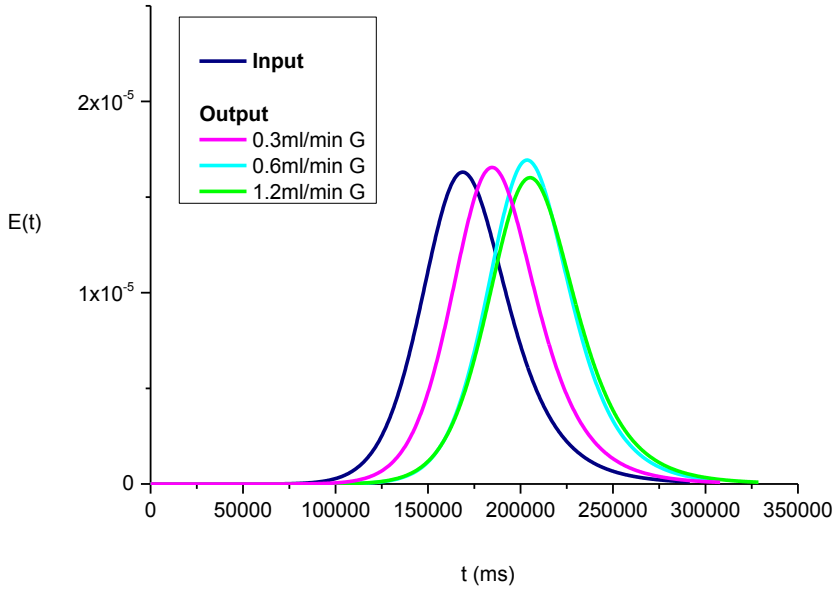

Figure 10.9 *Input and output E(t) curves for various gas flowrates: 0.3 Nml/min, 0.6 Nml/min, 1.2 Nml/min at a liquid flowrate of 20 µl/min.*

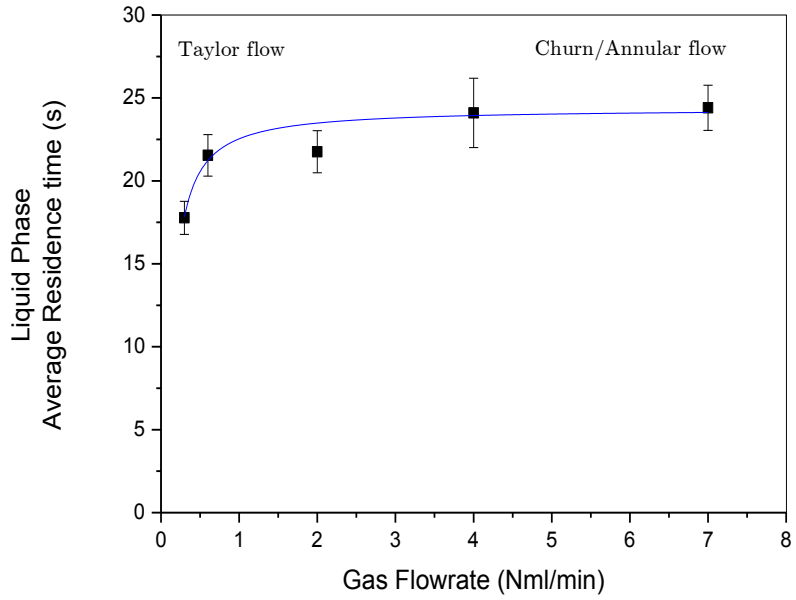

Figure 10.10 *Impact of gas flowrate on liquid phase residence time for gas-liquid flow in an empty channel. Error bars represent the standard deviation of duplicates. Liquid flowrate: 20 µl/min.*

The dispersion numbers were calculated for varying gas flowrate and the results are shown in **Table 10.2**. The results show a reduction in dispersion with increase in gas flowrate. The Taylor flow regime, which is observed up to a gas flowrate of approximately 4 Nml/min, has been demonstrated to have enhanced dispersion properties, where the degree of backmixing is diminished by the presence of the bubbles. The bubbles are essentially providing an environment that seals pockets of liquid, whereby the only mechanism of transfer from one liquid slug to the next is by diffusion from the slug to the film, and subsequent diffusion from the film to the adjacent slug [12]. The film thickness depends on the relative magnitude of viscous to surface tension forces, quantified by the dimensionless capillary number Ca= $\frac{\mu U_b}{\sigma}$, where U_b is the bubble velocity, μ is the liquid viscosity and σ is the surface tension. For very low capillary numbers Ca<10^{-4} (which takes place at low gas flowrates) the liquid film is only a few microns thin, and the level of backmixing is further reduced [3;13] (which would be expected to result in lower dispersion numbers). This can be used to explain the observed reduction in dispersion with increase in gas flowrate.

The decrease in axial dispersion by flow segmentation is a trend that is generally agreed upon in the literature [14;15]. The results are also in agreement with more recent work in microchannels, including that of Kreutzer et al. [4] who experimentally studied the effect of segmentation on dispersion in microchannels (although their gas-to-liquid ratios were significantly smaller, up to a maximum of 7.2) and Günther et al. [16] who used micro particle image velocimetry and fluorescence microscopy techniques to characterise microscaled segmented gas-liquid flow.

Table 10.2 *Impact of gas flow rate on the dispersion number* $\frac{D}{uL}$ *under slug flow at 20 µl/min liquid flowrate.*

Gas Flowrate (Nml/min)	$\frac{D}{uL}$
0.3	0.01314
0.6	0.00550
1.2	0.00528
4	0.00501

10.4 Conclusion

An on-chip RTD characterisation method using Raman spectroscopy was presented in this chapter. The method presented uses Raman spectroscopy to detect the tracer signal, in conjunction with a specially designed silicon-glass microstructured reactor that aids in the detection of the Raman signal under gas-liquid Taylor flow. The microstructured reactor employs "liquid-diversion" post structures to aid in trapping a liquid pocket for enhanced Raman spectroscopy signal acquisition.

The proposed RTD method was validated using single phase liquid flow, where the measured residence time was <10% different to the actual residence time. Initial studies under gas-liquid flow indicated a reduction in axial dispersion with increase in gas flowrate under segmented flow, which is in agreement with existing work in the literature.

An increase in residence time, followed by its levelling off with gas flowrate was also observed. The increase in residence time whilst in the gas-liquid segmented flow regime can be correlated with a reduction in the slug frequency and length, which is caused by the increase in gas flowrate. The plateauing of the residence time as the flow pattern transitioned from Taylor to annular flow can be linked to the flow pattern type, whereby the dependency of residence time on gas flowrate at > 4 Nml/min becomes

very weak as the gas phase occupies its own distinct space and exerts less of an influence on the liquid phase velocity.

This work builds the foundation for the on-chip detection of residence time distributions in three phase micro-packed beds.

10.5 References

1. Yue, J., Schouten, J.C., Nijhuis, T.A. **Integration of Microreactors with Spectroscopic Detection for Online Reaction Monitoring and Catalyst Characterization**. *Industrial & Engineering Chemistry Research* 2012, 51:14583-14609.

2. Al-Rifai, N., Cao, E., Dua, V., Gavriilidis, A. **Microreaction technology aided catalytic process design**. *Current Opinion in Chemical Engineering* 2013, 2:338-345.

3. Trachsel, F., Günther, A., Khan, S., Jensen, K.F. **Measurement of residence time distribution in microfluidic systems**. *Chemical Engineering Science* 2005, 60:5729-5737.

4. Kreutzer, M.T., Günther, A., Jensen, K.F. **Sample Dispersion for Segmented Flow in Microchannels with Rectangular Cross Section**. *Analytical Chemistry* 2008, 80:1558-1567.

5. Lohse, S., Kohnen, B.T., Janasek, D., Dittrich, P.S, Franzke, J., Agar, D.W. **A novel method for determining residence time distribution in intricately structured microreactors**. *Lap Chip* 2008, 8:431-438.

6. Faridkhou, A., Hamidipour, M., Larachi, F. **Hydrodynamics of gas-liquid micro-fixed beds - Measurement approaches and technical challenges**. *Chemical Engineering Journal* 2013, 223:425-435.

7. Autrey, T., Kandanarachchi, P., Franz, J.A. **Comparison of Diffusion Coefficients of Aryl Carbonyls and Aryl Alcohols in Hydroxylic Solvents. Evidence that the Diffusion of Ketyl Radicals in Hydrogen-Bonding Solvents Is Not Anomalous?** *Journal of Physical Chemistry A* 2001, 105:5948-5953.

8. Levenspiel, O. ***Chemical Reaction Engineering***, 3rd Edition. New York: John Wiley & Sons; 1999.

9. Qian, D., Lawal, A. **Numerical study on gas and liquid slugs for Taylor flow in a T-junction microchannel**. *Chemical Engineering Science* 2006, 61:7609-7625.

10. Hecht, K. ***Microreactors for Gas/Liquid Reactions: The Role of Surface Properties***. Wyoming: Western Engineering, Inc.; 2014.

11. Zhang, H., Tang, S., Liang, B. **Residence time distribution in two-phase flow mini-channel reactor**. *Chemical Engineering Journal* 2011, 174:652-659.

12. Kreutzer, M.T., Kapteijn, F., Moulijn, J.A., Heiszwolf, J.J. **Multiphase monolith reactors: Chemical reaction engineering of segmented flow in microchannels**. *Chemical Engineering Science* 2005, 60:5895-5916.

13. Thulasidas, T.C., Abraham, M.A., Cerro, R.L. **Dispersion during bubble-train flow in capillaries**. *Chemical Engineering Science* 1999, 54:61-76.

14. Pedersen, H., Horvath, C. **Axial dispersion in a segmented gas-liquid flow**. *Industrial & Engineering Chemistry Fundamentals* 1981, 20:181-186.

15. Muradoglu, M., Günther, A., Stone, H.A. **A computational study of axial dispersion in segmented gas-liquid flow**. *Physics of Fluids* 2007, 19:072109.

16. Günther, A., Khan, S.A., Thalmann, M., Trachsel, F., Jensen, K.F. **Transport and reaction in microscale segmented gas-liquid flow**. *Lab Chip* 2004, 4:278-286.

XI.

Conclusions & Future Outlook

The use of microreactors for catalyst and reaction performance evaluation, as well as systems for the acquisition of data for reaction kinetics determination, has been demonstrated in this thesis. In this chapter, the highlights of this research are presented and recommendations for future work are given.

11.1 Conclusions

11.1.1 Microreaction Systems for the Acquisition of Reaction Kinetics and its use for the Identification of Kinetic Models of Methanol Oxidation over Silver Catalyst

Microstructured reactors have been demonstrated as valuable tools in the study of catalytic processes from both a mechanistic and a process operational perspective. Interference of heat and mass transfer non-uniformities, common in larger diameter reactors, masks the study of intrinsic kinetics and surface phenomena taking place on the catalyst surface. In microfluidic environments, improved control of reaction conditions allows safer, more efficient investigations of chemical reactions. The application of microfluidic reactors to a challenging high temperature oxidation reaction has been demonstrated in **Chapter IV**. A continuous flow microfluidic experimental system capable of automated analysis of the entire product range of the partial oxidation of methanol to formaldehyde on silver catalyst was presented. The microreactor and heating assembly design allows operation up to 800°C, without compromising on the temperature uniformity across the reaction zone.

11.1.2 Reaction and Deactivation Studies of Gold-Palladium Catalyst during Benzyl Alcohol Oxidation

A key discovery in the last two decades has been the realisation that gold, when prepared as supported nanoparticles, is exceptionally effective as an oxidation catalyst. Supported Au-Pd catalysts are widely used in industry to perform various chemical processes, such as oxidations and hydrogenations. Recently their use in catalysing the conversion of benzyl alcohol oxidation was found to be promising in the quest for environmentally friendly alternatives. It has been shown in **Chapter V** that the activity and stability of such catalysts depends strongly on their preparation. In particular, the amount of Au and excess Cl used in their preparation has the ability to influence the rate of Au-Pd catalyst deactivation. Although Au and Cl are required to produce catalysts that are more selective with a more uniform nanoparticle size distribution, their presence in excess results in the catalyst becoming unstable with time on stream.

TEM examination of catalysts post-reaction showed an amorphous surface film covering the catalyst surface and Raman spectroscopy revealed the presence of carbon species on the catalyst surface, dependent on the axial position in the reactor. Oxidative regeneration of the catalyst was possible by flowing oxygen through the reactor. Further catalyst characterisation using methods such as temperature programmed oxidation (TPO) and thermogravimetric (TG) analysis would be useful to determine the nature of these carbon deposits. In addition, experiments where we introduce the products (benzaldehyde, toluene, benzoic acid, benzyl benzoate) in the feed may help indicate the role of the products in the deactivation. The optimal catalyst formulation within the catalysts studies was M_{Im} 0.05 wt% Au - 0.95 wt% Pd/TiO_2 and this catalyst was chosen to conduct further hydrodynamic and reaction studies in **Chapters VI**, **VII** and **VIII**.

11.1.3 Hydrodynamics of Multiphase Packed Bed Microreactors: Mass Transfer, Catalyst and Reactor Performance

When scaling down three-phase reactors, the hydrodynamics change significantly to those in industrial and laboratory reactors due to a shift in the dominant forces to viscous and surface tension forces. As a result, the hydrodynamics and correlations available in the literature for conventional scale trickle-bed reactors cannot be extrapolated. In **Chapter VI**, a new flow regime classification for micro-packed bed reactors was presented. Five flow regimes were identified, some of which were analogous to large scale reactor flow regimes. However, for the most part, the flow regime transitions were found to differ from conventional flow regime maps for bench scale reactors.

The interconnected nature of hydrodynamics, mass transfer, reaction performance and catalyst deactivation (portrayed in **Figure 11.1**) was studied in **Chapters VI-VIII**. Despite microreactors having enhanced heat and mass transfer, highly active catalysts are likely to experience internal and external mass transfer resistances. The former can be reduced by reducing particle size, while the latter can be minimised by operating at high G:L flow ratios. Operating at elevated G:L ratios resulted in higher benzaldehyde selectivity, however, beyond a certain point, the hydrodynamics changed significantly

and deactivation was observed in the partially wetted and gas phase flow regimes. The drop in selectivity to the high molecular weight by-products indicates that the deactivation was due to deposition of these by-products. Further work characterising the used, deactivated catalyst (using methods such as TEM, TPO and TG) would aid in confirming this hypothesis.

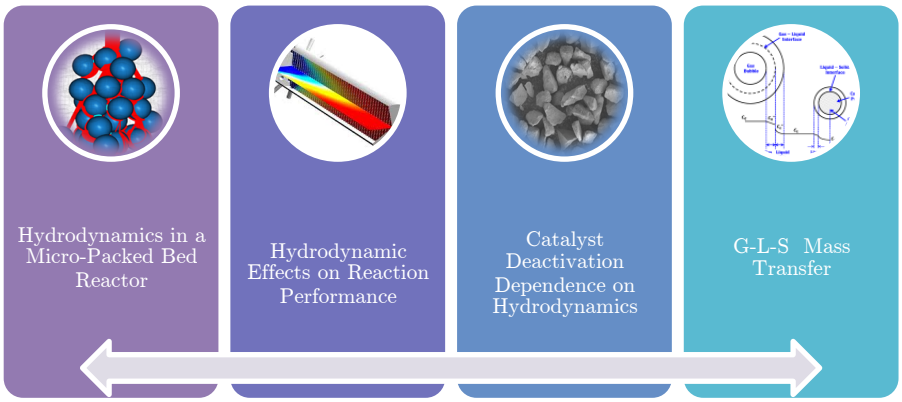

Figure 11.1 *Interconnected nature of hydrodynamics, mass transfer, reaction performance and catalyst deactivation shown in this thesis research.*

11.2 Future Outlook

The current status for micro-reaction technology and its applications for the design of catalytic processes was discussed in **Chapter II**. The recent literature in this field was reviewed, including the use of micro- reactors for intrinsic kinetic studies, in-situ catalyst characterisation, and as part of automated systems for optimisation of operating conditions and kinetics determination. The prospects for advancing catalytic process development by combined application of in-situ spectroscopies and optimisation techniques with microstructured flow reactors were also discussed. The following sections will provide a more specific direction and examples of applications on this front.

11.2.1 Model-Based Design of Experiments with Automated Microfluidic Platforms for Rapid Kinetic Modelling

Significant advances in the robustness and efficiency of model discrimination algorithms have been established in the past where the primary focus has been the selection of the most appropriate criterion for model discrimination approaches. Incorporating these

model discrimination techniques with experimental data are less reported and the experimental design is often obtained beforehand, or updated offline after data collection. Imbedding an automated feedback mechanism to perform experiments, collect data and update the sequential experimental design has been proven to improve the speed of model discrimination (see **section 2.4**). The same concept can also be used as a "black-box" optimisation of reactions (yield/selectivity) without understanding the fundamental kinetics of the reaction. The ultimate aim is to maximise the information obtained from one single experiment. Having a more targeted and dynamic approach to experimentation is considered to have substantial benefits to kinetic data acquisition. Thus, the next step leading on from **Chapter IV**, would be to feed the initial results obtained into a design of experiments algorithm, which would select sequential experiments, maximising the amount of useful information extracted. Initial results of this work have been published, where a model-based design of experiments procedure was used to optimally design experiments for both discriminating among competing models and for improving the estimation of kinetic parameters [1].

11.2.2 Obtaining Correlations Applicable to Micro-Packed Bed Reactors

Micro-packed bed reactors are proving to be ideal lab investigation tools. The limited amount of information on the dominating physical phenomena in those reactors and how they differ to conventional scale reactors restricts their use to the full potential. The RTD method presented in **Chapter X** can be used for a packed bed microreactor to determine residence time distributions, the results of which can be used to determine axial and radial dispersion characteristics, as well as develop mass transfer correlations applicable to micro-packed bed reactors. Simulation tools can be used to effectively design micro-reactors for hydrodynamic and mass transfer purposes. Integrating hydrodynamic and mass transfer studies with reaction performance of various catalytic alcohol oxidation and hydrogenation reactions will enable the study of both reaction kinetics and the optimisation of reaction performance. To enable a more accurate analysis (reduce the experimental uncertainty) as well as eliminate the contribution of the dispersion associated with the flow from the injection valve to the microchannel, on-chip introduction of the tracer is recommended.

11.2.3 Multiplexed Microreactor Systems

Addressing the characterisation of working catalysts and catalytic reactors by the integration of multi-technique approaches for operando catalyst characterisation would provide significant improvements to information generation from microreactor systems. The development of multi-technique approaches for operando catalyst characterisation, by integration of various non-invasive tomographic and spectroscopic techniques such as Infrared, Raman, X-ray Tomography, X-Ray Diffraction, and Liquid Transmission Electron Microscopy (TEM) would offer a toolkit of measurement capabilities over a hierarchy of length-scales – from nm to mm – to address the characterisation of catalysts and catalytic reactors, in terms of elucidation of reaction mechanisms, catalyst start-up and deactivation behaviour, and enhancement of selectivity through catalyst and reactor design. Integration of one or more of these characterisation techniques in flow would allow more efficient, information-rich probing of catalytic reactions and in doing so, improve the selectivity and performance of catalysts, as well as learn how to prepare them as efficiently as possible. The integrated nature of those tasks is portrayed in **Figure 11.2**.

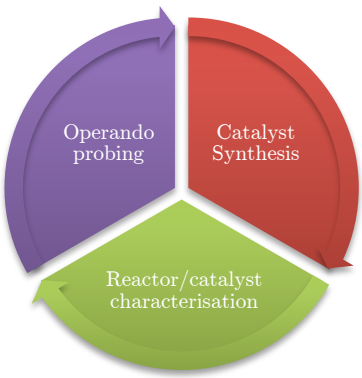

- Development of microreactor systems for the production of chemicals, by the use of multi-step processes with multi-functional catalysts.
- Methods of control over catalyst attributes during its preparation stage, via in-situ synthesis and in-situ spectroscopic observation.
- Operando investigation of catalyst and reactor start-up, reaction, deactivation behaviour and routes to reactivation, for highly active catalysts (such as supported platinum group metals).

Figure 11.2 *Elements constituting the integrated approach to the use of catalytic microsystems.*

An interesting reaction system to apply this methodology to is the synthesis of furan derivatives from biomass. Hexose monosaccharides such as glucose and fructose can be catalytically dehydrated into 5-hydroxymethylfurfural (HMF), which is a chemical precursor for the production of various furan derivatives such as Furandicarboxylic acid (FDA) and Dimethylfuran (DMF). These are important biomass-derived fuels with the

potential to replace non-environmentally friendly alternatives. The process of producing these fuels is currently a challenging task, as it requires two steps, involving the isolation and purification of HMF as an intermediate, followed by separation of the catalyst from the main stream, before the products can be fed into the second stage (**Figure 11.3**) - a labour and cost-intensive process. "One-pot" synthesis has been demonstrated in a batch reactor, where direct synthesis from sucrose to the end furan products has been carried out, but this has been shown to be inefficient given the many reaction routes and product alternatives. A continuous and integrated flow system, formed by assembling a series of microfluidic reactors, each with a catalyst targeted for a specific reaction product outlined in **Figure 11.3** would be an efficient alternative to the batch system, allowing for possibilities to fine tune and target specific products by altering the catalyst, reactor design and reaction conditions. Initial results of this type of work has been demonstrated in capillary reactors [2].

Operando characterisation of the reactions at relevant temperatures and pressures in the presence of reactants would need to be carried out, where the catalytic activity and selectivity of the catalyst material are determined via on-line product analysis (mainly using chromatographic/mass spectrometric methods) in tandem with spectroscopic analysis of the reactor and catalyst surface, thus making it possible to identify important structure-activity relationships. The study of surface species and reaction intermediates to enable elucidation of reaction schemes and to obtain a mechanistic insight into the reaction on the catalyst surface would enable acquisition of reaction kinetics.

Acquiring sufficient, detailed information about the catalyst material during its synthesis and immobilisation is key to optimising the catalyst formulation and its preparation method. *In-situ* characterisation is necessary to understand factors affecting the precursor transport within the support during catalyst preparation, without interruption of the preparation process; this technique would replace conventional catalyst characterisation methods, usually achieved by analysis of bisected catalysts at the different stages of their preparation. Integrating *in-situ* synthesis of the catalyst and its immobilisation with reaction would bridge the gap between two rather inter-dependent but currently disconnected activities.

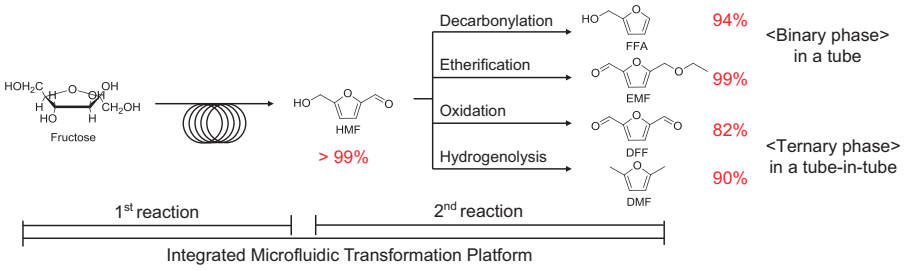

Figure 11.3 *Step-wise conversion of fructose into the four types of furanics via 5-hydroxymethylfurfural (HMF) [2].*

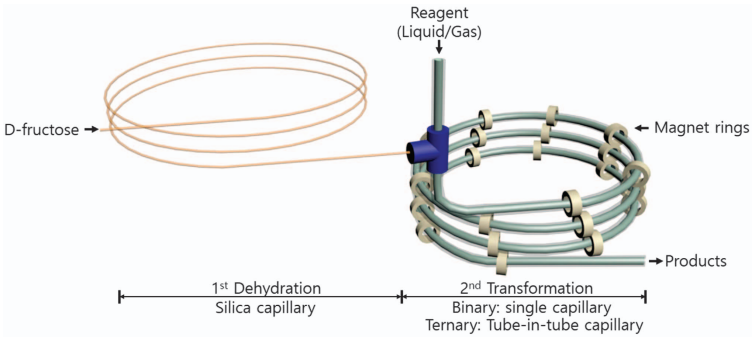

Figure 11.4 *Illustrative scheme of integrated multi-step microreactor system for direct conversion of fructose into furanics [2].*

11.3 References

1. Galvanin, F., Cao, E., Al-Rifai, N., Dua, V., Gavriilidis, A. **Optimal design of experiments for the identification of kinetic models of methanol oxidation over silver catalyst**. *Chimica Oggi-Chemistry Today* 2015, 33:51-57.

2. Jeong, G.Y., Singh, A.K., Sharma, S., Gyak, K.W., Maurya, R.A., Kim, D.P. **One-flow syntheses of diverse heterocyclic furan chemicals directly from fructose via tandem transformation platform**. *NPG Asia Materials* 2015, 7:e173.

Appendix A

Methanol Oxidation to Formaldehyde in a Wall-Coated Microreactor Supplementary Information

This Appendix presents supporting information for the gas phase methanol oxidation to formaldehyde system, including the following:

A1. Analytical Method Development

Gas Chromatograph General Description

Gas chromatography (GC) is a technique typically used in analytical chemistry for separating and analysing compounds. The technique relies on a mobile phase and an inert carrier gas to sweep the sample through a glass or metal column lined with a stationary phase consisting of a liquid or polymer, on an inert solid support. To be suitable for GC analysis, a compound must have sufficient volatility and thermal stability. If all or some of a compound's molecules are in the gas or vapour phase at 400-450°C or below, and they do not decompose at these temperatures, then the compound is suitable for GC analysis.

Principle of Operation

The GC internal layout is shown in **Figure A1**. The sample is introduced into the first column through the switching of a gas sampling valve. The vaporised solutes are transported by helium into the column, which is maintained in a temperature controlled oven. The gaseous compounds interact with the walls of the column, causing each compound to elute at a different time, known as the retention time. The separated components then travel to the thermal conductivity detector (TCD) which compares the thermal conductivities of two gas flows; pure carrier (or reference) gas and the column effluent (carrier gas plus sample components). The detector contains a filament that is heated electrically; the filament temperature is held constant while alternate streams of reference gas and column effluent pass over it. When a sample component appears in the effluent, the power required to keep the filament temperature constant changes. The two gas streams are switched over the filament five times per second and the power differences are measured and recorded.

An electronic signal is generated and the size of the signal is recorded by a data system (Agilent ChemStation software) and is plotted against elapsed time to produce a chromatogram [1]. The gas chromatograph used here consists of 4 columns (**Table A1**). Initially, a bonded polystyrene divinylbenzene based column (HP-Plot Q) was unable to separate water and formaldehyde. These results are in-line with previous

work where a similar column, the Porapaq-Q, (also containing divinylbenzene as the stationary phase) could not separate water and formaldehyde [2]. The column was then substituted with a GS-Carbon PLOT (Porous layer open tubular), equivalent to the Carboxen 1006, commonly used for the separation of formalin (water, formaldehyde and methanol) solutions. Other columns present in the GC are the HP PLOT Molesieve to resolve for the permanent gases, a Haysep Q pre-column for back flushing of unwanted and heavy molecular weight compounds, and a final fourth column specific for heavy molecular weight hydrocarbon analysis.

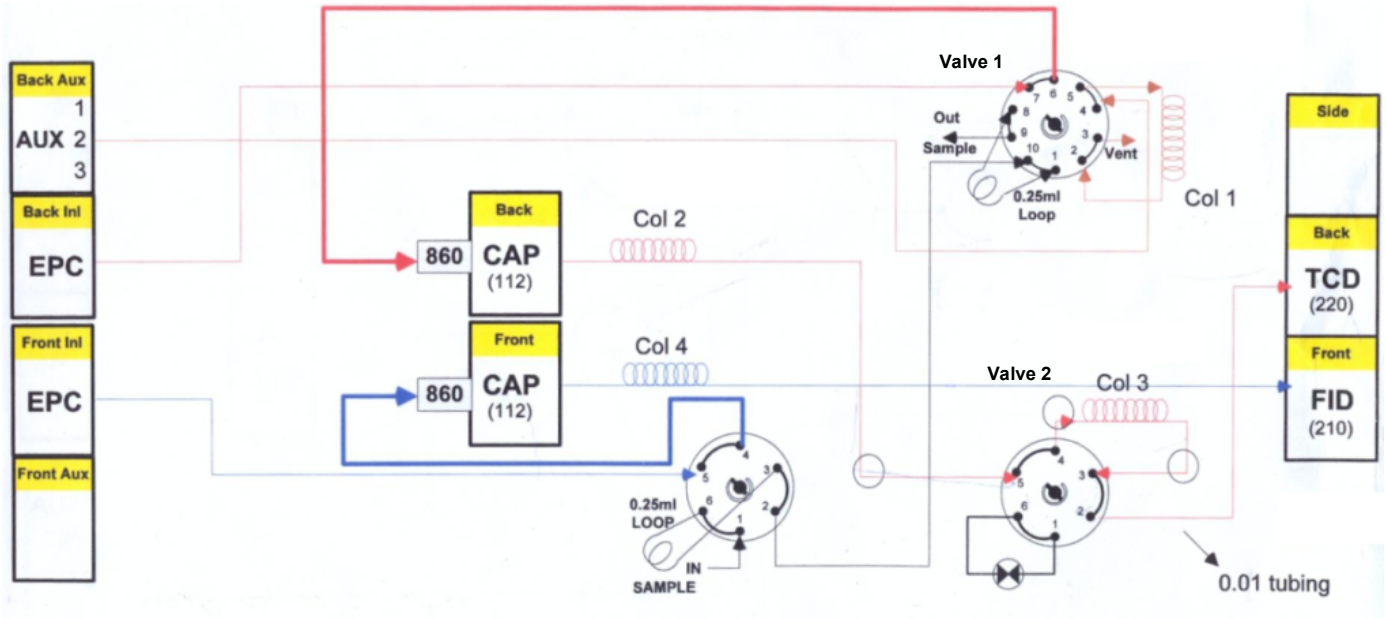

Abbreviations:

AUX: Auxillary unit

TCD: Thermal Conductivity Detector

FID: Flame Ionisation Detector

EPC: Electronic Pneumatic Controller

Figure A1. *Gas chromatograph internal layout.*

Table A1. *Gas Chromatographic Columns.*

Column Name	Column type	Application
1/Haysep Q	Packed Column	Back flush unwanted components
2/GS-Carbon PLOT	Bonded monolithic carbon layer	C1-C5 hydrocarbons, CO2, air/CO, trace acetylene in ethylene, methane
3/HP PLOT Molesieve	5Å molecular sieve zeolite	Permanent and noble gases
4/HP-FFAP	Polyethylene glycol-acid modified	Organic acids, alcohols, aldehydes, ketones, acrylate

Peak Identification

The main reactants and products in the oxidative dehydrogenation of methanol to formaldehyde reaction are methanol, oxygen, formaldehyde, CO_2, CO, H_2 and H_2O. Common by-products of the reaction are formic acid and methyl formate. Formalin solution (consisting of formaldehyde, water and methanol) were evaporated using the microevaporator and passed through the GC for peak identification. Similarly, a standard calibration gas containing 10 mol% oxygen, 2 mol% carbon dioxide, 0.5 mol% hydrogen, 0.1 mol% CO was used for peak identification. **Figure A2** shows a typical chromatogram.

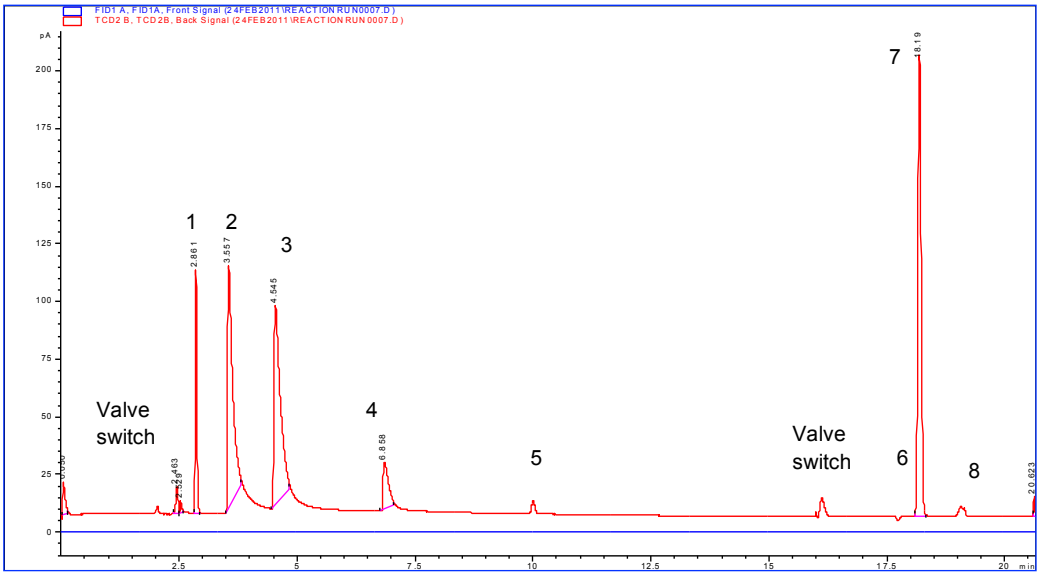

Figure A2. *Typical chromatogram of product mixture 1) Carbon dioxide, 2) Water, 3) Formaldehyde, 4) Methanol, 5) Unidentified peak, 6) Hydrogen, 7) Oxygen, 8) Unidentified peaks.*

Valve Event System

The gas chromatograph contains 3 valves, 2 of which are used in this analytical technique; a gas sampling valve (valve 1) to introduce the sample into the column, and a valve (valve 2) to isolate the molecular sieve. A valve event system was required to avoid the CO_2 from trapping on the molecular sieve, as this is damaging to column 3 (HP-PLOT Molesieve). The usual pathway for the analytes as they are injected into the sampling loop is the following: Column 1 > Column 2 > Column 3 > TCD. The valve event system was coordinated to trap the O_2, H_2, CO on column 3 (HP-PLOT Molesieve) before the CO_2 has the chance to elute from column 2 to column 3. At time 0, when the gas sampling valve is switched on, the sample is sweeped through column 1. The permanent gases travel faster and reach the HP-PLOT Molesieve (Column 3) at a time of 3 minutes, just before CO_2. The Molesieve (Column 3) is then isolated by switching Valve 2 ON, trapping the permanent gases there until the CO_2, methanol, formaldehyde and water are separated on Column 2 and reach the TCD producing a signal. The Molesieve (Column 3) is then brought back in line by switching valve 2

OFF and the permanent gases (O_2, CO, H_2) are resolved for and eluted onto the TCD. Column 4 - connected to the FID - is specific to high molecular weight hydrocarbons and is not used in this analysis. **Figure A3** and **Table A2** summarise this sequence of events.

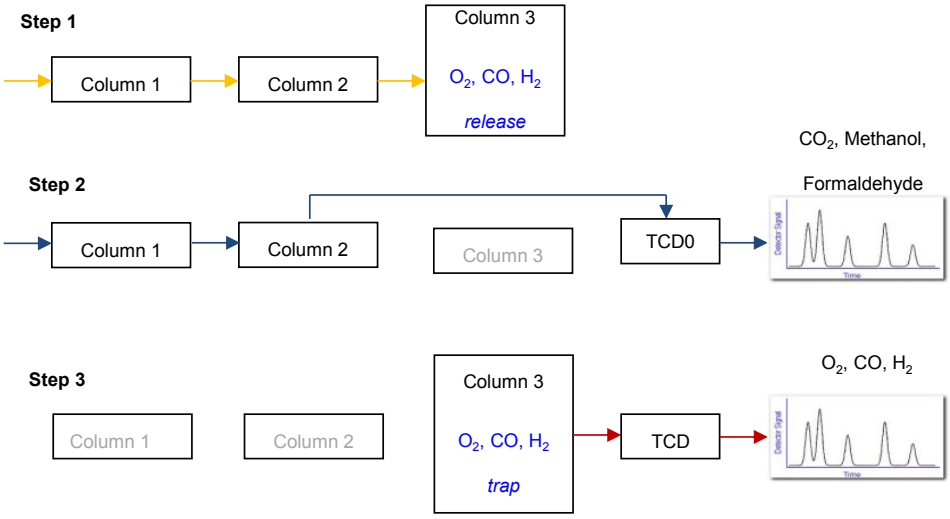

Figure A3. *Valve event system*

Table A2. *Valve event system*

Time (min)	Valve Number	Event	Action
0.01	1	ON	Switches the sampling valve ON and allows sample in to columns
0.01	2	OFF	Brings the Molecular Sieve in line to trap permanent gases
1.00	1	OFF	Switches the sampling valve OFF to allow refilling of sample loop
3.00	2	ON	Isolates the Molecular Sieve and analyses for the hydrocarbons, CO_2 and water
12.0	2	OFF	Brings the Molecular Sieve back in line and analyses for the permanent gases

Optimised GC Operating Conditions

The aim of the GC method optimisation is to achieve well-resolved, sharp, Gaussian peaks. This is carried out through an optimisation of the carrier gas velocity, oven temperature and oven temperature ramp rate. Additional constraints are present in this system: a time-gap is essential between the O_2 and the CO_2 retention time at the beginning of the run, to enable trapping of the CO_2. Generally, an increase in the temperature and flowrate through the column results in the peaks eluting quicker and closer to each other. This means that the temperature and flowrate for the first 3 minutes need to be kept low in order to increase the time difference between the O_2 and CO_2 peak elution. The temperature is then ramped up for the water, formaldehyde, methanol and ramped back down again to promote separation of the permanent gases. **Table A3.** below shows the finalised GC method parameters.

Table A3. *GC Operating Conditions.*

Oven		
Temperature (°C)	**Ramp (°C/min)**	**Hold time (min)**
70	0	3
200	15	0
70	40	5
Carrier Gas		
Flowrate (ml/min)	4	
Reference (ml/min)	20	
Make-up (ml/min)	5	
TCD Detector		
Temperature (°C)	250	
Injector		
Temperature (°C)	200	
Split ratio	5:1	

A2. Gas Chromatograph Calibrations

Pressure Control

The state of an amount of gas is determined by its pressure, volume, and temperature. Thus, gas chromatographic signals are highly influenced by the pressure at the inlet and outlet of the gas sampling loop. For this reason, it is important to carry out the calibrations at the same pressures used in the reaction. The pressure is selected to either boost certain weak signals, or for other reasons based on the design of the experimental set-up. There are three considerations for this experimental set-up:

1) The hydrogen signal is weak due to a similarity in the thermal conductivities between hydrogen and the carrier gas helium;
2) Higher pressure at the gas sampling loop exit (P_3) will force more liquid to condense at the liquid trap before the backpressure regulator and thus would require emptying at more frequent intervals. Three different gas sampling loop outlet pressures (P_3) between 1.3-1.55 bar (absolute) were studied to test their impact on the peak areas. The pressure at the gas sampling loop inlet was kept constant at 1.6 bara through the use of a backpressure regulator (BPR).

It would allow flexibility if one was able to change pressures in the system without having to recalibrate the GC signal. This is particularly useful for the components that are difficult to calibrate for, such as methanol and formaldehyde. An average peak area per bar of pressure (pressure measured at P_3) was calculated, this can be used in the future if the outlet pressures were to be changed without the need for recalibration. The results for this analysis are shown in **Table A4.**

Table A4. *Impact of sample loop pressure on peak areas.*

Component	P3 (bara)	Average Peak Area (uV.min)	Peak area/bar [at P3] (uV.min/bar)	Average peak area/bar [at P3] (uV.min/bar)	%RSD
O_2	1.30	1905.5	1465.8	1466.0	2.2%
	1.55	2223.4	1434.5		
	1.60	2396.4	1497.8		
CO_2	1.30	481.525	370.4	360.1	2.5%
	1.55	548.991	354.2		
	1.60	569.04	355.7		
CO	1.30	21.48	16.52	16.12	2.8%
	1.55	25.10	16.19		
	1.60	25.03	15.64		
H_2	1.30	3.75	2.9	3.1	5.8%
	1.55	4.73	3.1		
	1.60	5.18	3.2		

Formaldehyde GC Calibration

Formaldehyde is an unstable gas that readily converts to its polymer paraformaldehyde at room temperature. For this reason, there is no calibration standard available. There are formalin solutions (37% (w/w) formaldehyde in methanol/water) available, however when evaporated using the microevaporator and analysed using the GC, the formaldehyde and the water peaks co-eluted due to the high proportion of water in the mixture and the inability of the column to resolve between the two at the high concentration of water present.

A logical method of producing formaldehyde is by dry heating the solid paraformaldehyde at different temperatures to yield different concentrations of the gas. In order to determine the amount of formaldehyde being produced, an inert gas can be used as an internal standard to monitor the change in volume as the paraformaldehyde is heated to its formaldehyde monomer.

Figure A4 is a diagram of the experimental set-up used for the calibration of formaldehyde. Paraformaldehyde (4.9 g) was packed into a steel column (in earlier trials a glass column was used, both are shown in **Figure A4**). The powder was tapped until no further change in volume was observed. The tapped volume was 8 ml. The outlet from the column was directed towards the valve box and then to the GC. The temperature of the column was changed sequentially between 40°C and 80°C via a fibreglass heating coil attached to a temperature controller; heating the paraformaldehyde to different temperatures would yield different formaldehyde concentrations. Temperature controllers were also used to keep the temperature in the exit stream high enough to prevent the condensation of the formaldehyde.

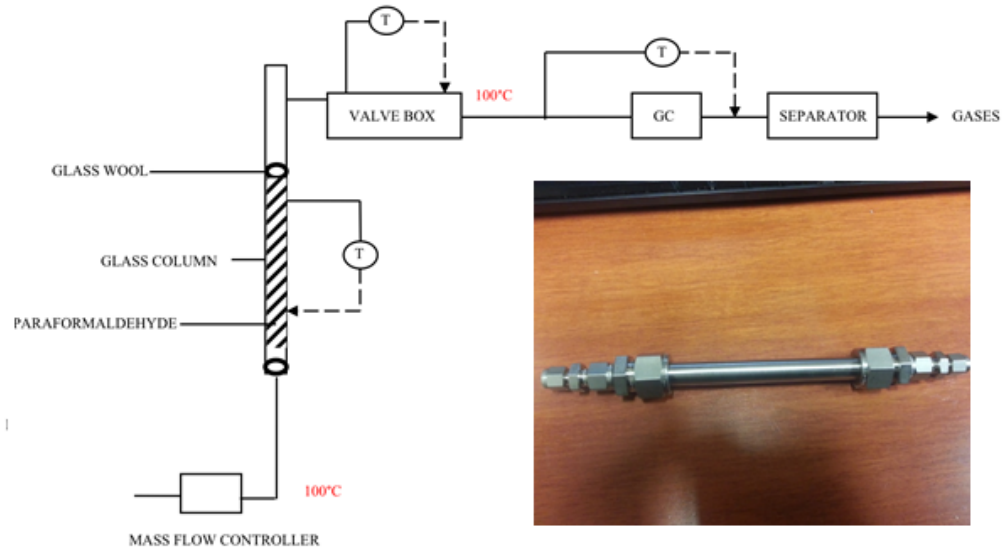

Figure A4. *Formaldehyde calibration apparatus and steel column.*

Internal Standard Calibration Method

The internal standard calibration method utilises a constant amount of an internal standard, a chemical or gas with a distinct retention time to the analyte, which is added to the sample at a constant concentration. The change in its concentration with the introduction of the analyte of interest is then monitored. The increase in volume can be calculated based on the detected decrease in concentration of the internal standard through the following equation:

$$C_1V_1 = C_2V_2 \qquad (A.1)$$

Where C_1 is the inlet internal standard concentration (set), V_1 is the total inlet volumetric flowrate (set), C_2 is the internal standard outlet concentration (measured) and V_2 is the outlet volumetric flowrate following introduction of the formaldehyde (calculated).

The internal standards tested were oxygen and CO_2, the former diluted with helium (C_1 was selected to be 10 mol %), V_1 (15 ml/min) is the total inlet gas volumetric flowrate, C_2 is the measured nitrogen (or oxygen) concentration and V_2 is the calculated final volumetric flowrate.

Due to the evaporation of formaldehyde into the flowing stream, the concentration of nitrogen in the exit stream (C_2) decreases and the total exit volume (V_2) increases. The change in volume, V_2 -V_1 is thus the volume of formaldehyde produced as a result of the dry heating and was translated to a number of moles of formaldehyde produced.

The internal standard method was initially unable of giving an accurate prediction of the methanol concentrations. It was later concluded that it was as a result of mass flow controller fluctuations when mixing the internal standard (oxygen) with the diluent (helium) to achieve a 10 mol% inlet concentration C_1. The fluctuations in mass flow controller 1 (helium) used to dilute the internal standard to the required concentration were +/-3% of the set value, which results in large inaccuracies in the inlet concentration predictions. It may also be partially due to the use of O_2 as the internal standard, as even when a calibration standard gas containing the exact concentration of internal standard was used (without diluting with helium), the reproducibility of the

oxygen peak areas was still unacceptable (the reproducibility is acceptable under normal operating conditions, but not precise enough for the internal standard method which requires a reproducibility of <0.5%).

The problem was eventually resolved by using a CO_2 calibration standard with the required internal standard concentration. The internal standard used was 2% CO_2 with a total flowrate of 15ml/min (helium mass flow controller used after being calibrated for the gas mixture) from a gas mixture containing 10% O_2, 2% CO_2, 1% H_2, 0.1% CO and helium as balance. It was notable that the reproducibility of the CO_2 GC peak areas was better than the reproducibility of the O_2 peak areas, where the relative standard deviation (RSD) of 5 repeats was double in the O_2 situation (**Table A5**). The calibration results are shown in **Figure A5** .

Table A5. *Comparison of the reproducibility of the oxygen and carbon dioxide peak areas using the gas chromatograph. The measure for reproducbility used is the percentage difference between the maximum and the minimum peak area.*

	Inlet CO_2 Peak Area (uV.min)	Inlet O_2 Peak Area (uV.min)
	498	2010
	501	2026
	503	2054
	501	2046
	504	2057
Relative Standard Deviation (%)	0.46	0.98

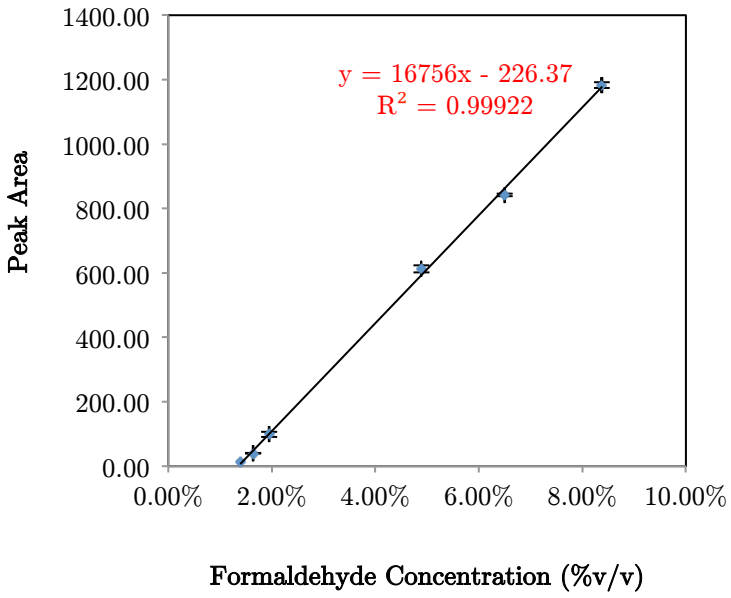

Figure A5. *Formaldehyde GC calibration graph.*

Methanol Calibration

Two methods for the methanol calibration were investigated:

i. internal standard method
ii. theoretical prediction based on vapour-liquid equilibria.

It will be shown that the second method was found to be the most accurate.

Methanol calibration using internal standard

Helium/oxygen gas mixtures with a known total volumetric flowrate and oxygen concentration (10 mol% Oxygen) were first flowed through the GC. Methanol was then pumped into the system using a milliGAT rotary piston pump and evaporated in the microevaporator (set to a temperature of 40°C) where it mixed with the gas mixture entering the evaporator at a temperature of 70°C. The outlet oxygen and methanol peaks were then analysed. The increase in volume due to the methanol being in the system (V2-V1) was then translated to number of moles of methanol.

The results showed that the molar flowrate of methanol calculated from the internal standard method is 1.204 x 10^{-4} mol/min and that set by the pump is 1.240 x 10^{-4}

mol/min indicating agreement between the actual amount and the amount inputted by the pump (see Internal Standard Calculation below).

Calculation: Internal standard method to validate methanol calibration

To calculate the moles of methanol inputted into the system, the volumetric flowrates set by the piston pump were converted to molar flowrates as follows:

Set flowrate: 5µl/min = 0.0844µl/s

Basis: minutes

v_o=0.005ml

ρ=0.792g/ml,

∴ mass= $\rho \times v_o$= 0.792 g/ml × 0.005ml = 0.000396g methanol

moles = mass/RMM = 0.00396/32=**0.000124 mol methanol inputted by pump**

To calculate the moles of methanol reaching the detector, this is done through the internal standard method:

Using equation (A.1) and the concentrations and volumes of oxygen internal standard,

C_1=9.62 mol% O_2

V_1=25 ml/min (at 25°C), so 25 ml/min (STP*) $\times \frac{273}{298}$

C_2=8.60 mol% (measured O_2 at exit using the GC)

$V_2 = \frac{C_1 V_1}{C_2} = \frac{9.62\ \text{mol\%} \cdot 25\ \text{ml/min (STP)} \times \frac{273}{298}}{8.60\ \text{mol\%}} = 25.61$ ml/min STP

To convert the volumetric flowrate to a molar flowrate, the following relationship is used:

$$\frac{V}{22.4 \frac{L}{mol}(STP)} = moles$$

* *STP: Standard temperature and pressure (0°C and 1 atm, IUPAC)*

$$\frac{2.7\times10^{-3}L}{22.4\frac{L}{mol}(STP)}$$

= **0.0001205 mol methanol calculated using internal standard method**

This value and the actual value calculated by the pump are very similar, and therefore this validates the internal standard method for methanol calibration.

Theoretical Prediction using Vapor-Liquid Equilibrium (VLE)

Calculation of the vapour pressure of methanol was carried out using the Antoine equation:

$$\ln(P_i) = \left(\frac{a-b}{T+c}\right)$$

Where $a = 18.5875, b = 3636.55,\ c = -34.29$ and P_i is the vapour pressure of methanol, T is temperature [K].

Conversion of this value to a mole fraction was carried out using the following equation:

$$X_i = P_i/P_T$$

Where P_T is the total pressure.

A 100 ml flask bottle with 3 ports was filled with methanol and placed in a water bath set to temperatures of 5°C, 10°C, 15°C and 18°C to achieve different methanol vapour pressures. The total pressure P_T was measured at one of the bottle exit ports using a digital manometer (**Figure A6**). Using the theoretical prediction of the methanol concentrations, the goodness of fit of the resulting calibration graph is very good (**Figure A7**). However, the internal standard prediction could not be fitted to a straight line. Nevertheless, if a line is fitted through the internal standard prediction,

the two results give very similar concentration predictions within the desired methanol concentration range.

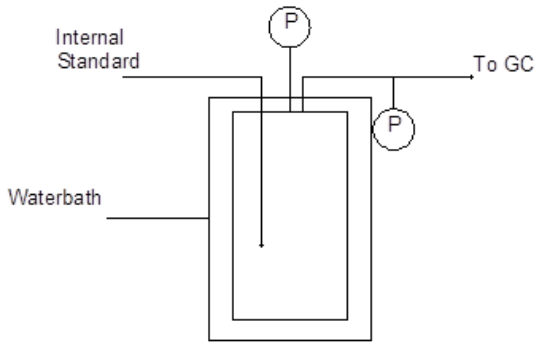

***Figure A6**. Schematic of methanol calibration apparatus using the theoretical VLE method.*

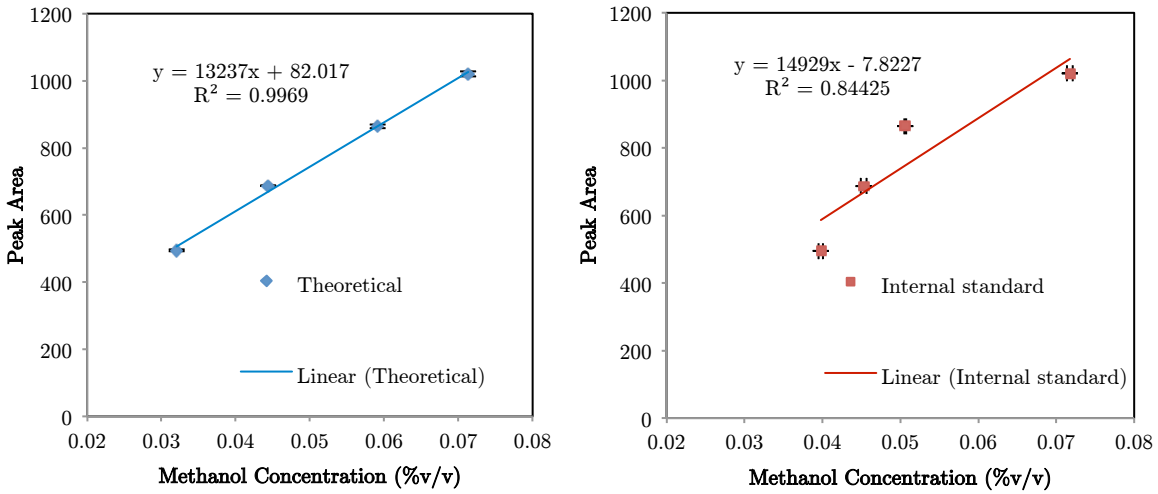

***Figure A7.** Methanol calibration using the theoretical VLE prediction and the internal standard method (CO_2 was used as the internal standard here). X-error bars represent the standard deviation in the methanol concentration calculated and the y-error bars represent the standard deviation in the methanol peak area.*

Gas Calibrations

One level gas calibrations were carried out using a gas calibration standard containing 10% Oxygen, 0.1%CO, 2% CO2 and 0.5% hydrogen with helium as balance. The calibrations of the permanent gases are shown below in **Table A6.**

A3. Equipment Calibrations

Mass Flow Controller Calibrations

The mass flow controllers were calibrated for the correct gases by the manufacturing company. To check this calibration, the actual flowrate they are supplying was measured by passing the gas through a bubble meter. The time the bubble takes to travel up the cylinder was measured and the flowrate calculated. All volumetric flowrates are recorded at STP (0°C and 1 atm, IUPAC) and converted from a wet to dry basis using a combination of Dalton's law of partial pressure and the combined gas law:

$$V_D = \frac{P - P_w}{P} \times V_W$$

where V_W= Wet gas volume, V_D=Dry gas volume, P=Atmospheric pressure, P_W=Vapour pressure of water at lab temperature.

Table A7 shows the accuracy of the flowrates obtained using this method, first after correcting for the moisture content, and then after making the correction for the temperature. As the results are corrected for the moisture and the temperature, the flowrate is brought closer to the initial set value and the percentage error decreases from ~5% to ~1.5%. The remaining error is suspected to be associated with inaccuracy in reading the meniscus. As a result, the calibrations carried out using the bubble meter were not used and the set flowrates were only corrected for the temperature in the lab, which varied between 19 – 24°C.

Table A6. *Permanent gas calibration results for H_2, O_2 and CO on the HP Plot Molesieve and on the GS-CarbonPLOT for the CO_2*

	Concentration (%)	Sample 1	Sample 2	Sample 3	Average	STDEV	RSD	%RSD	Response Factor
CO2	**2.00%**	516	514.7	509.9	513.5	3.213	0.00626	0.626	25677
H2	**1.00%**	11.6	11.6	11.5	11.6	0.058	0.00499	0.499	1157
O2	**10.00%**	2006	2017	1999	2007.3	9.074	0.00452	0.452	20073
CO	**0.10%**	18.4	18.3	17.6	18.1	0.436	0.02408	2.408	18100

Table A7. *Accuracy of mass flow controller calibration using a bubble meter*

Set flowrate (ml/min)*	AAF¥ (ml/min) (23°C, 1 atm)	% Error in AAF¤ repeated samples	AAF¥ corrected for M† (ml/min) (23°C, 1 atm)	% Error in AAF¥ corrected for M† repeated samples	AAF¥ corrected for T‡ and M† (ml/min) (20°C, 1 atm)	% Error in AAF¥ corrected for T‡ and M†
20	21.1	5.50%	20.54	2.70%	20.29	1.45%
20	21.1	5.50%	20.54	2.70%	20.29	1.45%
20	20.95	4.75%	20.36	1.80%	20.12	0.60%

*Mass flow controller calibrated at 20°C, 1 atm by manufacturer † M: moisture ‡ T: temperature; ¥AAF: Actual Actual Flowrate;

Liquid Pump Calibration

The pump calibration was carried out using a 1 ml graduated glass cylinder. The size of the cylinder was selected based on the flowrates that were required. The flowrates selected for the calibration were 2-10 µl/min based on preliminary checks of the residence times that will be used during the reaction. The smallest graduation on the 1ml cylinder is 10 µl, thus making the measurement easier and more accurate for this flow rate range. The calibrations confirmed that the set flowrate was indeed accurate and therefore no calibration graph was used for the liquid pump.

A4. Microfabrication

Standard Microfabrication Procedure

Photolithography

The microreactors used in this work were fabricated by photolithography and deep reactive ion etching, a conventional semi-conductor processing technique used in the micro-electromechanical systems. A thick photoresist layer (Rohm and Haas, SPR-220-7) was spun-coated on a silicon wafer at 4000rpm, followed by soft-baking at 110°C for 90 seconds. The microreactor patterns were transferred from a photomask to the photoresist using UV exposure carried out in a contact aligner (Quintel Q4000-6). The exposure energy for the photoresist was 470mJ/cm^2, which is approximately equivalent to exposure of 300nm UV light for 35 seconds. The photoresist was then aged for 30 minutes at room conditions to reinforce its adhesion to the silicon surface. The patterns were developed by immersing the wafer into a standard photoresist developer (Shipley Microposit MF-26A), for 80 seconds. After thorough rinsing, a final post-baking process at 110°C for 90 seconds was carried out.

Deep Reactive Ion Etching

The patterned wafers were etched using a deep reactive ion etcher (STS ASE) (details in **Table A8**). The etched depth of the micro-channels was measured using a surface

profiler (Veeco Dektak 8). The wafers were then finally cut into the designed dimension using an automated precision dicing saw (Disco DADS 3230).

Anodic Bonding

The final step of the microreactor fabrication was sealing of the silicon with a glass piece using anodic bonding. The etched microreactors and purchased glass pieces (Corning 7740, Newcastle Optical) were first cleaned with Piranha solution (sulphuric acid and hydrogen peroxide in a 3:1 (v/v) ratio) at 100°C for 15 minutes to remove organic contaminants from the wafer surfaces. Both the silicon chip and the glass were rinsed with de-ionized water and dried thoroughly by nitrogen blowing. The glass and silicon were contacted and anodically bonded, a method that provides sealing via the use of high temperature and an externally applied electric field. This was done by assembling the silicon and glass on top of each other and heating on a hotplate (Stuart SD162) to a temperature of 420°C. A D.C. power supply connected to the assembly (such that the positive terminal was connected to the silicon wafer and the negative terminal was connected to the Pyrex glass wafer) was then switched on to apply an electric field of 500 V across the assembly for as long as necessary for the bonding to take place (usually <1 minute). The resulting bond is essentially irreversible.

Table A8. *DRIE parameters used in microfabrication.*

Coil Power	600W (Dep) 800W (Etch)
Platen Power	0W (Dep) 12W (Etch)
Chamber Pressure (mTorr)	35
Flowrate of SiF_6 (ml/min)	0 (dep) 130 sccm (Etch)
Flowrate of O_2 (ml/min)	0 (dep) 6 sccm (Etch)
Flowrate of C_4H_8 (ml/min)	85 sccm(dep) 0 (Etch)
Passivation cycle time (s)	6
Etching cycle time (s)	8

Two-step single side photolithography

The first step of the two-step single side photolithography procedure involved a normal photolithography and DRIE procedure, etching to the required 120μm depth (as described in the *Standard Microfabrication Procedure*). This was followed by manual coating of the etched channels with SPR 220-7 photoresist, leaving the halo areas exposed (**Figure A8**). The exposed halos were then etched all the way through using DRIE, while the channels remained protected by the photoresist. This procedure was challenging and not successful; the challenges faced related to the poor control of photoresist thickness applied, which often resulted in photoresist layers that were too thick and therefore difficult to bake.

Two-step double side alignment and photolithography

The two-step double side alignment and photolithography procedure required two masks: one mask for the patterning of the front side of the wafer (**Figure A9a**) and the other for patterning the back-side of the wafer (**Figure A9b**). The first step involved a normal photolithography and DRIE procedure, etched to the required 120μm depth (as described in the *Standard Microfabrication Procedure*) using the mask in **Figure A9a**.

The second step involved patterning the backside of the wafer with the mask in **Figure A9b** and etching until the white halo areas were completely removed. The patterning required perfect alignment between the front and backside of the wafer, which was carried out using the infrared function of the mask aligner (Q4000-6, Quintel). The specially designed alignment marks were used to align the pattern (**Figure A10a**) on the front side of the wafer, with the pattern (**Figure A10b**) on the backside of the wafer such that the features in the latter fit inside the larger features in the former. This two-step double side alignment was found to be the preferred procedure for etching halo features on silicon devices.

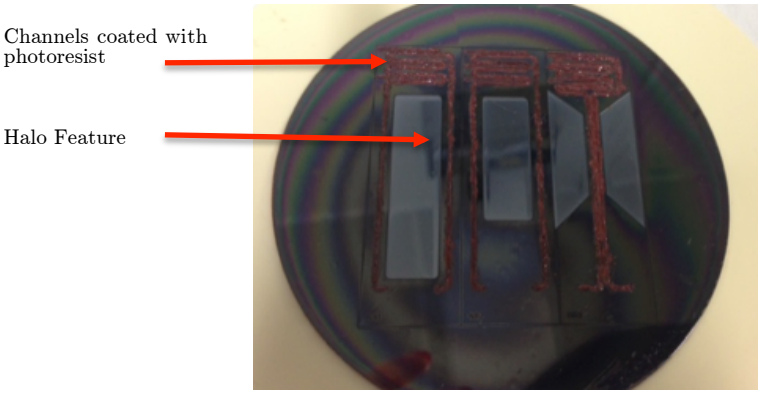

Figure A8. *Schematic of silicon wafer undergoing two-step single side photolithography for the creation of halo features in microchannels.*

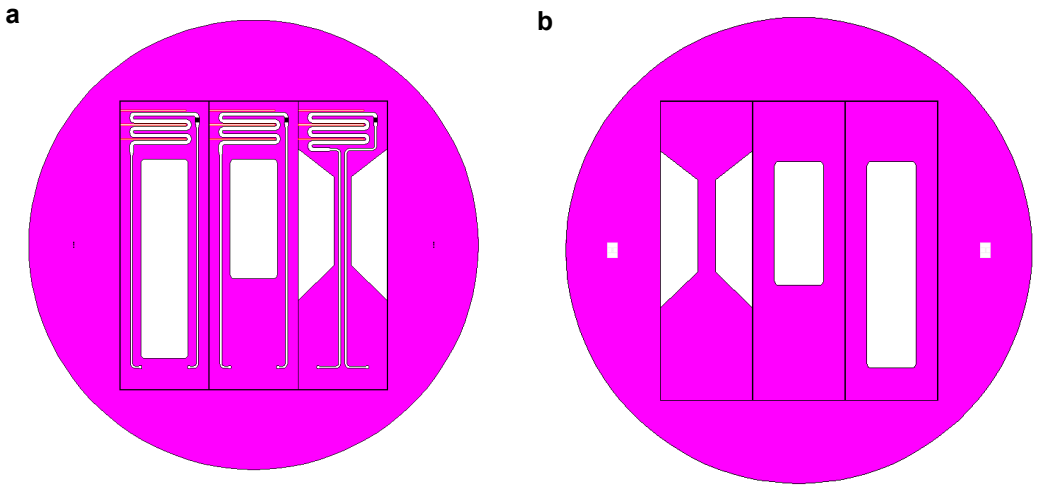

Figure A9. *Silicon wafer that has undergone photolithography and DRIE, followed by manual coating of the channels with photoresist.*

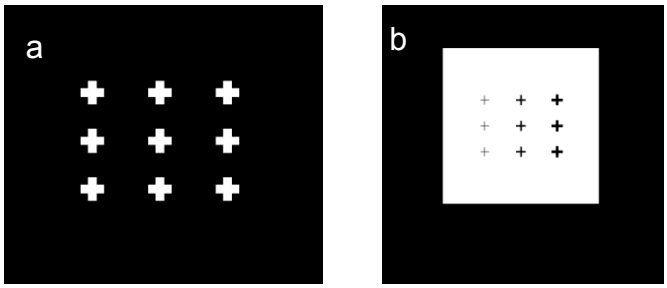

Figure A10. *Alignment marks positioned on the (a) front-side mask and (b) back-side to aid the alignment when using the infrared.*

A5. Calculation of Feed Flow rates

The calculation of the input feed flowrates was based on the required residence time and reactant mole fractions (**Table A9**). The **total feed flowrate required, F_{A0}** was calculated based on the reactor volume and required residence time. This was then used to calculate the **molar flowrate**, N_{A0}, in the reactor at reaction conditions, using the PV=nRT relationship. This molar flowrate was then multiplied by the required c**omponent mole fraction** of each component in the feed, which was then converted to a **feed flowrate** through the use of the **density**. Example outputs of the calculation are shown in **Table A9**.

A6. Dependence of Conversion and Selectivity on Residence Time

Details of the experiment conducted in **Chapter IV** which looked at investigating the dependence of conversion and selectivity on the residence time can be found in **Table A10.**

Table A9. Example spreadsheet showing the calculation of feed flowrates based on desired mole fractions and residence time.

Reactor volume, V (mm3)	11
Residence time, τ (ms)	6.7
Total Feed Flowrate, F_{A0} (mm3/ms)	1.641791045

P (Pa)	160000
V (m^3/s)	1.64179E-06
R (J/Kmol)	8.314472
T (K)	808

Molar Flowrate (N_{A0}/s)	3.91E-05
T in lab (K)	297

	Component Mole Fraction (%)	Moles/s	Mass (g)	density @ STP (g/cm3)	Volume STP (cm^3)	Actual volume (µl/s)	Feed Flowrate ml/min
CH_3OH	9.82%	3.8E-06	0.000123	0.791000	1.55E-04	1.55E-01	9.32E-03
O_2	4.36%	1.7E-06	0.000055	0.001429	3.82E-02	4.16E+01	2.49E+00
H_2O	7.44%	2.9E-06	0.000052	0.999000	5.24E-05	5.24E-02	3.14E-03
He	78.38%	3.1E-05	0.000123	0.000177	6.93E-01	7.54E+02	4.52E+01

Total Volume CH3OH and H2O (µl/s)	0.21
Water (v/v) %	25.23%
CH3OH (v/v) %	74.77%

Table A10. *Details of experiment probing the impact of residence time on conversion and selectivity.*

					R1, L_{Az}=8.81 cm	R2, L_{Az}=3.57 cm	R3, L_{Az}=1.78 cm
				V_r (cm³)	0.00952	0.00386	0.0019
Flow Conditions	$v_{t,o}$, (Nml/min)	y_{in}	u_g (P_{avg},T) (m/s)				
$v_{l,o}$=0.273 µl/s	73.13		17.03	Pin, bara	2.6	2.9	2.9
				Pavg, bar	2.1	2.25	2.25
	CH_3OH	0.0994		t, ms	5.18	2.21	1.09
	O_2	0.0415		X_{CH3OH}	86.89	85.96	70.09
	H_2O	0.0753		S_{CH2O}	91.03	93.28	91.11
				S_{CO2}	9.43	8.51	4.95
				S_{CO}	0.48	0.20	0.09
				S_{H2}	21.81	23.38	25.00
				C balance	100.82	101.71	97.30
				X_{O2}	100.00	96.09	71.06
				$v_{t,f}$, Nml/min	76.78	76.42	76.42
Flow Conditions	$v_{t,o}$, (Nml/min)	y_{in}	u_g (P_{avg},T) (m/s)	V_r (cm³)	0.00952	0.00386	0.0019
$v_{l,o}$=0.156 µl/s	41.67		9.70	Pin, bara	2.2	2.4	2.4
				Pavg, bar	1.9	2	2
	CH_3OH	0.0997		t, ms	9.09	3.88	1.91
	O_2	0.0414		X_{CH3OH}	90.01	90.03	74.01
	H_2O	0.0755		S_{CH2O}	88.16	87.55	106.85
				S_{CO2}	8.30	9.91	5.43
				S_{CO}	0.41	0.29	0.10
				S_{H2}	22.17	23.20	24.87
				C balance	97.19	97.97	109.16
				X_{O2}	100.00	98.63	81.39
				$v_{t,f}$, Nml/min	43.96	43.96	43.75

(continued)

Table A10. *continued.*

					R1, L_{Az}=8.81 cm	R2, L_{Az}=3.57 cm	R3, L_{Az}=1.78 cm
Flow Conditions	$v_{t,o}$, (Nml/min)	y_{in}	u_g (P_{avg},T) (m/s)	V_r (cm³)	**0.00952**	**0.00386**	**0.0019**
	29.12		6.78	Pin, bara	2	2.2	2.2
				Pavg, bar	1.8	1.9	1.9
	CH_3OH	0.0996		t, ms	13.00	5.55	2.73
	O_2	0.0414		X_{CH3OH}	89.46	92.52	79.52
	H_2O	0.0755		S_{CH2O}	87.25	88.63	91.18
$v_{l,o}$=0.107 µl/s				S_{CO2}	7.63	9.26	4.22
				S_{CO}	0.53	0.33	0.08
				S_{H2}	21.75	23.82	21.49
				C balance	95.90	98.35	96.41
				X_{O2}	100.00	96.54	86.36
				$v_{t,f}$, Nml/min	30.28	30.86	30.72

References

1. Agilent J&W GC Column Selection Guide. 2012.
2. Lebedeva SP, Likhtman TV, Rudenko BA, Shitkin VM: Study of a solution of formaldehyde in ethanol by gas chromatography. *Pharmaceutical Chemistry Journal* 1979, 13:664-666.

Appendix B

Benzyl Alcohol Oxidation in a Micro-Packed Bed Reactor Supplementary Information*

This appendix presents supporting information for the benzyl alcohol oxidation reaction system, including the following:

** Catalyst preparation carried out by Moataz Morad. Procedures also available from Morad M, Sankar M, Cao E, Nowicka E, Davies TE, Miedziak PJ, Morgan DJ, Knight DW, Bethell D, Gavriilidis A, Hutchings GJ:* ***Solvent-free aerobic oxidation of alcohols using supported gold palladium nanoalloys prepared by a modified impregnation method****. Catal.Sci.Technol. 2014,* ***4:****3120-3128.*

B1. Catalyst Preparation Procedures

Conventional Impregnation Method (C_{Im})

1 wt% Au-Pd bimetallic catalyst with 1:1 weight ratio of the metals on TiO_2 support

An aqueous solution of $HAuCl_4.3H_2O$ was dissolved in deionised water to form a solution with a gold concentration of 8.9 mg/ml. The requisite amount of solid $PdCl_2$ (0.016 g) was added to 1.123 ml of HAuCl4.$3H_2O$ and stirred vigorously at 80 flC for a few minutes until the palladium salt had apparently dissolved. The requisite amount of the support, 1.98 g, was then added to this solution under vigorous stirring conditions. The solution was agitated in this way until it formed a paste, which was then dried at 120 flC for 16h and then reduced at 400 flC for 4h under 5% H_2 in Ar.

Modified Impregnation Method Varying Cl ($M_{Im,\ vary}$)

1wt% Au-Pd bimetallic catalyst with 1:1 weight ratio of the metals on TiO_2 support

The modified impregnation catalyst synthesis is similar to the CIm catalyst method, but with the addition of excess HCl. An aqueous solution of $HAuCl_4.3H_2O$ was dissolved in deionised water to form a solution with a gold concentration of 8.9 mg/ml. The $PdCl_2$ salt was dissolved in a 0.58M aqueous HCl solution (36% concentration HCl, diluted using the requisite amount of deionised water) with gentle warming and vigorous stirring to form a solution with a Pd concentration of 6 mg/ml. This solution was cooled and used as the palladium precursor. The requisite amount of aqueous gold (8.9 mg ml^{-1}) and palladium solution (6 mg ml^{-1}; HCl concentration 0.58M) were charged into a 50 mL round-bottom flask fitted with a magnetic stirrer bar. The volume of the solution was adjusted using deionized water to a total volume of 15mL.

The flask was then immersed into an oil bath sitting on a magnetic stirrer hot plate. The solution was stirred vigorously at 1000 rpm and the temperature of the oil bath was raised from 27 °C to 60 °C over a period of 10 min. 1.98g of TiO_2 was added slowly over a period of 8-10min with constant stirring. After the completion of the addition of the support material, the slurry was stirred at 60 °C for an additional 15min. Following

this, the temperature of the oil bath was raised to 95 °C and the slurry was stirred at that temperature for a further 16h until all the water had evaporated, leaving a dry solid.

The solid powder was transferred into a mortar and pestle and was ground thoroughly to form a uniform mixture. This was stored and designated as a "dried only" sample. 400mg of the unreduced sample was transferred and spread out over a glass calcination boat (13cm in length). This boat was then put inside a calcination furnace fitted with an inlet and outlet valve. The temperature of the furnace was raised from 30 °C to 400 °C at a heating rate of 10 °C /min under a steady flow of 5%H2 in Ar. The sample was reduced at 400 °C for 4h under 5%H_2 in Ar or calcined in static air at 400 °C for 3h. Finally, the furnace was cooled in approximately (15 to 30 min) and this reduced sample was used as the M_{Im} varying Cl- catalyst.

Modified Impregnation Method Constant Cl ($M_{Im,\ const}$)

1wt% Au-Pd bimetallic catalyst with 1:1 weight ratio of the metals on TiO2 support

Aqueous gold $HAuCl_4.3H_2O$ (8.9 mg ml^{-1}) and palladium salt $PdCl_2$ and a fixed amount of Cl- (9.7×10^{-4} mol) from HCl solution were charged into a 50 mL round-bottom flask fitted with a magnetic stirrer bar. The volume of the solution was adjusted using deionized water to a total volume of 15mL. (*The remainder of the procedure is identical to the M_{Im} varying Cl method but will be presented for completion*). The flask was then immersed into an oil bath sitting on a magnetic stirrer hot plate. The solution was stirred vigorously at 1000rpm and the temperature of the oil bath was raised from 27 °C to 60 °C over a period of 10 min. Then, 1.98g of TiO2 (Degussa P25) was added slowly over a period of 8-10min with constant stirring. After the completion of the addition of the support material, the slurry was stirred at 60 °C for an additional 15min. Following this, the temperature of the oil bath was raised to 95 °C and the slurry was stirred at that temperature for a further 16h until all the water had evaporated, leaving a dry solid.

The solid powder was transferred into a mortar and pestle and was ground thoroughly to form a uniform mixture. This was stored and designated as a “dried only” sample. 400mg of the unreduced sample was transferred and spread out over a glass calcination boat (13cm in length). This boat was then put inside a calcination furnace fitted with an inlet and outlet valve. The temperature of the furnace was raised from 30 °C to 400 °C at a heating rate of 10 °C /min under a steady flow of 5%H2 in Ar. The sample was reduced at 400 °C for 4h under 5%H2 in Ar or calcined in static air at 400 °C for 3h. Finally, the furnace was cooled in approximately (15 to 30 min) and this reduced sample was used as the M_{Im} constant Cl- catalyst.

Table B1. *Composition of 1wt% Au Pd Conventional Imp. Calculations made per gram of catalyst.*

Au (wt/wt%)	0.00	0.05	0.10	0.15	0.20	0.25	0.30	0.35	0.40	0.45	0.50
Au in 1g catalyst (g)	0	0.0005	0.001	0.0015	0.002	0.0025	0.003	0.0035	0.004	0.0045	0.005
Pd (wt/wt%)	1.00%	0.95%	0.90%	0.85%	0.80%	0.75%	0.70%	0.65%	0.60%	0.55%	0.50%
Pd in 1g catalyst (g)	0.01	0.0095	0.009	0.0085	0.008	0.0075	0.007	0.0065	0.006	0.0055	0.005
$HAuCl_4.3H_2O$ Salt (g)	0.00E+00	1.00E-03	2.00E-03	3.00E-03	4.00E-03	5.00E-03	6.00E-03	7.00E-03	8.00E-03	9.00E-03	1.00E-02
PdCl2 Salt (g)	1.67E-02	1.58E-02	1.50E-02	1.42E-02	1.33E-02	1.25E-02	1.17E-02	1.08E-02	1.00E-02	9.16E-03	8.33E-03
$HAuCl_4.3H_2O$ Salt (mol)	0.00E+00	2.54E-06	5.08E-06	7.62E-06	1.02E-05	1.27E-05	1.52E-05	1.78E-05	2.03E-05	2.28E-05	2.54E-05
PdCl2 Salt (mol)	9.40E-05	8.93E-05	8.46E-05	7.99E-05	7.52E-05	7.05E-05	6.58E-05	6.11E-05	5.64E-05	5.17E-05	4.70E-05
Cl from Au salt (mol)	0.00E+00	1.02E-05	2.03E-05	3.05E-05	4.06E-05	5.08E-05	6.09E-05	7.11E-05	8.12E-05	9.14E-05	1.02E-04
Cl from Pd salt (mol)	1.88E-04	1.79E-04	1.69E-04	1.60E-04	1.50E-04	1.41E-04	1.32E-04	1.22E-04	1.13E-04	1.03E-04	9.40E-05
Total moles Cl	1.88E-04	1.89E-04	1.89E-04	1.90E-04	1.91E-04	1.92E-04	1.92E-04	1.93E-04	1.94E-04	1.95E-04	1.96E-04

Table B1. *continued.*

Au (wt/wt%)	0.55%	0.60%	0.65%	0.70%	0.75%	0.80%	0.85%	0.90%	0.95%	1.00%
Au in 1g catalyst (g)	0.0055	0.006	0.0065	0.007	0.0075	0.008	0.0085	0.009	0.0095	0.01
Pd (wt/wt%)	0.45%	0.40%	0.35%	0.30%	0.25%	0.20%	0.15%	0.10%	0.05%	0.00%
Pd in 1g catalyst (g)	0.0045	0.004	0.0035	0.003	0.0025	0.002	0.0015	0.001	0.0005	0
$HAuCl_4.3H_2O$ Salt (g)	1.10E-02	1.20E-02	1.30E-02	1.40E-02	1.50E-02	1.60E-02	1.70E-02	1.80E-02	1.90E-02	2.00E-02
PdCl2 Salt (g)	7.50E-03	6.67E-03	5.83E-03	5.00E-03	4.17E-03	3.33E-03	2.50E-03	1.67E-03	8.33E-04	0.00E+00
$HAuCl_4.3H_2O$ Salt (mol)	2.79E-05	3.05E-05	3.30E-05	3.55E-05	3.81E-05	4.06E-05	4.32E-05	4.57E-05	4.82E-05	5.08E-05
PdCl2 Salt (mol)	4.23E-05	3.76E-05	3.29E-05	2.82E-05	2.35E-05	1.88E-05	1.41E-05	9.40E-06	4.70E-06	0.00E+00
Cl from Au salt (mol)	1.12E-04	1.22E-04	1.32E-04	1.42E-04	1.52E-04	1.62E-04	1.73E-04	1.83E-04	1.93E-04	2.03E-04
Cl from Pd salt (mol)	8.46E-05	7.52E-05	6.58E-05	5.64E-05	4.70E-05	3.76E-05	2.82E-05	1.88E-05	9.40E-06	0.00E+00
Total moles Cl	1.96E-04	1.97E-04	1.98E-04	1.99E-04	1.99E-04	2.00E-04	2.01E-04	2.02E-04	2.02E-04	2.03E-04

Table B2. *Composition of 1wt% Au Pd Modified Impregnation (varying Cl). Calculations made per g of catalyst.*

Au (wt/wt%)	0.00%	0.05%	0.10%	0.15%	0.20%	0.25%	0.30%	0.35%	0.40%	0.45%	0.50%
Au in 1g catalyst (g)	0	0.0005	0.001	0.0015	0.002	0.0025	0.003	0.0035	0.004	0.0045	0.005
Pd (wt/wt%)	1.00%	0.95%	0.90%	0.85%	0.80%	0.75%	0.70%	0.65%	0.60%	0.55%	0.50%
Pd in 1g catalyst (g)	0.00E+00	1.00E-03	2.00E-03	3.00E-03	4.00E-03	5.00E-03	6.00E-03	7.00E-03	8.00E-03	9.00E-03	1.00E-02
$HAuCl_4.3H_2O$ Salt (g)	0.00E+00	1.00E-03	2.00E-03	3.00E-03	4.00E-03	5.00E-03	6.00E-03	7.00E-03	8.00E-03	9.00E-03	1.00E-02
PdCl2 Salt (g)	1.67E-02	1.58E-02	1.50E-02	1.42E-02	1.33E-02	1.25E-02	1.17E-02	1.08E-02	1.00E-02	9.16E-03	8.33E-03
$HAuCl_4.3H_2O$ Salt (mol)	0.00E+00	2.54E-06	5.08E-06	7.62E-06	1.02E-05	1.27E-05	1.52E-05	1.78E-05	2.03E-05	2.28E-05	2.54E-05
PdCl2 Salt (mol)	9.40E-05	8.93E-05	8.46E-05	7.99E-05	7.52E-05	7.05E-05	6.58E-05	6.11E-05	5.64E-05	5.17E-05	4.70E-05
Cl from Au salt (mol)	0.00E+00	1.02E-05	2.03E-05	3.05E-05	4.06E-05	5.08E-05	6.09E-05	7.11E-05	8.12E-05	9.14E-05	1.02E-04
Cl from Pd salt (mol)	1.88E-04	1.79E-04	1.69E-04	1.60E-04	1.50E-04	1.41E-04	1.32E-04	1.22E-04	1.13E-04	1.03E-04	9.40E-05
	Addition HCl from 0.58 M HCl solution										
Volume of (6 mg ml-1) solution used (ml)	1.67E+00	1.58E+00	1.50E+00	1.42E+00	1.33E+00	1.25E+00	1.17E+00	1.08E+00	1.00E+00	9.17E-01	8.33E-01
Volume of (6 mg ml-1) solution used (L)	1.67E-03	1.58E-03	1.50E-03	1.42E-03	1.33E-03	1.25E-03	1.17E-03	1.08E-03	1.00E-03	9.17E-04	8.33E-04
Cl from HCl solution (mol)	9.67E-04	9.18E-04	8.70E-04	8.22E-04	7.73E-04	7.25E-04	6.77E-04	6.28E-04	5.80E-04	5.32E-04	4.83E-04
Total moles Cl	**1.15E-03**	**1.11E-03**	**1.06E-03**	**1.01E-03**	**9.64E-04**	**9.17E-04**	**8.69E-04**	**8.22E-04**	**7.74E-04**	**7.26E-04**	**6.79E-04**

(continued)

Table B2. *continued.*

Au (wt/wt%)	0.55%	0.60%	0.65%	0.70%	0.75%	0.80%	0.85%	0.90%	0.95%	1.00%
Au in 1g catalyst (g)	0.0055	0.006	0.0065	0.007	0.0075	0.008	0.0085	0.009	0.0095	0.01
Pd (wt/wt%)	0.45%	0.40%	0.35%	0.30%	0.25%	0.20%	0.15%	0.10%	0.05%	0.00%
Pd in 1g catalyst (g)	1.10E-02	1.20E-02	1.30E-02	1.40E-02	1.50E-02	1.60E-02	1.70E-02	1.80E-02	1.90E-02	2.00E-02
$HAuCl_4.3H_2O$ Salt (g)	1.10E-02	1.20E-02	1.30E-02	1.40E-02	1.50E-02	1.60E-02	1.70E-02	1.80E-02	1.90E-02	2.00E-02
PdCl2 Salt (g)	7.50E-03	6.67E-03	5.83E-03	5.00E-03	4.17E-03	3.33E-03	2.50E-03	1.67E-03	8.33E-04	0.00E+00
$HAuCl_4.3H_2O$ Salt (mol)	2.79E-05	3.05E-05	3.30E-05	3.55E-05	3.81E-05	4.06E-05	4.32E-05	4.57E-05	4.82E-05	5.08E-05
PdCl2 Salt (mol)	4.23E-05	3.76E-05	3.29E-05	2.82E-05	2.35E-05	1.88E-05	1.41E-05	9.40E-06	4.70E-06	0.00E+00
Cl from Au salt (mol)	1.12E-04	1.22E-04	1.32E-04	1.42E-04	1.52E-04	1.62E-04	1.73E-04	1.83E-04	1.93E-04	2.03E-04
Cl from Pd salt (mol)	8.46E-05	7.52E-05	6.58E-05	5.64E-05	4.70E-05	3.76E-05	2.82E-05	1.88E-05	9.40E-06	0.00E+00
Addition HCl from 0.58 M HCl solution										
Volume of (6 mg ml-1) solution used (ml)	7.50E-01	6.67E-01	5.83E-01	5.00E-01	4.17E-01	3.33E-01	2.50E-01	1.67E-01	8.33E-02	0.00E+00
Volume of (6 mg ml-1) solution used (L)	7.50E-04	6.67E-04	5.83E-04	5.00E-04	4.17E-04	3.33E-04	2.50E-04	1.67E-04	8.33E-05	0.00E+00
Cl from HCl solution (mol)	4.35E-04	3.87E-04	3.38E-04	2.90E-04	2.42E-04	1.93E-04	1.45E-04	9.67E-05	4.83E-05	0.00E+00
Total moles Cl	**6.31E-04**	**5.84E-04**	**5.36E-04**	**4.89E-04**	**4.41E-04**	**3.93E-04**	**3.46E-04**	**2.98E-04**	**2.51E-04**	**2.03E-04**

Table B3. *Composition of 1wt% Au Pd Modified Impregnation (constant Cl). Calculations made per g of catalyst.*

Au (wt/wt%)	0	0.05	0.1	0.15	0.2	0.25	0.3	0.35	0.4	0.45	0.5
Au (g)	0	0.0005	0.001	0.0015	0.002	0.0025	0.003	0.0035	0.004	0.0045	0.005
Pd (wt/wt%)	1.00%	0.95%	0.90%	0.85%	0.80%	0.75%	0.70%	0.65%	0.60%	0.55%	0.50%
Pd (g)	0.01	0.0095	0.009	0.0085	0.008	0.0075	0.007	0.0065	0.006	0.0055	0.005
Total moles Cl	6.79E-04	6.79E-04	6.79E-04	6.79E-04	6.79E-04	6.79E-04	6.79E-04	6.79E-04	6.79E-04	6.79E-04	6.79E-04

Table B3*. continued.*

Au (wt/wt%)	0.55	0.6	0.65	0.7	0.75	0.8	0.85	0.9	0.95%	1.00%
Au (g)	0.0055	0.006	0.0065	0.007	0.0075	0.008	0.0085	0.009	0.0095	0.01
Pd (wt/wt%)	0.45%	0.40%	0.35%	0.30%	0.25%	0.20%	0.15%	0.10%	0.05%	0.00%
Pd (g)	0.0045	0.004	0.0035	0.003	0.0025	0.002	0.0015	0.001	0.0005	0
Total moles Cl	6.79E-04	6.79E-04	6.79E-04	6.79E-04	6.79E-04	6.79E-04	6.79E-04	6.79E-04	6.79E-04	6.79E-04

B2. Benzyl Alcohol Oxidation Analytical Procedure

Calibration for Liquid Phase Components

Whenever samples are handled or prepared, additional errors are introduced from the many variables involved with the sample preparation, such as: volume or weight measurement errors, losses on surfaces of containers or because of evaporation, contamination and transfer errors.

In addition to the errors introduced by sample preparation, there can also be variability inherent in the GC system and analysis method themselves. The highest variability in GC usually stems from sample introduction (injection + evaporation + transfer to the column). The *internal standard* (ISTD) method of calibration aims to compensate for these potential sources of errors. By adding a *surrogate* (compound of similar chemical attributes to the analyte of interest) of a known amount to the sample, prior to any sample preparation and/or analysis, the surrogate should experience the same changes as the analyte of interest. By developing a calibration curve based on the relative response of the target analytes to the amount of the surrogate, much of the variation can be removed.

The calibration procedure involved preparation of sample mixtures of different concentrations, ones that were representative of typical reaction mixtures, corresponding to 10%, 30%, 50% and 90% conversion and selectivity to benzaldehyde and toluene of approximately 65% and 20%, respectively (**Table B4**). 500µl of internal standard (3% butanol in o-xylene) was then added to 10 µl of the mixture prepared in **Table B 4**. The following calculation shows the generalised procedure for obtaining the calibration curve.

Concentration of component:

$$C_i = F_{i\times}A_i$$

Concentration of standard

$$C_{is} = F_{is\times}A_{is}$$

Ratio of concentrations:

$$\frac{C_i}{C_{is}} = \frac{F_i \times A_i}{F_{is} \times A_{is}}$$

Where C_i is the concentration of component i, C_{is} is the concentration of standard, F_i is the response factor of component i, F_{is} is the response factor for the standard, A_i is the GC peak area of component i, and A_{is} is the GC peak area of the standard. F_i/F_{is} is termed internal response factor (IRF). Calculating the concentration of the component is therefore

$$C_i = IRF \times \frac{A_i}{A_{is}} \times C_{is}$$

This equation relates the concentration of any component to its peak area and the concentration and peak area of the internal standard. During the calibrations, all concentrations and peak areas are known and the IRF is then calculated for each component. **Figure B1** shows results of the calibration.

The obtained concentrations were normalised according to a procedure that assumes that all the carbon entering the system exits (i.e. that the carbon balance closes). The normalisation procedure relies on the assumption that the total number of carbons is conserved in the chemical reaction.

Consider the reaction:

$$A \rightarrow B + C + D$$

Definitions

N_{atoms} = Number of carbon atoms

$N_{A,\ molecules}$ = Number of molecules of A

$C_{i,A}$ = moles of compound A per unit volume per unit time as calculated by GC.

The number of carbon atoms entering the system is calculated by:

$$N_{atoms,\ IN} = N_{atoms} \text{ in one molecule of compound A} * N_{A,\ molecules} \qquad (B\ 1)$$

The $N_{A,\ molecules}$ can be obtained from the number of moles of A through the relationship:

$$N_{A,\ molecules} = n_A * \text{Avogadro's constant } (6.022*10^{23}) \quad (B\ 2)$$

(Note: Avogadro's constant will cancel out in the calculation)

Combining equations *(B 1* and *(B 2*,

$$N_{atoms,\ IN} = N_{atoms} \text{ in one molecule of compound A} * n_A * 6.022*10^{23}$$

The number of carbon atoms exiting the system is a summation of the total number of carbons in the products:

$N_{B,\ atoms,\ OUT} = N_{atoms}$ in one molecule of compound B $* n_B * 6.022*10^{23}$

$N_{C,\ atoms,\ OUT} = N_{atoms}$ in one molecule of compound C $* n_C * 6.022*10^{23}$

$N_{D,\ atoms,\ OUT} = N_{atoms}$ in one molecule of compound D $* n_D * 6.022*10^{23}$

Example of applying the correction to component C

$$\textbf{\textit{Corrected mol of C}} = \underbrace{\frac{N_{atoms,IN}}{\sum N_{B,OUT}, N_{C,OUT}, N_{D,OUT}}}_{\text{Normalisation factor}} \times C_{c,A}$$

***Table B4**. Exemplary calculation of volumes added to calibration mixtures. Table shows yield calculations for a hypothetical situation of 10% benzyl alcohol conversion.*

	Retention Time (min)	Molecular Weight (g/mol)	Density (g/cm^3)	Benzyl Alcohol in Feed (mol/L)	Selectivity Fraction	Yield (mol/L)†	Mass (g)‡	Volume (µl)
Balcohol	8.58	108.14	1.045	0.00965	-	0.008689	0.9396	899.14
Baldehyde	6.55	106.2	1.044	-	0.65	0.000628	0.0666	63.83
Benzene	2.63	78.11	0.874	-	0.03	0.000029	0.0023	2.59
Toluene	3.05	92.14	0.865	-	0.2	0.000193	0.0178	20.57
DBE	11.15	198.26	1.043	-	0.04	0.000019	0.0038	3.67
Benzoic acid	11.37	122.12		-	0.04	0.000039	0.0047	4.72
Benzyl benzoate	12.85	212.24	1.118	-	0.04	0.000019	0.0041	3.67

† **Yield** = *Selectivity* × *Conversion* × *Mol Benzyl Alcohol in Feed*

‡ ***Mass*** = *Molecular weight* × *Yield*

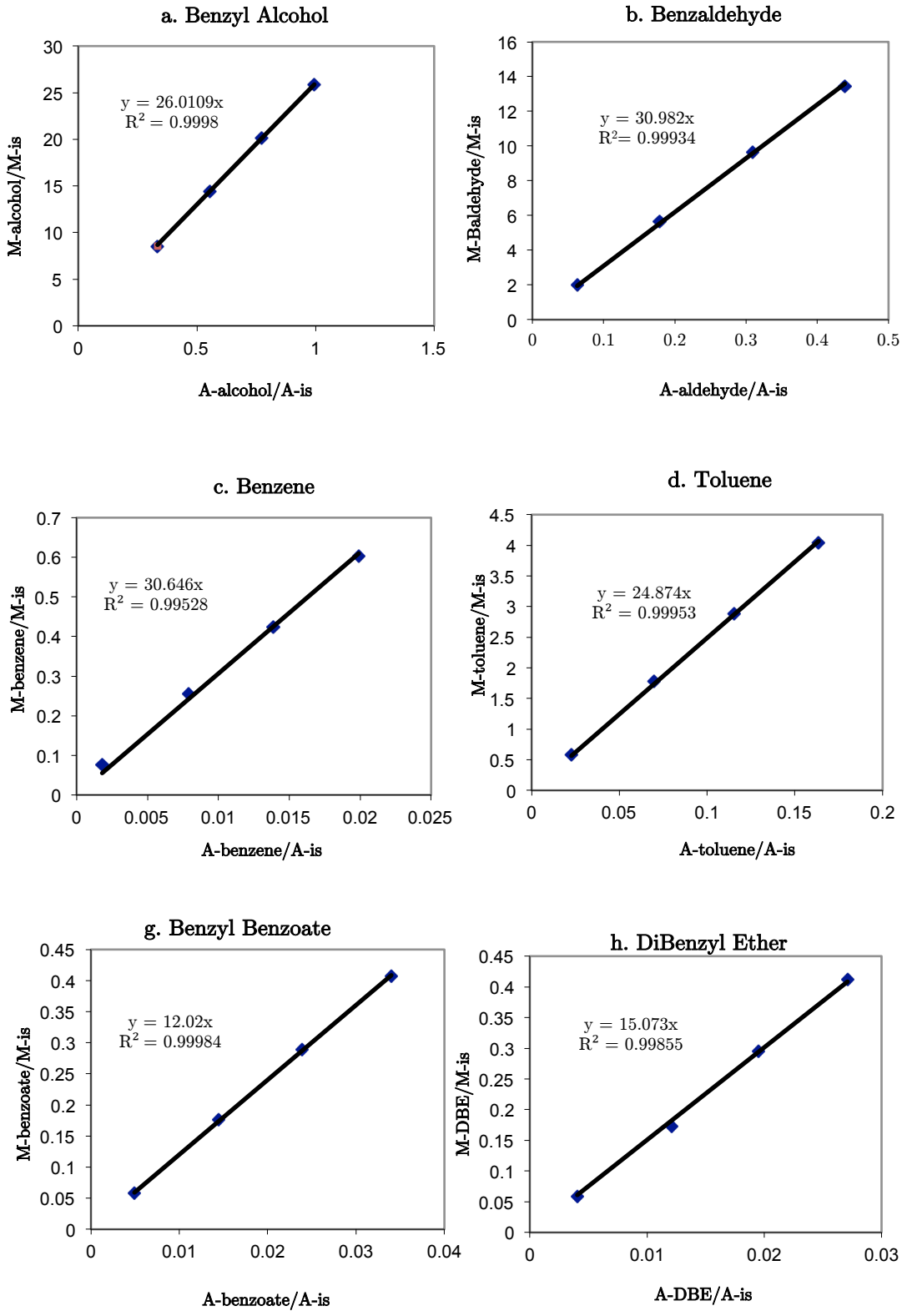

Figure B1. *Benzyl alcohol component calibration graphs.*

B3. Weisz-Prater Analysis

The influence of internal mass transfer on reaction was examined using the Weisz Prater criterion.

$$N_{W-P} = \frac{R_{v,i}^{obs} R_P^2}{C_{O_{2,s}} D_{eff}}$$

Various parameters were calculated to obtain the Weisz Prater number, details of which are shown below.

Concentration of Oxygen at the Catalyst Surface, $C_{O_{2,s}}$

$C_{O_{2,s}}$, the concentration of oxygen at the catalyst surface, was assumed to be equal to the bulk oxygen concentration in the benzyl alcohol. The mole fraction of oxygen in the benzyl alcohol medium, x_{O_2}, was calculated from the Henry's constant, H, based on the equation:

$$x_{O_2} = \frac{p_{O_2}}{H}$$

where p_{O_2} is the partial pressure of the gaseous solute above the solution. The Henry's constant used for oxygen dissolved in benzyl alcohol was 2440 bar (Unpublished data). The calculated value of $C_{O_{2,s}}$ was 7.92×10^{-6} mol/cm^3.

Effective Diffusivity, D_{eff}

D_{eff}, the effective diffusivity of the oxygen molecules in the liquid-filled pores, was evaluated by applying a series of correction factors to the diffusivity of the solute molecule in the bulk liquid phase, D_b, as proposed by Ternan (1987) [1]:

$$D'_{eff} = D_b \frac{(1-\lambda)^2}{1+P\lambda}$$

Where λ is the ratio of the radius of the diffusing molecule to the pore radius (i.e. $\frac{r_{molecule}}{r_{pore}}$) and P is a fitting parameter determined individually for the catalyst using data in the literature, where values of 2 - 16.5 are possible, depending on the pore size, temperature, polarity of the solvent, and shape of the molecule; a value of 11 is used in

the following calculation due to the similarity in pore size of the particles to the data from which the P value is derived [2]. Average pore radius r_{pore} was obtained from BET results and was found to be 10nm.

In the evaluation of the effectiveness factor, the effective diffusivity based on the entire catalyst particle, D_{eff}, is needed. The relationship between D_{eff} and D'_{eff} can be expressed as:

$$D_{eff} = \varepsilon D'_{eff}$$

Where ε is the porosity, estimated to be 0.4 [2].

Bulk Diffusivity, D_b

The bulk diffusivity of oxygen in benzyl alcohol, D_b, is calculated using a correlation by Wilke and Chang [3], usually used when the mole fraction of the gas in the liquid is very low. The bulk diffusivity of solute 1 in solvent 2, D_{12}^0 is:

$$D_b = D_{12}^0 = 1.1728\times10^{-16}\frac{T\sqrt{\chi M_2}}{\eta_2 V_1^{0.6}}$$

where χ is the solvent association parameter, M is the molecular weight, V is the molar volume, T is the temperature, and η is the viscosity. D_b was calculated to be 6.99E-09 m^2/s, while D_{eff} was calculated to be 5.69E-09 m^2/s.

Table B5. *Physical properties of Oxygen and Benzyl alcohol used in calculation of D_b.*

χ[4]	T (K)	η_2 (@ 393K) (kg/m^{2}s)	V_1 [5] (m^3/kmol)	M_2 (kg/kmol)
1	393	5.86E-04	0.028	108.14

Table B6. *Effective diffusivity of oxygen in benzyl alcohol at 393K using correlation 2.*

P	$r_{molecule}$ (nm)	r_{pore} (nm)	$\lambda = \frac{r_{molecule}}{r_{pore}}$	D_b (m^2/s)	D'_{eff} (m^2/s)	D_{eff} (m^2/s)
11	0.12	10.06	0.012	6.99E-09	6.03E-09	2.41E-09

Observed Oxygen Reaction Rate, $R_{v,i}^{obs}$

$R_{v,i}^{obs}$, the observed reaction rate of oxygen, was calculated for the liquid dominated flow regime. Since the measured conversion is the benzyl alcohol conversion, the oxygen reaction rate had to be delineated from this information. The dual reaction scheme is presented below:

$$PhCH_2OH + \frac{1}{2}O_2 \rightarrow PhCHO + H_2O \quad (\textbf{\textit{Reaction}}\ \mathbf{1}\text{: Oxidation})$$

$$2PhCH_2OH \rightarrow PhCHO + PhCH_3 + H_2O \ (\textbf{\textit{Reaction}}\ \mathbf{2}\text{: Disproportionation})$$

Since disproportionation of benzyl alcohol results in an equimolar mixture of benzaldehyde and toluene, while the oxidation reaction produces benzaldehyde exclusively, the oxygen reaction rate can be calculated from the total benzyl alcohol conversion, X_B, by using the following equation:

$$R_{oxid}\left[\frac{mol}{g.s}\right] = F_{B0}\left[\frac{mol}{s}\right] \times X_B \times (S_{ald} - S_{tol})/2g_{cat}[g]$$

Where S_{ald} is the selectivity to benzaldehyde, S_{tol} is the selectivity to toluene, F_{B0} is the inlet molar flowrate of benzyl alcohol and g_{cat} is the mass of catalyst used. $R_{v,i}^{obs}$ is then obtained as a reaction rate per cm^3 from R_{oxid} by using the catalyst bulk density of $0.72 g/cm^3$.

The calculation is carried out under the gas-continuous regime, where there are no external mass transfer resistances, and thus the W-P criterion would apply. A typical value for $R_{v,i}^{obs}$ under the gas-continuous (fully wetted) flow regime is 1.55. For values of W-P below 0.3, the entire particle is available for reaction with oxygen, while for values of >4 the entire particle is starved of reactant. For the W-P value calculated, it can be concluded that there are some internal diffusional limitations present that are not rate limiting.

Table B7. *Calculation of $R_{v,i}^{obs}$ for the different flow regimes.*

Catalyst Mass, g_{cat} (mg)	1
Gas Flowrate, G (ml/min)	3
Liquid Flowrate, L (µl/min)	0.75
Benzyl Alcohol Conversion, X_B	0.97
Benzaldehyde Selectivity, S_{ald}	0.77
Toluene Selectivity, S_{tol}	0.175
Benzyl Alcohol Molar Flowrate, F_{A0} (mol/s)	1.21E-07
Total Reaction Rate, R_{total} (mol/cm^{3}s)	8.43E-05
Oxidation Reaction Rate, $R_{v,i}^{obs}$ (mol/cm^{3}s)	2.49E-05

Table B8. *Components of the calculation of Weisz-Prater number.*

Flow Regime	$R_{v,i}^{obs}$ (mol/cm^{3}s)	R_p (cm)	$C_{O_{2,s}}$ (mol/cm^3)	Weisz-Prater
Gas-continuous (fully wetted)	2.49E-05	3.45E-03	7.92E-06	1.55

B4. Kinetic Parameter Estimation*

Sankar et el. [6] presented a general mechanism for the overall benzyl alcohol oxidation reaction. The mechanism is based on the two stoichiometric reactions:

$$2PhCH_2OH \rightarrow PhCHO + PhCH_3 + H_2O$$

$$PhCH_2OH + \frac{1}{2}O_2 \rightarrow PhCHO + H_2O$$

Initial rates experiments in a batch reactor using oxygen only, helium only, varying oxygen pressure, as well as experiments assessing the effect of diluent, all at 80°C were conducted in the referenced paper. The general expression presented by Sankar et al. was:

$$v_x = \frac{C * [BzOH]}{K_D^B + [BzOH]} * \left\{k_{1x} + \frac{k_{2x} * [O_2]}{K_D^O + [O_2]}\right\}$$

where v_x (mol/s) is the rate of change of concentration of X (reactant disappearance or product formation), characterized by the rate coefficients $\boldsymbol{k_{1X}}$ and $\boldsymbol{k_{2X}}$ for the reaction in the absence and presence of O_2. The authors present $\mathbf{C}$ as the total number of catalytic sites on the surface, proportional to the weight of catalyst. Here we define C for 0.02 g catalyst. $\mathbf{K_D^B}$ and $\mathbf{K_D^O}$ are dissociation constants for benzyl alcohol and oxygen from the adsorbed state (mol/kg). $[O_2]$ and $[BzOH]$ are the substrate concentrations (mol/kg).

Here we use the Henry's constant H (89.2 MPa) of (toluene+O_2) at 75 ° C. Therefore, the mol fraction of oxygen x_{O_2} (mol_{O_2}/mol_{sol}) can be calculated through the following equation:

---

* *Parameter estimation work carried out by Gaowei Wu, UCL.*

$$x_{O_2} = \frac{p_{O_2}}{H}$$

In 1 g BzOH solution,

$$[O_2] = \frac{x_{O_2 *} n_{sol}}{m_{sol}} = \frac{x_{O_2 *} \frac{1}{108}}{0.001} \; mol/_{kg}$$

Effect of diluent for the reaction at 1 bar O_2 (catalyst:0.02g, P_{O2}=1 bar)

Using the data presented in the paper by Sankar et al. [6] on the effect of diluent on reaction rate at 1 bar oxygen (***Table B9***), and defining a constant M_2 as:

$$M_2 = k_{1x} + \frac{k_{2x} * [O_2]}{K_D^O + [O_2]} = constant$$

(as in this set of experiments, the oxygen concentration does not change) v_x then becomes:

$$v_x = \frac{C * [BzOH]}{K_D^B + [BzOH]} * M_2$$

Rearranging,

$${v_x}^{-1} = \frac{K_D^B}{M_2 C} * \frac{1}{[BzOH]} + \frac{1}{M_2 C}$$

Plotting ${v_x}^{-1}$ vs $\frac{1}{[BzOH]}$ therefore yields a graph with a slope of $\frac{K_D^B}{M_2 C}$ and an intercept of $\frac{1}{M_2 C}$ (**Figure B2**).

Table B9. *Effect of diluent for the benzyl alcohol oxidation reaction under 1 bar oxygen, taken from [6].*

	Benzyl alcohol		Benzaldehyde		Toluene	
BzOH : *o*-Xy (w/w)	d[BzOH]/d*t*/ $\times 10^{-7}$ mol s^{-1}	R^2	d[Ald]/d*t*/$\times 10^{-7}$ mol s^{-1}	R^2	d[Tol]/d*t*/$\times 10^{-7}$ mol s^{-1}	R^2
100 : 0	−5.420 ± 0.46	0.986	4.808 ± 0.46	0.982	0.755 ± 0.15	0.95
75 : 25	−4.577 ± 0.37	0.99	3.980 ± 0.38	0.986	0.567 ± 0.08	0.972
50 : 50	−3.158 ± 0.15	0.997	2.742 ± 0.14	0.996	0.417 ± 0.03	0.992
25 : 75	−2.462 ± 0.26	0.984	2.218 ± 0.22	0.986	0.243 ± 0.04	0.96
15 : 85	−1.815 ± 0.15	0.989	1.680 ± 0.14	0.986	0.134 ± 0.01	0.987

[a] Substrate mixture: 1 g; catalyst: 0.02 g; temp: 80 °C; stirring: 1000 rpm; O_2: 1 bar.

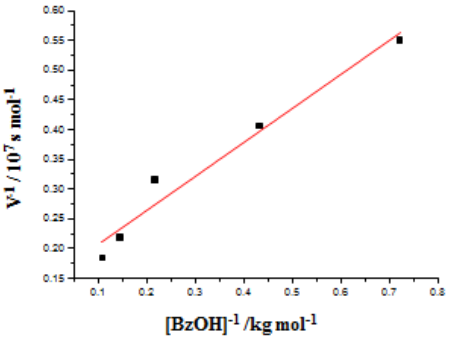

Y=0.14952+0.5728*X, R_2=0.9547

So:
M_2C=6.7 *10^{-7} mol/s
K_B=3.8 mol/kg

Figure B2. *Plot of* v_x^{-1} *vs* $\frac{1}{[BzOH]}$ *using data presented in* ***Table B9.***

Effect of diluent for the reaction at 1 bar He (catalyst:0.08g, P_{O2}=0 bar)

Using the data presented in the paper by Sankar et al. [6] on the effect of diluent on reaction rate at 1 bar helium (**Table B10**), and equating the terms in the rate equation that include oxygen to zero:

$$\frac{k_{2x} * [O_2]}{K_D^O + [O_2]} = 0$$

v_x then becomes

$$v_x = \frac{4C * [BzOH]}{K_D^B + [BzOH]} * k_{1x}$$

Rearranging,

$$v_x{}^{-1} = \frac{K_D^B}{4Ck_{1x}} * \frac{1}{[BzOH]} + \frac{1}{4Ck_{1x}}$$

Table B10. *Effect of diluent for the benzyl alcohol oxidation reaction under 1 bar oxygen, taken from [6].*

	Benzyl alcohol		Benzaldehyde		Toluene	
BzOH : *o*-Xy (w/w)	d[BzOH]/d*t*/ $\times 10^{-7}$ mol s^{-1}	R^2	d[Ald]/d*t*/$\times 10^{-7}$ mol s^{-1}	R^2	d[Tol]/d*t*/$\times 10^{-7}$ mol s^{-1}	R^2
100 : 0	−4.925 ± 0.430	0.989	2.725 ± 0.373	0.973	2.20 ± 0.3	0.973
75 : 25	−3.198 ± 0.323	0.980	1.833 ± 0.19	0.979	1.418 ± 0.151	0.983
50 : 50	−2.690 ± 0.393	0.960	1.487 ± 0.232	0.955	1.202 ± 0.163	0.963
25 : 75	−1.657 ± 0.076	0.997	0.913 ± 0.005	0.995	0.745 ± 0.006	0.989
15 : 85	−1.591 ± 0.062	0.999	0.840 ± 0.005	0.997	0.751 ± 0.001	0.999

[a] Catalyst: 0.08 g; substrate mixture: 1 g; He: 1 bar; stirring: 1000 rpm.

Plotting $v_x{}^{-1}$ vs $\frac{1}{[BzOH]}$ therefore yields a graph with a slope of $\frac{K_D^B}{4Ck_{1x}}$ and an intercept of $\frac{1}{4Ck_{1x}}$ (**Figure B3**).

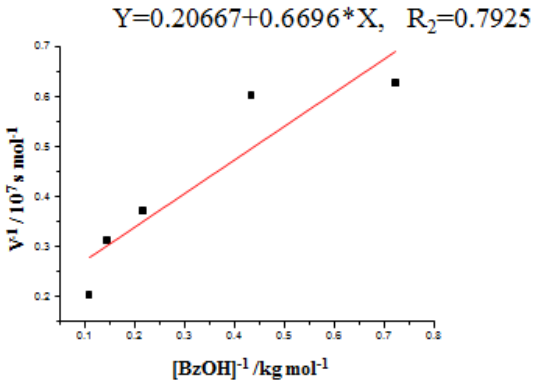

So:
$k_{1x}C=1.21 \ *10^{-7}$ mol/s
$K_B=3.24$ mol/kg

Figure B3. *Plot of* v_x^{-1} *vs* $\frac{1}{[BzOH]}$ *using data presented in* **Table B10.**

Effect of atmosphere on the reaction (BzOH:1g, catalyst:0.02g)

The concentration of benzyl alcohol $[BzOH]$ expressed in mol/kg is obtained through the following:

$$[BzOH] = \frac{m_{Bz}}{108\frac{g}{mol} * 0.001 kg_{sol}}$$

Setting $\frac{[BzOH]}{K_B+[BzOH]}$ to a constant M_1 as this does not vary in the experiments specified in **Table B11:**

$$M_1 = \frac{[BzOH]}{K_B + [BzOH]} = \frac{9.247}{3.8 + 9.247} = 0.7087$$

Table B11. *Effect of oxygen pressure for the benzyl alcohol oxidation reaction using 1g of BzOH, taken from [6].*

	Benzyl alcohol	
Gas/*P*	d[BzOH]/d*t*/×10⁻⁷ mol s⁻¹	R^2
~~He~~	~~−0.795 ± 0.04~~	~~0.959~~
Air	−2.288 ± 0.17	0.989
O_2/1 bar	−5.420 ± 0.46	0.986
O_2/2 bar	−6.440 ± 0.29	0.996
O_2/3 bar	−6.313 ± 0.38	0.995

[a] Benzyl alcohol: 1 g; catalyst: 0.02 g; te

Vx	$1/(v_X/M_1-k_{1x}*C)$	P_{O2}	$[O_2]$	$1/[O_2]$
~~0.795~~	~~-11.3989~~	~~0~~	~~0~~	
2.288	0.4953	0.21	0.00218	458.7428571
5.42	0.1553	1	0.01038	96.336
6.44	0.1269	2	0.020761	48.168
6.313	0.1298	3	0.031141	32.112

From a previous calculation, we already know $k_{1x}C=1.21*10^{-7}$ mol/s

$$v_x = CM_1 * \left\{k_{1x} + \frac{k_{2x} * [O_2]}{K_O + [O_2]}\right\}$$

Therefore,

$$\frac{v_x}{M_1} - Ck_{1x} = \frac{Ck_{2x} * [O_2]}{K_O + [O_2]}$$

Rearranging,

$$\frac{1}{\frac{v_x}{M_1} - Ck_{1x}} = \frac{K_O + [O_2]}{Ck_{2x} * [O_2]} = \frac{K_O}{Ck_{2x}} * \frac{1}{[O_2]} + \frac{1}{Ck_{2x}}$$

Plotting $\frac{1}{\frac{v_x}{M_1} Ck_{1x}}$ vs $\frac{1}{[O_2]}$ therefore yields a graph with a slope of $\frac{K_O}{Ck_{2x}}$ and an intercept of $\frac{1}{Ck_{2x}}$ (**Figure B4**).

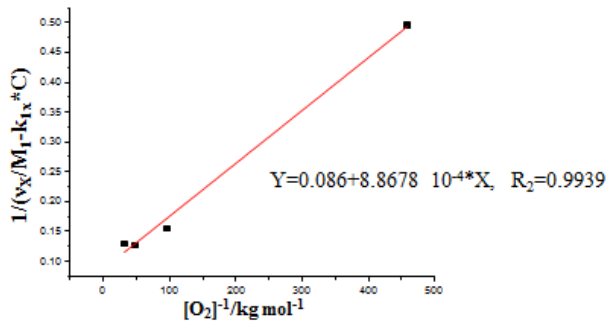

So:
$k_{2x}C=11.63*10^{-7}$ mol/s
$K_o=0.01031$ mol/kg

Figure B4. *Plot of* $\frac{1}{\frac{v_x}{M_1}-Ck_{1x}}$ *vs* $\frac{1}{[O_2]}$ *using data presented in* ***Table B11.***

We therefore obtain the rate equation for the initial reaction rate:

$$v_x = \frac{m_{cat}}{0.02} * \frac{[BzOH]}{3.8 + [BzOH]} * \left\{1.21 + \frac{11.63 * [O_2]}{0.01031 + [O_2]}\right\} * 10^{-7}$$

v_x: mol/s; [BzOH]/[O_2]: mol/kg; m_{cat}: g

References

[1] Ternan, M. 1987. The diffusion of liquids in pores. *Can. J. Chem. Eng* 65, 244.

[2] Satterfield, N.C. et al. 1973. Restricted diffusion in liquids within fine pores. AIChE Journal 19, 628.

[3] Wilke, C.R., Chang, P. 1955. Correlation of diffusion coefficients in dilute solutions. *AIChE J.* 1, 264.

[4]Vannice, M, A., 2005. Kinetics of Catalytic Reactions. Springer Science+Business Media, New York.

[5] Daubert, T.E., Danner, R.P. 1985. Data compilation tables of properties of pure compounds. Design Institute for Physical Property Data – American Institute of Chemical Engineers (DIPPR-AIChE), New York.

[6] Sankar M, Nowicka E, Tiruvalam R, He Q, Taylor SH, Kiely CJ, Bethell D, Knight DW, Hutchings GJ. 2011. Controlling the Duality of the Mechanism in Liquid-Phase Oxidation of Benzyl Alcohol Catalysed by Supported AuGÇôPd Nanoparticles. *Chem.Eur.J.* 17:6524-6532.

Appendix C

On-Chip RTD Measurements using Raman Spectroscopy Supplementary Information

This appendix presents supporting information for the on-chip RTD measurement using Raman Spectroscopy, including the following:

C1. Method Validation using Liquid Phase RTD Measurements

Data Processing Steps with Example F, E(t) and E(θ) curves

The steps involved in calculation of the F(t), E(t), and E(θ) curves are shown in **Figure C1**. Inaccuracies in the Raman signal peak integration are evident towards the end of the step signal curve where a few outliers above the main step curve are visible (**Figure C1a**). This was later resolved as will be shown in **section C2** by improving the peak area integration method using OriginPro. The broadening of the E(t) curve is shown in **Figure C1b** due to the added dispersion taking place in the reactor.

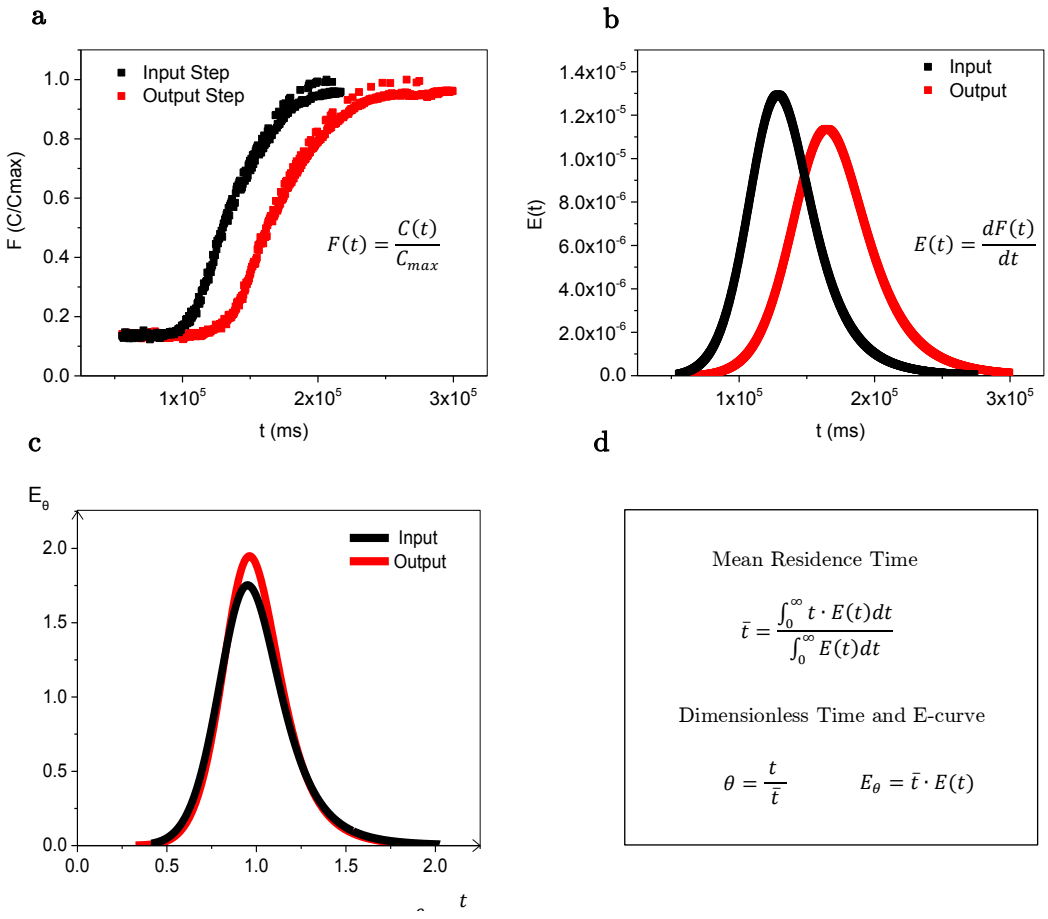

Figure C 1. *(a) Exemplary input and output F-curves acquired from the step signals (b) corresponding E(t) and (c) E(θ) curves (d) equations used in the calculation of the mean residence time, dimensionless E(θ) and dimensionless time θ.*

C2. Gas-Liquid RTD Measurements

*Data Processing Steps with Example F(t) and E(**θ**) curves*

The F(t) curves for the gas-liquid RTD curves presented in **Chapter X** are shown in **Figure C2**. The corresponding dimensionless E(θ) curves are shown in **Figure C3**. The improvement in the signal processing of the tracer concentration is evident in **Figure C2**, in comparison to the previous scatter observed in **Figure C1**.

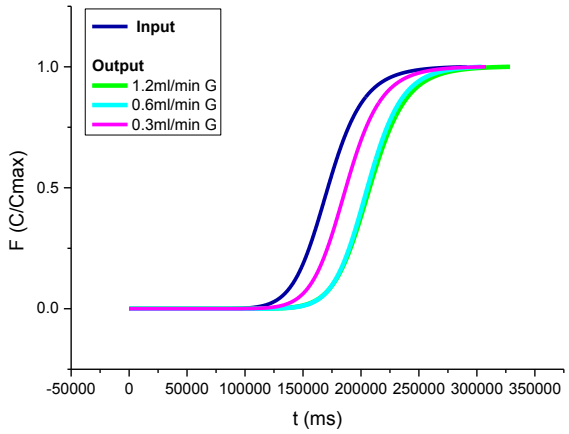

Figure C2. *F(t) curves corresponding to* ***Figure 10.9****. F-curves for the input signal as well as output signals at various gas flowrates are presented.*

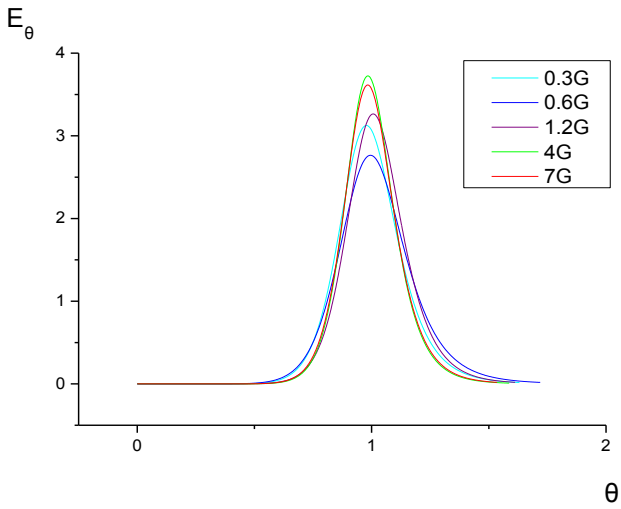

Figure C3*. E(θ) curves for gas-liquid flow at varying gas flowrates.*